Hybrid Simulation of Wind Turbine Blades

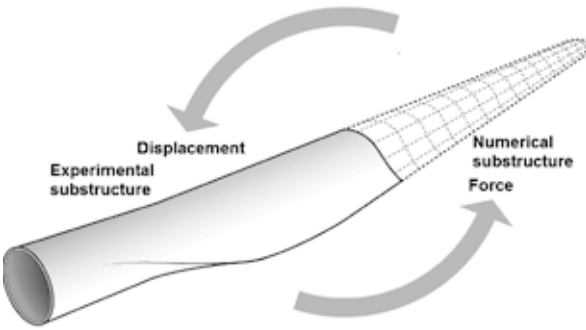

Jacob Paamand Waldbjørn

PhD Thesis

Department of Civil Engineering
2016

DTU Civil Engineering Report - R-354

DTU Civil Engineering
Department of Civil Engineering

Title Page for the PhD Dissertation

Hybrid Simulation of Wind Turbine Blades

A dissertation presented
by

Jacob Paamand Waldbjørn
Department of Civil Engineering
Technical University of Denmark
April 2016

A thesis submitted in partial fulfilment
of the requirements for the degree of
Doctor of Philosophy

FrontPage illustration is visualized by KIRT x THOMSEN

This page is intentionally left blank

Preface and acknowledgement

This thesis is submitted in partial fulfilment of the requirements for the Danish degree of Doctor of Philosophy (PhD). The PhD thesis includes the scientific work undertaken during the PhD study and the results achieved. The presented work was primary carried out at the department of Civil Engineering, Technical University of Denmark (DTU) with associated professor Jacob Wittrup Schmidt as the principle supervisor. Additionally, professor Henrik Stang and associated professor Christian Berggreen were acting as co-supervisors. Furthermore, an external stay at Lyles School of Civil Engineering, Purdue University has been organized as a part of this PhD study. The stay was completed under the guidance of professor Shirley Dyke in close corporation with members of her PhD group. The PhD study was financially supported by the Danish Centre for Composite Structures and Materials for Wind Turbines (DCCSM) funded by the Danish Council for Strategic Research within Sustainable Energy and Environment (grant 09-067212) and DTU. Furthermore, funding were granted by the COWI and Otto Moensted Foundation to partially cover the expenses for the external stay abroad and courses related to this PhD study.

First sincere thanks are directed towards the sponsors of this PhD study. Without their financial support, this work would not have been possible. I also acknowledge the support from my supervisor team.

A great gratitude goes to my current and former colleagues at the department of Civil Engineering, section for structural engineering for creating a comfortable and relaxing work atmosphere for the entire duration of the PhD study. Furthermore, great thanks are directed towards professor Shirley Dyke and members of her PhD group for hosting me and for being a great inspiration and support throughout my external stay at Purdue University.

Amin Maghareh is greatly acknowledged for his hospitality and support during my external stay at Purdue University. I really enjoyed the valuable discussions we had along with the essential technical assistance you provided. I hope we will maintain contact in the future.

Last but not least very special thanks goes to my beloved wife and children for being supportive, understanding and patient during my occasionally very stressful period as a PhD student.

Lyngby, April 2016

Jacob Paamand Waldbjørn

Preface to the published version of the thesis

The thesis was defended in public the 12 of September 2016. Official opponents were Professor Kristian Dahl Hertz, Technical University of Denmark; Dr. Shawn You, MTS Systems, USA; Professor Riadh Al-Mahaidi, Swinburne University of Technology, Australia.

Minor editorial changes has been implemented compared to the original version of the thesis.

Lyngby, October 2016

Jacob Paamand Waldbjørn

Abstract

Wind turbines are progressively used as a substitute to fossil fuels enhancing the demand for larger and more energy efficient wind turbine blades. These wind turbine blades are typically made from composite materials among those glass and carbon fibre reinforced plastics along with lightweight cores. Hence, the ambition to improve the structural and operational performance of the wind turbine blade has resulted in extensive research within large composite structures. In these efforts testing has primary been focusing on two length scales including laminate and structural scale testing. However, to reveal the structural response of the wind turbine blade during service, experimental testing covering length scales from micro through structural scale testing is required. To establish a link between laminate and structural scale testing within the industry of wind energy a Hybrid Simulation (HS) technique is implemented which facilitates substructural scale testing.

Structural assessment through HS is a substructural technique where the behaviour of emulated structure is revealed by combining the advantages of numerical modelling with those of experimental testing. The coupling governed through the interface between the numerical and experimental substructure – referred to here as the shared boundary – is achieved by maintaining compatibility and equilibrium at the interface. During the test, a predefined external load is applied the numerical substructure and the corresponding response computed. Through a communication loop, the displacement at the shared boundary is induced on the experimental substructure through an e.g. Proportional Integral Derivative (PID) regulated servo-hydraulic actuator – referred to here as the transfer system. The forces required to deform the experimental substructure – referred to here as the reaction force – are fed back to the numerical substructure to reveal the response of the emulated structure. The experimental and numerical substructure, communication loop and transfer system combine to form the HS.

The research within HS has to date expanded upon numerous branches including civil and mechanical engineering – referred to here as conventional HS. Common to conventional HS is that the shared boundary is defined by a discrete point operated within a few Degree-Of-Freedom (dof)s. This configuration has become a mature and reliable approach however; it imposes some limitations in the effort of spreading the HS technique within new application areas including large composite structures. Therefore, a new generation of HS is presented capable of handling a shared boundary covering a continuous edge or plane – referred to here as single-component HS. The implementation of single-component HS induces some distinctive challenges in the experimental substructure including compliance in the transfer system driven by slack and deformations in the load train and boundary introduction zone along with inertia effects induced by the mass of the load train and boundary introduction zone. These errors governs a significant impact on the accuracy and stability within single-component HS, hence two compensators are introduced named high precision tracking compensator and inertia compensator. The high precision compensator is capable of reducing the discrepancy between the desired and achieved displacement by tracking the shared boundary through an external Data Acquisition (DAQ) system using i.a. Digital Image Correlation (DIC). The compensator proved successful in both the Quasi-Static (QS) and Real-Time (RT) regime. The inertia compensator revealed sound performances in erasing the majority of the inertia effects induced by the mass of the load train and load introduction zone in the RT regime.

A communication loop capable of accommodating single-component HS in the QS and Pseudo-Dynamic (PsD) regime is designed and implemented in the Laboratory Engineering Workshop (LabVIEW). Here the numerical substructure, transfer system capable of operating the experimental substructure on an extended time scale along with relevant interface compensators are operated sequentially in a state-machine framework. This configuration provides a simple and flexible multi-processing platform, which is easy to extend and modify throughout the design phase. The system architecture is successfully verified through a single-component and conventional HS application.

To reveal the inherent dynamics of the experimental substructure a Real-Time Hybrid Simulation (RTHS) communication loop capable of accommodating single-component applications is designed and implemented in

LabVIEW. To attain a continuous time history of displacement, velocity or acceleration at the shared boundary an operation rate that is 10-25 times faster than the mode of interest is required. Given the enhanced complexity of the numerical model within single-component HS, an integration time equivalent to the required operation rate of the experimental substructure, can be difficult to attain. Hence, a multi-rate Real-Time Hybrid Simulation (mrRTHS) approach is implemented capable of operating the numerical and experimental substructure at two different rates while including rate transitioning to link the substructure appropriately. Here the numerical substructure, transfer system capable of operating the experimental substructure with RT constraints along with relevant compensators is operated in parallel across multiple threads. Implemented on a RT-target which provides reduced latency and tight jitter tolerances the system architecture is successfully verified through a single-component and conventional HS application.

A representative experimental substructure of an SSP34m wind turbine blade is identified through a numerical analysis for evaluating the increase of stresses in the leading edge governed by the cross section of the blade being distorted in transverse shear. Here an 8m root section of the wind turbine blade is identified as a representative substructure, capable of physically replicating the cross sectional shear distortion. Furthermore, a boundary introduction zone of 6m is added to erase the distortion induced by the load train, entailing that the entire experimental substructure covers the inner 14m root section of the wind turbine blade. A fatigue rated multi-axial test setup is designed to accommodate the inner 14m inner root section of the wind turbine blade. Finally an initial HS architecture and strategy is presented to form the basis for an upcoming single-component HS on the SSP34m wind turbine blade.

Altogether, this PhD thesis presents a single-component HS approach, which aims to form an important milestone in the effort of extending the application portfolio within HS for structural assessment of large composite structures. Two compensation techniques were designed capable of enhancing the accuracy and stability within single-component HS. A communication loop capable of accommodating single-component HS were designed and implemented in LabVIEW. The system proved successful within the QS and RT regime for the operation of a shared boundary including a discrete point with up to three dofs. The presented work is based upon seven appended papers along with related research activities, which were not possible to convey through scientific publications.

Resume

Vindmøller anvendes i stigende grad som erstatning til fossile brændstoffer, hvilket øger efterspørgslen på større og mere energieffektive vindmøllevinger. Disse vindmøllevinger er typisk lavet af kompositmaterialer herunder glas og kulfiber forstærket plast materialer kombineret med en letvægts kerne af skum eller lign. Derfor har ambitionen om at forbedre den strukturelle og operationelle virkningsgrad af vindmøllevingen resulteret i omfattende forskning inden for kompositkonstruktioner. I disse bestræbelser har testning a vindmøllevinger været fokuseret indenfor laminat og fuld skala forsøgsprøvning. Men for fuldt ud at afdække det strukturelle respons af vindmøllevinger, er det fundet nødvendigt at udføre strukturel forsøgsprøvning der dækker fra materialeforståelse via nano/micrometerskala til testning af fulde konstruktioner på dekameter skala. For delvist at imødekomme dette krav er en hybrid testning metode introduceret som en effektiv forsøgsmetode til substrukturel testning af vindmøllevinger.

Hybrid testning er en substrukturel forsøgsprøvning teknik, hvor det strukturelle respons af den fulde konstruktion er afdækket ved at kombinere fordelene ved numerisk modellering og forsøgsprøvning. Koblingen mellem de to del konstruktioner - benævnt her som den fælles rand - opnås ved at opretholde ligevægt på den fælles rand. Under testen er en foruddefineret ekstern belastning påført den numeriske del konstruktion og det tilsvarende respons beregnet. Gennem et kommunikations loop er flytningen på den fælles rand induceret på den eksperimentelle del konstruktion gennem f.eks. en servo-hydraulisk aktuator. De kræfter, der kræves for at deformere den eksperimentelle del konstruktion - nævnt her som reaktionskraften - føres tilbage til den numeriske del konstruktion for at afdække det fulde respons. Den eksperimentelle og numeriske del konstruktion, kommunikation loop og servo hydraulisk aktuator kombineres for at danne en hybrid test.

Hybrid testning er en kendt forsøgsprøvningsmetode indenfor flere forskellige brancher, herunder bygge og maskinindustrien - nævnt her som konventionel hybrid testning. Fælles for konventionel hybrid testning er at den fælles rand er defineret ved et diskret punkt, som styres med få friheds grader. Denne konfiguration er gennem årende blevet en kendt og pålidelig test metode som dog introducere nogle begrænsninger i bestræbelserne på at implementere hybrid test metoden indenfor nye anvendelsesområder herunder kompositkonstruktioner. Af denne grund er en ny hybrid testning teknik introduceret til håndtering af en fælles rand som dækker over en kontinuerlig kant eller flade - her benævnt single-komponent hybrid testning. Gennemførelsen af single-komponent hybrid testning inducerer dog nogle centrale udfordringer i den eksperimentelle del konstruktion herunder deformationer i last toget forårsaget af slør i bolte og samlinger, udbøjning i lastindførings riggen samt inerti effekter induceret af massen fra last toget. Disse fejl forårsager en betydelig indvirkning på nøjagtigheden og stabiliteten i en single-komponent hybrid test, hvorfor to kompensatorer er designet herunder høj præcision sporing kompensator og inerti kompensator. Høj præcision sporing kompensatoren er i stand til at reducere forskellen mellem den ønskede og opnåede deformation på den fælles rand ved at monitorer den fælles rand gennem et eksternt data opsamlings system ved brug af bl.a. DIC. Kompensatoren viste sig at være effektiv indenfor både det kvasistatiske samt real tid regime. Inerti kompensatoren udviste fornuftige egenskaber til håndtering af inerti effekterne induceret af massen fra last toget i real tids regimet.

Et kommunikations loop til håndtering af en single-komponent hybrid test i det kvasistatiske og pseudo dynamiske regime er designet og implementeret i LabVIEW. Her er den numeriske del konstruktion, servo-hydrauliske aktuator til håndtering af den eksperimentelle del konstruktion i det kvasistatiske regime samt relevante kompensatorer implementeret og opereret i en prædefineret sekventiel rækkefølge. Systemet er verificeret via en single-komponent og konventionel hybrid test setup.

For at inkludere de dynamiske effekter fra den eksperimentelle del konstruktion er et kommunikations loop til håndtering af en single-komponent hybrid test i real tid designet og implementeret i LabVIEW. For at opnå en kontinuerlig styring af den fælles rand kræves der en opdateringsfrekvens som er 10-25 gange hurtigere end den dominante egen svingnings frekvens af den fulde konstruktion. Dette kan dog blive besværligt grundet den forøgede

kompleksitet af den numeriske model indenfor single-komponent hybrid testning. Derfor er et system der muliggør eksekvering af den numeriske og eksperimentelle del konstruktionen med to forskellige hastigheder implementeret for på den måde at reducere den påkrævede beregnings kapacitet. Her er den numeriske del konstruktion, servo-hydraulisk aktuator til håndtering af den eksperimentelle del konstruktion i real tid samt relevante kompensatorer derfor implementeret i et RT-target for at reducere forsinkelser i beregningerne samt skærpe jitter tolerancen. Systemet er verificeret via en single-komponent og konventionel hybrid test setup.

En repræsentativ eksperimental del konstruktion af en SSP34m vindmøllevinge er identificeret gennem en numerisk analyse til evaluering af spændinger i forkanten af vingen. Her er en 8m sektion af roden på vindmøllevingen identificeret som en repræsentativ del konstruktion, der fysisk kan efterligne de faktiske deformationer i tværsnittet. Derudover indføres en belastnings introduktions zone på 6m til at eliminerer de utilsigtede mekaniske påvirkninger fra last toget. En multiaksial testopstilling er designet til at rumme den 14m lange rodsektion af vindmøllevingen. Endelig præsenteres en indledende hybrid test arkitektur og strategi som skal danne grundlag for en kommende single-komponent hybrid test på en SSP34m vindmøllevinge.

Overordnet præsentere denne ph.d.-afhandling en single-komponent hybrid testning metode, som kan danne en vigtig milepæl i bestræbelserne på at udvide anvendelsesområderne indenfor hybrid testning. To kompensation teknikker blev designet som var i stand til at forbedre nøjagtigheden og stabiliteten indenfor single-komponent hybrid testning. Et kommunikations loop blev designet og implementeret i LabVIEW til håndtering af en single-komponent hybrid testning. Systemet viste gode egenskaber i både det kvasistatiske og real tids regime med en fælles rand som indeholdt et diskret punkt med op til tre friheds grader. Det præsenterede arbejde er baseret på syv publikationer samt relateret forskningsaktiviteter, som ikke var muligt at formidle gennem videnskabelige artikler.

List of abbreviations

A/D	Analogue-to-Digital
AMRI	Adaptive Multi-Rate Interface
APDL	ANSYS Parametric Design Language
CFD	Computational Fluid Dynamics
DAQ	Data Acquisition
D/A	Digital-to-Analogue
DIC	Digital Image Correlation
DLL	Direct Link Library
DOF	Degree-Of-Freedom
DSP	Digital Signal Processor
FBG	Fibre Bragg Grating
FPGA	Field Programmable Gate Array
GFRP	Glass Fibre Reinforced Polymers
GOM	Geseltshaft für Optische Messtechnik
GPIB	General Purpose Interface Bus
HS	Hybrid Simulation
IGES	Initial Graphics Exchange Specification
LabVIEW	Laboratory Engineering Workshop
LE	Leading Edge
LTT	Leading Towards Trailing edge
LVDT	Linear Variable Differential Transformer
MDOF	Multiple Degree-Of-Freedom
mrRTHS	multi-rate Real-Time Hybrid Simulation
PID	Proportional Integral Derivative
PsD	Pseudo-Dynamic
QS	Quasi-Static
RMS	Root-Mean-Square
RT	Real-Time
RT-HPC	Real-Time High-Performance Computing
RTHS	Real-Time Hybrid Simulation
SCPI	Standard Commands for Programmable Instruments
SDOF	Single Degree-Of-Freedom
SFR	Sampling Frequency Ratio
TCP/IP	Transmission Control Protocol/Internet Protocol
TE	Trailing Edge
TTL	Trailing Towards Leading edge
UDP	User Datagram Protocol
USB	Universal Serial Bus

Table of Contents

1. Introduction and background

Wind turbines are progressively used as a substitute to fossil fuels enhancing the demand for larger and more energy producing wind turbine blades. These demands yields for lighter, stronger and more reliable wind turbine blades that can withstand the static and dynamic forces along with fierce weather conditions acting on the blade during service when sited both on- and offshore. Wind turbine blades are usually made from composite materials including glass and carbon fibre reinforced plastics along with lightweight cores such as e.g. honeycomb, foam, etc. Hence, the ambition to improve the structural and operational performance within the industry of wind turbines [1] has resulted in extensive research within large composite structures. In these efforts, testing has primary been focusing on two length scales including laminate and structural scale testing [2]. A representation of the multiscale approach for structural evaluation are illustrated in figure 1.1. Structural scale testing provides valuable knowledge concerning the structural behaviour but is time consuming and expensive to perform due to the large dimensions of the wind turbine blade [1]. The structure is typically tested in a simple load configuration which is a significant simplification compared to the actual forces acting on the blade during service. In order to investigate the material characteristics of the individual materials in the composite structure, coupon testing on laminate scale is conducted [3]. Such tests are performed on specially designed specimens, resulting in idealized stress and strain states. Consequently, they do not account for the complex stress states and interactions, which often occur within structural scale testing leading to advanced failure modes among these mixed mode de-lamination, laminate failure, etc. Such failures often initiate from joints, bearings and other critical details [4], [5] thereby weaken the structure locally and change the structural response.

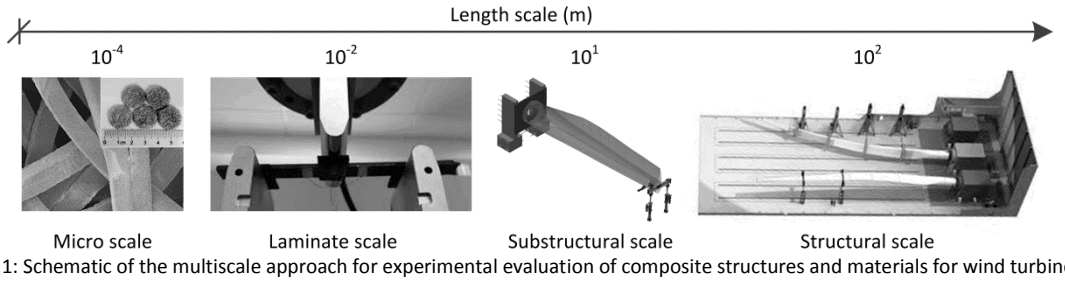

Figure 1.1: Schematic of the multiscale approach for experimental evaluation of composite structures and materials for wind turbine blades

To reveal the real-world service conditions of a wind turbine blade, experimental testing that cover length scales from micro through structural scale testing is required [6]. To establish a service link between laminate and structural scale testing within the industry of wind energy the Hybrid Simulation (HS) technique is implemented to facilitate substructural scale testing. Structural assessment through HS introduces a cost-effective substructural technique by combining the advantages of numerical modelling with those of experimental testing [7], [8]. Here the experimental substructure represents the portion of special interest and is therefore physically replicated to reveal the structural response when exposed to e.g. viscoelasticity, buckling, crack propagation, delamination, rate dependent properties, etc. The remaining portion – which typically covers the majority of the emulated structure – is handled in a numerical substructure representing either predictable mechanical behaviour or is considered uncritical for the analysis conducted. The coupling governed through the interface between the numerical and experimental substructure – referred to here as the shared boundary – is achieved by maintaining the compatibility and equilibrium at the interface.

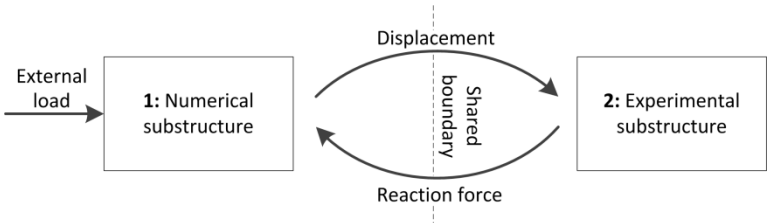

Figure 1.2: Schematic block diagram representing the overall principles of HS for structural assessment

From the block diagram outlined in figure 1.2 the HS is initiated through an external load that is applied the numerical substructure in **(1)**. The external load both allow the implementation of static and dynamic forces governed by e.g. wind, gravity, vibrations, etc. Through a communication loop, the corresponding displacement at the shared boundary is computed and applied to the experimental substructure through an e.g. Proportional Integral Derivative (PID) regulated servo hydraulic actuator – referred to here as the transfer system **(2)**. The forces required to impose the prescribed deformation at the experimental substructure – referred to here as the reaction force – are fed back to the numerical substructure to reveal the response of the emulated structure. The experimental and numerical substructure, communication loop and transfer system combine to form the HS technique.

1.1. Conventional hybrid simulation for structural assessment

The HS technique originated in the late 1960s, where it was used in the Pseudo-Dynamic (PsD) regime for e.g. structural assessment of simple frame structures subjected to an earthquake as an alternative to shake table tests [9]. Since then the research within HS for structural assessment has expanded upon numerous branches including civil and mechanical engineering [10]. Within civil engineering the main focus is on evaluation of seismic protection of building structures on a Real-Time (RT) and extended time-scale [11], [12], [13], [14]. Here a typical application includes the use of dampers for seismic protection of civil engineering structures exposed to e.g. earthquakes and winds – see figure 1.3 for illustration of the basic principles.

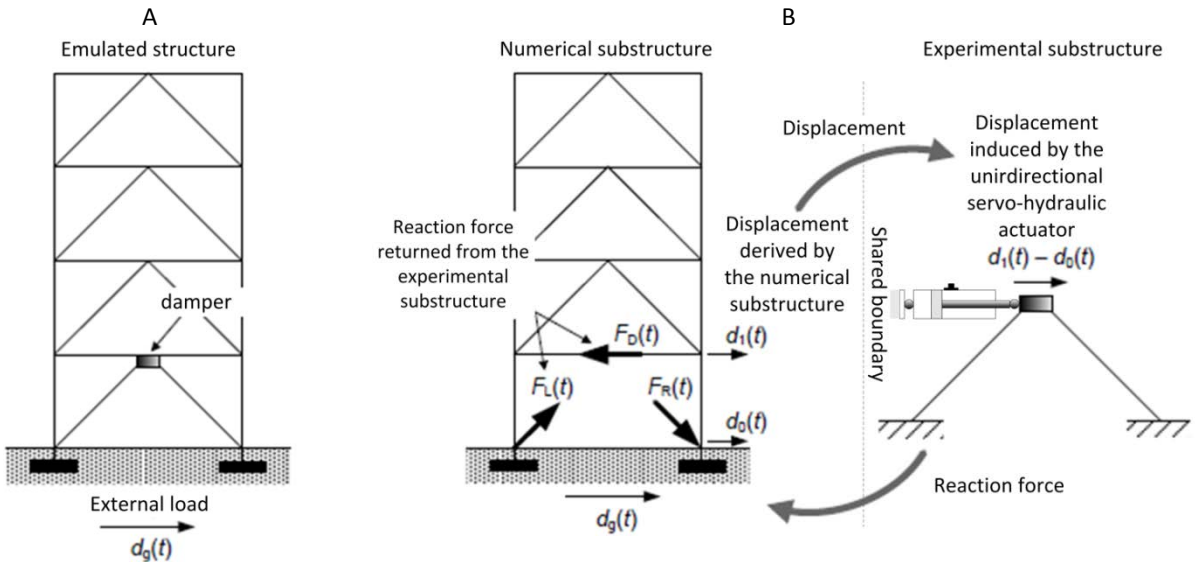

Figure 1.3: principle of conventional HS for structural assessment of a multi-story frame structure: a) emulated structure and b) partitioning [10]

Here the load carrying structure, being the multi-story building without the damper, is discretized in a numerical model while the damper itself is handled experimentally including elastomer [15], stud types [16], [17] or magneto-rheological [18], [19], [20]. The damper is typically operated through a unidirectional servo-hydraulic actuator which governs a clearly defined hinge with a single Degree-Of-Freedom (dof) – referred to here as conventional HS. Common to conventional HS is that the shared boundary is defined by a discrete point operated within a few dofs [7], [10]. This configuration has become a mature and reliable approach, which opens the opportunity to use the HS technique within other application areas [10] including large composite structures within the industry of wind energy.

1.2. Single-component hybrid simulation for structural assessment

Handling of the HS technique within large composite structures involve a shared boundary that includes a continuous edge or plane instead of a clearly defined hinge as seen within conventional HS. Therefore, a new generation of HS is presented in this thesis, capable of handling the complex force and displacement distribution induced at the

partitioning between the numerical and experimental substructure – referred to here as single-component HS. In theory, an infinite number of contact points are needed to accurately simulate the behaviour of the shared boundary within single-component HS. However, due to the inherent limitations within common experimental and numerical methods, simplifications at the shared boundary are needed by e.g. discretizing the shared boundary in a finite number of points, each with a predefined number of dofs. An illustration of the basic principle is outlined in figure 1.4.

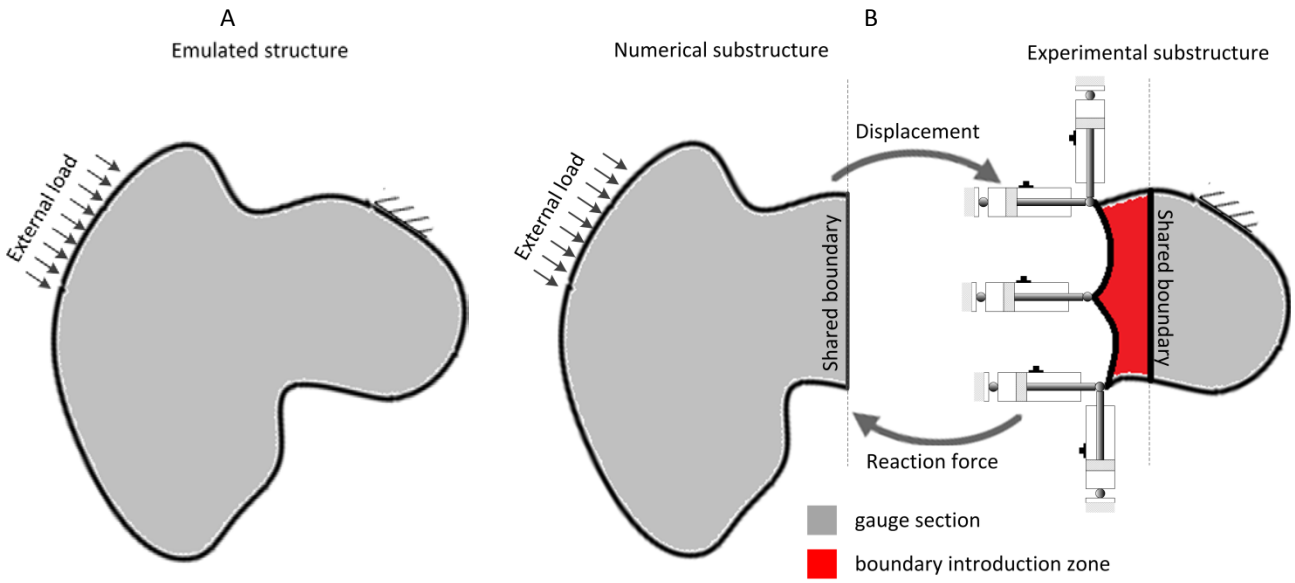

Figure 1.4: principle of single-component HS for structural assessment of an arbitrary solid: a) emulated structure and b) partitioning

Through a boundary introduction zone marked by red cf. figure 1.4, the stress concentrations induced at the shared boundary of the experimental substructure by the finite number of loading points is erased. The boundary introduction zone is followed by the experimental substructure – referred to here as the gauge section. Given that the shared boundary is located between the boundary introduction zone and gauge section, the operation of the shared boundary is complicated by the compliant connection established between the loading points and shared boundary relative to conventional HS. In addition, the weight contribution governed by the load introduction rig itself and added boundary introduction zone may compromise the ability to represent the underlying dynamics of the system. Furthermore, the enhanced complexity of the numerical model governed by the complex geometry and material characterization relative to the conventional approach may restrict the feasible integration time within Real-Time Hybrid Simulation (RTHS) to an unacceptable level, compromising the ability to represent good actuator control.

1.3. Research hypotheses and related objective of the PhD study

Conventional HS poses significant limitations in the ability to expand upon new application areas due to the shared boundary, which typically includes a discrete point with a single dof. In the effort of implementing the HS technique within large composite structures the following research hypothesis are defined:

1. A shared boundary that includes a continuous edge can be operated with a high level of precision and accuracy.
2. Establishment of a single-component HS is enabled through a high-level programming environment both covering the Quasi-Static (QS) and RT regime.
3. The computational resources required to perform single-component RTHS is decreased by operating the numerical and experimental substructure at different rates.
4. Single-component HS provides a cost effective approach for structural assessment of wind turbine blades.

The aim of this research is to develop and demonstrate a HS platform that enable both QS and RT substructural testing of large composite structures – referred to here as single-component HS. The focus of the present research includes the operation/handling of the experimental substructure along with the communication between the HS software and transfer system. Based on the above listed research hypothesis the following objectives are defined:

1. Development and implementation of compensators capable of improving the accuracy and stability of the single-component HS – both covering the QS and RT regime.
2. Development and implementation of a HS communication loop in the QS regime capable of handling a substructure loaded in a discrete point comprising multiple dofs.
3. Development and implementation of a multi-rate Real-Time Hybrid Simulation (mrRTHS) platform strategy capable of handling computational heavy numerical algorithms while maintaining good actuator control.
4. Development and implementation of a single-component mrRTHS platform capable of handling a substructure loaded in a discrete point comprising multiple dofs.
5. Verification of the developed HS platform in the QS and RT regime through a case study comprising multiple dofs in a discrete point.
6. Development and setup of a relevant experimental substructure for structural assessment of an SSP34m wind turbine blade through single-component HS.

1.4. Approach and methods to fulfil objectives

The work of this PhD study is separated into seven appended papers (six journal papers and one conference paper) along with a single associated journal paper. The candidate is the corresponding author on four of the eight papers enclosed in the thesis. Each paper partially covers the objectives of the PhD study, dividing the work into manageable portions. A connection between the individual papers is established through the PhD thesis, which pulls together the various strands of the work done and provides the space to present research that was not possible to expand upon in the papers. Figure 1.5 illustrates a schematic representation of the workflow throughout the PhD project.

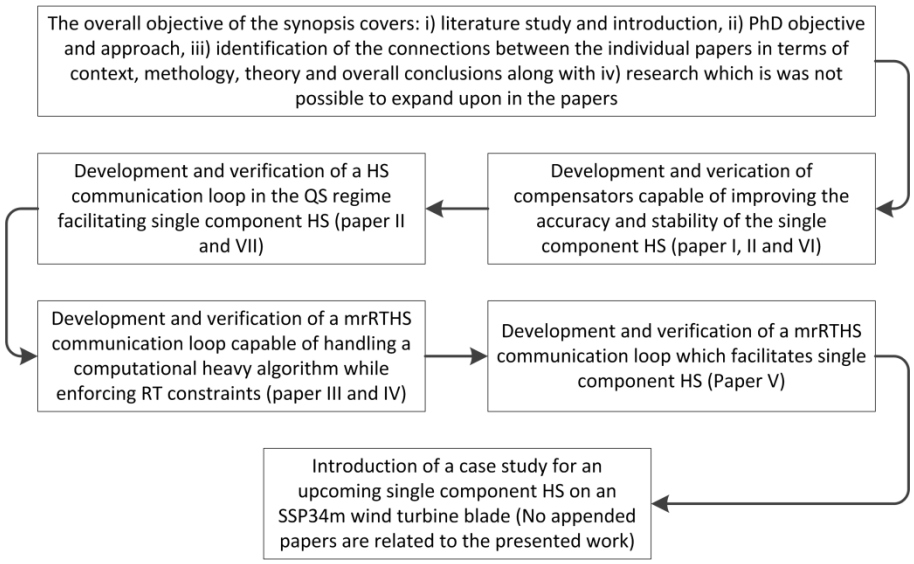

Figure 1.5: Schematic block diagram representing the overall work flow throughout the PhD study

"*Paper I: Strain and Displacement Controls by Fibre Bragg Grating and Digital Image Correlation"* is introducing a compensation method capable of reducing the discrepancy between the desired and achieved displacement or strain at the shared boundary through a correction technique. This discrepancy is mainly driven by compliance in the transfer system governed by slack and deformations in the load train. The technique proved to enhance the accuracy of the transfer system in the QS regime. (Appended journal paper published in Strain (2014))

"Paper II: Quasi-Static Single-Component Hybrid Simulation of a Composite Structure with Multi-Axis Control" is demonstrating the single-component HS technique in the QS regime presented in paper VII on a composite beam with a shared boundary comprising a discrete point with three dofs. (Appended journal paper published in Strain (2015)).

"Paper III: Multi-rate Real Time Hybrid Simulation operated in a flexible LabVIEW real-time platform" is introducing an mrRTHS strategy capable of extending the boundaries of conventional RTHS by operating the numerical and experimental substructure at different time steps while including a rate-transitioning algorithm to link the components appropriately. This configuration enables the operating system to handle a computational heavy numerical model while enforcing stringent real-time constraints at the shared boundary. The technique was successfully demonstrated on a mass-spring-damper system through a flexible LabVIEW real-time platform that facilitates multiple threads to execute simultaneously across multiple processors. (Appended journal paper submitted in Smart Structures and Systems (2016)).

"Paper IV: Adaptive multi-rate interface: development and experimental verification for real-time hybrid simulation" is investigating the different existing rate transitioning algorithms capable of linking the numerical and experimental substructure appropriately within mrRTHS. Furthermore, a new developed rate-transitioning algorithm is investigated and the tracking performance evaluated for comparison. Finally, the mrRTHS approach is compared with a Real-Time High-Performance Computing (RT-HPC) strategy and conventional RTHS through a multi-story frame structure with a shared boundary comprising a discrete point with a single dof. (Appended journal published in earthquake engineering and structural dynamics (2016)).

"Paper V: Single-component multi-rate real-time hybrid simulation pilot test on a composite structure" is demonstrating the mrRTHS technique presented in paper III and IV on a single-component structure with a shared boundary comprising a discrete point with three dofs. This test furthermore acts as a pilot test for an upcoming HS on an SSP34m wind turbine blade (SSP Technology, Stenstrup, Denmark) which is presented in chapter 5. (Appended journal paper submitted in Strain (2016))

"Paper VI: Compensation Methods in Real-Time Hybrid Simulation" extends the compensator presented in paper I to reduce the discrepancy between the dynamically imposed displacement on the shared boundary of the experimental substructure and desired displacement governed by the numerical substructure. Furthermore, a compensator capable of erasing the inertia effects induced by the mass of the load train is presented. The technique proved to enhance the accuracy and stability of single-component RTHS through a case study further described in paper V. (Appended journal paper submitted in Strain (2016))

"Paper VII: Hybrid Simulation of Composite Structures with Single-axis control" is introducing a base for single-component HS in the QS regime operated on a flexible platform through the Laboratory Engineering Workshop (LabVIEW). The system was successfully verified through a conventional frame structure with a shared boundary comprising a single dof. (Appended conference paper presented in the 19th International Conference on Composite Materials (ICCSM19))

"Paper VIII: Life cycle strain monitoring in glass fibre reinforced polymer laminates using embedded fibre Bragg grating sensors from manufacturing to failure" is demonstrating the use of the Fibre Bragg Grating (FBG) technique for internal strain monitoring in fibre-reinforced polymers. The gained experience in the use of the FBG is applied in paper I to obtain the internal strain in a composite structure loaded in a three-point bending test. (Associated journal paper published in journal of composite materials (2013)).

1.5. Thesis guide

The main body of this PhD thesis is based upon seven appended and one associated paper. In addition, related research activities that were not possible to convey through scientific publications is presented in this thesis. Each chapter throughout the thesis is introduced by a description of the issue addressed along with the papers related to the subject. Next, a presentation of the used theory and considerations are presented along with the related research activities. These research activities are included as a summary of key results extracted from the related papers. For a more detailed review of the presented key results, the author refers to the appended papers, which are added in appendix. Finally, each chapter is completed by a summary of the key findings and conclusions.

Chapter 2 introduces two interface compensation techniques that are relevant in relation to single-component HS. This chapter is based upon research activities presented in paper I, II and VI.

Chapter 3 presents a platform capable of handling a single-component HS in the QS or PsD regime. The system architecture is verified through two case studies that comprises both a conventional and single-component HS. This chapter is based upon research activities presented in paper II and VII.

Chapter 4 introduces a platform capable of handling a computational heavy numerical model while enforcing real-time constraints at the shared boundary. The system architecture is verified through two case studies that comprises both a conventional and single-component RTHS. This chapter is based upon research activities presented in paper III, IV and V.

Chapter 5 presents a case study for an upcoming single-component HS on an SSP34m wind turbine blade. No appended papers are related to this scientific work.

Chapter 6 conclusions and suggestions for future research activities

2. Compensation methods for single-component hybrid simulation

Accuracy and stability within conventional HS is compromised by systematic (epistemic) and random (aleatoric) experimental errors induced at the shared boundary such as transfer system dynamics, communication delay, sensor miscalibration, measurement noise and random truncations in the Analogue-to-Digital (A/D) and Digital-to-Analogue (D/A) conversion [21], [22]. However, the operation of the shared boundary within single-component HS induces additional types of experimental errors at the shared boundary including compliance in the transfer system driven by slack and deformations in the load train and boundary introduction zone [23] along with inertia effects induced by the mass of the load train [24]. In this chapter, two compensators are presented capable of accommodating the experimental errors related to the operation of the shared boundary within single-component HS – referred to here as a) high precision tracking compensator and b) inertia compensator. The high precision tracking compensator is capable of reducing the discrepancy between the desired and achieved displacement or strain imposed at the shared boundary and is further described in paper I, II and VI. The inertia compensator handles the inertia effects induced by the mass of the load train and is further described in paper VI.

2.1. High precision tracking compensator

The experimental substructure is typically loaded by a servo hydraulic transfer system that in turn operates the shared boundary according to the inputs received by the numerical substructure. The reaction force required to meet these boundary conditions are fed back to the numerical substructure to achieve compatibility and equilibrium at the interface. Inconsistencies between the desired and achieved displacement at the shared boundary leads to inaccurate reaction forces, compromising the fidelity of the HS [25]. Therefore, a reliable HS is dependent on reducing the discrepancy between the desired and achieved displacement at the shared boundary to an acceptable tolerance. This tolerance is mainly quantified by the stiffness ratio between the numerical and experimental substructure [25].

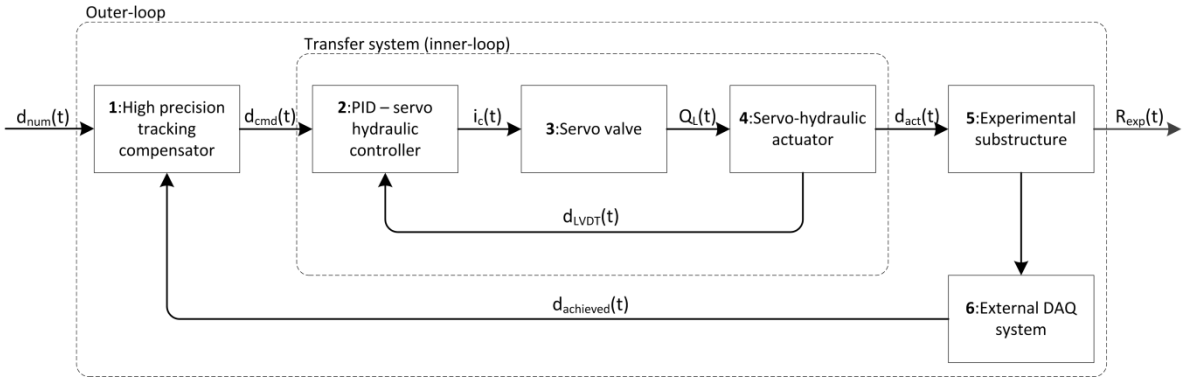

Figure 2.1: schematic block diagram representing the overall control loop algorithm for high precision tracking of the shared boundary

The research within conventional HS focuses on systems with a shared boundary comprising a discrete point with a few dofs operated on a RT or extended time scale. Here the experimental substructure is loaded by a deformation controlled unidirectional actuator through a PID controller. The actual piston displacement is acquired from an internally mounted Linear Variable Differential Transformer (LVDT). With the assumption of having a well-tuned PID loop a low discrepancy between the desired and achieved displacement at the shared boundary is attained given that the connection between the actuator and shared boundary is rigid. However, within single-component HS the shared boundary comprise multiple dofs through a discrete point. This is typically handled through multiple unidirectional hydraulic actuators connected by a test rig. Due to slack and deformations in the joints and bearings a high precision compensator is implemented capable of operating the experimental substructure from a feedback signal acquired directly on the shared boundary [26], [23], [27].

A schematic block diagram including the high precision tracking compensator, transfer system, experimental substructure and external Data Acquisition (DAQ) system is presented in the time domain t – separated in 6 units labelled from **(1)** to **(6)** cf. figure 2.1**.** Here the desired displacement $d_{num}(t)$ generated by the numerical substructure in the HS is operated with a time step $\triangle t$. The outer-loop including the high precision tracking compensator **(1)**, experimental substructure **(5)** and external DAQ system **(6)** is operated through LabVIEW with the time step δt – referred to here as the correction step. The inner-loop which covers the transfer system including PID controller **(2)**, servo valve **(3)** and actuator **(4)** is operated with the fine time step φt through the PID controller with a typical execution rate of 3 kHz i.e. φt = 0.34ms. The desired displacement $d_{num}(t)$ and achieved displacement $d_{achieved}(t)$ acquired at the shared boundary in **(6)** are imported into the high precision tracking compensator in **(1)** to generate $d_{cmd}(t)$ according to eq. (2.2) and (2.10) for the QS and RT domain respectively. From the command signal $d_{cmd}(t)$ and current position of the actuator $d_{LVDT}(t)$ – being the displacement feedback from the LVDT – a electrical current $i_c(t)$ is generated by the PID controller in **(2)** to operate the servo-valve **(3)**. The servo-valve directs the oil-flow $Q_L(t)$ in the actuator **(4)** making the piston to move accordingly – imposing the prescribed displacement $d_{act}(t)$ on the experimental substructure in **(5)**. Finally, the achieved displacement $d_{achieved}(t)$ at the shared boundary is tracked through **(6)** using an external DAQ system to generate the next displacement feedback for the high precision tracking compensator in **(1)**.

2.1.1. Quasi-statically imposed high precision tracking performance

Within QS and PsD HS, the operation of the experimental substructure is conducted on an extended time scale i.e. the transfer system is handled in the QS regime. This enables the user to predefine an error tolerance β that will be fulfilled by allowing adjustments of the shared boundary through multiple correction steps δt within each time step $\triangle t$ in the overall control loop algorithm presented in figure 2.1.

$$d_{error}(t) = d_{num}(t) - d_{achieved}(t) \tag{2.1}$$

$$d_{cmd}(t) = d_{cmd}(t - \delta t) + d_{error}(t) \tag{2.2}$$

From the desired displacement $d_{num}(t)$ generated by the numerical substructure along with the actual achieved displacement $d_{achieved}(t)$ received from the external DAQ system in **(6)** the error $d_{error}(t)$ is derived by the high precision tracking compensator in **(1)**. If the error $d_{error}(t)$ is above the acceptable error tolerance β i.e. $|d_{error}(t)| > \beta$ it will be added with the previous command signal $d_{cmd}(t-\delta t)$ to derive the current command signal $d_{cmd}(t)$ cf. eq. (2.2). This process will be repeated for the required number of adjustments by performing multiple correction steps δt within a given time step $\triangle t$. The next desired displacement $d_{num}(t+\triangle t)$ will be handled when the error $d_{error}(t)$ is within the predefined error tolerance β i.e.$|d_{error}(t)| \leq \beta$.

<u>Related key results presented in paper I</u>

In paper I, the high precision tracking compensator is operated in the control loop algorithm outlined in figure 2.1 through LabVIEW 8.6. The system is verified in the QS domain through a three point bending test on a Glass Fibre Reinforce Polymers (GFRP) beam presented in figure 2.3. The shared boundary is located at the centre position of the beam and loaded by a single unidirectional actuator – yielding a discrete point with a single translational DOF in the y-direction. The coordinate system and related notation is given in figure 2.3b. The response of the shared boundary is monitored using two external DAQ system techniques including Digital Image Correlation (DIC) and FBG.

The DIC technique is a non-contact, full field measurement method based on grey-value digital images. The system includes two imaging sensors capable of tracking the shape, motion and displacement of an object surface in three dimensions [28]. Thus, with the aim of dealing with a complex specimen geometry and/or load train, the

measurement technique represents a substitute to a large number of conventional analogue gauges. Through the commercial DIC system of the type ARAMIS from the company Geseltshaft für Optische Messtechnik (GOM) the three measurement points labelled MP-1, MP-2 and MP-3 in figure 2.3b are tracked RT using the IVIEW software [29]. The 3D displacement in the form $[u_x;u_y;u_z]$ for each of the three measurement points are transferred to the LabVIEW software through a Transmission Control Protocol/Internet Protocol (TCP/IP) connection. The TCP/IP connection and RT image processing performed by IVIEW, is handled in a Python macro using the commands from the GOM package [30]. The relation between the displacement of the shared boundary and displacement at the given coordinate x in figure 2.3b is derived from the Bernoulli-Euler theory cf. eq. (2.3) and (2.4).

$$u_{max} = \frac{u(x)}{3\left(\frac{x}{L}-\frac{4}{3}\left(\frac{x}{L}\right)^3\right)} \text{ for } x \leq \frac{L}{2} \tag{2.3}$$

$$u_{max} = \frac{u(x)}{4\left(\left(1-\frac{x}{L}\right)\left(\frac{2x}{L}-\frac{1}{4}-\left(\frac{x}{L}\right)^2\right)\right)} \text{ for } x \geq \frac{L}{2} \tag{2.4}$$

Here x denote the position in the x-direction, u_{max} the displacement of the shared boundary in the y-direction, L the length between the supports and u(x) the displacement in the y-direction at the position x. The displacement of the shared boundary $d_{achieved}$ is obtained by averaging u_{max} defined for each of the three measurement points.

The FBG technique refers to an optical transducer consisting of several thousand of organized layers with varying indices written into a single mode fibre. Each of the two fibres, which are embedded into the GFRP beam, contains three FBG sensors with a gauge length of 4.00mm. By emitting a broad – band light through the FBG a reflection spectrum is returned cf. Fresnel equation [31] and analysed through a stand-alone interrogator type I-MON 512 E-USB with a wavelength range of 1510-1595 nm [32]. By changing the grating period a shift in the peak reflectivity is generated as illustrated in figure 2.2, which is convertible to multiple physical quantities including strain, temperature and vibrations. Thus, when performing test within different length scales covering material to field testing where a certain strain state is difficult to obtain due to complex test rig/geometry, it is beneficial to use FBG for control since they can measure strains directly on the specimen or even inside. Furthermore, the FBG sensor detects cracks and delamination, which are key information in composite materials including GFRP [33], [34], [35].

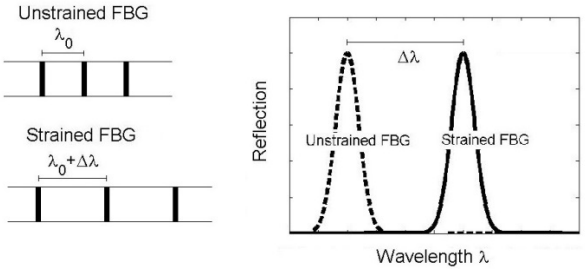

Figure 2.2: the change in peak reflectivity as a function of the grating period

Knowing the initial wavelength λ_0, wavelength change $\Delta\lambda$ and temperature change ΔT of the specimen, the strain is derived cf. eq. (2.5). Here the gauge factor coefficients k_ε and k_t are equal to 7.75E-7με and 6.27E-6K^{-1} respectively.

$$\frac{\Delta\lambda}{\lambda_o} = \varepsilon k_\varepsilon + k_t \Delta T \tag{2.5}$$

Through the six measurement points labelled FBG-1 to FBG-6 in figure 2.3b the strain are tracked RT through the interrogation monitor. Through the Universal Serial Bus (USB) port, the data is imported into the LabVIEW environment using a Direct Link Library (DLL) and analysed according to [36]. The relation between the displacement of the shared boundary and strain at the given location x are outlined in eq. (2.6) and (2.7).

$$u_{max} = \frac{1}{24}\frac{L^3\varepsilon(x)}{xz} \text{ for } x \leq \frac{L}{2} \quad (2.6)$$

$$u_{max} = \frac{1}{24}\frac{L^3\varepsilon(x)}{(L-x)z} \text{ for } x \geq \frac{L}{2} \quad (2.7)$$

Here x denote the position in the x-direction, z the distance from the neutral axis to the FBG sensor in the y-direction, u_{max} the displacement of the shared boundary in the y-direction, L the length between the supports and ε(x) the strain in the x-direction at the position x. The coordinate system and related notation is given in figure 2.3b. The displacement of the shared boundary $d_{achieved}$ is obtained by averaging u_{max} defined for each of the three measurement points.

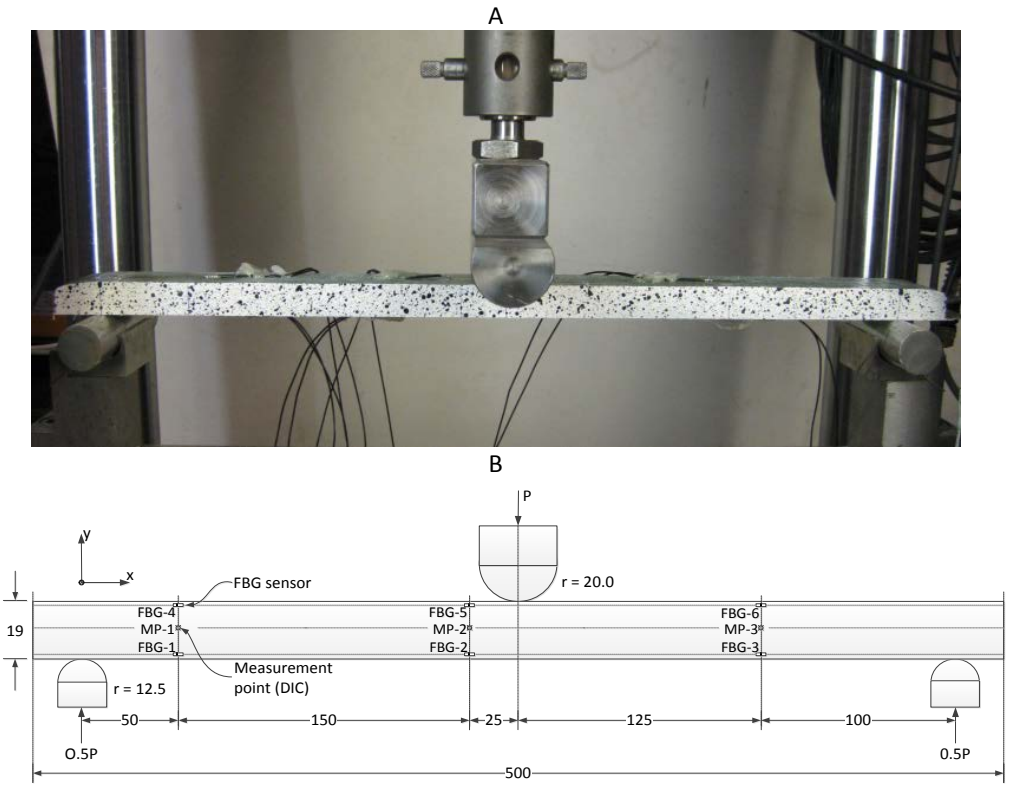

Figure 2.3: three-point bending test: a) GFRP applied speckle pattern and FBG sensors and b) overall dimensions along with numbering and location of FBG sensors and measurement points

The performance of the high precision tracking compensator is investigated in the QS regime with the desired displacement $d_{num}(t)$ covering 91 time steps forming a triangular waveform with five peaks cf. figure 2.4a and 2.5a. From the available accuracy and precision offered by the DIC system an error tolerance of β = ±0.01mm is chosen cf. figure 2.4b – which is equivalent to 0.17% of the peak-to-peak displacement. For the FBG system an error tolerance of β = ±20 με is obtained cf. figure 2.5b – which corresponds to 0.69% of the peak-to-peak strain. For each time step Δt the discrepancy between the desired displacement $d_{num}(t)$ and achieved displacement of the shared boundary $d_{achieved}(t)$ is kept within the predefined error tolerance β.

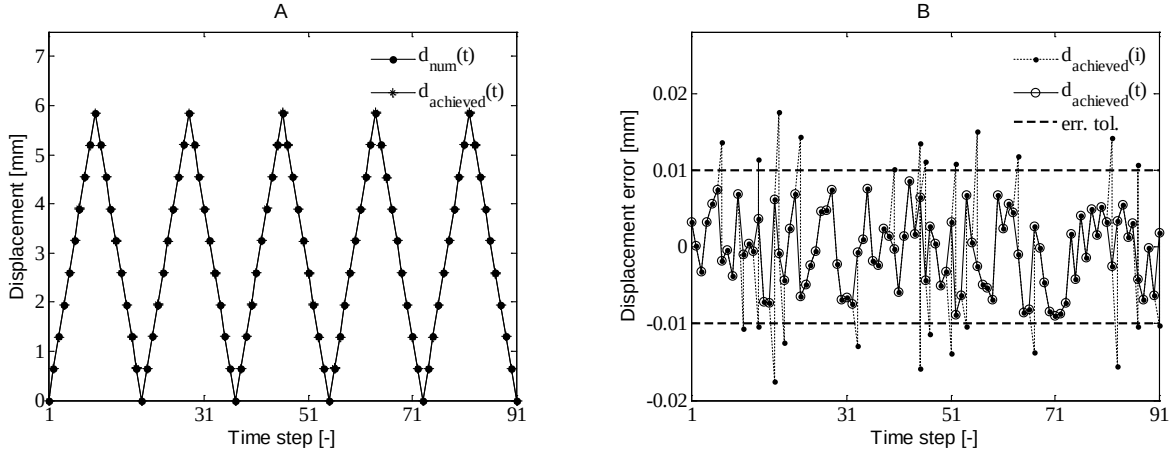

Figure 2.4: QS high precision tracking control by DIC: a) desired and achieved disp. and b) discrepancy between the desired and achieved disp.

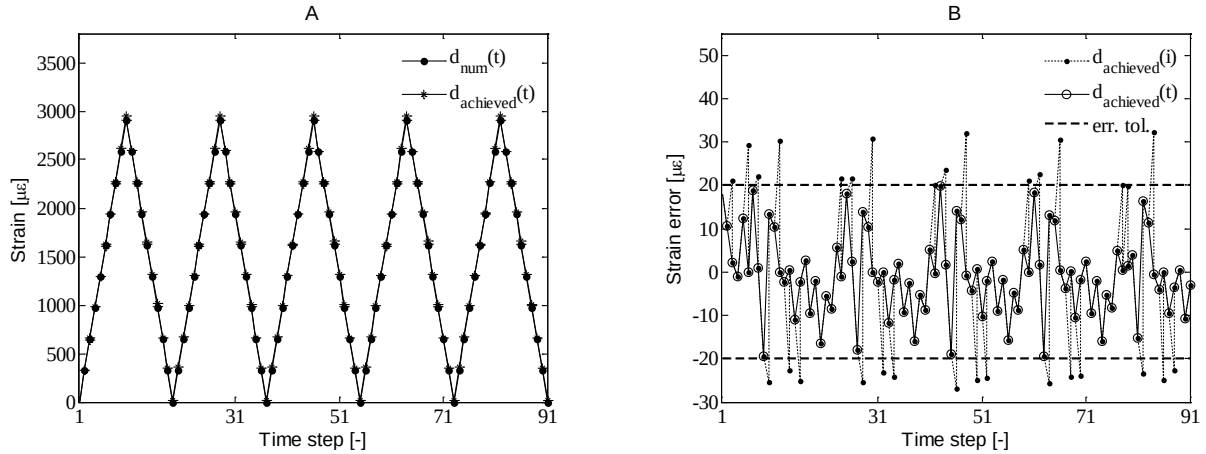

Figure 2.5: QS high precision tracking control by FBG: a) desired and achieved strain and b) discrepancy between the desired and achieved strain

The high precision tracking compensator was capable of improving the tracking performance of the shared boundary on the three point bending test even though the given load train exhibited a low compliance. Through a total of 17-25 adjustments for a sample of three tests, the high precision tracking control trough DIC proved successfully with an error tolerance of β = ±0.01mm. For the high precision tracking control through FBG an error tolerance of β = ±20 με generated 24-28 adjustments for a sample of three tests. The number of required adjustments is dependent on the error tolerance for the given application.

Related key results presented in paper II

In paper II, the high precision tracking compensator is verified in the QS domain for the test setup presented in figure 2.7 including a cantilever GFRP beam loaded by three unidirectional actuators labelled A, B and C. The shared boundary is defined by a discrete point with three dofs translation in the x- and y-direction along with rotation around the z-axis – referred to here as φ. The coordinate system and related notation is given in figure 2.6. The high precision tracking compensator is operated in the control loop algorithm outlined in figure 2.1 through LabVIEW 13.0. In this test no error tolerance β is defined meaning that the time step Δt and correction step δt is operated sequentially i.e. Δt = δt. The response of the shared boundary is monitored using the external DAQ system DIC.

The relation between the desired displacement $d_{num}(t)$ at the shared boundary in the format $[d_x(t);d_y(t);\varphi(t)]$ and the corresponding displacement of the actuators is derived through a trigonometric algorithm following the assumption of rigid body motion.

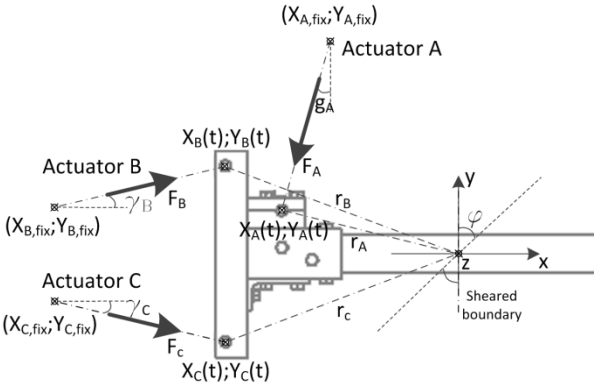

Figure 2.6: coordinate system and related notation

Here the actuator displacement $d_{act}(t)$ for each correction step δt is derived cf. eq. (2.8) from the distance between the actuator fix point $[x_{m,fix};y_{m,fix}]$ and actuator loading point $[x_m(t);y_m(t)]$ – where m denotes the actuator label.

$$d_{act}(i) = \begin{bmatrix} \sqrt{\left(x_A(t) - x_{A,fix}\right)^2 + \left(y_A(t) - y_{A,fix}\right)^2} \\ \sqrt{\left(x_B(t) - x_{B,fix}\right)^2 + \left(y_B(t) - y_{B,fix}\right)^2} \\ \sqrt{\left(x_C(t) - x_{C,fix}\right)^2 + \left(y_C(t) - y_{C,fix}\right)^2} \end{bmatrix}^T \tag{2.8}$$

Like in paper I the shared boundary is tracked RT by the commercial DIC system ARAMIS through the IVIEW software [29]. The 3D displacement in the form $[u_x;u_y;u_z]$ for each of the three measurement points are transferred to the LabVIEW software through a TCP/IP connection. The TCP/IP connection and RT image processing performed by IVIEW, is handled in a Python macro using the commands from the GOM package [30]. The displacement of the shared boundary is derived by three measurement points labelled MP-1, MP-2 and MP-3 cf. figure 2.7b. The equivalent three dof displacement of the shared boundary $d_{achieved}$ is obtained with the assumption of having linear cross sectional deformation at the shared boundary. Here the in-plane translation in the x- and y-direction is calculated as the average displacement of the three measurement points while the rotation is derived by the change of angle between MP-1 and MP-3.

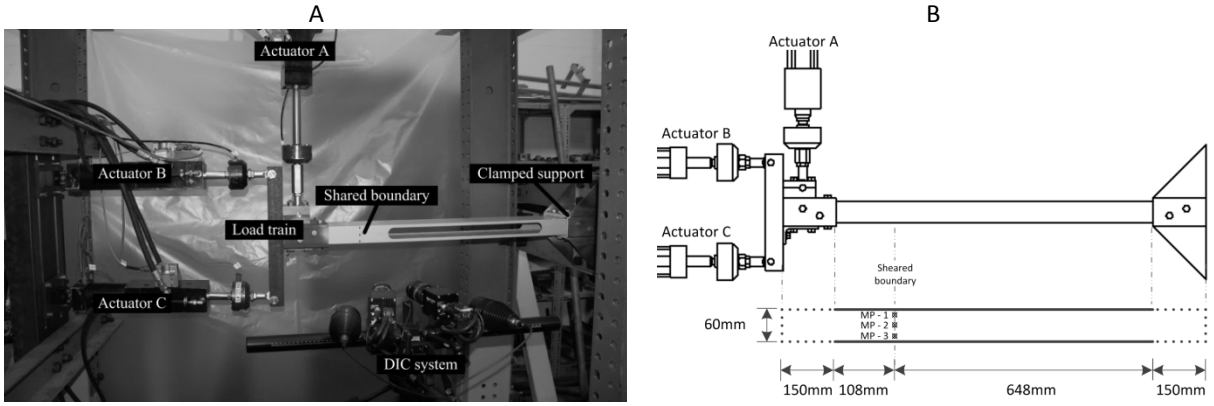

Figure 2.7: Test rig including: a) overall test setup including load train, DIC system, etc. and b) overall dimensions

The performance of the high precision tracking compensator is evaluated in the QS regime for each dof included in the shared boundary with the desired displacement $d_{num}(t)$ covering 181 time steps forming a triangular waveform with three peaks cf. figure 2.8a, 2.8b and 2.8c. The peak-to-peak amplitude of the desired displacement $d_{num}(t)$ is -0.105mm and -6.79mm in the x- and y-direction respectively while the rotation around z-axis is determined to -0.013 degrees.

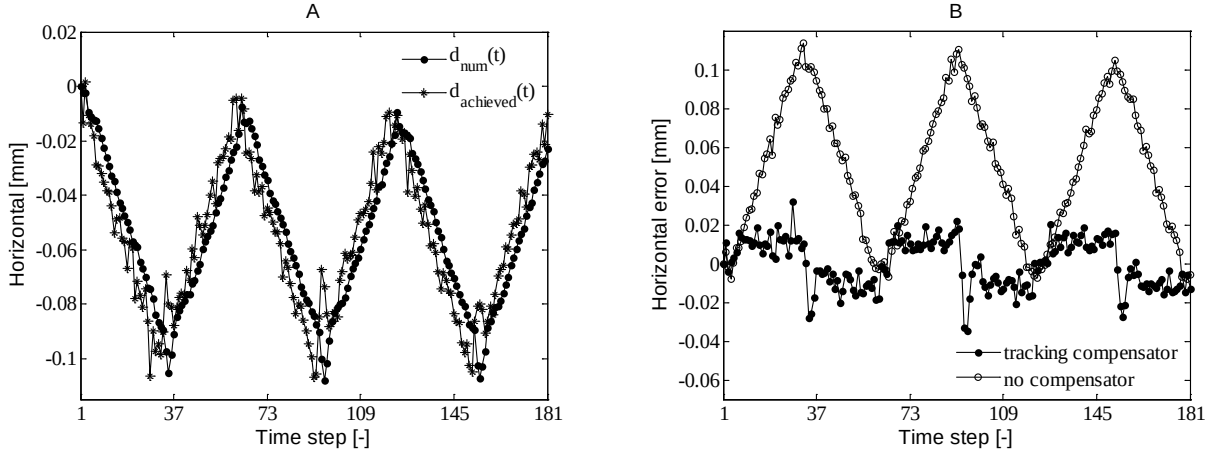

Figure 2.8: QS high precision tracking control in the x-direction: a) desired and achieved disp. and b) discrepancy between the desired and achieved disp.

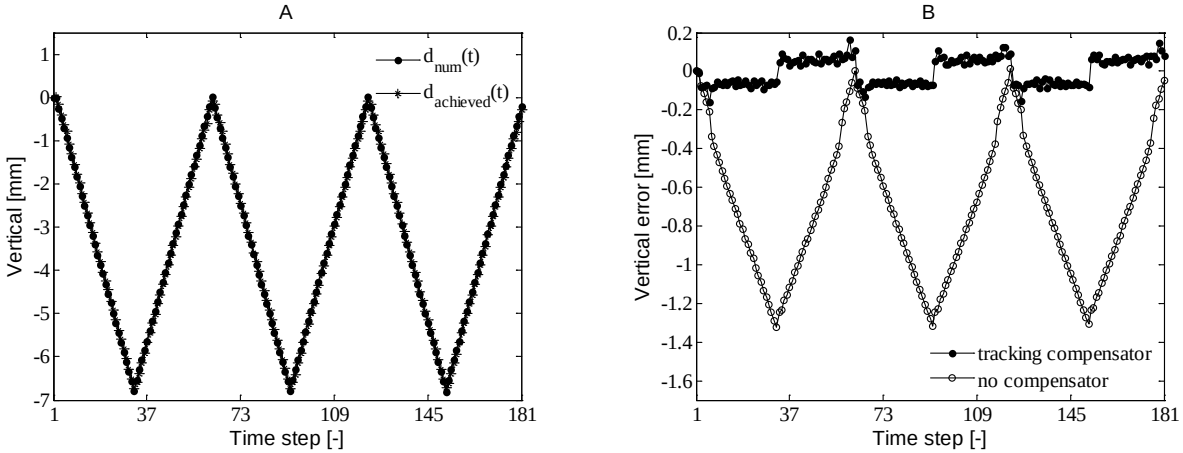

Figure 2.9: QS high precision tracking control in the y-direction: a) desired and achieved disp. and b) discrepancy between the desired and achieved disp.

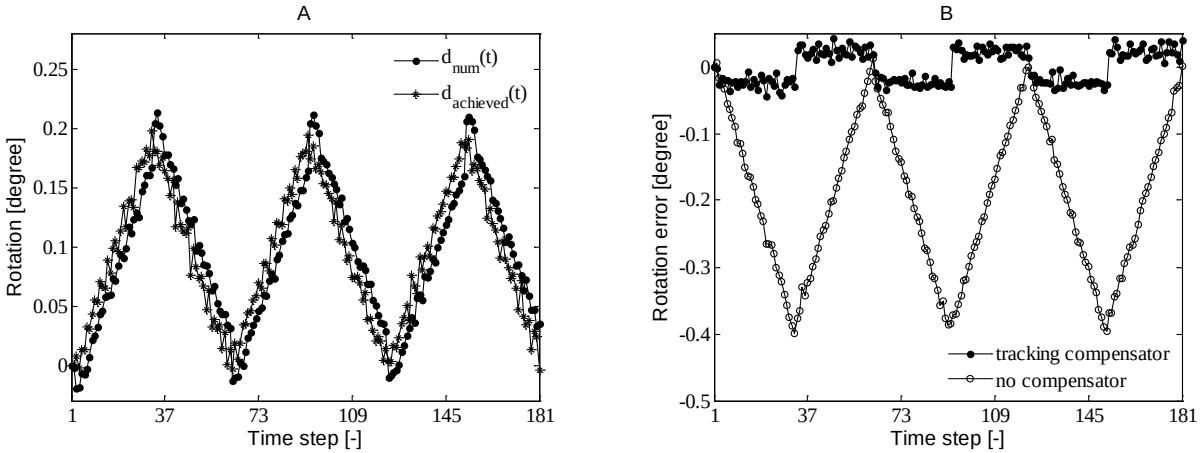

Figure 2.10: QS high precision tracking control in rotation around the z-axis: a) desired and achieved disp. and b) discrepancy between the desired and achieved disp.

The high precision tracking compensator was capable of improving the tracking performance of the shared boundary including multiple dofs at the shared boundary. The discrepancy between the desired $d_{num}(t)$ and achieved $d_{achieved}(t)$ displacement were reduced by 69%, 87% and 89% in the x- and y-direction along with rotation around the z-axis respectively by including the high precision tracking compensator. An even higher degree of improvement would be attained if correction steps of the shared boundary where enforced by defining an error tolerance β.

2.1.2. Dynamically imposed high precision tracking performance

Within RTHS, the operation of the experimental substructure is executed in RT to include the inherent dynamics in the reaction force obtained at the shared boundary, which in turn are fed back to the numerical substructure to achieve compatibility and equilibrium at the interface. This entails that the time step $\triangle$t and correction step δt is operated sequentially i.e. $\triangle$t = δt cf. figure 2.1, given that the shared boundary has to follow a continues history of displacement, velocity and acceleration [37].

$$d_{error}(t) = d_{num}(t) - d_{achieved}(t) \tag{2.9}$$

$$d_{cmd}(t) = d_{cmd}(t - \Delta t) + K_{gain} d_{error}(t) \tag{2.10}$$

As an alternative to the adjustment technique presented in section 2.1.1 a coefficient of proportionality named: K_{gain} is introduced in the high precision tracking compensator in **(1)** cf. eq. (2.10) in order to avoid overshooting behaviour [25]. Through an open loop system identification the K_{gain} factor is adjusted empirically for each of the dofs included in the shared boundary. This factor is dependent on the given waveform, frequency and peak-to-peak displacement of the shared boundary. If the response of the shared boundary is varying throughout the test series, an online adjustment of the K_{gain} factor may be required to sustain the performance of the high precision tracking compensator.

<u>Related key results presented in paper VI</u>

In paper VI, the high precision compensator is verified in the RT domain for the test setup presented in figure 2.7, which is further described in section 2.1.2. Here the high precision tracking compensator is operated in the control loop algorithm outlined in figure 2.1 through LabVIEW 15.0 with a rate of 50Hz i.e. the time step $\triangle$t = 20ms. The response of the shared boundary is monitored using the external DAQ system DIC.

The relation between the desired displacement $d_{num}(t)$ at the shared boundary and the corresponding displacement of the actuators labelled A, B and C is determine cf. eq. (2.8) following the assumption of rigid body motion. The corresponding displacement of the shared boundary $d_{achieved}(t)$ is obtained with the assumption of having linear cross sectional deformation at the shared boundary.

The three measurement points labelled MP-1, MP-2 and MP-3 in figure 2.7b are tracked RT by the commercial DIC system ARAMIS through the PONTUS Live software vs. 8. The 3D displacement in the form $[u_x;u_y;u_z]$ for each measurement point are transferred to the LabVIEW software through a Ethernet cable by the User Datagram Protocol (UDP) [38] and Standard Commands for Programmable Instruments (SCPI) [39]. With the given shutter time and measurement volume a sampling rate of 100Hz by the DIC system where achieved. However, the communication between the DIC system and LabVIEW comes with a delay of 160ms – measured from a displacement is induced on the shared boundary to the data is available in LabVIEW.

The performance of the high precision tracking compensator is evaluated in the RT regime for each dof included in the shared boundary for the desired displacement $d_{num}(t)$ covering a sinusoidal waveform with the frequency f of 0.074Hz, 0.74Hz, 1.48Hz, 2.22Hz and 2.96Hz. For all five frequencies of interest the peak-to-peak amplitude of the desired displacement $d_{num}(t)$ are 0.39mm and 22.12mm in the x- and y-direction respectively while the rotation around the z-axis is -0.048 degrees. For a duration of 24 sec. the desired and achieved displacement at the shared boundary along with the discrepancy between the two when enabling and disabling the high precision tracking compensator are outlined in figure 2.11, 2.12 and 2.13 for a frequency f = 0.074Hz.

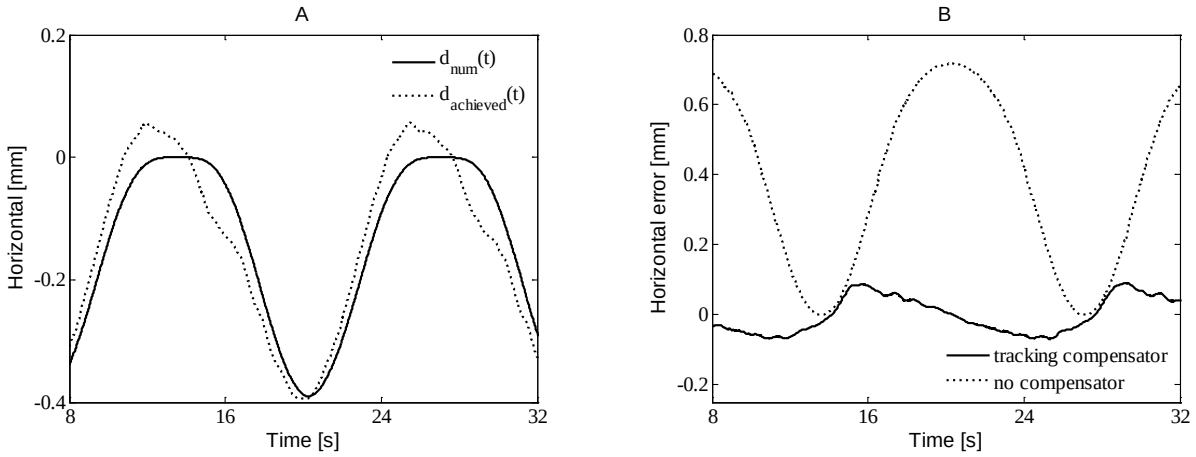

Figure 2.11: RT high precision tracking control in the x-direction for f = 0.074Hz: a) desired and achieved disp. and b) discrepancy between the desired and achieved disp.

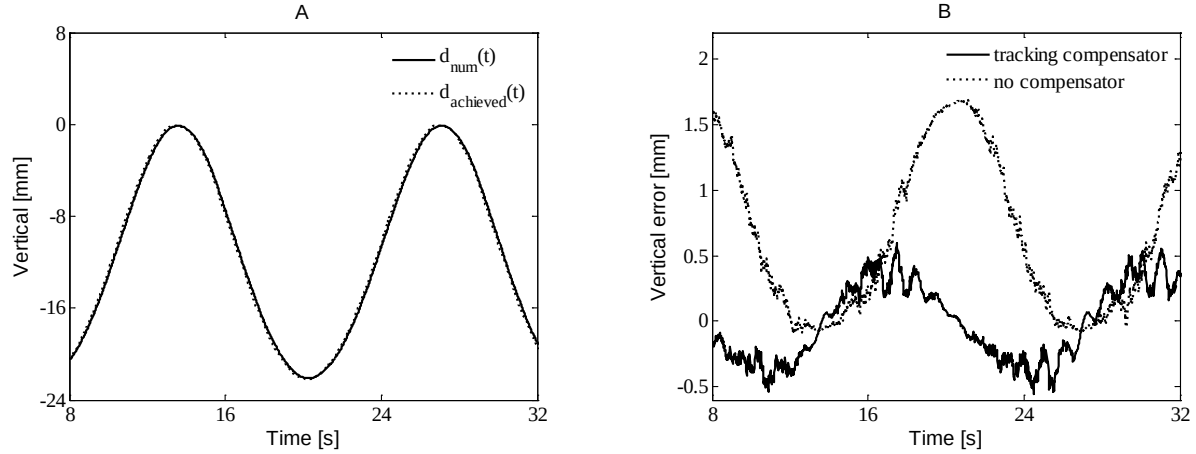

Figure 2.12: RT high precision tracking control in the y-direction for f = 0.074Hz: a) desired and achieved disp. and b) discrepancy between the desired and achieved disp.

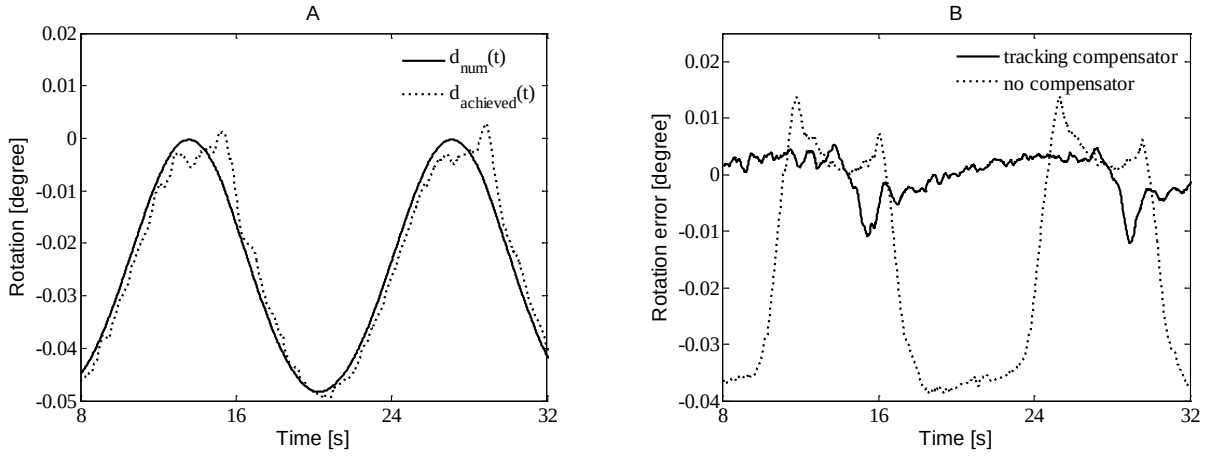

Figure 2.13:RT high precision tracking control in rotation around the z-axis for f = 0.074Hz: a) desired and achieved disp. and b) discrepancy between the desired and achieved disp.

From figure 2.11b, 2.12b and 2.13b it is concluded that the K_{gain} factor is well tuned given that the deviation between the desired and achieved displacement is centred around zero – meaning that a further increase of K_{gain} will result in overshooting. The performance of the high precision tracking compensator is quantified by deriving the standard deviation of the error between the desired and achieved displacement when the high precision tracking compensator is enabled and disabled. The relative improvement is given in figure 2.14 for all five frequencies investigated and corresponding K_{gain} factor.

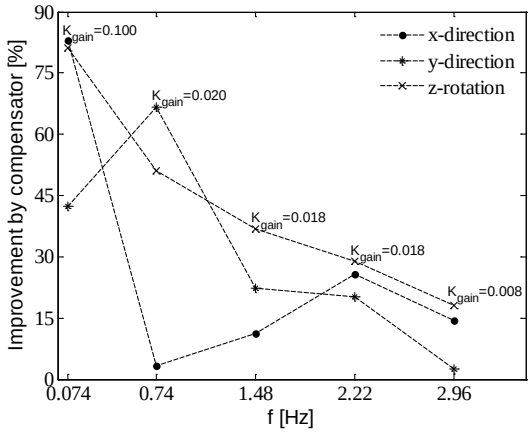

Figure 2.14: Improvement by including the high performance tracking compensator and corresponding K_{gain} factor

From figure 2.14, it is identified that the high precision tracking compensator improves the correlation between the desired and achieved displacement. However, the effect of the compensator is reducing as a function of an increasing frequency. This is properly due to the communication delay between the DIC system and control algorithm operated in LabVIEW, which corresponds to nearly 50% of a full period for a frequency of 2.96Hz. The communication delay could be handled through a delay compensator capable of e.g. extrapolating ahead in time.

2.2. Inertia compensator

Within RTHS the inherent dynamics of the experimental substructure including inertia and damping is obtained through the reaction force in the shared boundary which in turn is feed back to the numerical substructure to achieve compatibility and equilibrium at the interface between the two. However, within single-component RTHS the mass of the multi-axial test rig that is mounted on the experimental substructure may induce considerable inertia forces in relation to the reaction forces received from the experimental substructure itself – see e.g. [24] and subchapter 5.4. This inertia contribution will in some circumstances induce a major influence on the reaction force at the shared boundary – compromising the fidelity of the HS. Therefore, an inertia compensator is introduced capable of eliminating the inertia forces induced by the lumped mass represented by the test rig.

$$\sum F_d(t) = m_d a_d(t) \;\; for \;\; d = x, y, z \tag{2.11}$$

$$\sum \tau_a(t) = I_a \alpha_a(t) \;\; for \;\; a = x, y, z \tag{2.12}$$

From the translational acceleration a_d and mass m_d of the test rig – the inertia force F_d acting in the centre of gravity is described by newton's second law in the time domain t cf. eq. (2.11) – where d denote the direction of the inertia force. The inertia torque τ_a with respect to the axis a through the centre of mass is described in the time domain t by the rotational analog for newton's second law presented in eq. (2.12) – where I_a accounts for the moment of inertia and α_a the angular acceleration. By knowing the inertia contribution from the test rig itself – the inertia and damping effects from the stand-alone experimental substructure can be isolated by subtracting F_d and τ_a from the reaction force acquired at the shared boundary.

Related key results presented in paper VI

In paper VI, the performance of the inertia compensator is investigated for the configuration presented in figure 2.7. Here the displacement in the y-direction is included with the desired displacement $d_{num}(t)$ represented in figure 2.12a for a frequency of 0.74Hz, 1.48Hz, 2.22Hz and 2.96Hz. The reaction force when enabling and disabling the inertia compensator is presented for a duration of 2 sec. in figure 2.15. The remaining dofs at the shared boundary including

translation in the x-direction and rotation around the z-axis is neglected given that the contribution is negligible relative to the corresponding reaction force at the shared boundary. The acceleration of the shared boundary is determine as the double derivative to the desired displacement $d_{num}(t)$.

The mass m_y of the test rig in the y – direction is determined from a test sequence without the experimental substructure meaning that the test rig is acting as a lumped mass connected to the hydraulic actuators. For the desired displacement $d_{num}(t)$ in the y-direction described by a sinusoidal waveform with an amplitude and frequency of 9.25mm and 2.96Hz respectively the reaction force $F_y(t)$ vs. the acceleration $a_y(t)$ is acquired. A best-fit first order trend line is fitted in the data set in order to identify m_y as the slope of this trend line cf. eq. (2.11).

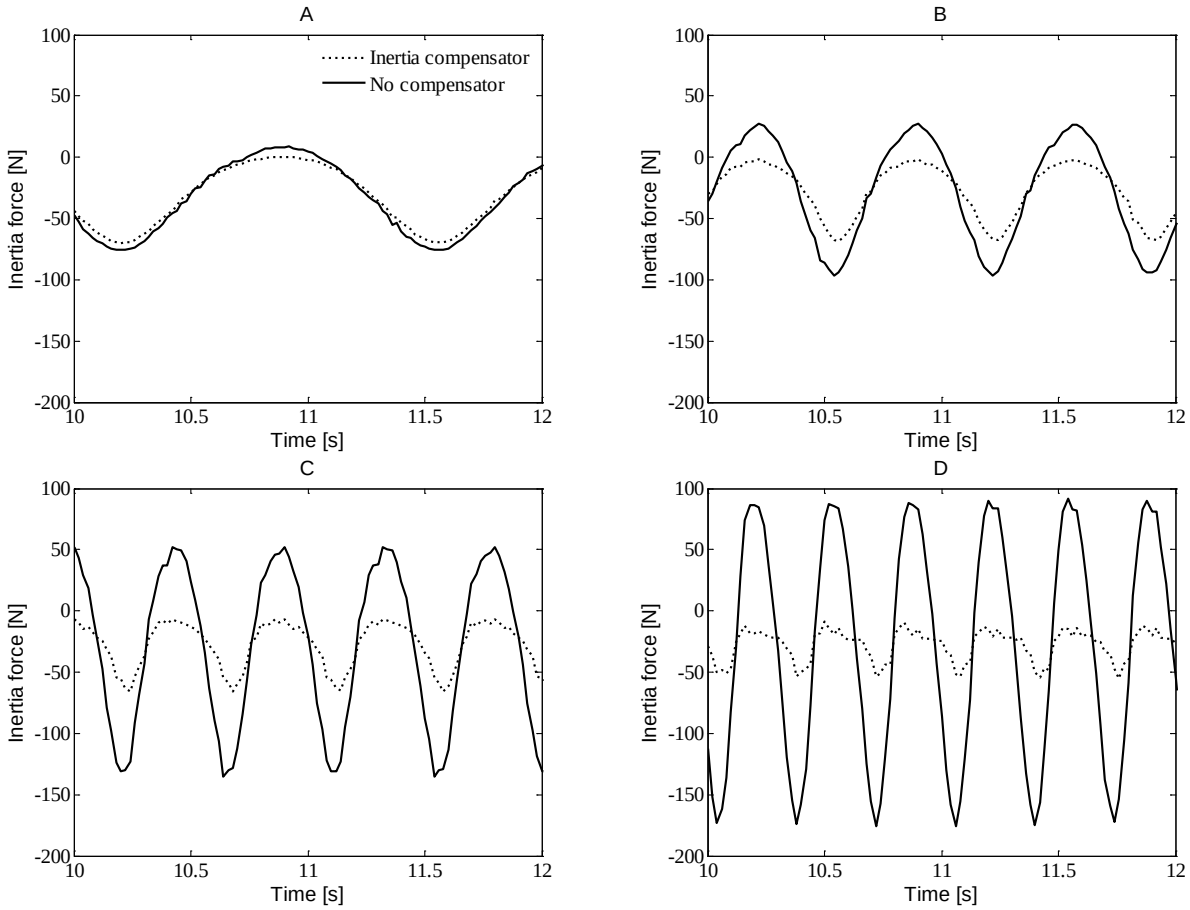

Figure 2.15: Inertia compensator performance for: a) f = 0.74Hz, b) f = 1.48Hz, c) f = 2.22Hz and d) f = 2.96Hz

From figure 2.15, it is seen that the effect of the inertia compensator is gradually increasing as a function of the frequency. For a frequency of 0.74 and 2.96Hz the achieved reduction of the inertia contribution is equivalent to 22.23 and 83.77% respectively. Ideally, the compensated inertia force should be zero (100% reduction of the inertia contribution) for the entire duration of the test – however due to dynamics in the transfer system, friction in the swivels and hinges connecting the actuators to the test rig, etc. some unavoidable inertia effects will still be present. Also – a major source of error includes the fact that the acceleration of the shared boundary is derived directly from the desired displacement $d_{num}(t)$. A much more reliable and precise approach would be to use an accelerometer capable of feeding RT measurements directly into the control loop of the RTHS.

2.3. Chapter summery

Two interface compensation methods named high precision tracking compensator and inertia compensator were presented capable of improving the accuracy and stability within single-component HS by reducing the experimental errors induced at the shared boundary.

The high precision tracking compensator was capable of reducing the discrepancy between the desired and achieved displacement or strain imposed at the shared boundary. Within the QS regime the compensator were operating the shared boundary with a predefined error tolerance by allowing multiple adjusting correction steps within a single time step. The technique was verified through a three point bending test on a GFRP beam loaded by a unidirectional actuator with an internally mounted LVDT. By tracking the shared boundary through DIC the high precision tracking compensator proved successful with an error tolerance of ±0.01mm – which corresponds to 0.17% of the peak-to-peak displacement – through a total of 17-25 adjusting correction steps for a sample of three tests. Also, the shared boundary was tracked through internally mounted FBGs with an error tolerance of ±20με that corresponded to 0.69% of the peak-to-peak strain. Through a total of 24-28 adjustments for a sample of three tests, the compensator was capable of keeping the discrepancy between the desired and achieved strain at the shared boundary within the predefined tolerance. The number of required adjustments was found to be dependent on the assigned error tolerance for the given application. The compensator was also verified on a cantilever GFRP beam loaded by three unidirectional actuators with internally mounted LVDT's. The shared boundary was here defined by a discrete point with three dofs including in-plane translation and rotation. In the QS regime the discrepancy between the desired and achieved displacement were reduced by 69%, 87% and 89% even though that no error tolerance were defined. In the RT regime, improvements in the range of 3% to 84% were achieved for a sinusoidal wave with a frequency of 0.074 and 2.96Hz respectively.

The inertia compensator was included in the RT regime to erase the inertia forces induced by the lumped mass represented by the test rig. For a single dof translation with a frequency of 0.74 and 2.96Hz the achieved reduction of the inertia contribution were 22.23 and 83.77% respectively.

3. Quasi-static and pseudo-dynamic single-component hybrid simulation

A platform capable of accommodating a QS or PsD single-component HS is presented. Here the overall system architecture of the HS communication loop including the numerical substructure, transfer system capable of operating the experimental substructure on an extended time scale along with relevant interface compensators are presented and discussed. The HS communication loop is implemented in LabVIEW and verified through two case studies including a) conventional QS HS – further described in paper VII and b) single-component QS HS – further described in paper II.

3.1. Overall system architecture

Structural assessment through QS or PsD HS is a substructuring technique capable of mimicking the response of the emulated structure by combining the advantages of numerical modelling with those of experimental testing. The coupling governed through the shared boundary is achieved by maintaining the compatibility and equilibrium at the interface – entailing that the deformation of the shared boundary which is included in the vector x can be written cf. eq. (3.1) and (3.2) in the extended time domain i.

$$P_{ext}(i) = M_{num}\ddot{x}(i) + C_{num}\dot{x}(i) + k_{num}x(i) + R_{exp}(i) \tag{3.1}$$

$$R_{exp}(i) = k_{exp}x(i) \tag{3.2}$$

Here the matrices M, C and K represent the mass, damping and stiffness while the vectors R and P includes the reaction force at the shared boundary and external load respectively. The indexes “num” and “exp” refer to the numerical and experimental substructure respectively while each overdot denotes a single time derivative. Within QS HS, the inherent dynamics of the entire emulated structure is suppressed entailing that the mass and damping contribution in eq. (3.1) is neglected. PsD HS only exclude the inherent dynamics of the experimental substructure meaning that the response of the shared boundary is described in the form represented in eq. (3.1) and (3.2).

Through the HS communication loop represented in figure 3.1 the numerical and experimental substructure is operated with an iteration step of $\triangle$i. Here the numerical substructure is discretized to derive the upcoming displacement d_{num}(i) based on the external load P_{ext}(i) and last available reaction force R_{exp}(i-$\triangle$i). By tracking the shared boundary through the external DAQ system, the actual achieved displacement $d_{achieved}$(i) is obtained in order to derive the commanded displacement d_{cmd}(i) through the high precision tracking compensator cf. eq. (2.2). The commanded displacement d_{cmd}(i) is imposed on the experimental substructure through the transfer system and the corresponding reaction force R_{exp}(i) returned to the numerical substructure to reveal the response of the emulated structure in the subsequent iteration step i+$\triangle$i. The numerical and experimental substructure, communication loop, external DAQ system and transfer system combine to form the single-component HS.

The HS communication loop is operated in LabVIEW, which offers a graphical based object-oriented programming environment developed by National Instruments. Here various pre- and user defined functions are implemented using graphical drag-and-drop icons as substitutes to text-based programming. The execution order between each function is handled through graphical dataflow programming. Communication between LabVIEW and various hardware resources like control and data acquisition systems can be achieved through different communication protocols including General Purpose Interface Bus (GPIB), USB, Ethernet, serial, etc. The graphical based object-oriented programming induces an ideal software platform, which provides simple, flexible and extensible software architecture for the designer. Other software platforms have been implemented to facilitate HS including Open Fresco [40] and Simulink [41].

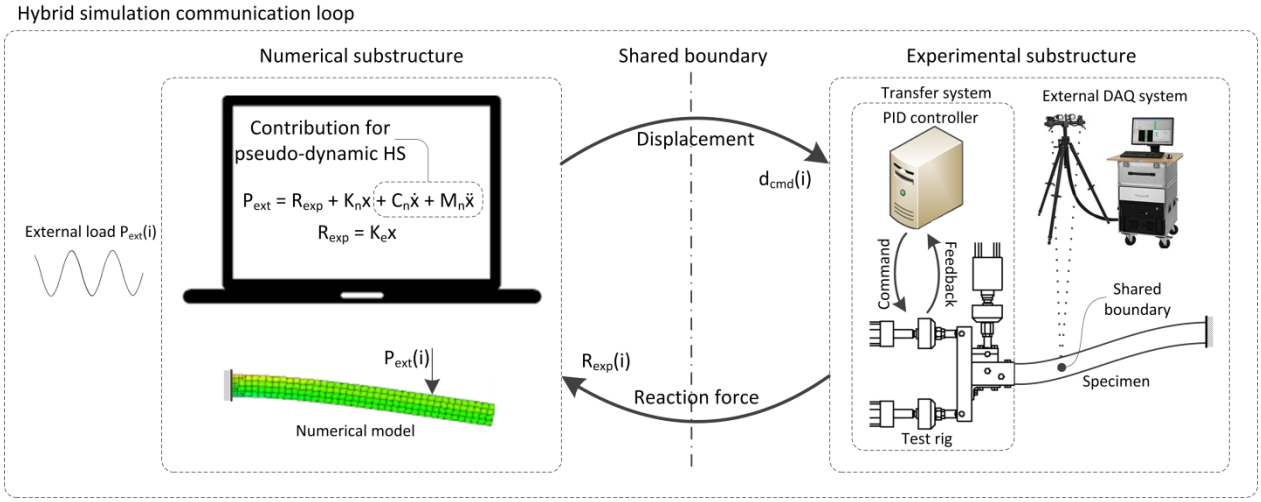

Figure 3.1: Schematic block diagram representing the overall architecture of the single-component HS communication loop

Within QS and PsD HS the inherent dynamics of the experimental substructure is suppressed entailing that the HS communication loop is operated at an extended time scale. This allow the communication loop including numerical substructure, external DAQ system, transfer system, etc. to operate sequentially in a state machine framework by separating the different subroutines in the HS communication loop in suitable and well-defined states [42]. The state machine architecture provides a very simple and flexible multi-processing platform, which is easy to extend and modify throughout the design phase. However, these separate states also induce a repeated process of loading and pausing at the shared boundary cf. figure 3.2, which is generally referred to as the ramp-hold procedure [43]. During the hold period – while the numerical substructure (state I) and external DAQ system (state II) is executed to derive the subsequent commanded displacement $d_{cmd}(i)$ – force relaxation may occur in the experimental substructure, compromising the fidelity of the reaction force $R_{exp}(i)$ which is fed back to the numerical substructure cf. figure 3.1. In order to avoid these holding periods a continuous flow of displacement signals are required to impose a smooth actuator displacement time history – referred to as continues PsD HS in [43].

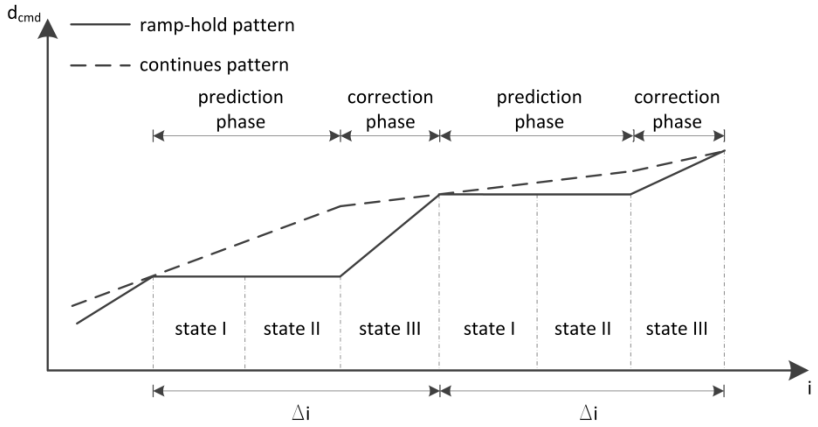

Figure 3.2: Outline of the continuous PsD HS technique

This technique separates each iteration step Δi of the HS communication loop in two phases named prediction phase and correction phase. Through the correction phase the current commanded displacement $d_{cmd}(i)$ is induced on the experimental substructure through the transfer system (state III) while the corresponding reaction force $R_{exp}(i)$ is returned to derive the subsequent commanded displacement $d_{cmd}(i+\Delta i)$. While the numerical substructure (state I) and external DAQ system (state II) are executed in a predefined subsequent order, the transfer system (state III) awaits the upcoming desired displacement – inducing a period in which the transfer system pauses. For this reason –

while the upcoming commanded displacement $d_{cmd}(i+\triangle i)$ is yet unknown – a prediction phase is introduced capable of predicting the upcoming commanded displacement $d_{pred}(i)$ through a forward prediction scheme with a fine iteration step δi [44]. Once the upcoming commanded displacement is available the system enters the correction phase where the transfer system moves to the defined commanded displacement $d_{cmd}(i)$.

3.1.1. Numerical substructure

The numerical substructure typically includes the majority of the emulated structure and represents either predictable mechanical behaviour or is considered uncritical for the analysis conducted. The numerical substructure is discretized through an either explicit or implicit FE-formulation with a time integration performed with e.g. Central Difference Method [45], Newmark scheme [44], Operator-splitting method, etc. Within PsD HS the dynamics of the numerical substructure is taken into account meaning that the integration time has to be adjusted to fit the system frequency of interest in order to ensure precision and stability of the HS.

By having the inherent dynamics of the experimental substructure suppressed leaves the HS communication loop with no time constraints for all the different subroutines included. This entails that no restrictions exists regarding the execution time needed for each discrete time integration meaning that the characteristics and refinement of the numerical model can be defined without having to worry about the available computational resources.

Within this PhD study two commercially available platforms named MATLAB [46] and ANSYS (ANSYS, Inc, Canonsburg, PA, USA) [47] are included to handle the numerical substructure. The communication interface between LabVIEW and MATLAB is established through a predefined and configurable MATLAB script node [48], which is implemented directly in the LabVIEW environment as a single graphical drag-and-drop icon. The design of the numerical model including model geometry, material properties, discretization, boundary conditions and loads is defined through the script language, which is directly implemented into the MATLAB script node while the variables including the external load along with reaction force and displacement at the shared boundary is handled as inputs and outputs. The link between LabVIEW and ANSYS is established through the Windows command prompt, which is operated through the drag-and-drop icon named System Exec VI [49]. Through an ANSYS Parametric Design Language (APDL) script, the design of the numerical model is defined and solved using the FE-engine in ANSYS BATCH mode to save computational resources. For each run of the FE-analysis, a macro file defines the sequence of events including update of the reaction and external force in the APDL script, execute the FE-engine solver, save the displacement of the shared boundary in an output file and close the solver to free all the related resources.

3.1.2. Experimental substructure

The experimental substructure includes the part of special interest and is therefore physically replicated to reveal the effects of e.g. buckling, viscoelasticity, mechanical damage or other non-linear effects. The QS imposed displacement on the experimental substructure is within this PhD study applied through a servo-hydraulic transfer system including a PID controller and servo-hydraulic actuators. Furthermore, an operating computer is included to handle the HS communication loop along with the A/D and D/A chassis, which enables the communication interface between the PID controller and operating computer along with data acquisition from the load cell and LVDT. Furthermore, an external DAQ system is connected to the operating computer in order to monitor the QS imposed displacement of the shared boundary cf. section 2.1.1. The overall hardware setup and communication flow is illustrated in figure 3.3.

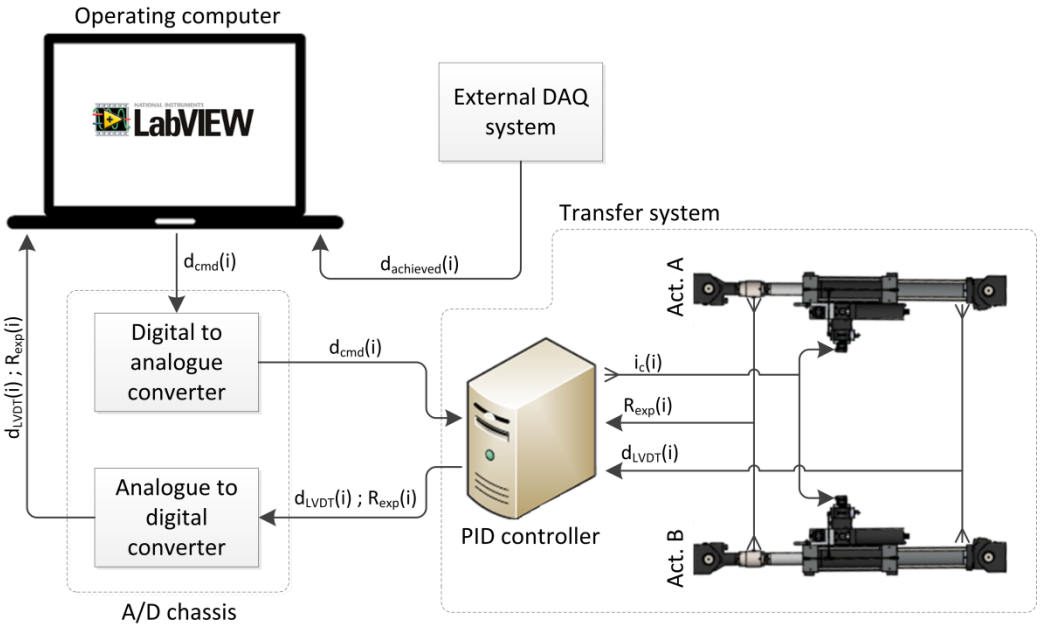

Figure 3.3: representation of the overall hardware setup

Through the operating computer a command displacement $d_{cmd}(i)$ is generated for each of the actuators included in the transfer system which is transferred to the D/A converter. Here $d_{cmd}(i)$ is converted to an equivalent analogue signal which is transferred to the PID controller. From the command signal $d_{cmd}(i)$ and current position of the actuator $d_{LVDT}(i)$ the corresponding electrical current $i_c(i)$ is generated by the PID controller to operate the servo valve – causing the piston to move accordingly. In parallel the achieved displacement $d_{LVDT}(i)$ and corresponding reaction force induced at the load cell $R_{exp}(i)$ is obtained and returned to the operating computer through the A/D converter. As an alternative to the analogue communication interface between the operating computer and PID controller a digital solution is implemented in order to omit the random truncations generated by the A/D and D/A conversion. By replacing the A/D chassis with a TCP/IP access, a digital communication interface is established through a library of MTS drivers that is implemented directly in the LabVIEW environment [50]. It is noted that these MTS drivers are only convertible with PID controllers operated by the MTS 793 software. Through the operating computer a predefined command signal $d_{cmd}(t)$ is generated – causing each actuator included in the transfer system to move accordingly in a ramped monotonic motion. When the desired displacement is achieved, the actuator pauses and holds in that position while the corresponding feedback signals from e.g. LVDTs and load cells are acquired. The operation of the actuators and acquiring of the desired feedback signal are therefore executed in two different sequences which are running sequentially – entailing that the digital communication interface preclude RT operation of the actuators.

3.1.3. Interface compensator

The interface between the numerical and experimental substructure is governed through the HS communication loop, which in turn operates the numerical and experimental substructure to maintain compatibility and equilibrium at the shared boundary. To maintain accuracy and stability within HS in the QS and PsD regime a number of systematic and random experimental errors has to be taken into account including communication delay, compliance in the load train, sensor miscalibration, measurement noise and random truncations in the A/D and D/A conversion.

Due to communication delay governed by the external load $P_{ext}(i)$ being a single discrete iteration step $\triangle i$ ahead of the corresponding reaction force $R_{exp}(i-\triangle i)$ a compensator is implemented capable of extrapolating either the upcoming desired displacement $d_{num}(i)$ or the corresponding reaction force $R_{exp}(i)$ ahead in time by using forward prediction schemes or performance estimation algorithms [44]. Within forward prediction schemes many algorithms exist capable of facilitate communication delay compensation including exact polynomial fitting extrapolation [51], least-

square polynomial fitting extrapolation [52], extrapolation based on linearly predicted acceleration [53], etc. The exact polynomial fitting extrapolator is the most widely used in the field – capable of extrapolating the desired displacement $d_{exp}(i)$ after a constant delay from the current and previews data points $d_m(i)$ provided by the numerical substructure and a_i which are polynomial coefficients generated through the Lagrange formula. The desired displacement $d_{exp}(i)$ is then fed to the transfer system as the commanded displacement. For an Nth order polynomial fit a number of N+1 data points are included in the extended time domain i cf. eq. (3.3).

$$d_{exp}(i) = \sum_{m=0}^{N} a_m d_m(i) \tag{3.3}$$

Other improved methods exist including the performance estimation algorithm capable of dealing with higher delays as compared with the smallest period of interest for the structure [54]. However, this compensation method has not been included in any of the appended papers and will therefore not be discussed any further in this PhD study.

The compliance in the load train is handled by tracking the imposed displacement of the shared boundary through an external DAQ system. By a control loop algorithm for high precision tracking of the shared boundary outlined in figure 2.1 the QS imposed displacement at the experimental substructure is adjusted to fit the desired displacement. With the option of performing multiple adjusting corrections within a given iteration step Δi a predefined error tolerance β can be defined. The technique is further described in section 2.1.1.

The random experimental errors including measurement noise and random truncations in the A/D and D/A conversion is handled through oversampling once the transfer system pauses and holds the position prior to receiving the next desired displacement $d_{num}(i)$. This is a simple and effective filtering approach, which does not introduce any additional communication delay to the system. If no pause sequence is included in the experimental substructure a low-pass filter is included with a cut-off frequency that is low enough to avoid aliasing and at the same time does not induce an unacceptable communication delay in the communication loop [44].

3.2. Case study for verification of the single-component hybrid simulation platform

The overall system architecture outlined in subchapter 3.1 for QS and PsD HS is verified through two case studies including conventional QS HS and single-component QS HS.

3.2.1. Quasi-static hybrid simulation on an conventional application

The QS HS communication loop presented in figure 3.1 is investigated for a conventional application to reduce the complexity in verifying the software capabilities.

Related key results presented in paper VII

A QS HS is conducted on the emulated structure outlined in figure 3.4 to reduce the complexity in verifying the software capabilities.

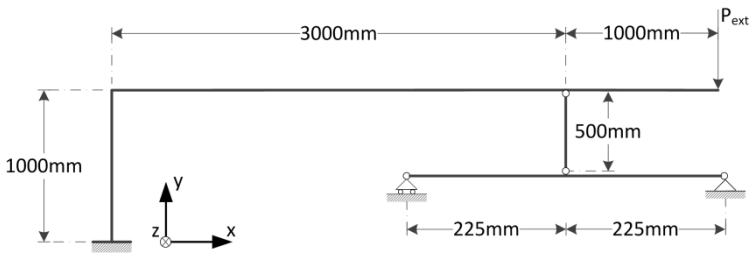

Figure 3.4: emulated structure representing the overall dimensions, external load and boundary conditions

The emulated structure is partitioned in a numerical and experimental substructure cf. figure 3.5 – referred to here as part A and B. The shared boundary between the two substructures is defined by a discrete point with a single dof including translation in the y-direction. In addition, a small translation in the x-direction is present at the shared boundary – however this contribution is neglected due to the relatively small magnitude.

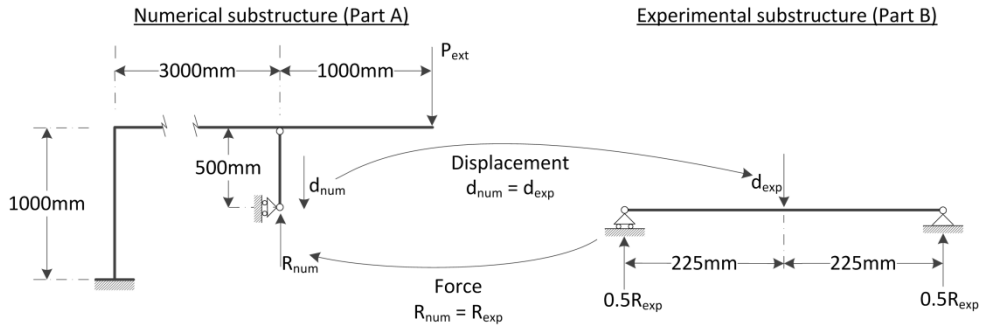

Figure 3.5: emulated structure separated in: a) numerical substructure and b) experimental substructure

The QS HS communication loop is operated in a state machine architecture [42] through LabVIEW 8.6. The outline of the dataflow in the HS communication loop is presented in figure 3.6.

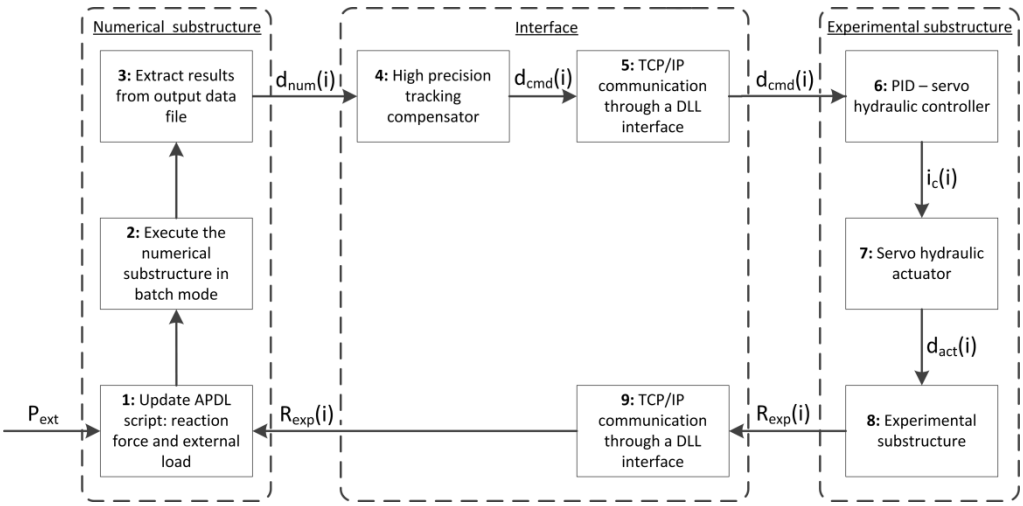

Figure 3.6: schematic block diagram representing the QS HS communication loop

The numerical substructure is defined in ANSYS 12.1 through a APDL script which is updated with the current external load P_{ext} and last available reaction force $R_{exp}(i)$ in **(1)**. Through the APDL script the numerical substructure is executed in batch mode by **(2)** to derive the upcoming displacement $d_{num}(i)$. Here the numerical substructure is discretized through an 8-node plane beam element with two dofs in each node including translation in the x and y direction. Finally the upcoming displacement $d_{num}(i)$ is extracted from the output data file in **(3)**.

The interface between the numerical and experimental substructure is governed at the shared boundary, which is located at the centre of the GFRP beam outlined in figure 2.3. The shared boundary is tracked through the three measurement points labelled MP-1, MP-2 and MP-3 using DIC. The relation between the displacement of the shared boundary and displacement at the given measurement point is derived from the Euler-Bernoulli theory cf. eq. (2.3) and (2.4). Based on the displacement $d_{num}(i)$ and actual achieved displacement tracked through the 3 measurement points a command displacement $d_{cmd}(i)$ is derived in **(4)** cf. eq. (2.2). Through the high precision tracking compensator technique presented in section 2.1.1 an error tolerance of β = 0.01mm is obtained. The commanded displacement $d_{cmd}(i)$ is transferred to the servo hydraulic PID controller in **(6)** through the TCP/IP port using a DLL interface [50]

presented in **(5)**. The corresponding reaction force $R_{exp}(i)$ is through the same communication technique returned to the numerical substructure in **(9)**.

Through the experimental substructure the GFRP beam is loaded by a unidirectional hydraulic actuator in **(7)** operated by a servo hydraulic PID controller in **(6)** through an electrical current $i_c(i)$. The piston of the actuator moves accordingly with the displacement $d_{act}(i)$ – deforming the experimental substructure. The corresponding reaction force $R_{exp}(i)$ is obtained in **(8)**.

The global stability of the HS is compromised by the systematic and random experimental errors induced at the shared boundary including communication delay, compliance in the load train, sensor miscalibration, measurement noise and random truncations in the A/D and D/A conversion. The impact of these experimental errors is dependent on the ratio between the global stiffness of the experimental and numerical substructure. The global stiffness of the numerical and experimental substructure named k_n and k_e respectively is defined cf. eq. (3.4)

$$k_n = \frac{P_{ext}}{d_{num}} \quad \text{and} \quad k_e = \frac{R_{exp}}{d_{exp}} \tag{3.4}$$

Given that no communication delay compensator is included in the QS HS – a global stability analysis is performed through a parametrical study. In this study, the numerical substructure is defined in a FE-model while the response of the experimental substructure is handled analytically through a Bernoulli-Euler formulation. By implementing these two models in the HS communication loop outlined in figure 3.6 the stability is evaluated by adjusting the stiffness ratio between the numerical and experimental substructure - referred to here as a performance analysis. In this performance analysis only the influence of the communication delay is included.

For each load step of the external load P_{ext} ranging from 0 to 20kN the history of the reaction force at the shared boundary is evaluated through the performance analysis including three different stiffness ratios cf. figure 3.7.

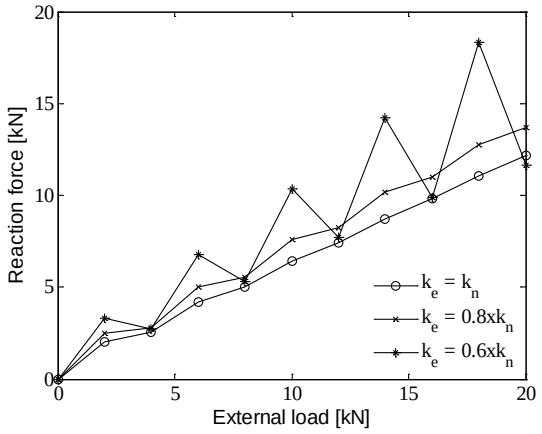

Figure 3.7: history of reaction force at the shared boundary as a function of the external load P_{ext}

From figure 3.7 instability is identified for a configuration where the global stiffness of the numerical substructure is equivalent to or lower than 60% of the experimental substructure i.e. $0.60k_e \geq k_n$. If the HS communication loop is inverted entailing that the numerical and experimental substructure receives a deformation and force input respectively – instability is present when $0.60k_e \leq k_n$. Given that the global stiffness of the numerical substructure is 4.94 times higher than the experimental substructure in the present HS i.e. $4.94k_e = k_n$ – no instability is expected even though some additional experimental errors will be present which were not included the performance analysis.

The performance of the single-component HS communication loop is investigated in the QS regime for a gradually increasing external load ranging from 0 to 18kN – applied over 20 equally distributed load steps. The equivalent vertical displacement at the shared boundary is 0 to 6mm. The HS is verified against two additional analyses including reference and performance analysis. The reference is a pure FE-model of the emulated structure outlined in figure 3.4. The response of the experimental substructure is in the reference calibrated to fit the global stiffness obtained from the three-point-bending test presented in figure 2.3. The performance analysis is further described in the former paragraph.

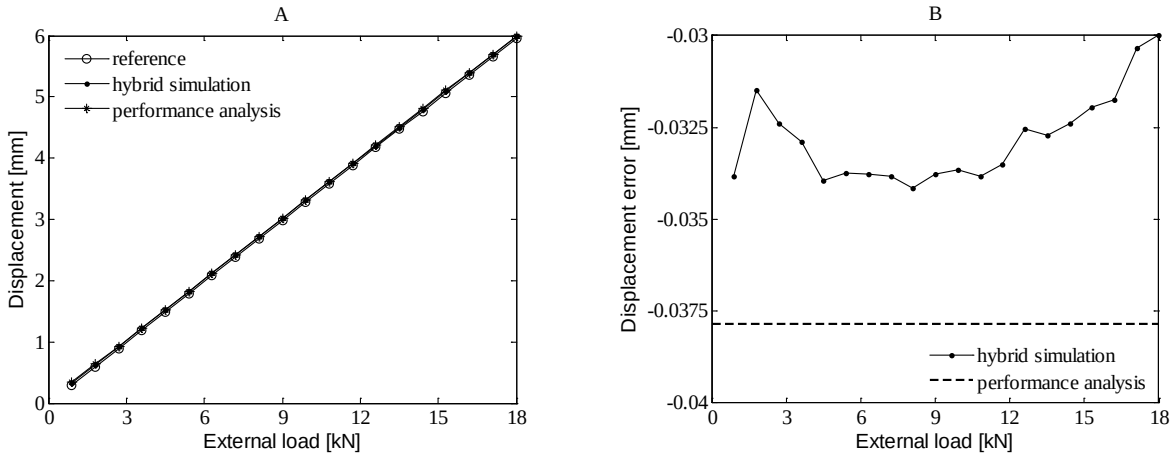

Figure 3.8: QS single-component HS: a) response at the shared boundary and b) discrepancy between the HS, performance analysis and reference

From figure 3.8, a sound correlation between the HS, performance analysis and reference is achieved. According to figure 3.8b, a constant discrepancy between the reference and performance analysis is identified which is equivalent to 0.64% of the total displacement at the shared boundary. This error is exclusively governed by the communication delay, which is constant throughout the 20 equally distributed load steps. The discrepancy between the HS and reference is identified to 0.57% of the peak-to-peak displacement at the shared boundary. This error is influenced by several additional parameters besides the communication delay including compliance in the load train, sensor miscalibration, measurement noise and random truncations in the A/D and D/A conversion. From figure 3.8b, it is identified that the displacement error achieved for the HS exhibits an improved performance in relation to the performance analysis for an increasing external load. This may not be the case for a decreasing external load meaning that the errors besides the communication delay may magnify the resulting displacement error.

3.2.2. Quasi-static hybrid simulation on an single-component application

The performance of the HS communication loop presented in section 3.2.1 is investigated on a single-component application with a shared boundary covering three dofs.

Related key results presented in paper II

A single-component QS HS is conducted on a GFRP beam that is clamped in both ends and loaded by an external displacement d_{ext}. The overall geometry, boundary conditions and external load of the emulated structure is presented in figure 3.9.

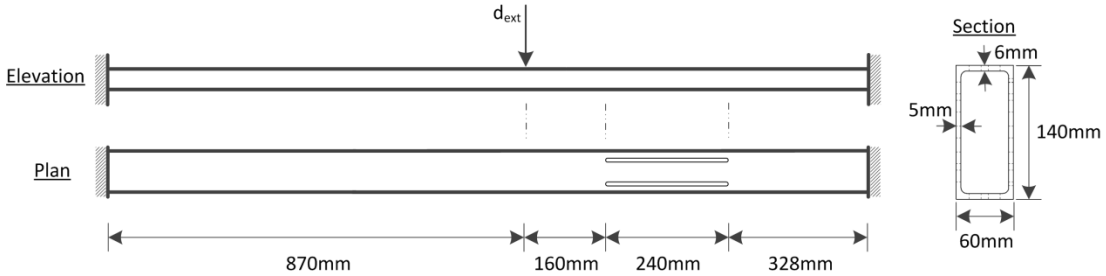

Figure 3.9: emulated structure representing the overall dimensions, external load and boundary conditions

The emulated structure is partitioned in a numerical and experimental substructure – referred to here as part A and part B respectively. Two slits are located at the compression flange to yield a geometrical non-linear response of the experimental substructure due to buckling. Each substructure along with the coupling between them is outlined in figure 3.10.

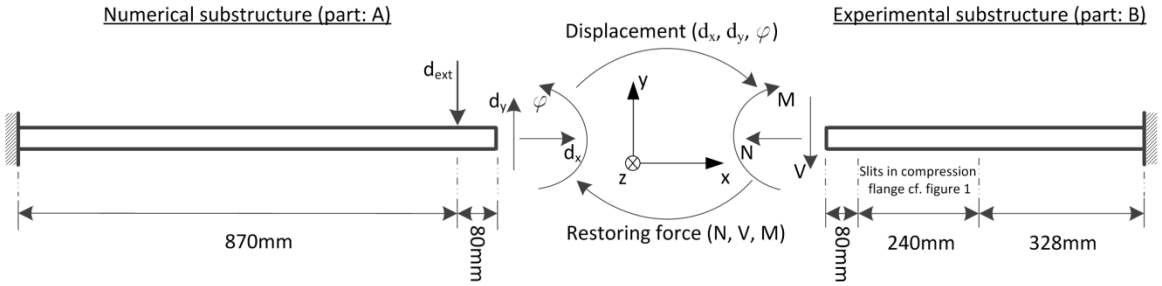

Figure 3.10: emulated structure separated in: a) numerical substructure and b) experimental substructure

The shared boundary between the numerical and experimental substructure is defined by a discrete point with three dofs including translation in the x- and y-direction along with rotation around the z-axis – referred to here as φ.

The experimental substructure is loaded in a stiff frame structure by three actuators named actuator A, B and C. The structural response is tracked by DIC through the measurement points labelled MP-7 to MP-11 while the strain at the compression and tension flanged is monitored through strain gauges labelled SG-3 to SG-5. The overall geometry, boundary conditions, measurement points, etc. of the experimental substructure is presented in figure 3.11a.

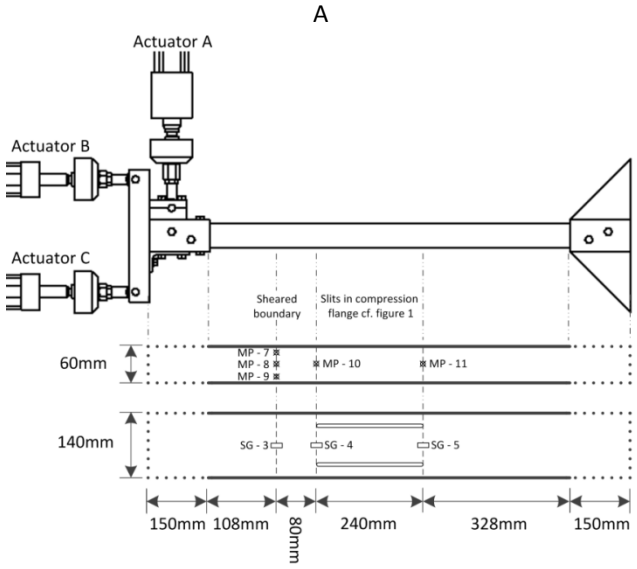

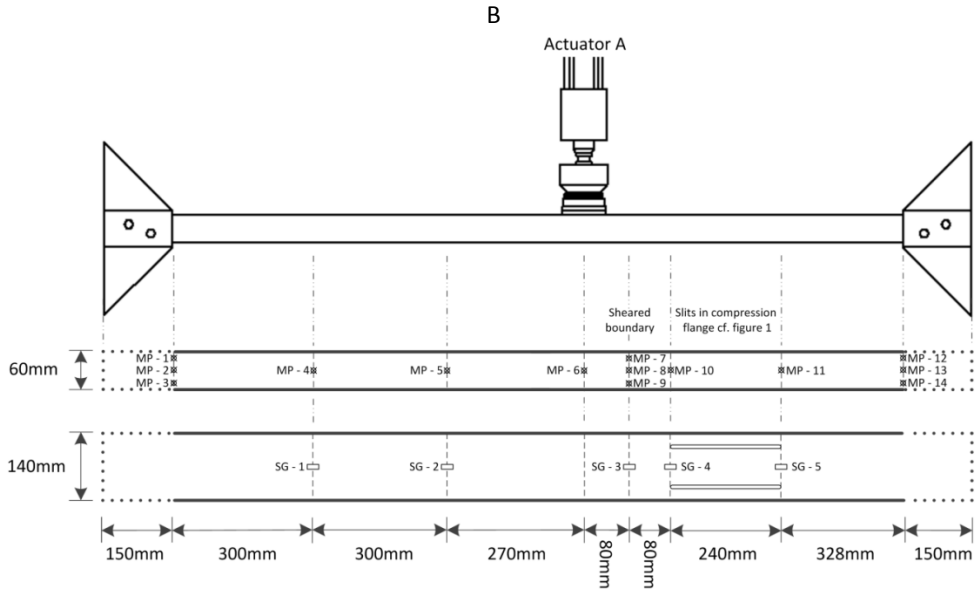

Figure 3.11: experimental setup including: a) experimental substructure and b) reference

To validate the output from the QS HS an experimental test of the emulated structure is conducted – referred to here as the reference. The structural response is here tracked through the measurement points labelled MP-1 to MP-14 while the strain at the compression and tension flanged is monitored through strain gauges labelled SG-1 to SG-5. The overall geometry, boundary conditions, measurement points, etc. of the reference is presented in figure 3.11b.

The QS HS communication loop is operated in a state machine architecture [42] through LabVIEW 13.0. The outline of the dataflow in the HS communication loop is presented in figure 3.12. The numerical substructure is defined in ANSYS 15.0 through the APDL script which is updated with the current external displacement d_{ext} and last available reaction $\underline{R}_{exp}(i+\triangle i)$ in **(1)**. Through the APDL script the numerical substructure is executed in batch mode by **(2)** to derive the upcoming displacement $\underline{d}_{num}(i)$ in the format $[d_x(i);d_y(i);\varphi(i)]$. Here the numerical substructure is discretized using isoperimetric quadrilateral 8-node shell element of the type shell281 [55]. Finally the upcoming displacement $\underline{d}_{num}(i)$ is extracted from the output data file in **(3)**.

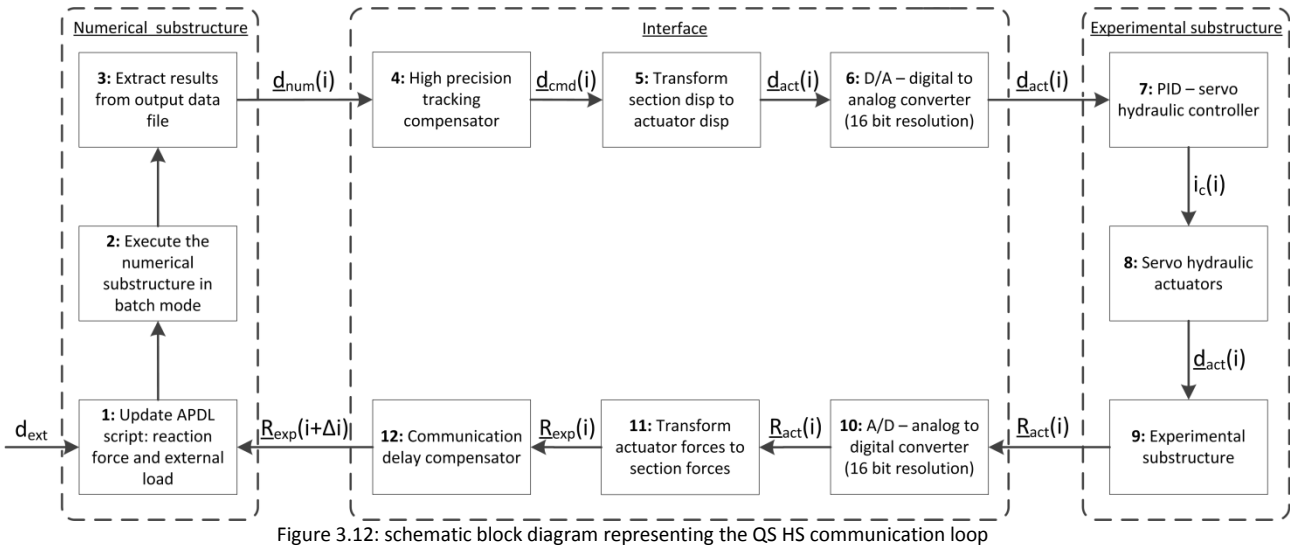

Figure 3.12: schematic block diagram representing the QS HS communication loop

The interface between the numerical and experimental substructure is governed at the shared boundary, which is outlined in figure 3.10. The shared boundary is tracked through the three measurement points labelled MP-7, MP-8

and MP-9 using DIC. The relation between the displacement of the shared boundary and displacement at the three measurement points is obtained with the assumption of having a linear cross sectional deformation at the shared boundary. Here the in-plane translation in the x- and y-direction is calculated as the average displacement of the three measurement points while the rotation is derived as the change of angle between MP-7 and MP-9. Based on the displacement $\underline{d}_{num}(t)$ and actual achieved displacement tracked through the three measurement points at the shared boundary a command displacement $\underline{d}_{cmd}(i)$ is derived in **(4)** cf. eq. (2.2) with no predefined error tolerance β. The relation between the commanded displacement $\underline{d}_{cmd}(i)$ at the shared boundary and corresponding displacement of the actuators $\underline{d}_{act}(i)$ with the format $[d_A(i);d_B(i);d_C(i)]$ is derived through a trigonometric relation in **(5)** with the assumption of rigid body motion. The relation is derived from eq. (2.8) with the coordinate system and notation outlined in figure 2.6. The commanded displacement $d_{act}(i)$ for each of the three actuators is transferred to the servo hydraulic PID controller in **(7)** through the D/A converter presented in **(6)**. The corresponding reaction force $\underline{R}_{act}(i)$ obtained in each of the three actuators in the format $[R_A(i),R_B(i),R_C(i)]$ is through the same communication technique returned to the numerical substructure in **(10)**. These actuator forces $\underline{R}_{act}(i)$ are transferred to section forces $\underline{R}_{exp}(i)$ in the format $[R_V(i);R_H(i);M(i)]$ through a trigonometric relation in **(11)** – assuming rigid body motion. The relation is derived from eq. (3.5) to (3.7) with the coordinate system and notation outlined in figure 2.6. The communication delay at the interface is handled in **(12)** by predicting the upcoming reaction force $\underline{R}_{exp}(i+\Delta i)$ through extrapolation by the 4 previous sets of external displacement d_{ext} and reaction force $\underline{R}_{exp}(i)$. This extrapolation is achieved through a linear regression [56].

$$R_V = R_A cos(\gamma_A) + R_B sin(\gamma_B) + R_C sin(\gamma_C) \tag{3.5}$$

$$R_H = R_A sin(\gamma_A) + R_B cos(\gamma_B) + R_C cos(\gamma_C) \tag{3.6}$$

$$\begin{aligned} M = {} & R_A\Big(cos(\gamma_A)\big(x_A(i) - x(i)\big) + sin(\gamma_B)\big(y(i) - y_A(i)\big)\Big) \\ & + R_B\Big(cos(\gamma_B)\big(y(i) - y_B(i)\big) + sin(\gamma_B)\big(x_B(i) - x(i)\big)\Big) \\ & + R_C\Big(cos(\gamma_C)\big(y(i) - y_C(i)\big) + sin(\gamma_C)\big(x_C(i) - x(i)\big)\Big) \end{aligned} \tag{3.7}$$

Through the experimental substructure the GFRP beam is loaded by three unidirectional hydraulic actuators in **(8)** operated by a servo hydraulic PID controller in **(7)** through an electrical current $i_c(i)$. The piston of the actuator moves accordingly with the displacement $\underline{d}_{act}(i)$ and the corresponding reaction force $\underline{R}_{exp}(i)$ is obtained in **(9)**.

The performance of the QS HS communication loop is evaluated for an external displacement d_{ext} covering 60 steps per period forming a triangular waveform with a peak-to-peak amplitude of 6.5mm. The equivalent vertical reaction force at the shared boundary is 5.00kN. The overall deformation pattern of the reference and HS is evaluated for two different vertical reaction forces at the shared boundary represented in figure 3.13. Here a sound correlation between the reference and HS is identified – measured in the measurement points represented in the top part of the graph. The maximum deviation between the reference and HS is identified to 2.1% relative to the reference.

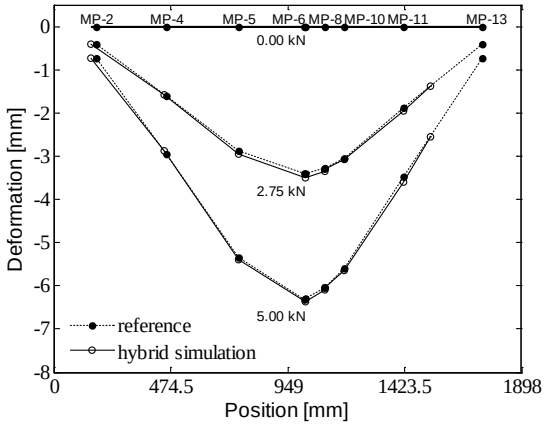

Figure 3.13: structural response of the GFRP including: HS and reference

The vertical and horizontal translation along with rotation of the shared boundary is tracked through MP-7, MP-8 and MP-9 for both the reference and HS by DIC. The output from the HS is partitioned in two parameters named $\underline{d}_{num}(i)$ and $\underline{d}_{achieved}(i)$. Here $\underline{d}_{num}(i)$ represents the desired displacement at the shared boundary derived by the numerical substructure and $\underline{d}_{achieved}(i)$ the actual response of the shared boundary tracked through MP-7, MP-8 and MP-9 by DIC.

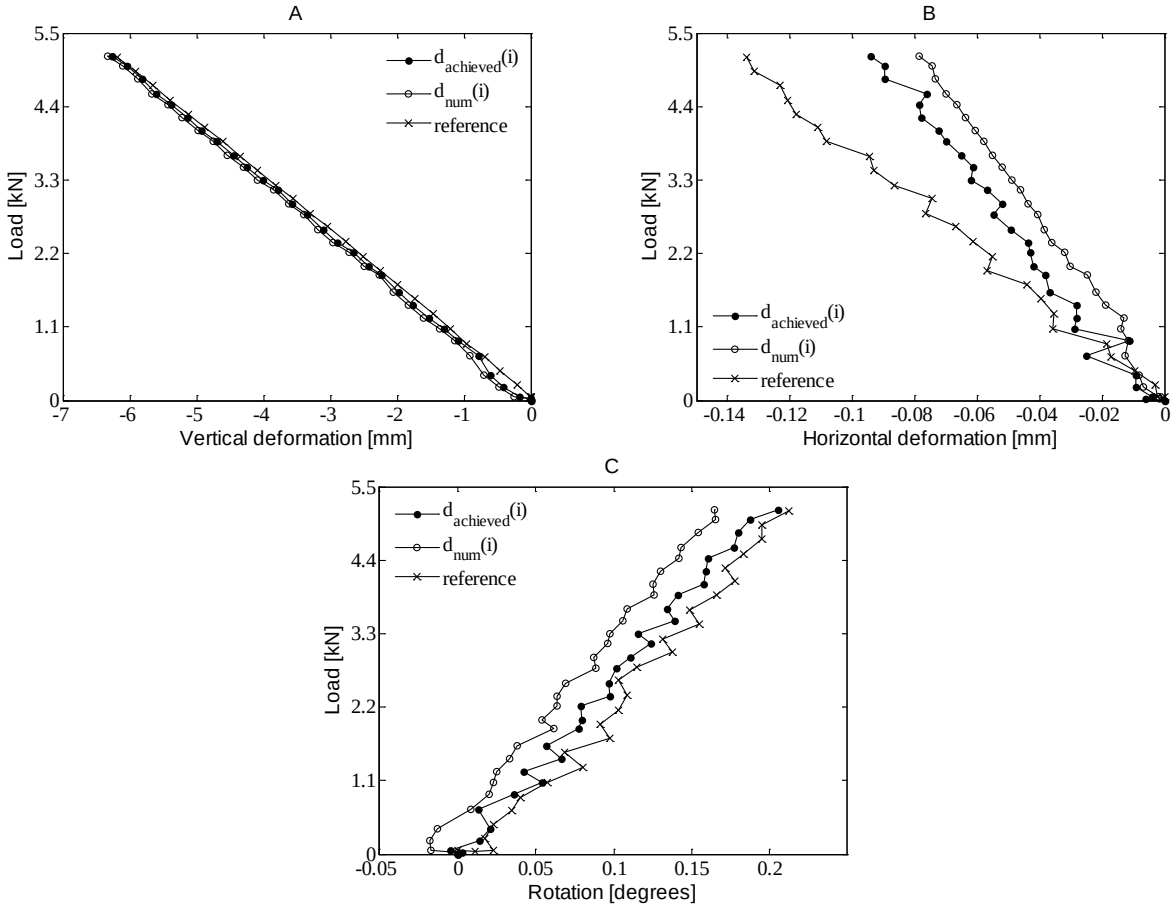

Figure 3.14: displacement at the shared boundary: a) vertical, b) horizontal and c) rotation

A sound correlation between the HS and reference is identified in figure 3.14 in terms of vertical and rotational stiffness of the shared boundary. In the horizontal direction – outlined in figure 3.14b – a deviation in stiffness is identified between the reference and HS. In figure 3.14c an offset between the reference, $\underline{d}_{num}(i)$ and $\underline{d}_{achieved}(i)$ is

identified. For the reference test – this offset is most likely induced by contact issues in the loading nose while the offset between $\underline{d}_{num}(i)$ and $\underline{d}_{achieved}(i)$ is triggered by compliance in the load train.

The strain distribution at the top and bottom flange is compared between the reference and HS through a number of strain gauges mounted on the compression and tension flange of the experimental substructure and reference cf. figure 3.11a and 3.11b respectively.

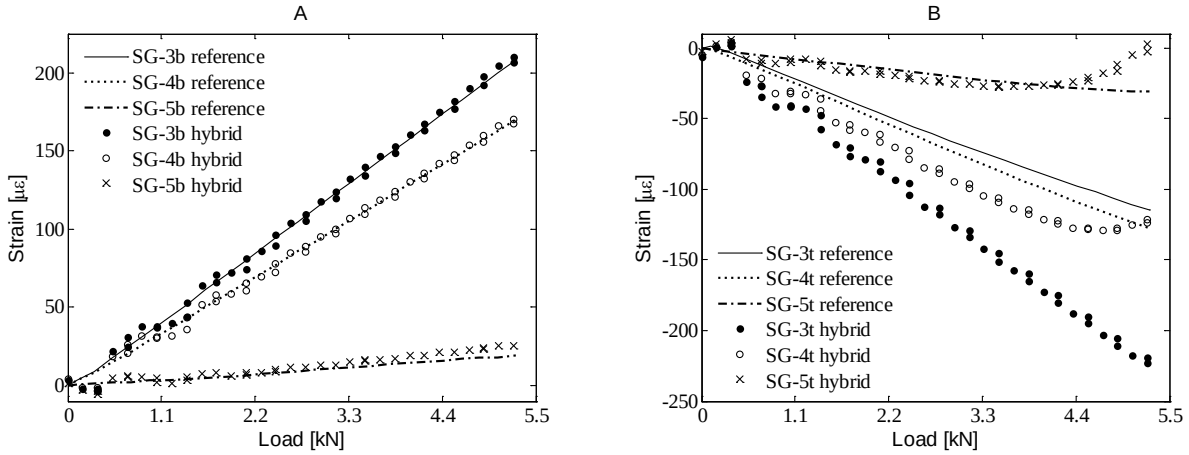

Figure 3.15: strain gauge measurement at the experimental substructure: a) bottom flange and b) top flange

For SG-3t, SG-4t and SG-5t represented in figure 3.15b some non-linear effects is observed – most likely induced by the initiated slits in the top flange of the GFRP beam. The relative maximum deviation between the reference and HS is here found to 47% for SG-3t, 17% for SG-4t and 6.2% for SG-5t relative to the reference. In the bottom flange, all strain gauges reveal a linear response cf. figure 3.15a. For SG-3b, SG-4b and SG-5b the maximum deviation between the reference and HS is found to 2.3%, 0.7% and 2.4% respectively – relative to the reference.

3.3. Chapter summary

A communication loop capable of accommodating single-component HS within the QS and PsD regime was presented. Here the numerical and experimental substructure, external DAQ system and transfer system were operated sequentially in a state-machine framework, which provided a very simple and flexible multi-processing platform. Operated through the LabVIEW environment the overall system architecture was verified through a conventional and single-component QS HS.

To reduce the complexity in verifying the capability of the overall system architecture for QS single-component HS a conventional application were analysed including a simple frame structure with a shared boundary defined by a single translational dof in a discrete point. Initially the global stability of the QS HS were evaluated through a parametrical study. Here the numerical substructure was discretized through a FE-model while the experimental substructure was handled through an analytical formulation. By implementing these two models in the HS communication loop the global stability were evaluated by adjusting the global stiffness of the numerical and experimental substructure named k_n and k_e respectively. With the influence of communication delay, instability were identified for a configuration where the global stiffness of the numerical substructure were equivalent to or lower than 60% of the experimental substructure i.e. $0.60k_e \geq k_n$. If the HS communication loop were inverted meaning that the numerical and experimental substructure received a deformation and force input respectively – instability were identified when $0.60k_e \leq k_n$. Given that the investigated configuration offered a numerical substructure which had a global stiffness which were 4.94 times higher than the experimental substructure i.e. $4.94k_e = k_n$ – no instability were expected. Through a linearly increasing external load applied over 20 equally distributed load steps the performance of the QS HS were evaluated through two different analysis including reference and HS. The reference were generated through

a FE-model of the entire emulated structure while the HS was handling the majority of the emulated structure through a FE-model while the remaining part was investigated experimentally as a three point bending test. Here a discrepancy between the HS and reference were found to 0.57% of the peak-to-peak displacement at the shared boundary.

Through a QS single-component HS, the overall system architecture were verified through a GFRP beam which were clamped in both ends and partitioned by a shared boundary defined by a discrete point with three dofs including in-plane translation and rotation. Through an external displacement covering 60 equally distributed load steps per period forming a triangular waveform with a peak-to-peak amplitude of 6.5mm the single-component QS HS was evaluated through two different analysis including reference and HS. Here the reference was defined by a FE-model of the entire emulated structure while the HS were mimicking the response of the emulated structure by combining the numerical and experimental substructure. A sound correlation between the reference and HS were identified – evaluated in 8 different measurement points located throughout the length of the GFRP beam. The maximum deviation between the reference and HS were identified to 2.1% relative to the reference.

4. Real-time single-component hybrid simulation

Within RTHS, the inherent dynamics of the experimental substructure is included in the analysis by operating the shared boundary with a frequency of operation that is 10-25 times higher than the mode of interest in order to attain a continuous time history of displacement, velocity or acceleration. Within conventional RTHS, the complexity of the numerical model and available computational resources allows the numerical model and shared boundary to operate sequentially at an identical rate. However, within single-component RTHS the enhanced complexity of the numerical model makes it difficult to attain an integration time, which is equivalent to the required operation rate of the experimental substructure due to the implementation of e.g. advanced geometry, comprehensive material layup and characterization, etc. A platform is presented capable of operating the numerical and experimental substructure with RT constraints at two different rates while including rate transitioning to link the substructures appropriately – referred to here as mrRTHS. The overall system architecture is presented and discussed including the numerical substructure, transfer system capable of operating the experimental substructure in RT along with relevant interface compensators. The strategy is implemented on a RT target that provides reduced latency and tight jitter tolerances. The mrRTHS architecture is verified through an a) mrRTHS on a conventional application – further described in paper III and IV and b) mrRTHS on a single-component application – further described in paper V.

4.1. Overall system architecture

Structural assessment through RTHS is a substructuring technique capable of mimicking the response of the emulated structure by combining the advantages of numerical modelling with those of experimental testing. The coupling governed through the shared boundary between the numerical and experimental substructure is achieved by maintaining the compatibility and equilibrium at the interface – entailing that the deformation of the shared boundary which is included in the vector x can be written cf. eq. (4.1) and (4.2) in the time domain t.

$$P_{ext}(t) = M_{num}\ddot{x}(t) + C_{num}\dot{x}(t) + k_{num}x(t) + R_{exp}(t) \tag{4.1}$$

$$R_{exp}(t) = M_{exp}\ddot{x}(t) + C_{exp}\dot{x}(t) + k_{exp}x(t) \tag{4.2}$$

Here the matrices M, C and K represent the mass, damping and stiffness while the vectors R_{exp} and P_{ext} includes the reaction force at the shared boundary and external load respectively. The indexes “num” and “exp” refer to the numerical and experimental substructure respectively while each overdot denotes a single time derivative. Within the RT regime, the inherent dynamics of the entire emulated structure is included in the analysis meaning that the RTHS communication loop is operated within stringent RT constraints. To obtain the inherent dynamics of the experimental substructure the shared boundary has to follow a continuous time history of displacement, velocity and acceleration with a frequency of operation that is 10-25 times higher than the mode of interest [37]. Within conventional RTHS the numerical substructure and shared boundary is operated at an identical rate. However, given the increased complexity of the numerical substructure induced by e.g. advanced geometry, material layup and characterization, etc. this execution frequency can be difficult to achieve due to the available computational resources. Furthermore, if the numerical substructure is handled through a commercial FE-software [23], [57] it may induce a non-deterministic network connection to an external operating system. For all these reasons, the time required to solve the computational demanding numerical substructure may be extended, compromising the ability to represent the underlying dynamics of the system and/or introduce delays that can degrade the stability and performance of the RTHS. To optimize the available computational resources and enhance flexibility to the conventional RTHS architecture the numerical and experimental substructure is executed at two different rates while including a rate-transition scheme to link the components appropriately. This architecture is referred to here as mrRTHS with a communication loop that is separated in three components named transfer system along with main and outer loop cf. figure 4.1.

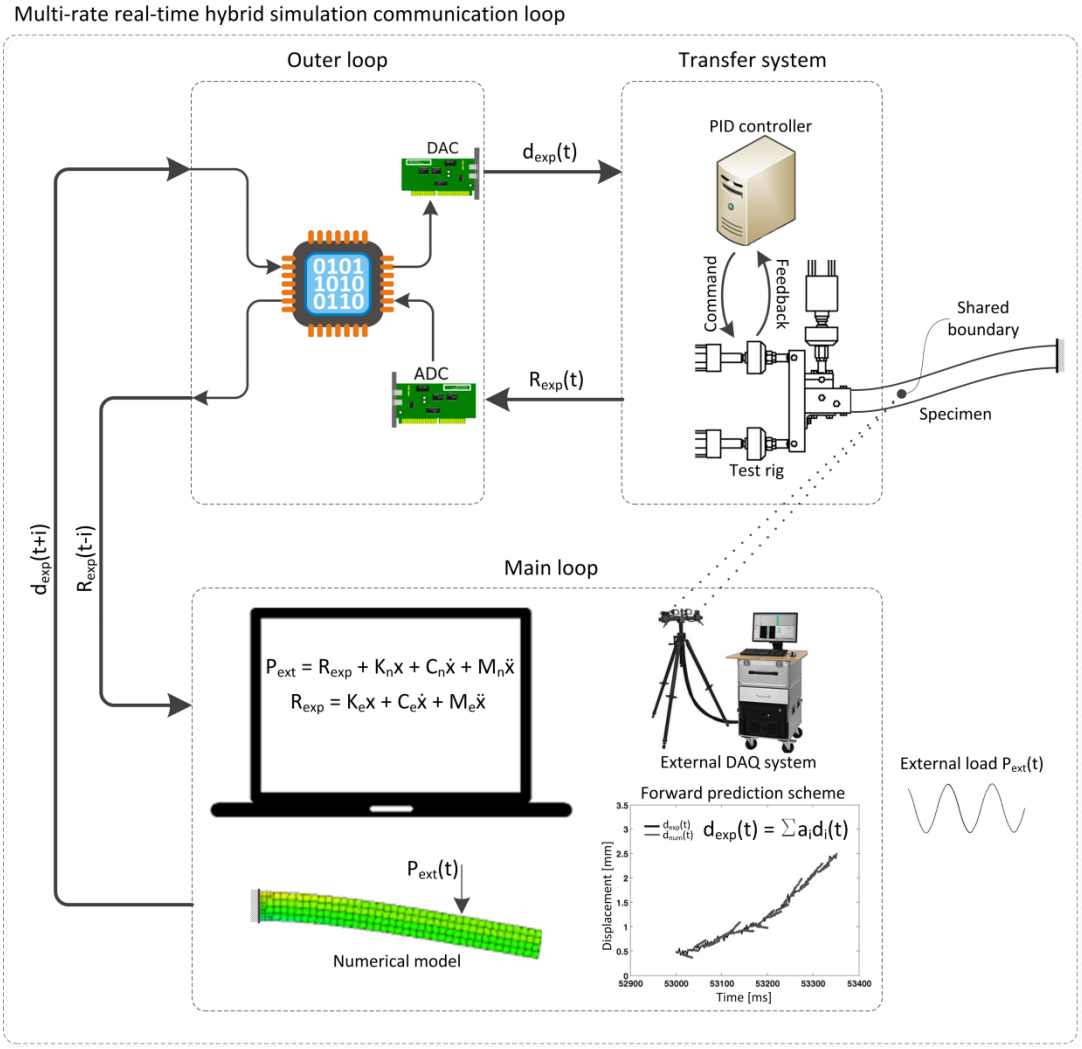

Figure 4.1: Schematic block diagram representing the overall architecture of the mrRTHS communication loop

Through the main loop, the numerical substructure is operated with a coarse time step Δt to allow adequate time to solve the computational demanding numerical model. Here the numerical substructure is discretized in order to compute the upcoming desired displacement $d_{num}(t)$ based on the external load $P_{ext}(t)$ and last available reaction force at the shared boundary $R_{exp}(t-i)$ for $i \in [0;\Delta t]$ with a fine time step δt. By the high precision tracking compensator the actual achieved displacement at the shared boundary is obtained through the external DAQ system in order to derive the commanded displacement $d_{cmd}(t)$ cf. eq. (2.10). Based on the current and previews generated commanded displacements a rate-transition link is established by generating a resampled displacement signal $d_{exp}(t+i)$ for $i \in [0;\Delta t]$ through extrapolation with a fine time step δt for actuator control purposes [44]. The extrapolated displacement $d_{exp}(t)$ is transferred to the outer loop which is operated with a fine time step δt. Here the extrapolated displacement data are imposed on the experimental substructure through the transfer system by a D/A communication interface. In parallel the reaction force obtained at the shared boundary $R_{exp}(t)$ is returned to the outer loop where it is buffered. In turns the buffer including the obtained reaction forces at the shared boundary $R_{exp}(t-i)$ for $i \in [0;\Delta t]$ is emptied by the main loop. Here the newest available reaction force is returned to the numerical substructure to reveal the response of the emulated structure in the subsequent time step $t+\Delta t$. The experimental and numerical substructure, communication loop, external DAQ system and servo-hydraulic transfer system is combined to form the single-component mrRTHS.

The overall mrRTHS communication loop including numerical substructure, external DAQ system, transfer system, etc. is operated through a platform that facilitates multiple threads to execute simultaneously across multiple processors. In contrast to the state machine framework outlined in subchapter 3.1 – this parallel RT platform allows for faster and larger-scale execution, which facilitate the RT constraints induced by RTHS. Through LabVIEW an mrRTHS platform are developed capable of operating the main and outer loop simultaneously across multiple processors [42]. In order to reduce latency and restrict jitter tolerances the software is operated on a RT target. Alternative commercially available RT systems covers xPC targets, which are operated through Matlab and Simulink along with the dSpace,'s RT interface [58]. In addition, a closed source C++ platform has been developed named Mercury, which allow for the use of more advanced finite element models within RTHS [59].

4.1.1. Numerical substructure

The numerical substructure typically comprises the majority of the emulated structure, which exhibits either predictable mechanical behaviour or is considered uncritical for the analysis conducted. Through an FE-formulation, the numerical substructure is typically discretized through the explicit time integration scheme of the type Central difference method [14], [60], [45]. Within RTHS, the time required to solve the numerical model is restricted. This typically entails that an idealized numerical model is included which are limited in the ability to represent the underlying dynamics compromising the fidelity of the simulation [61].

To overcome this challenge some methods exists capable of optimizing the computational cost to operate the numerical model including Taylor basis and adaptive multi scale models. The Taylor basis method reduces the computational cost of the numerical substructure by projecting the equation-of-motion onto a reduced basis [62], [63]. This reduced basis combines a set of linear modes and their associated modal derivatives representing the higher order effects of the deformations induced by these linear modes. The adaptive multi scale model represents an approach capable of – as the simulation progresses – refining the regions of interest in the numerical substructure to capture local phenomena that affects local behaviour [58]. The adaptive multi-scale approach have not yet been incorporated within RTHS – however it is by the author found as an promising approach to reduce the computational cost of the numerical substructure.

4.1.2. Experimental substructure

The experimental substructure includes the part of special interest and is therefore physically replicated to reveal the effects of the structural phenomena's which are difficult and comprehensive to represent in a numerical model. The dynamically imposed displacement on the experimental substructure is within this PhD study applied through a servo-hydraulic transfer system including PID controller and servo-hydraulic actuators. Furthermore, an operating RT target with an embedded A/D and D/A converter is included to handle the HS communication loop capable of executing multiple threads across multiple processors. The embedded A/D and D/A converter enable a fast and reliable communication interface between the PID controller and RT target along with data acquisition from the load cell and LVDT. A detailed description of the analogue communication interface between the PID controller and RT target is given in section 3.1.2. Furthermore, an external DAQ system is connected to the operating RT target in order to monitor the dynamically imposed displacement at the shared boundary cf. section 2.1.2. A user interface along with data storage is facilitated through a monitoring PC that typically comprises ample on-board memory and computational resources. The overall hardware setup and communication flow is illustrated in figure 4.2.

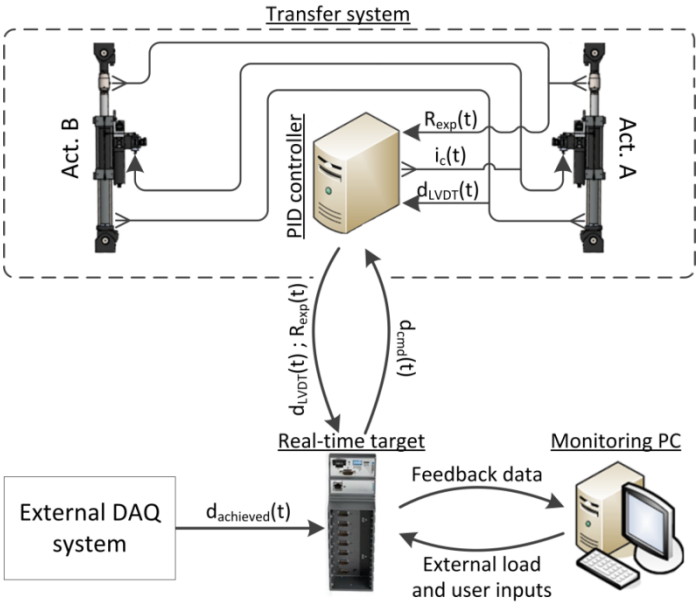

Figure 4.2: representation of the overall hardware setup

4.1.3. Interface compensator

The interface between the numerical and experimental substructure is governed through the HS communication loop, which in turns operate the numerical and experimental substructure to maintain compatibility and equilibrium at the shared boundary. To maintain accuracy and stability within RTHS a number of systematic and random experimental errors has to be taken into account including transfer system dynamics, time and communication delay, compliance in the load train, sensor miscalibration, measurement noise and random truncations in the D/A and A/D conversion.

The interface compensators including communication delay, compliance in the load train, sensor miscalibration, measurement noise and random truncations in the D/A and A/D conversion are related to HS within the QS and PsD regime which is thoroughly described in section 3.1.3. Time delay and lags induced by the dynamics of the transfer system and communication delay is however exclusively related to RTHS given that the system is operated with RT constraints.

Communication delay is a constant frequency independent parameter governed by computation time and communication between the individual hardware included in the HS communication loop including external DAQ system, transfer system and RT target cf. figure 4.2. This delay is typically handled by fitting the known displacement with a polynomial (e.g. exact polynomial fitting extrapolator represented in eq. (3.3)) in the time domain to predict the displacement after the predefined time delay. This extrapolated displacement is fed to the transfer system as the commanded displacement to cancel the communication delay [54].

$$G_a(s) = \frac{K}{\prod_{i=1}^{N}(s-p_i)} \tag{4.3}$$

The dynamics of the entire transfer system including servo-hydraulic actuator and PID controller represents a significant source of time delay and lags within the RTHS communication loop [43]. Thus, compensation is crucial to ensure accuracy and stability within RTHS [64]. Because the time lag included in the dynamics of the transfer system is dependent upon frequency, amplitude and structural response of the experimental substructure a transfer function model is needed to understand the system behaviour in the frequency and amplitude range of interest [54]. Based on empirical data obtained through an e.g. open loop system analysis a linearized transfer function model is generated capable of representing the transfer system performance cf. eq. (4.3). Here the system behaviour G_a is described in the frequency domain s where N is the number of poles p_i and K the gain of the model. By inverting G_a a feed forward

(FF) compensator is implemented capable of cancel the dynamics of the transfer system [54]. For a three-pole model, an inverted representation will take the form cf. eq. (4.4).

$$G_{FF}(s) = \frac{\prod_{i=1}^{3}(s-p_i)}{K} = a_0 + a_1 s + a_2 s^2 + a_3 s^3 \tag{4.4}$$

To represent the FF compensator in the time domain t – eq. (4.4) is rewritten to the form represented in eq. (4.5)

$$u_{FF}(t) = a_0 r(t) + a_1 \dot{r}(t) + a_2 \ddot{r}(t) + a_3 \dddot{r}(t) \tag{4.5}$$

Other compensation techniques exist including the feedback compensator [54]. However, given that this compensation method is not included in any of the appended papers it will not be discussed any further in this PhD study.

4.2. Case study for verification of the single-component mrRTHS platform

The overall system architecture outlined in subchapter 4.1 is build-up and verified through a conventional and single-component mrRTHS.

4.2.1. Implementation of the mrRTHS platform on a conventional application

The architecture outlined in subchapter 4.1 is implemented on a platform capable of facilitating multiple threads simultaneously. The system is verified through a case study including a conventional application. Furthermore, the tracking performance for the different existing and novel rate-transitioning algorithm is investigated for comparison. Finally, the mrRTHS technique is compared with a RT-HPC strategy and conventional RTHS.

Related key results presented in paper III

An mrRTHS is conducted on a Multiple Degree-Of-Freedom (MDOF) and Single Degree-Of-Freedom (SDOF) mass-spring-damper system outlined in figure 4.3 in order to reduce the complexity in verifying the software capabilities. Here the scalars m, c and k represents the mass, damping and stiffness while R_{exp} and d_{cmd} includes the reaction force and commanded displacement at the shared boundary respectively. The indexes n and e refer to the numerical and experimental substructure respectively. The system is loaded by the Chichi earthquake – referred to here as the external load $P_{ext}(t)$.

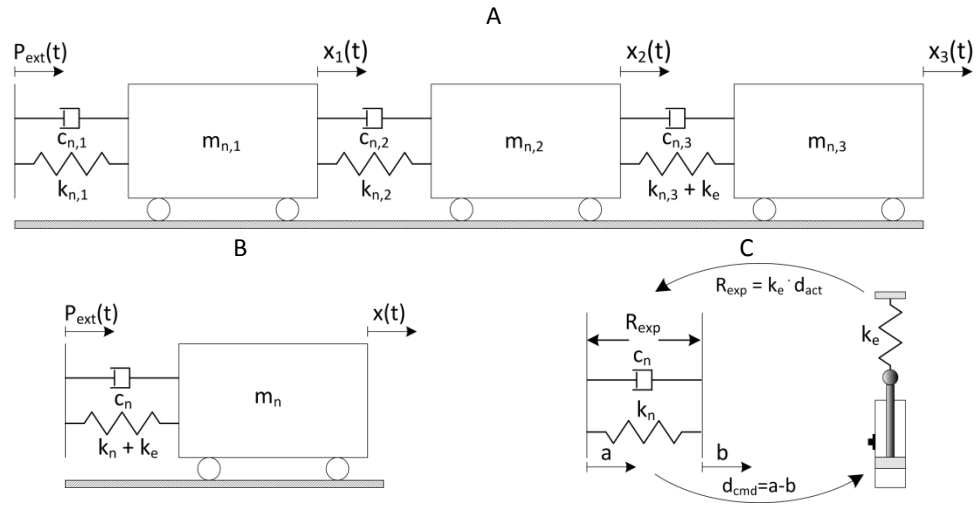

Figure 4.3: emulated structurer including: a) MDOF system, b) SDOF system and c) details of the shared boundary

The overall structural parameters of the numerical and experimental substructure are represented in table 4.1.

Table 4.1: structural parameters of the numerical and experimental substructure

Structure [-]	Module [-]	m_n [kg]	c_n [N·sec/m]	k_n [kN/m]	k_e [kN/m]	Mode [-]	Modal period [Hz]	Mode damping [%]
MDOF	1	440	880	275	-	1	1.77	1.78
	2	440	880	275	-	2	4.96	4.99
	3	440	880	165	110	3	7.17	7.21
SDOF	1	630	2370	110	110	1	1.00	2.99

The mrRTHS communication loop is operated through a LabVIEW RT target of the type CompactRIO - 9074 that facilitates multiple threads to execute simultaneously across multiple processors. The outline of the dataflow in the mrRTHS communication loop is presented in figure 4.4.

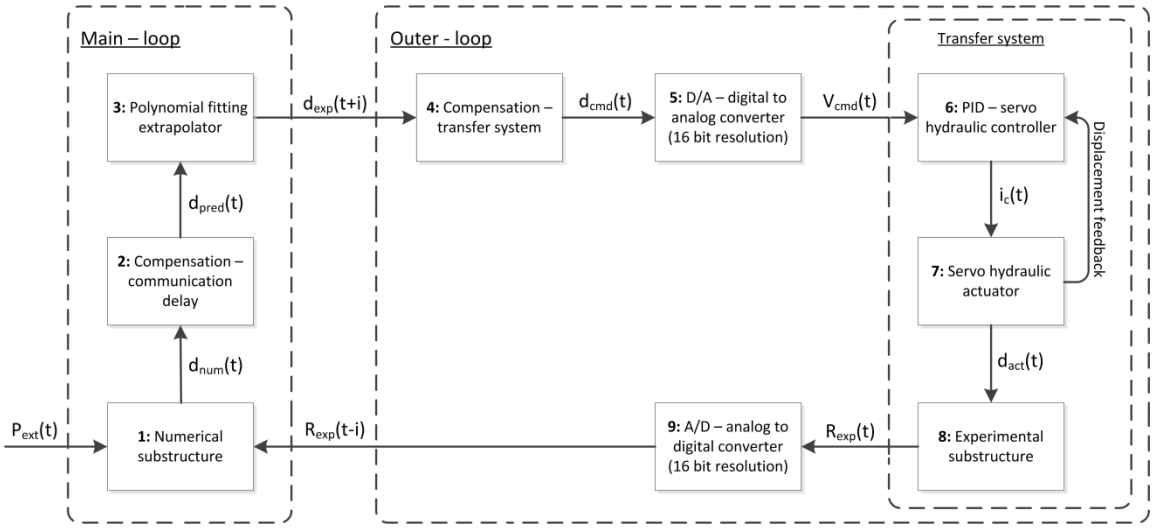

Figure 4.4: schematic block diagram representing the overall architecture for the mrRTHS communication loop

The overall architecture of the mrRTHS communication loop includes a transfer system along with two loops named main and outer loop. The outline of the dataflow in the mrRTHS communication loop is separated in 9 units labelled from **(1)** to **(9)** cf. figure 4.4. The main loop is operated through the Digital Signal Processor (DSP) with the coarse time step Δt to safe computational resources. Here the numerical substructure in **(1)** is handled through an explicit state-space representation using Matlab to compute the upcoming desired displacement $d_{num}(t)$ based on the external load $P_{ext}(t)$ and last available reaction force at the shared boundary $R_{exp}(t-i)$ for $i \in [0;\Delta t]$ with a fine time increment of δt. Through the current and previous data points provided by **(1)** the predicted system response $d_{pred}(t)$ after the communication delay is derived in **(2)** by using the exact polynomial fitting extrapolator represented in eq. (3.3). Between each data point provided by **(2)** the displacement signal is resampled through extrapolation $d_{exp}(t+i)$ in **(3)** with the time increment δt for $i \in [0;\Delta t]$ to form the transition-link between the main and outer loop. This transition-link is generated through a 3rd order exact polynomial fitting extrapolator with the form represented in eq. (4.7). To allow a fully independent time increment in the extrapolator between $d_i(t)$ and $d_{exp}(t+i)$ the polynomial coefficients a_i generated through the Lagrange formula is taking the form outlined in eq. (4.8) to (4.11) cf. [44].

Through the outer loop which is executed through the Field Programmable Gate Array (FPGA) with the fine time step δt the extrapolated displacement $d_{exp}(t+i)$ is fed into a discrete third order FF compensator cf. eq. (4.5) in **(4)** to generate $d_{com}(t)$. From the data points provided by **(4)** an equivalent D/A signal $V_{com}(t)$ is generated in **(5)** through an embedded I/O module to operate the transfer system. The servo hydraulic transfer system obtains $d_{com}(t)$ through the PID controller in **(6)** which operates the servo hydraulic actuator to impose the displacement $d_{act}(t)$ at the shared boundary of the experimental substructure in **(8)**. The corresponding reaction force is returned from the transfer system in an analogue format $V_{exp}(t)$ and converted to a digital signal in **(9)** through the embedded I/O module. The

upcoming response of the numerical substructure $d_{num}(t+\Delta t)$ is derived in **(1)** based on the last available reaction force $R_{exp}(t-i)$. The ratio between the Δt and δt is an integer – referred to as Sampling Frequency Ratio (SFR).

The performance of the mrRTHS communication loop is investigated through the SDOF and MDOF mass-damper-spring configuration represented in figure 4.3 for a duration of 70 sec with the outer loop running at a constant rate of 1kHz i.e. δt = 0.001sec. Here the mrRTHS architecture is evaluated using the normalized relative error between the mrRTHS and reference cf. eq. (4.6).

$$error(t) = \frac{|mrRTHS(t) - REF(t)|}{max(|REF(t)|)} \cdot 100 \qquad (4.6)$$

The reference is a full numerical model of the emulated structure. The relatively displacement x(t) of the shared boundary for the SDOF and MDOF configuration is represented in figure 4.5 for an SFR of 10.

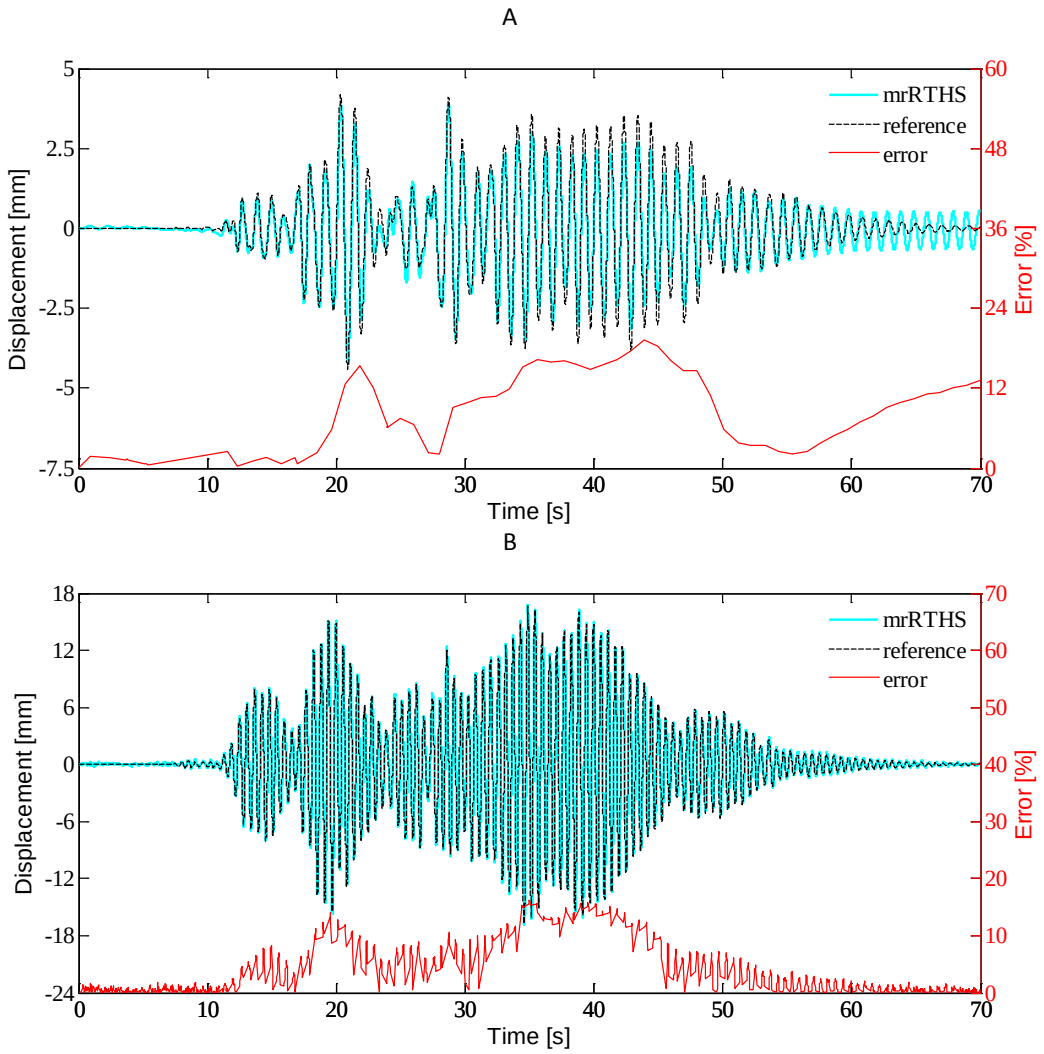

Figure 4.5: displacement response and error for an SFR of 10 including: a) SDOF and b) MDOF system

The Root-Mean-Square (RMS) and peak error obtained for the SDOF and MDOF configuration with a SFR of 5 is outlined in table 4.2. To isolate the error induced by the exact polynomial fitting extrapolator through the communication delay compensator and transition link, the experimental substructure is substituted by a numerical model – referred to here as numerical mrRTHS. With this modification, the experimental errors including transfer

system dynamics, sensor miscalibration, measurement noise and random truncations in the A/D and D/A conversion of the signal are eliminated.

Table 4.2: RMS and peak error obtained through mrRTHS and numerical mrRTHS

Structure [-]	SFR [-]	mrRTHS RMS error [%]	Num. mrRTHS RMS error [%]	mrRTHS peak error [%]	Num. mrRTHS peak error [%]
SDOF	5	7.45	1.10	20.64	3.21
	10	7.67	1.15	21.82	3.33
MDOF	5	2.50	0.70	7.14	2.07
	10	5.41	1.77	16.05	5.12

For the SDOF configuration, a relative RMS error of 7.45% and 7.67% is identified between the mrRTHS and reference for an SFR of 5 and 10 respectively. The same RMS error is identified to 2.50% and 5.41% for the MDOF configuration. This reduction of the RMS error is explained by the magnification of the amplitude for the MDOF configuration relative to the SDOF – see figure 4.5.

The error induced by the exact polynomial fitting extrapolator is found to include an irregular step between the last extrapolated point and consecutive displacement signal. This discontinuity introduces some chattering in the system, which is found distinct for the MDOF configuration for an SFR of 10 cf. figure 4.5b. To isolate the error induced by the polynomial fitting extrapolator operated in the main loop, the experimental substructure is replaced by a numerical model. From this analysis, it is found that 85% and 70% of the RMS error between the mrRTHS and reference is generated by other experimental errors for the SDOF and MDOF configuration respectively. This indicates that other sources of error including transfer system dynamics, sensor miscalibration, measurement noise and random truncations in the D/A and A/D conversion – which likewise appear in conventional RTHS – are attributed for the majority of the error between the mrRTHS and reference.

By reducing the frequency of the main loop by 50%, an equivalent reduction of the computational resources is achieved. These savings in computational resources comes with the cost of 4% and 60% increase of the RMS error between the mrRTHS and reference for the SDOF and MDOF configuration respectively.

Related key results presented in paper IV

The mrRTHS strategy is facilitated by allowing the numerical substructure and partitioning to run at two different rates to save computational resources while maintaining good actuator control. The numerical substructure is executed with a course integration time – referred to here as ΔT. Between each data point provided by the numerical substructure, a finer control signal is generated through a rate-transitioning link with a time increment of δt. Four rate-transitioning and compensation techniques are presented including **method I and II** based on polynomial extrapolation, **method III** based on the assumption of linear acceleration in the time domain and **method IV** which is a novel rate-transitioning link technique referred to here as Adaptive Multi-Rate Interface (AMRI).

In **method I** a continuous control signal is extrapolated through a technique well known for delay compensation based on the current and previews data points provided by the numerical substructure [64], [51]. For an Nth order polynomial fit, a number of N+1 data points are included in eq. (4.7).

$$d_{exp} = \sum_{i=0}^{N} a_i d_i \tag{4.7}$$

Where d_{exp} is the control signal with a time step of δt, d_i the current and previews displacement with a time step of ΔT and a_i polynomial coefficients generated through the Lagrange formula. The original prediction scheme published by [64] assumes identical time step of d_{exp} and d_i. For this reason [44] has reformulated a more general expression of a_i allowing a fully independent time step of d_{exp} and d_i for a third order polynomial fitting cf. eq. (4.8) through (4.11).

$$a_1 = \frac{\delta t}{\Delta T}\left(\frac{11}{6} + \frac{\delta t}{\Delta T} + \frac{1}{6}\left(\frac{\delta t}{\Delta T}\right)^2\right) \tag{4.8}$$

$$a_2 = -\frac{\delta t}{\Delta T}\left(3 + \frac{5}{2}\frac{\delta t}{\Delta T} + \frac{1}{2}\left(\frac{\delta t}{\Delta T}\right)^2\right) \tag{4.9}$$

$$a_3 = \frac{\delta t}{\Delta T}\left(\frac{3}{2} + 2\frac{\delta t}{\Delta T} + \frac{1}{2}\left(\frac{\delta t}{\Delta T}\right)^2\right) \tag{4.10}$$

$$a_4 = -\frac{\delta t}{\Delta T}\left(\frac{1}{3} + \frac{1}{2}\frac{\delta t}{\Delta T} + \frac{1}{6}\left(\frac{\delta t}{\Delta T}\right)^2\right) \tag{4.11}$$

This polynomial extrapolation method requires very little computational resources and is therefore well suited for RTHS.

In **method II** another polynomial extrapolation technique is investigated, named least-square polynomial fitting by [52]. Like the previews described polynomial extrapolation method, the control signal is extrapolated by the use of the current and previews data points provided by the numerical substructure. By the use of the forward prediction vector X_p and polynomial coefficients a, the extrapolated control signal d_{exp} is derived for a time step of δt cf. eq. (4.12).

$$d_{exp} = X_p a \text{ where } X_p = [1 \quad \delta t \quad \cdots \quad \delta t^N] \tag{4.12}$$

Where N is the order of the polynomial fitting and n the number of previews data points included in the extrapolation algorithm.

$$\begin{bmatrix} d_o \\ d_1 \\ \vdots \\ d_{n-1} \end{bmatrix} = \begin{bmatrix} 1 & T_0 & T_0^2 & \cdots & T_0^N \\ 1 & T_1 & T_1^2 & \cdots & T_1^N \\ \vdots & \vdots & \ddots & \vdots & \vdots \\ 1 & T_{n-1} & T_{n-1}^2 & \cdots & T_{n-1}^N \end{bmatrix} \begin{bmatrix} a_0 \\ a_1 \\ \vdots \\ a_N \end{bmatrix} \quad \text{where} \quad a = (T^T T)^{-1} T^T d \tag{4.13}$$

This polynomial extrapolation method is more computational expensive, relative to method I. However, it comes with a more generalized algorithm, where the order of the polynomial and number of previews data points included is easily adjusted.

In **method III** a continuous control signal is extrapolated by the use of the current and previews data points provided by the numerical substructure with the assumption of having a linear acceleration as a function of time [53]. The extrapolated displacement d_{exp} for a time step of δt is given by cf. eq. (4.14).

$$d_{exp} = d_0 + \delta t \dot{d}_0 + \left(\frac{1}{3}\delta t^2\right)\ddot{d}_0 + \left(\frac{1}{6}\delta t^2\right)\dddot{d} \tag{4.14}$$

Where $\dddot{d}$ is the predicted acceleration after δt, described by eq. (4.15).

$$\dddot{d} = 2\ddot{x}_0 - \ddot{x}_1 \tag{4.15}$$

The velocity and acceleration mentioned above is described in eq. (4.16) and (4.17) with a time step of ΔT.

$$\ddot{d}_i = \frac{(d_{i+1} - 2d_i + d_{i-1})}{\Delta T^2} \tag{4.16}$$

$$\dot{d}_i = \frac{(d_{i+1} - d_{i-1})}{2\Delta T} \tag{4.17}$$

In **method IV** an AMRI technique is presented – build on the successes of the previously presented techniques. For better understanding, the AMRI computations are divided into two sequential steps including compensation and rate transitioning.

$$C(z) = \alpha_1 z^{-p} + \alpha_2 z^{-p-1} + \cdots + \alpha_a z^{-p-a+1} \tag{4.18}$$

The compensation is established through a time varying discrete transfer function of the type cf. eq. (4.18). Here pΔt is the time to be compensated, p a positive integer, a the number of α coefficients for compensation while z is a complex variable in the Z-domain.

$$\begin{aligned} T_1(s) &= 1 \\ T_2(s) &= s \qquad \text{where } s = \frac{2x-(a+b)}{b-a} \\ T_{i+1}(s) &= 2sT_i(s) - T_{i-1}(s) \end{aligned} \tag{4.19}$$

The rate transitioning from Δt to δt is established through Chebyshev polynomials defined cf. eq. (4.19). Here the polynomials are adjusted to be within the general range of [a;b] where a = (p+r-1)Δt and b=pΔt. This adjustment is established through the parameter s where x corresponds to a variable in the range [-1;1].

$$NRMSE = \frac{\sqrt{\frac{1}{n-1}\sum_{i=1}^{n}\left(x_i^{sim} - x_i^{ref}\right)}}{max\left(\left|x_i^{ref}\right|\right)} \tag{4.20}$$

$$NE = \frac{max\left(\left|x_i^{sim} - x_i^{ref}\right|\right)}{max\left(\left|x_i^{ref}\right|\right)} \tag{4.21}$$

The tracking performance of the four presented rate-transitioning and compensation techniques are performed for various sampling frequency ratios through a chirped sine wave in the range 0-15Hz. The performance is quantified through a normalized RMS error which is outlined in eq. (4.20).

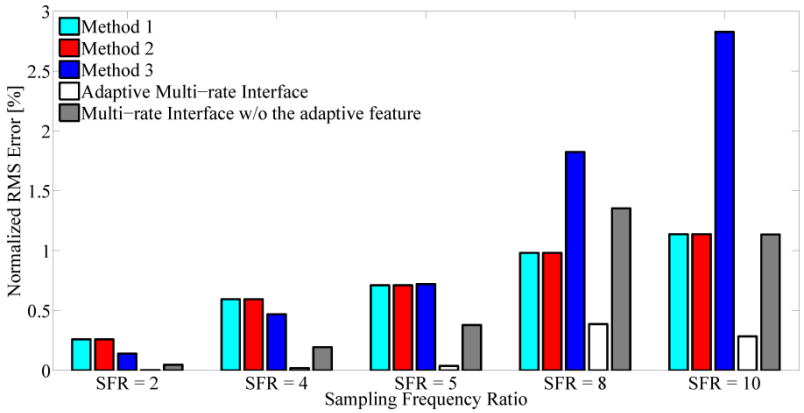

Figure 4.6: tracking performance for different rate-transitioning methods

From figure 4.6 an identical performance for method I and II is identified for all the investigated SFR. Method III exhibits improved performances compared to method I and II for SFR < 5. However, for SFR > 5 a significant increase in the normalized RMS error is identified – induced by signal chattering. Therefore, a new technique named AMRI is presented which exhibits a significant smaller error for all the investigated SFR compared to the remaining presented methods.

Within single-component RTHS which exhibits a computational expensive numerical model – three approaches may be considered including I) handling the computational model through a RT-HPC platform using a multi-core RT target (see figure 4.7), II) including a low-fidelity numerical model in a conventional RTHS (see figure 4.8) or III) implementing

the mrRTHS approach which facilitates a reduced execution rate for the numerical model to save computational resources (see figure 4.9).

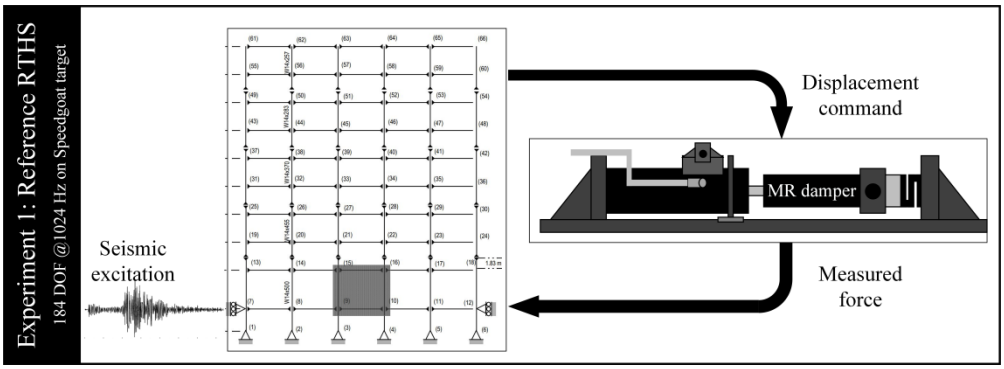

Figure 4.7: reference including a conventional RTHS with a high-fidelity numerical model

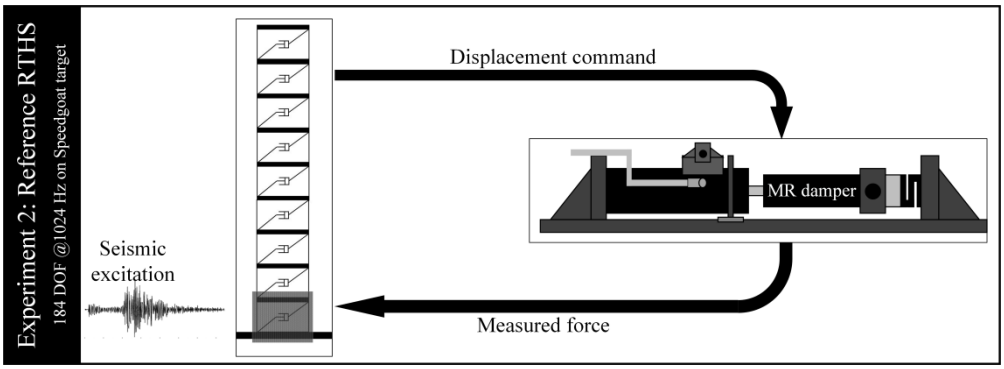

Figure 4.8: conventional RTHS including a low-fidelity numerical model

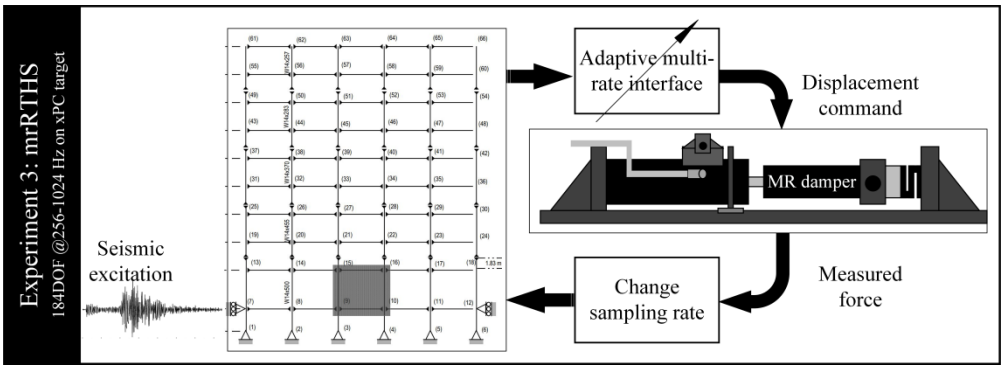

Figure 4.9: mrRTHS including a high-fidelity numerical model

The performance of three different approaches is evaluated through a 9-story frame structure with two levels of refinement including a low-fidelity model with nine dofs and high-fidelity model with a 184 dofs. It is verified that the low-fidelity model is capable of capturing the dominant dynamics of the more refined high fidelity model in terms of modal frequency and damping. With the RT-HPC approach as the reference, the conventional RTHS is compared with the mrRTHS outlined in figure 4.10. The performance is quantified through a normalized RMS error and normalized error cf. eq. (4.20) and (4.21) respectively.

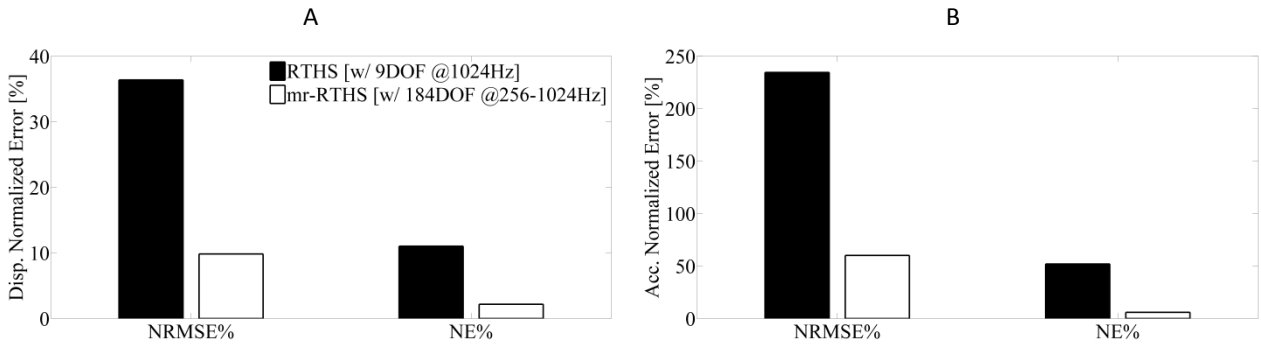

Figure 4.10: comparison of conventional RTHS and mrRTHS including: a) displacement and b) acceleration

From figure 4.10 it is concluded that the mrRTHS technique with an SFR = 4 and transition-link governed by the AMRI technique exhibits a significant reduced normalized error in terms of displacement and acceleration relative to the conventional RTHS approach.

4.2.2. Implementation of the mrRTHS platform on a single-component application

The performance of the mrRTHS communication loop presented in section 4.2.1 is investigated on a single-component application with a shared boundary covering a discrete point with three dofs.

Related key results presented in paper V

A single-component mrRTHS is conducted on a cantilever thin-walled GFRP beam with the overall dimensions, external load $P_{ext}(t)$ and boundary conditions outlined in figure 4.11. This configuration is studied to reduce the complexity and cost in verifying the mrRTHS communication loop for a wind turbine blade application in terms of geometry, scale and loads. Initial steps towards structural assessment of an SSP34m wind turbine blade through a single-component HS strategy is presented in chapter 5.

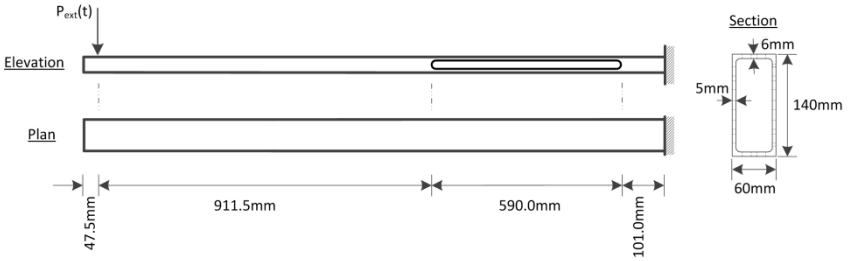

Figure 4.11 :emulated structure representing the overall dimensions, external load and boundary conditions

The emulated structure is partitioned in a numerical and experimental substructure named part A and B respectively cf. figure 4.12. A 590mm long and 40mm wide slit are initiated in both shear webs of the experimental substructure to weaken the shear stiffness – yielding a geometrical non-linear response. The shared boundary between the numerical and experimental substructure is defined by a discrete point with three dofs including translation in the x- and y-direction along with rotations around the z-axis – referred to here as φ.

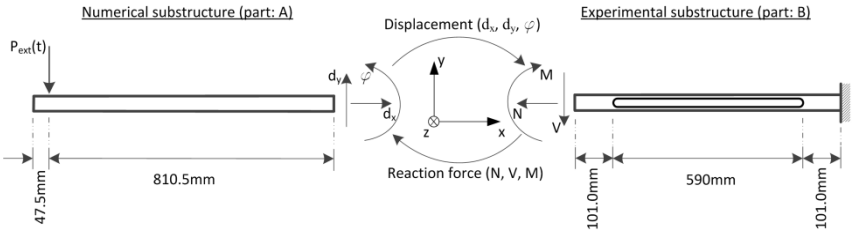

Figure 4.12: emulated structure separated in: a) numerical substructure and b) experimental substructure

The experimental substructure is loaded in a stiff frame structure by three actuators named actuator A, B and C. The response of the shared boundary is tracked by DIC through three measurement points labelled MP-1 through MP-3. The overall geometry, boundary conditions, measurement points, etc. of the experimental substructure is outlined in figure 4.13a. To validate the output from the mrRTHS an experimental test of the emulated structure is conducted – referred to here as the experimental reference. Here the response of the loading point and shared boundary is monitored through four measurement points labelled MP-1 through MP-4. The overall geometry, boundary conditions, measurement points, etc. of the experimental reference is outlined in figure 4.13b.

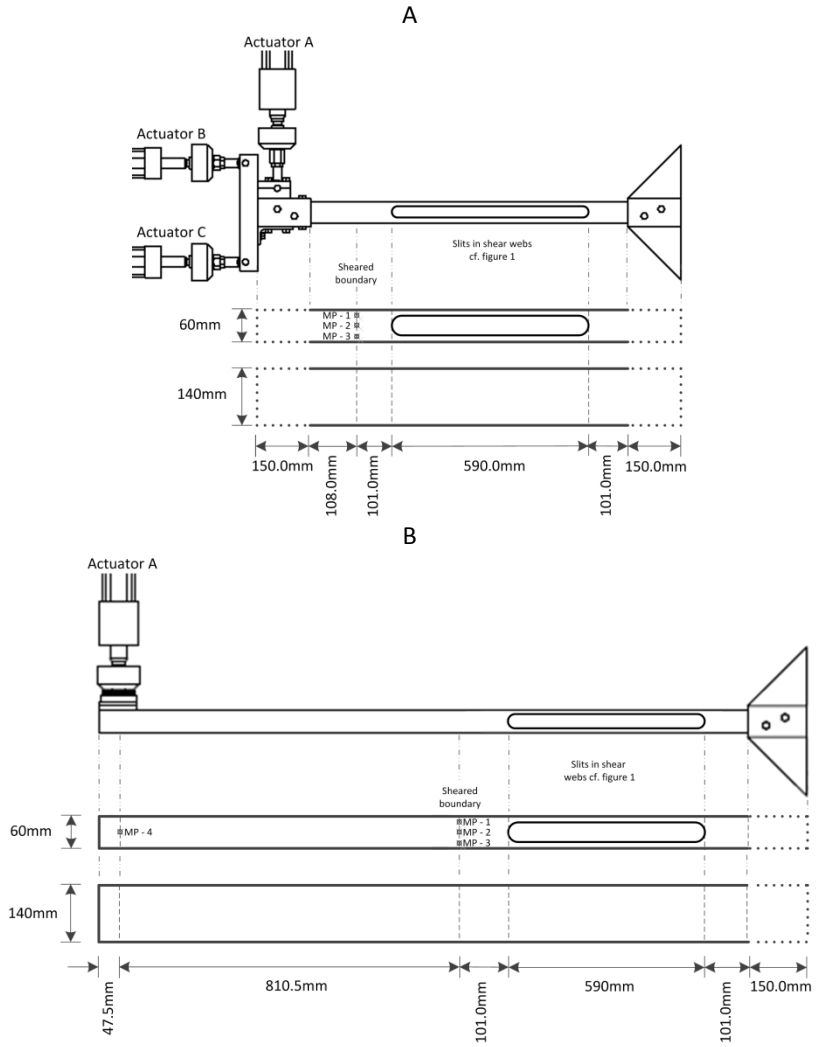

Figure 4.13: experimental setup including: a) experimental substructure and b) reference

The mrRTHS communication loop is operated through a LabVIEW RT target of the type CompactRIO - 9704 to facilitate multiple threads to execute simultaneously across multiple processors with stringent jitter tolerances and reduced latency. The main architecture of the mrRTHS communication is separated in three main portions, which are operated

in parallel named main-loop, outer-loop and transfer system. The outline of the dataflow in the mrRTHS communication loop is separated in 12 units labelled from (1) to (12) cf. figure 4.14.

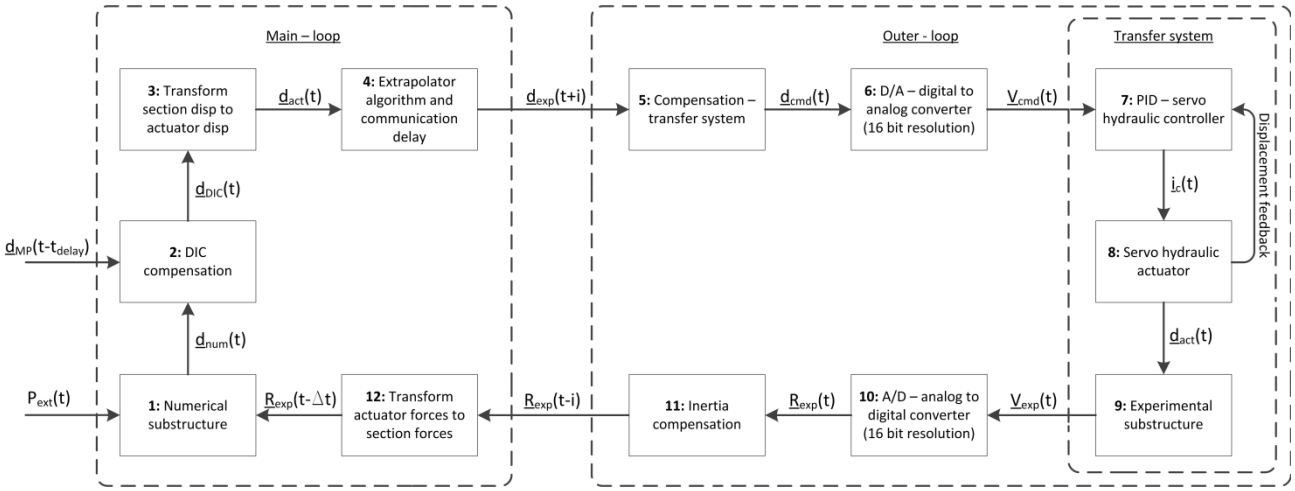

Figure 4.14: schematic block diagram representing the mrRTHS communication loop

The main loop is operated through the DSP on the RT target with the coarse time step Δt to safe computational resources. Here the numerical substructure in **(1)** is discretized through a two nodal plane Euler- Bernoulli beam element using the explicit time integration scheme named central difference method. Through Matlab the upcoming desired displacement $\underline{d}_{num}(t)$ with the format $[d_x(t);d_y(t);\varphi(t)]$ is computed based on the external load $P_{ext}(t)$ and last available reaction force at the shared boundary $\underline{R}_{exp}(t-\Delta t)$. To handle the effect of compliance in the load train a DIC compensator is implemented in **(2)**. Here the latest available in-plane translation for each of the three measurement points at the shared boundary $\underline{d}_{MP}(t-t_{delay})$ with the format $[d_x(t-t_{delay});d_y(t-t_{delay})]$ is acquired and transferred to the RT target upon request. The three in-plane measurement points are transformed to a three dof displacement $\underline{d}_{achieved}(t-t_{delay})$ on MP-2 with the format $[d_x(t-t_{delay});d_y(t-t_{delay});\varphi(t-t_{delay})]$ based on the assumption of linear cross sectional deformation at the shared boundary. Here the in-plane translation is derived as the average displacement of the three measurement points while the rotation is calculated as the change of angle between MP-1 and MP-3. The RT tracking rate achieved by the DIC system is 90Hz with a time delay of t_{delay} = 160ms. Knowing the target displacement $\underline{d}_{num}(t-t_{delay})$ and achieved displacement $\underline{d}_{achieved}(t-t_{delay})$ the compensated displacement $\underline{d}_{DIC}(t)$ with the format $[d_x(t);d_y(t);\varphi(t)]$ is derived cf. eq. (2.9) and (2.10). The compensated displacement $\underline{d}_{DIC}(t)$ is converted to an equivalent displacement for each of the three actuators $\underline{d}_{act}(t)$ with the format $[d_A(t);d_B(t);d_C(t)]$ through a trigonometric relation in **(3)** with the assumption of rigid body motion. The relation is derived from eq. (2.8) with the coordinate system and notation outlined in figure 2.6. The transition link between the main and outer loop along with communication and time delay is handled in **(4)** through a forward prediction scheme of the type third order polynomial fitting algorithm which is outlined in eq. (4.7). Here the communication and time delay is handled by extrapolating $\underline{d}_{act}(t)$ with a predefined time step which is equivalent to the communication and time delay t_{delay}. The transition link between the main and outer loop is defined by facilitating a fully independent time increment in the extrapolator between $\underline{d}_{act}(t)$ and $\underline{d}_{exp}(t+i)$ by implementing the polynomial coefficient a_i defined by eq. (4.8) to (4.11). Finally the reaction force $\underline{R}_{exp}(t-i)$ received for each of the three actuators by **(11)** with the format $[R_A(t-i);R_B(t-i);R_C(t-i)]$ is converted to a section force $\underline{R}_{exp}(t-\Delta t)$ at the shared boundary with the format $[R_V(t-i);R_H(t-i);M(t-i)]$ through a trigonometric relation cf. eq. (3.5) to (3.7) with the coordinate system and notation outlined in figure 2.6.

The outer-loop is operated through the FBGA with a fine time step of δt to generate a smooth command signal for the experimental substructure. Here the communication interface between the main and outer loop is defined with an SFR of 10. Through **(5)** the dynamics for each of the three actuators are handled by generating $\underline{d}_{cmd}(t)$ through a direct first order compensator which is further described in [65]. From the data provided by **(5)** an equivalent analogue

signal $\underline{V}_{cmd}(t)$ is generated in **(6)** to operate the transfer system. The corresponding reaction force $\underline{V}_{exp}(t)$ are acquired from the transfer system and converted to a digital signal $\underline{R}_{exp}(t)$ by **(10)**. In order to compensate for the inertia effects induced by the load train – which acts as a lumped mass applied on the tip of the cantilever beam – an inertia force compensator is implemented in **(11).** Through the vertical translation $d_y(t)$ of $\underline{d}_{num}(t)$ an equivalent acceleration is derived. Knowing the mass m_y of the load train and current acceleration $a_y(t)$ the equivalent inertia contribution $F_y(t)$ is derived cf. eq. (2.11). This inertia contribution $F_y(t)$ is subtracted from the corresponding vertical reaction force at the shared boundary $R_V(t)$ cf. subchapter 2.2.

The transfer system is operated against the RT analogue command signal $\underline{V}_{cmd}(t)$ generated by **(6)**. Through the PID controller in **(7)**, an electrical current $I_c(t)$ is generated with an execution frequency of 3kHz and passed to the servo hydraulic actuators in **(8)** causing the actuators to move $\underline{d}_{act}(t)$. The corresponding reaction forces induced on the load cells $\underline{V}_{exp}(t)$ is obtained from the experimental substructure in **(9)**.

Due to global instability issues in the presented single-component mrRTHS triggered by measurement noise and undesirable scattering induced by the extrapolator – a 75% reduction of the reaction force at the shared boundary is established to reduce the impact of the systematic and random experimental error. An alternative approach is to filter the generated displacement signal and/or corresponding reaction force; however that was not possible due to the lack of available computational resources offered by the RT target. The performance of the mrRTHS is therefore evaluated through a numerical reference in order to facilitate an adjustable global stiffness ratio between the numerical and experimental substructure.

The numerical reference is calibrated against the experimental reference in both the QS and RT regime outlined in figure 4.15a and 4.15b respectively. In figure 4.15a the force-displacement response of MP-4 for both the numerical and experimental reference is linear up to approximately 100N. Beyond this point the stiffness of the experimental reference structure decreases significantly with a local maxima of around P = 230 N. The response of the numerical reference structure seems to make a slight increase in the stiffness for a load P > 100N. It is expected that the behaviour of the numerical reference structure exhibits a higher stiffness than the experimental reference structure given that the former does not include shear flexibility.

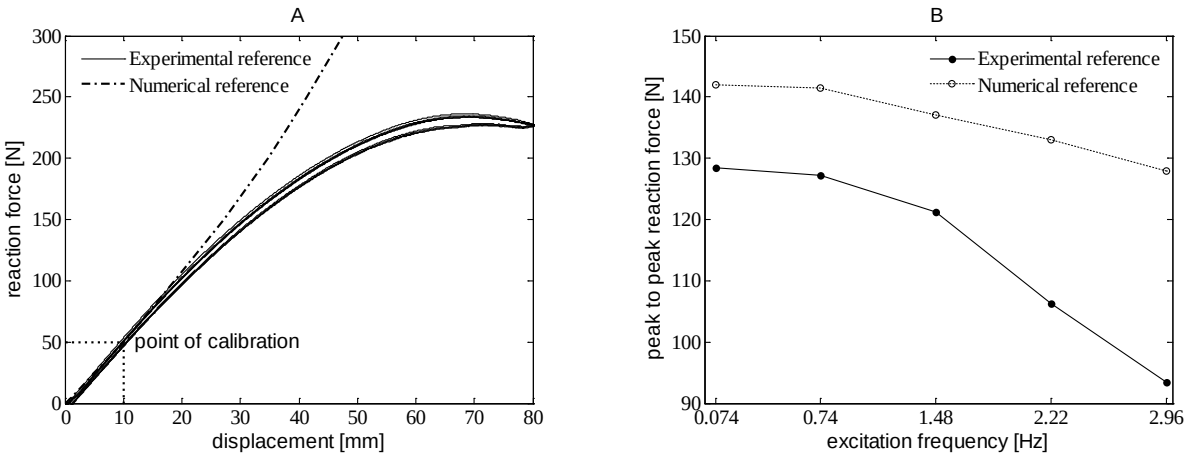

Figure 4.15: response of MP-4 in the reference structure: a) QS response and b) peak-to-peak reaction force for a deformation of 25mm at MP-4

To compare the global response of the experimental and numerical reference in the RT regime the GFRP beam is loaded by a sinusoidal deformation P_{ext} with a peak-to-peak amplitude of 25mm and excitation frequency of f_1 = 0.074Hz, f_2 = 0.74Hz, f_3 = 1.48Hz, f_4 = 2.22Hz and f_5 = 2.96Hz - equivalent to 1%, 10%, 20% 30% and 40% of the first natural frequency. From figure 4.15b the peak-to-peak reaction force decreases as a function of an increasing excitation frequency. This is explained by fact that more inertia is introduced into the system when the excitation frequency is increased. Furthermore, the experimental reference seems to be more affected by the inertia effects

than the numerical reference. This is most likely caused by the weight of the steel and rubber plate located between the load cell and GFRP beam – see figure 4.13b. The peak to peak reaction force of the numerical reference is shifted and located slightly higher than in the experimental reference. This is in accordance with the force-displacement curve in Figure 4.15a, where a 25 mm displacement is seen to be outside the linear domain, indicating that the stiffness of the numerical reference is higher than the experimental reference.

The global response of the cantilever GFRP beam is evaluated in the RT regime through a single-component mrRTHS. Here the GFRP beam is loaded by a sinusoidal external peak-to-peak load P_{ext} of 130N with an execution frequency of f_1 = 0.074Hz, f_2 = 0.74Hz, f_3 = 1.48Hz, f_4 = 2.22Hz and f_5 = 2.96Hz. The mrRTHS is evaluated using a normalized error between the mrRTHS and numerical reference represented in eq. (4.6).

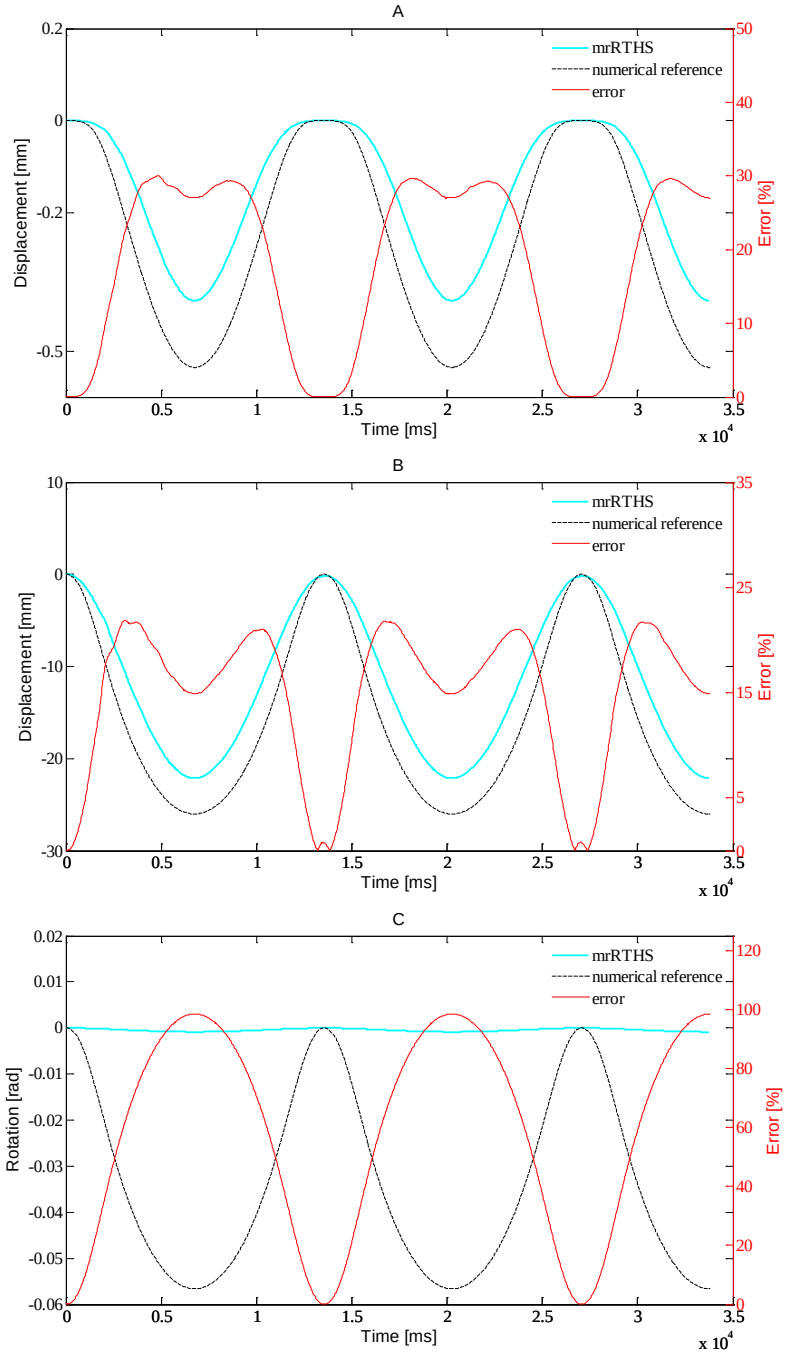

Figure 4.16: displacement response and error for ω_1=0.074Hz including: a) x-direction, b) y-direction and c) φ-rotation

In figure 4.16a and 4.16b the in-plane translation of the shared boundary for the excitation f_1 = 0.074Hz are represented. Here the deformations obtained through mrRTHS are found to be smaller and in phase with the numerical reference. The key results for all the investigated excitation frequencies (f_1 through f_5) are given in table 4.3. Here the peak-error is found to be increasing as a function of the excitation frequency. However, the root-mean-square (RMS) error is approximately constant as a function of the excitation frequency indicating that the increasing peak-error is generated by a local effect along the time scale and does not influence the overall wave shape. The difficulties in mimicking the dynamic effects through the mrRTHS method is most likely related to experimental errors including transfer system dynamics, communication delay, sensor miscalibration, measurement noise and random truncations in the A/D and D/A conversion of the communication interface between the RT target and PID controller, etc.

Table 4.3: peak-to-peak displacement and error obtained through single-component mrRTHS

direction		excitation frequency [Hz]				
		0.074	0.74	1.48	2.22	2.96
x-direction	peak-to-peak disp. ampl. [mm]	0.3906	0.4540	0.5123	0.5428	0.5394
	peak error [%]	30.03	30.26	46.98	56.75	58.05
	RMS error [%]	21.59	19.86	19.37	20.34	21.54
y-direction	peak-to-peak disp. ampl. [mm]	22.13	23.86	25.34	26.09	26.96
	peak error [%]	21.86	25.14	33.48	37.09	37.25
	RMS error [%]	16.23	15.32	15.01	15.06	15.64
z-rotation	peak-to-peak rot. ampl. [rad]	8.44e-4	9.09e-4	9.79e-4	10.25e-4	10.29e-4
	peak error [%]	98.51	98.46	98.40	98.78	98.81
	RMS error [%]	67.89	67.99	67.24	62.40	56.84

When considering the rotations of the shared boundary for the mrRTHS and numerical reference in Figure 4.16c and table 4.3, an evident difference appears. The rotation of the mrRTHS is significant smaller than the rotation in the numerical reference. The reason for this is that the rotation introduced into the transfer system was erroneously reduced by a factor $\pi/180$, as if converted from degrees to radians. However, as the output from the numerical substructure is in radians, this reduction is meaningless. The rotations in the mrRTHS are therefore approximately zero compared to the rotations in the numerical reference at the shared boundary. Due to the introduced rotation errors, a discussion of the results, are based primarily on the translational dofs at the shared boundary.

From the translational response in figure 4.16a and 4.16b, a higher stiffness of the mrRTHS is unexpected – considering the results presented in figure 4.15. However, two obvious reasons for the higher stiffness in the mrRTHS are given as the lack of rotations at the shared boundary and the applied modal basis. By restricting the rotation to be more or less zero when translations are imposed onto the shared boundary, a stiffer response is expected, compared to the case were the shared boundary were assigned a rotation which is a factor of $180/\pi$ higher. Furthermore, as only the first bending mode and its associated derivative are included in the applied basis, the local deformation in the region of the slits cannot be properly represented. Thus, by imposing the displacements of a pure bending mode onto the physical substructure, a further stiffness increase is expected.

4.3. Chapter summary

An mrRTHS communication loop was presented capable of operating the numerical and experimental substructure at two different rates to optimize the computational resources while maintaining good actuator control. Here the numerical and experimental substructure, external DAQ system and transfer system were operated through a platform that facilitated multiple threads to execute simultaneously across multiple processors. Through the LabVIEW environment the mrRTHS communication loop were operated on a RT target to facilitate stringent jitter tolerances and reduced latency.

To reduce the complexity in verifying the overall system architecture the mrRTHS configuration were demonstrated through an SDOF and MDOF mass-spring-damper system and the performance evaluated against the corresponding reference. Through a third order polynomial algorithm a rate-transition link was established with an SFR of 5 and 10 with the transfer system operated at a constant frequency of 1kHz. For the SDOF system an RMS error of 7.45% and 7.67% were achieved between the mrRTHS and reference for an SFR of 5 and 10 respectively. For the MDOF system a RMS error of 2.50% and 5.41% were identified. By reducing the operation rate of the main loop by 50% an equivalent reduction of the computational resources were achieved. These savings in computational resources came with the tradeoff of a 4% and 60% increase in the error between the mrRTHS and reference for the SDOF and MDOF configuration respectively.

The rate-transitioning link, which allows the computational demanding numerical substructure to be executed at a larger time interval than what is used within the experimental substructure plays a key rule within mrRTHS. Three different methods from the literature were presented including two polynomial extrapolation algorithms and a third approach based on linearly predicted acceleration. Furthermore, a new AMRI were developed and the tracking performance investigated and compared with the remaining three methods. Here it was proven that the AMRI method leaded to significant smaller errors than the already known algorithm – especially at higher SFRs. It was also demonstrated that the mrRTHS approach were leading to a smaller global error than the conventional RTHS approach where the order of the numerical substructure were reduced to meet the RT constraints.

The mrRTHS approach was demonstrated on a single-component application including a shared boundary with three dofs. With the high precision tracking and inertia compensator included the system performance were evaluated against a numerical model of the emulated structure. For the translational dofs at the shared boundary a RMS error of 19.37% to 21.59% in the x-direction and 15.01% and 16.23% in the y-direction were achieved between the mrRTHS and reference. The rotation at the shared boundary exhibited an RMS error of 56.84% to 67.99%. This was found as a significant RMS error, which was induced in the mrRTHS given that the commanded rotation defined by the numerical substructure was erroneously reduced by a factor of π /180. However, the overall system performance proved successful which was an important milestone in the effort of performing a successful single-component mrRTHS on a wind turbine blade.

5. Single-component hybrid simulation on a wind turbine blade (applied case study)

Structural assessment of a SSP34m wind turbine blade is conducted through a numerical model to define a representative experimental substructure suitable for evaluating the increase of stresses in the leading edge region governed by the cross section of the blade being distorted in transverse shear. The experimental substructure of interest is implemented in a fatigue rated multi-axial structural test setup to form the basis for a single-component HS strategy. Finally, an initial HS architecture and strategy is presented for the further studies on the existing framework for single-component HS represented in paper II and V.

5.1. Research motivation and approach

During operation a wind turbine blade are exposed to high stresses caused by gravity and aerodynamic forces, which have shown after few years of operation to result in damages [66]. These damages are among others observed near the leading edge as e.g. longitudinal cracks for a wide spectrum of operational wind turbine blades - see figure 5.1.

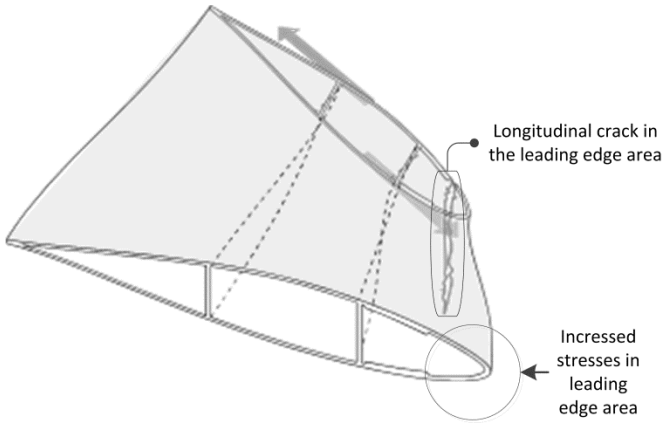

Figure 5.1: illustration of a wind turbine blade subsection distorted in transverse shear with a longitudinal crack located in the leading edge region – visualisation by KIRT x THOMSEN

Distortion of the cross section in transverse shear – referred to here as cross sectional shear distortion – has through FE-simulations, full-scale and field-testing proven to increase the stresses in the region of the leading edge [2]. This finding could explain the leading edge damages, which are frequently observed at blades in operation indicating that this mode of failure is not taken sufficiently into account in the current blade design methodology.

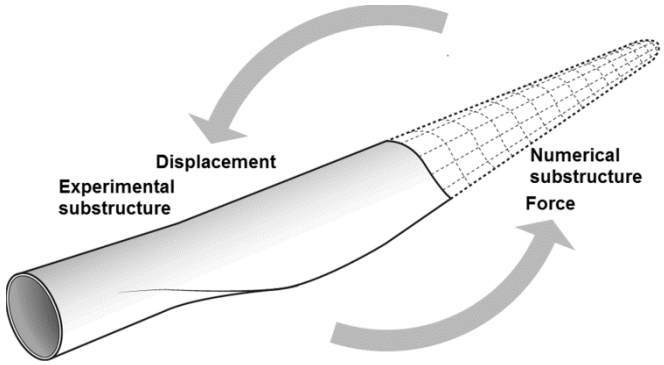

Figure 5.2: the wind turbine blade separated in an experimental and numerical substructure along with the communication flow over the partitioning – visualisation by KIRT x THOMSEN

For a better understanding of the cross sectional shear distortion, an experimental assessment of the SSP34m wind turbine blade is conducted. Normally, this is done through structural scale testing which provides valuable knowledge of the structural behaviour; however it requires large laboratory facilities and typically entails significant

simplifications of the load configurations applied, compared to the actual loads to which the structure is exposed during service [2]. To address shortcomings in structural scale testing, the single-component HS concept is implemented as a substructuring technique – capable of evaluating the global response of the emulated structure under the influence of local effects and when exposed to advanced load configurations. This is achieved by combining the experimental substructure with a numerical model representing the remainder of the SSP34m wind turbine blade as presented in figure 5.2.

To conduct a HS the overall structural response has to be evaluated with respect to the structural phenomena of interest. From this analysis, a representative experimental substructure is defined suitable for physically replicating the phenomena of special interest – in this case being the cross sectional shear distortion. The numerical substructure represents the remainder of the SSP34m wind turbine blade, which is considered uncritical for the analysis. The partitioning between the two substructures is achieved by maintaining the compatibility and equilibrium at the interface.

5.2. Numerical assessment of the SSP34m wind turbine blade

A representative FE-model of the entire SSP34m wind turbine blade – referred to here as the reference – is generated through ANSYS 15.0 using a higher order 3D solid element of the type SOLID186 [67]. The element exhibits quadratic displacement behaviour and is defined by 20 nodes – each exhibiting three dofs including translation in the x, y and z direction. The FE-model consists of 23041 elements and supports both homogenous and layered structural solids. The full geometry throughout the entire length of the reference is imported into the FE-software using the file format Initial Graphics Exchange Specification (IGES).

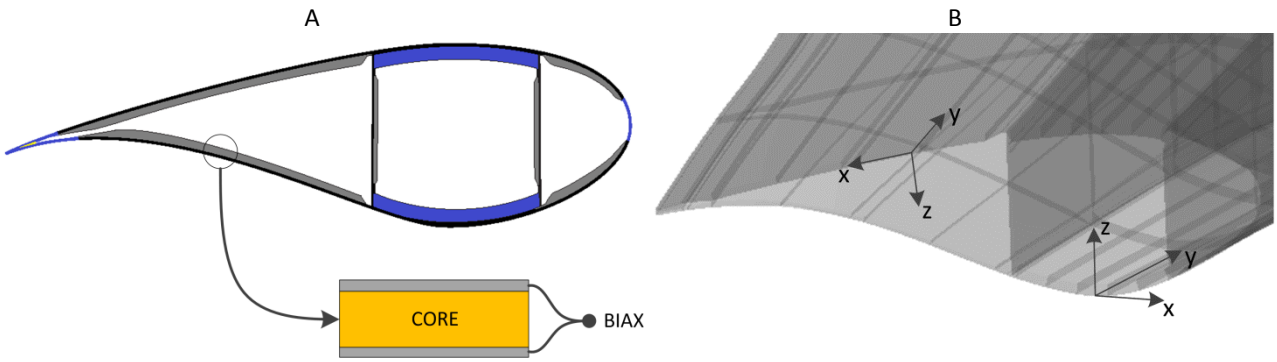

Figure 5.3: Illustration of: a) material layup for the individual regions of the cross section and b) coordinate system related to the stiffness properties

The material layup of the cross section is labelled with the colours grey and blue as outlined in figure 5.3a. Blue represents the regions where the material UD is implemented while the grey areas includes a sandwich structure including the material BIAX and core. The interface between the pressure and suction panels in the trailing edge along with the spar cabs and shear webs are governed by glue. The root section – being the region located 0 to 1.5m from the root in the longitudinal direction - is governed by pure UD material to ensure an adequate stiffness of that region. The linear elastic material properties and full names of all the individual materials included in the reference are outlined in table 5.1 following the coordinate system given in figure 5.3b.

Table 5.1: stiffness properties for the materials included in the reference

Material	UD	BIAX	core material	Glue
Name	EGL1600	XE600S	Core	Glue340
Type	Anisotropic	Anisotropic	Isotropic	Isotropic
E_{xx} [Pa]	4.13e10	1.28e10	4.85e7	3.00e9
E_{yy} [Pa]	1.14e10	1.28e10	-	-

E_{zz} [Pa]	1.14e10	1.28e10	-	-
ν_{xy} **[-]**	0.30	0.55	0.40	0.38
ν_{yz} **[-]**	0.00	0.00	-	-
ν_{zx} **[-]**	0.00	0.01	-	-
G_{xy} [Pa]	3.91e9	1.07e10	-	-
G_{yz} [Pa]	3.91e9	6.35e9	-	-
G_{zx} [Pa]	3.91e9	1.07e10	-	-

The load configuration investigated in the structural analysis covers a simplified distributed load in the Leading Towards Trailing edge (LTT) and Trailing Towards Leading edge (TTL) direction with a resulting force of 100kN as outlined in figure 5.4. Each point load is equally distributed over the entire cross section including the aerodynamic foil and load carrying bow girder.

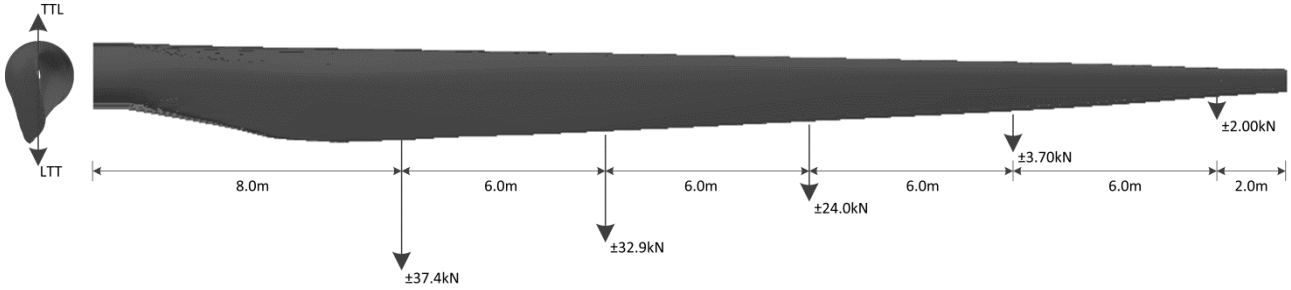

Figure 5.4: investigated load configuration for reference

The corresponding section force throughout the reference is outlined in figure 5.9. The reference is supported by constraining the root joint against translation in all directions. The structural response of the reference is evaluated through two parameters including global deformation and cross sectional shear distortion throughout the entire length of the wind turbine blade.

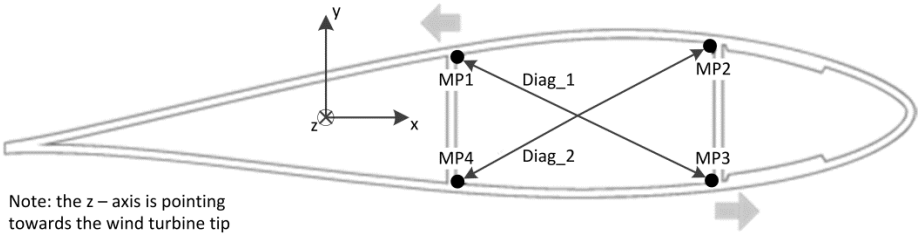

Figure 5.5: illustration of the cross section with the geometrical size of diagonal 1 and 2 and related coordinate system

The structural response of the reference is derived by tracking the three dimensional translation of the four measurement points named MP-1, MP-2, MP-3 and MP-4 cf. figure 5.5. Each measurement point is given in the format [$x_{n,init}$;$y_{n,init}$;$z_{n,init}$] and [$x_{n,def}$;$y_{n,def}$;$z_{n,def}$] for the initial and deformed state respectively – where n denotes the measurement point number. The translational displacement of the cross section in the x, y and z-direction along with the rotation around the z – axis is calculated cf. eq. (5.1) and (5.2) following the coordinate system given in figure 5.5.

$$u_x = \frac{\sum_1^N (x_{n,def} - x_{n,init})}{N}, u_y = \frac{\sum_1^N (y_{n,def} - y_{n,init})}{N}, u_z = \frac{\sum_1^N (z_{n,def} - z_{n,init})}{N}, \text{ for } n = 1,2,3,4 \quad (5.1)$$

$$\varphi_z = \frac{1}{2}\left(\tan^{-1}\left(\frac{(x_{1,def} - x_{1,init}) - (x_{4,def} - x_{4,init})}{(y_{1,def} - y_{4,def})}\right) + \tan^{-1}\left(\frac{(x_{2,def} - x_{2,init}) - (x_{3,def} - x_{3,init})}{(y_{2,def} - y_{3,def})}\right)\right) \quad (5.2)$$

For the investigated load configuration presented in figure 5.4 the global response throughout the entire length of the wind turbine blade covering translation in the x, y and z direction along with rotation around the z- axis are given in figure 5.6. The coordinate system related to the global response is outlined in figure 5.5.

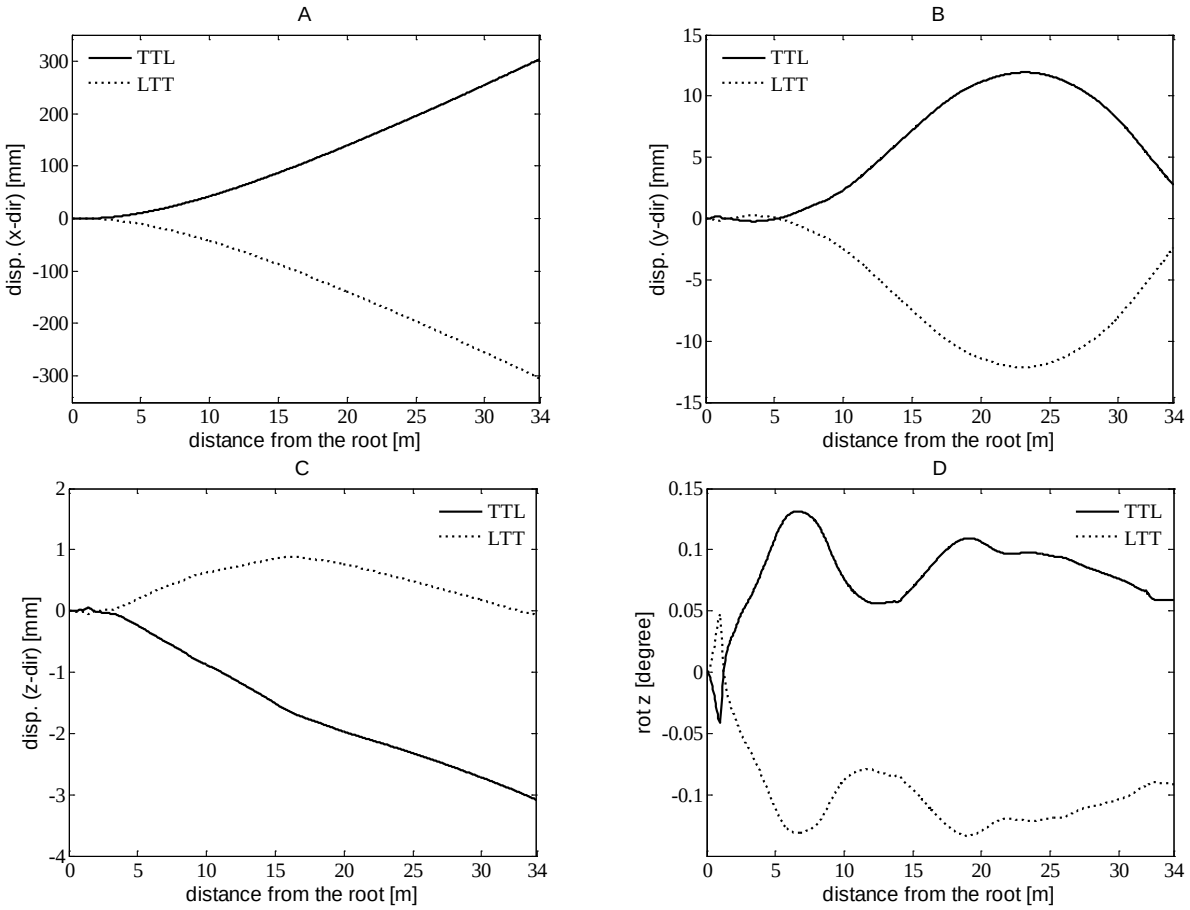

Figure 5.6: Global displacement including translation in the direction: a) x, b) y and c) z along with: d) rotation around the z-axis

Given that the TTL and LTT load are applied in the x – direction a clear coupling between the edgewise deformation and remaining investigated dofs are identified – induced by the complex non-symmetric geometry and material layup of the wind turbine blade.

The cross sectional shear distortion is quantified by the change of the geometrical length labelled diag_1 and diag_2 cf. figure 5.5. The change of length for each of the two diagonals is calculated according to eq. (5.3) through (5.5).

$$\mathrm{d_{n,init}} = \sqrt{\left(\mathrm{x_{n,init}} - \mathrm{x_{n+2,init}}\right)^2 + \left(\mathrm{y_{n,init}} - \mathrm{y_{n+2,init}}\right)^2 + \left(\mathrm{z_{n,init}} - \mathrm{z_{n+2,init}}\right)^2}, \text{for n} = 1,2 \qquad (5.3)$$

$$\mathrm{d_{n,def}} = \sqrt{\left(\mathrm{x_{n,def}} - \mathrm{x_{n+2,def}}\right)^2 + \left(\mathrm{y_{n,def}} - \mathrm{y_{n+2,def}}\right)^2 + \left(\mathrm{z_{n,def}} - \mathrm{z_{n+2,def}}\right)^2}, \text{for n} = 1,2 \qquad (5.4)$$

$$\mathrm{diag\_n} = \mathrm{d}_{n,def} - d_{n,init}, \text{for n} = 1,2 \qquad (5.5)$$

The corresponding cross sectional shear distortion for the investigated load configuration throughout the entire length of the wind turbine blade is given in figure 5.7. Here a distinct distortion of the cross section in shear is found for the max chord section of the wind turbine blade.

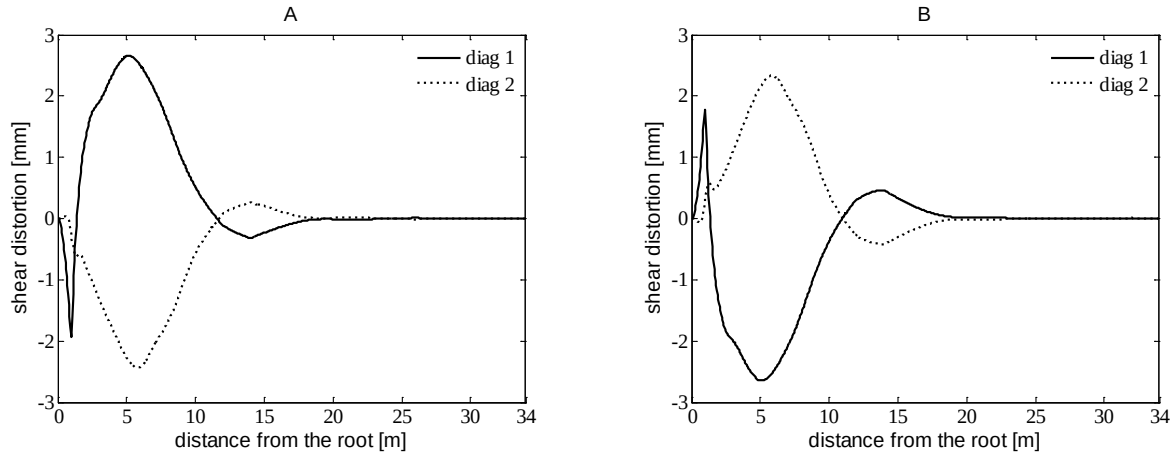

Figure 5.7: cross sectional shear distortion for the load configuration: a) LTT and b) TTL

5.3. Numerical assessment of the experimental substructure

From the numerical assessment of the emulated structure, a representative experimental substructure is defined, suitable for experimentally replicating the cross sectional shear distortion. The cross sectional shear distortion is cf. figure 5.7 identified in the max chord section meaning that the substructure of interest is identified as being in the inner root section covering the range 4m to 8m – measured from the root in the longitudinal direction. To enable a proper support of the experimental substructure and an adequate boundary introduction zone capable of erasing the influence induced by the boundary introduction rig - an experimental substructure is investigated covering the inner 14m root section cf. figure 5.8b.

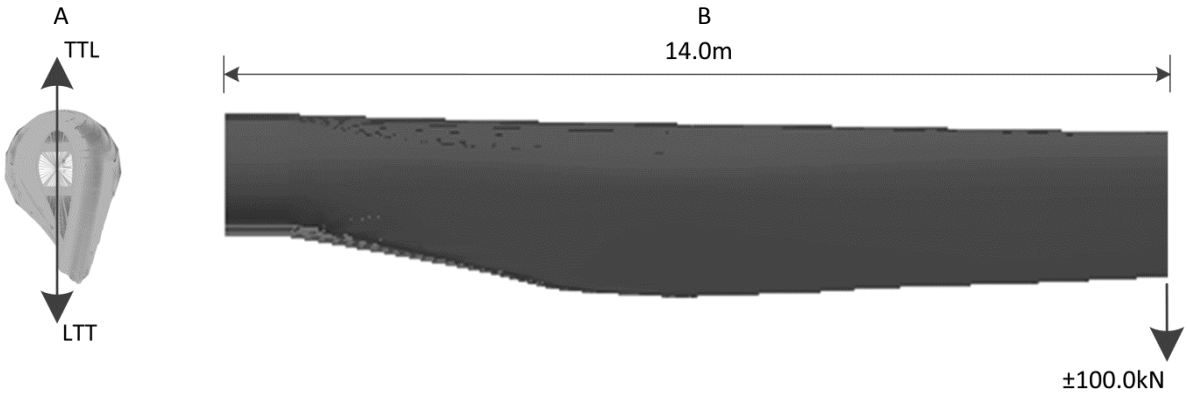

Figure 5.8: investigated load configuration including: a) applied rigid link connection and load and b) experimental substructure

A representative FE-model of the experimental substructure is generated using the same element type and material properties as utilized for the reference. Here the FE-model consists of 15210 elements. The point load at the tip of the experimental substructure is numerically replicated by a rigid link of the type mpc184 [68] connecting the entire cross section with a master node of the type mass21 [69] in which the external load is applied – see figure 5.8a. This load introduction technique is applied to replicate the boundary conditions induced by the load introduction rig – further described in subchapter 5.4. The experimental substructure is supported by constraining the root joint against translation in all directions. The equivalent section force to the applied load configuration throughout the entire length of the wind turbine blade is represented in figure 5.9. Here it is identified that for the inner 8m root section – identical section forces is present when comparing the reference and experimental substructure.

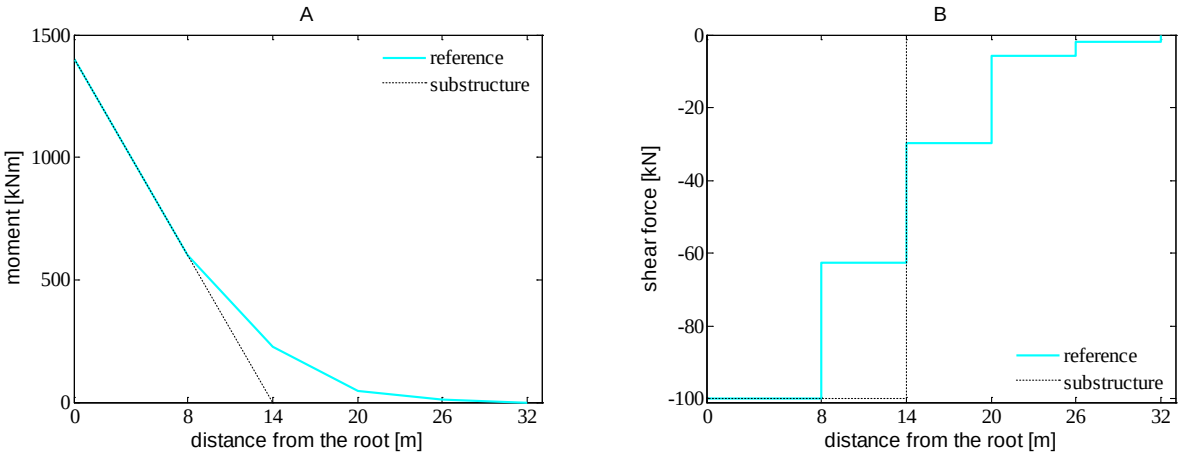

Figure 5.9: section forces throughout the emulated structure and substructure including: a) moment and b) shear force

For the investigated load configuration presented in figure 5.8 the global response throughout the entire length of the substructure covering translation in the x, y and z direction along with rotation around the z- axis are given in figure 5.10. The coordinate system related to the global response is presented in figure 5.5. For comparison the corresponding response of the reference is included in the graphs.

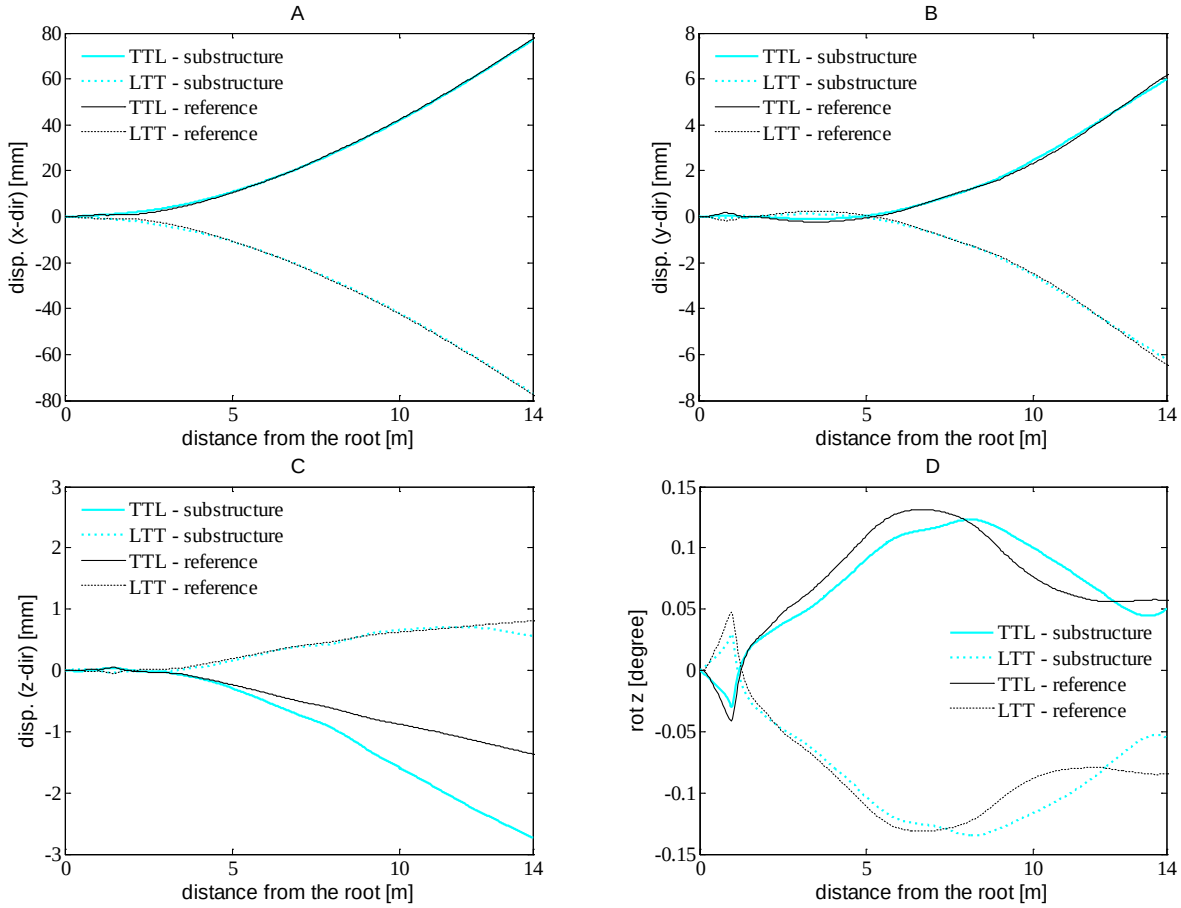

Figure 5.10: Global displacement including translation in the direction: a) x, b) y and c) z along with: d) rotation around the z-axis

From figure 5.10 a sound correlation between the global response for the reference and substructure is identified in the range 0m to 8m – measured from the root in the longitudinal direction. For the remaining part of the substructure – being the boundary introduction zone – an increasing deviation of the translation in the z-direction along with

rotation around the z-axis is identified. The corresponding cross sectional shear distortion for the investigated load configuration throughout the entire length of substructure is given in figure 5.11. Here a distinct distortion of the cross section in shear is identified for the max chord section of the wind turbine blade.

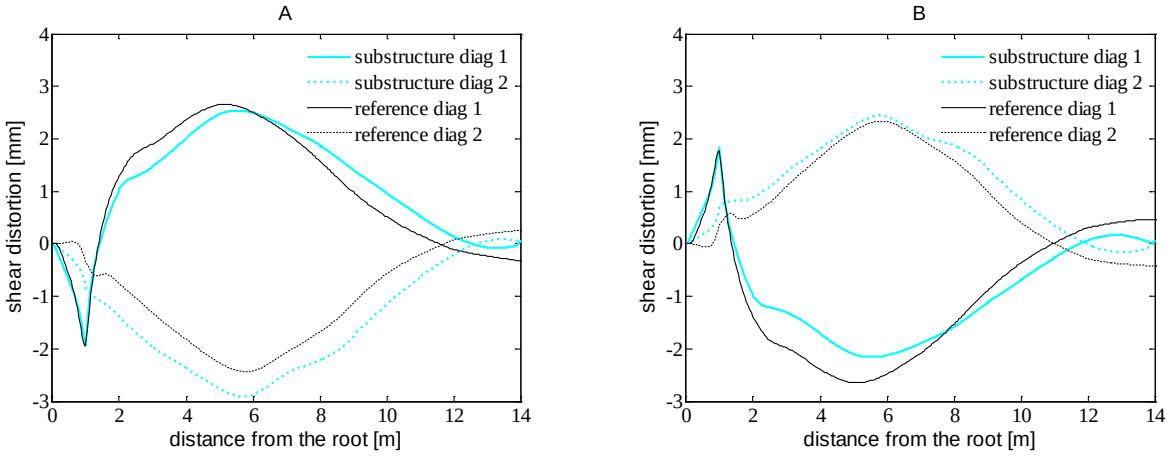

Figure 5.11: cross sectional shear distortion for the load configuration: a) LTT and b) TTL

From the numerical analysis outlined in figure 5.10 and 5.11 it is concluded that a representative experimental substructure suitable for physically replicating the cross sectional shear distortion is identified – covering the inner 8m root section of the wind turbine blade. Furthermore, a boundary introduction zone of 6m is added to the substructure entailing that the entire experimental substructure covers the inner 14m root section of the wind turbine blade.

5.4. Test rig design and setup for the experimental substructure

A fatigue rated multi-axial test rig for structural assessment of the inner 14m root section of the SSP34m wind turbine blade is designed – supported by the EUDP program with the project number 64013-0115. In the following, the test setup is presented in two sections including load train and clamped support.

The load train is designed capable of applying a discrete load at the free end of the substructure comprising three dofs including translation in the edge and flap wise direction along with twisting. The load is transferred to the free end of the wind turbine blade through a bulkhead, which is installed in the load carrying box girder cf. figure 5.12.

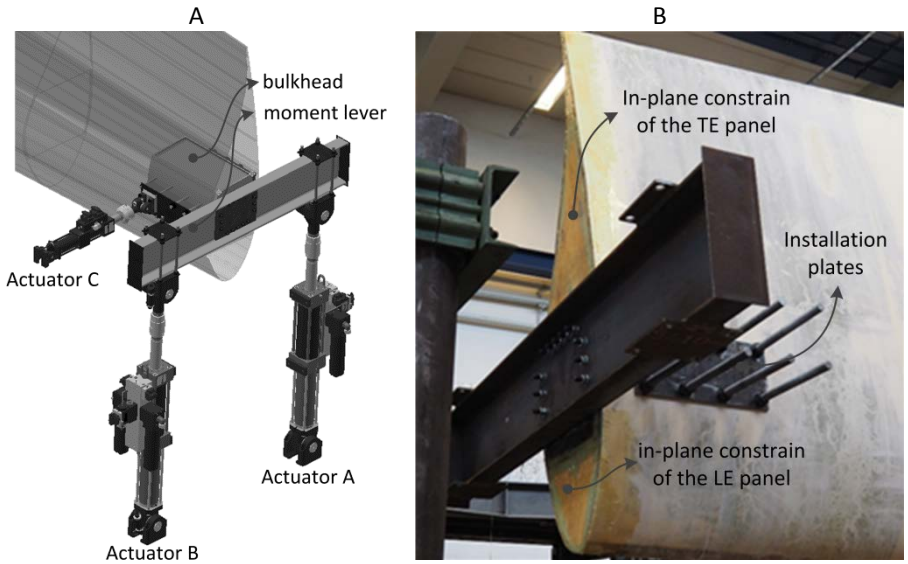

Figure 5.12: load train including: a) detailed 3D illustration and b) current project status

The bulkhead is extending 750mm into the free end of the load carrying box girder and is fixed to the inner surface of both spar caps using glue and thread bars. From the outside, the thread bars are pretensioned and the loads transferred into the aerodynamic skin through installation plates. To avoid critical peeling stresses in the adhesive bond line connecting the Trailing Edge (TE) and Leading Edge (LE) panels with the spar caps, the free end of the wind turbine blade is fully constrained against in-plane distortion. This is achieved by closing the cross section by installing plywood plates, which are over laminated with GFR fabrics cf. figure 5.12b. Attached to the bulkhead is a moment lever with a total length of 2400mm which accommodates the swivels of actuator A and B capable of inducing a edgewise and twisting deformation. Actuator A and B is a MTS model 244.31S which provide a force capacity of ±250kN with a static and dynamic stroke of 518.2mm and 508.0mm respectively. The hydraulic flow through the actuator is operated by two servo valves model MTS 252-25G-01 each with a capacity of 56l/min. The displacement of the actuator is monitored by an internally mounted LVDT and the force measured by an MTS load cell model 661.22D-01 with a capacity of ±250kN. The flap wise deformation is induced through actuator C with the swivel attached to the installation plate on the pressure side of the wind turbine blade cf. figure 5.12a. Actuator C is a MTS model 244.21 which provide a force capacity of ±50kN with a static and dynamic stroke of 401.3mm and 381.0mm respectively. The hydraulic flow through the actuator is operated by a servo valve model MTS 252.23G-01 with a capacity of 19l/min. The displacement of the actuator is monitored by an internally mounted LVDT and the force measured by an MTS load cell model 661.20F-02 with a capacity of ±50kN.

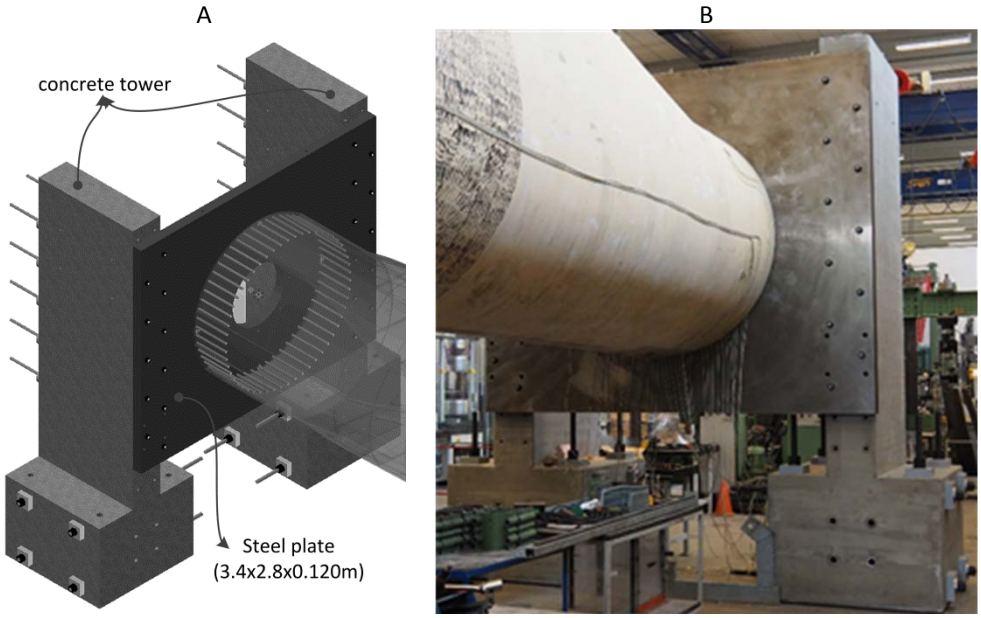

Figure 5.13: clamped support including: a) detailed 3D illustration and b) current project status

The clamped support of the root joint is achieved through a mobile vertical strong wall cf. figure 5.13. This vertical strong wall consists of two concrete towers, which are mounted to the horizontal strong floor using pretensioned thread bars. A steel plate with a width, height and thickness of 3.4m, 2.8m and 120mm respectively is mounted to the concrete towers using pretensioned thread bars. The SSP34m wind turbine blade is connected to the centre of the steel plate using 54 pretensioned thread bars.

A

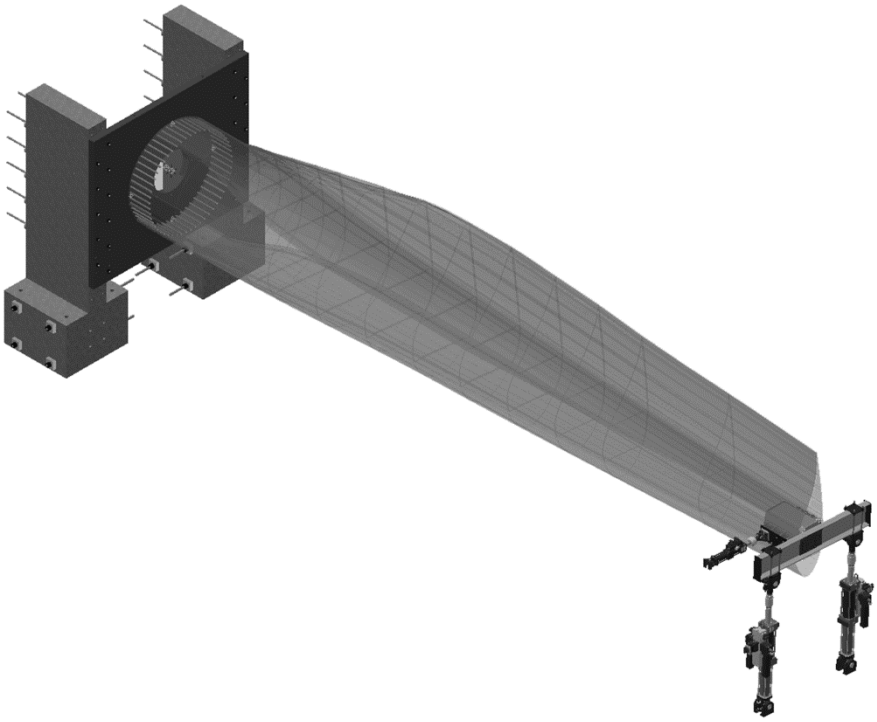

B

Figure 5.14: test setup for handling of the experimental substructure including: a) 3D illustration and b) current project status

The load train and clamped support presented in figure 5.12 and 5.13 respectively combine to form the fatigue rated test setup with a load capacity of ±50kN and ±100kN in the flap end edge wise direction respectively. Furthermore, a moment of 100kNm can be introduced. The entire experimental test rig is presented in figure 5.14.

5.5. Hybrid simulation architecture and strategy

The presented fatigue rated test setup for structural assessment of the inner 8m root section of the SSP34m wind turbine blade is in the following implemented as the experimental substructure in a single-component HS strategy. The numerical substructure comprises the remainder of the emulated structure, which is described in a FE-formulation. The partitioning between the two substructures – referred to here as the shared boundary - is defined by a discrete point with three dofs including translation in the x and y-direction along with rotation around the z-axis – referred to here as φ. A sketch of the emulated structure separated in the experimental and numerical substructure is presented in figure 5.15.

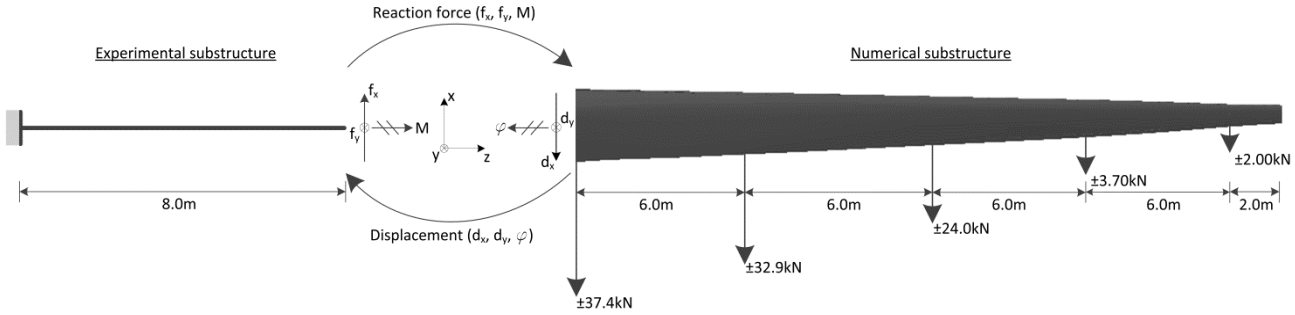

Figure 5.15: the emulated structure separated in an experimental and numerical substructure

The single-component HS operates the experimental and numerical substructure in a closed loop, which in turn maintains compatibility and equilibrium at the shared boundary to reveal the response of the emulated structure. The overall architecture of the dataflow in the single-component HS is outlined in figure 5.16.

During the HS the current displacement d_{num} of the shared boundary is derived by the numerical substructure **(1)** given the current predefined external load P_{ext} and corresponding restoring force R_{sec}. Here P_{ext} can include both dynamic and static contributions generated by e.g. wind and gravity while R_{sec} is obtained from the experimental substructure to enforce compatibility and equilibrium at the shared boundary. The numerical substructure is for the current setup statically undetermined in the stand-alone case. This is – in principle – not an issue given that the restoring force defined at the shared boundary ideally maintains force equilibrium. However, if the numerical substructure is handled in a commercial FE-software this configuration may not be feasible meaning that boundary conditions is needed in the numerical substructure to ensure force equilibrium in the stand-alone case. This could - for the given application - be handled by including the experimental substructure in the numerical model, described by e.g. beam elements with the initial mechanical properties obtained through preliminary tests. The response of the experimental substructure will be included by adjusting the mechanical properties of the beam elements throughout the single-component HS to fit the response at the shared boundary. An equivalent approach is presented in [70].

The restoring force input (R_{num}) and displacement output (d_{num}) to and from the numerical substructure **(1)** is given in the format [f_x, f_y, M] and [d_x, d_y, φ] respectively – referred to here as the section force and displacement. For the experimental substructure **(5)** the displacement input (d_{act}) and restoring force output (R_{act}) is given in the format [$d_{act\ A}$,$d_{act\ B}$,$d_{act\ C}$] and [$f_{act\ A}$,$f_{act\ B}$,$f_{act\ C}$] respectively – referred to here as actuator displacement and force. The transformation from section to actuator displacement is handled in **(3)** – derived through a trigonometric algorithm following the assumption of rigid body motion. The transformation of the actuator to section forces is handled in **(6)** by knowing the actuator forces obtained by the load cells along with the current position and angle of attack for each actuator in relation to the shared boundary. A much more detailed description of the calculations, assumptions and notations made in relation to the transformations in **(3)** and **(6)** are given in [23]**.**

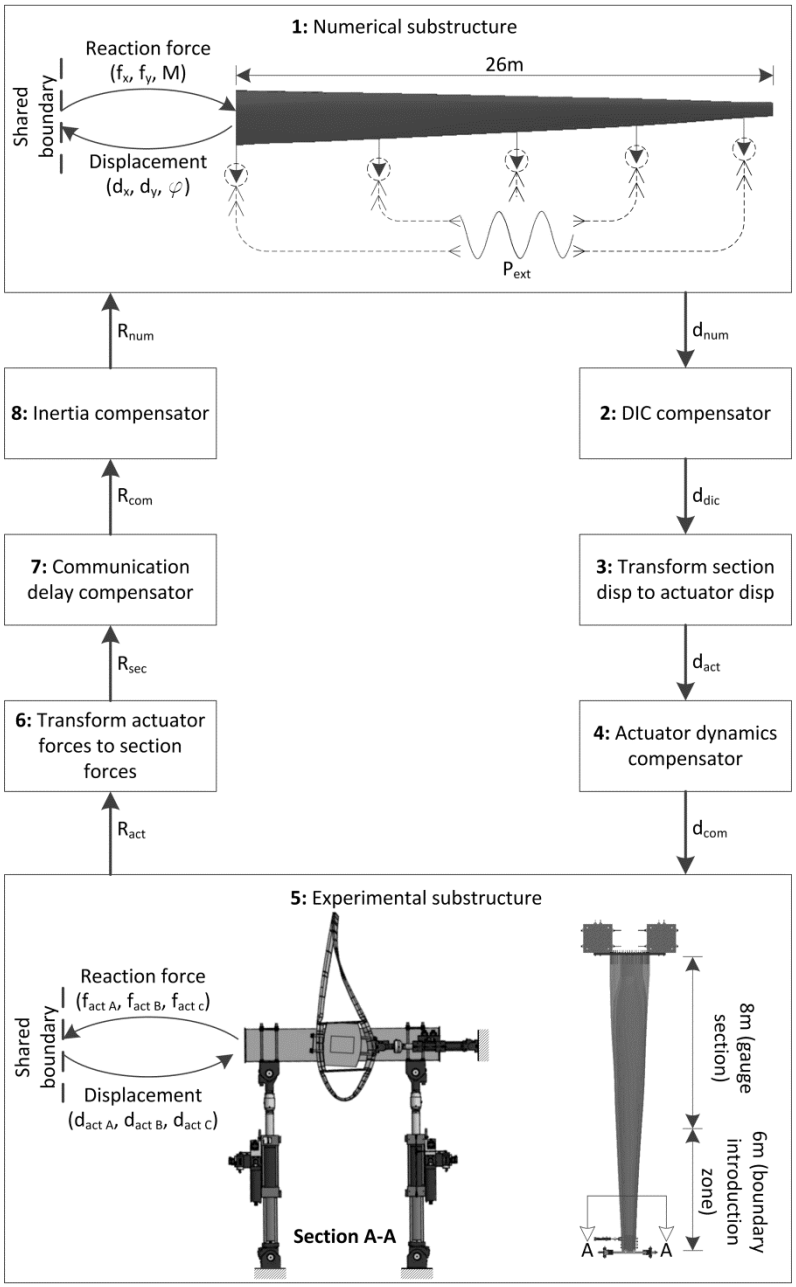

Figure 5.16: schematic block diagram representing the overall architecture for the single-component HS

The tracking performance of the transfer system is crucial to ensure accuracy and stability of the single-component HS. A significant source of error in the transfer system is governed by compliance in the load train including slack and deformations in the joints and bearings [25]. To eliminate the effect of compliance in the load train a DIC compensator **(2)** is implemented cf. chapter 2. Here the displacement of the shared boundary including translation in the y and x direction along with rotation around the z-axis is monitored by DIC through a number of measurement points applied on the aerodynamic skin [70], [23], [26]. From the commanded displacement d_{num} in the previews load step and monitored response of the shared boundary in the current load step a deviation is derived and added to d_{num} to generate the compensated displacement at the current load step d_{dic}.

For QS and PsD HS the delays/lags induced by the transfer system are not critical as the simulation is conducted on an extended time-scale. However, delays/lags within RTHS greatly undermine the accuracy and stability of the simulation [54] given that the effect of the energy introduced by a time delay/lag is equivalent to negative damping [64]. Time

delay is frequency independent and is induced by e.g. communication delay, A/D and D/A conversion and computation time. These delays are reduced by using faster and more efficient hardware and software solutions along with smaller numerical integration time steps. However, the communication delay can also be handled through a communication delay compensator **(7)** which predicts the desired restoring force/displacement to the current time through an e.g. polynomial fitting extrapolator [44]. In contrast to the time delay, which exhibits frequency independence – the time lag are an intrinsic part of the experimental substructure, which varies with both the frequency, and amplitude of the response of the shared boundary. Time lag is a result of the physical dynamics and limitations of the servo hydraulic actuators. To erase the dynamics of the transfer system over the frequency of interest an actuator dynamic compensator **(4)** is implemented using an e.g. feed forward (ff) algorithm [71]. To include the inherent dynamics of the experimental substructure in the RTHS a continuous time history of displacement, velocity and acceleration is required on the shared boundary. Given that the weight of the load train attached to the tip of the experimental substructure represents approximately 11% of the total weight of the experimental substructure, a significant inertia contribution is generated by the mass of the load train, which is included in the restoring force R_{act}. To erase this inertia effect on the experimental substructure an inertia force compensator **(8)** is implemented using newton's second law [24]. By knowing the current acceleration of the shared boundary and total mass of the load train the inertia effect from the load train can be quantified and subtracted from the restoring force measured in the load cells.

The experimental substructure in **(5)** is operated through a digital to analogue interface through which the compensated displacement d_{com} from **(4)** is transferred to a digital PID controller, which is operated in displacement mode. Here an electrical command signal is generated and passed to the servo valves, which operates each of the three actuators accordingly. The corresponding reactions forces are obtained through the load cells and transferred to **(6)** through an A/D and D/A interface.

5.6. Future work and directions

Prior to a successful single-component HS on the SSP34m wind turbine blade some further steps and considerations have to be done – described in the following.

The single-component HS architecture represented in figure 5.16 has to be implemented in a system design platform like e.g. LabVIEW, Simulink or OpenFresco, which is capable of executing the HS communication loop covering the numerical substructure, compensators, etc. Furthermore, a communication interface is required, which enable a reliable operation of the transfer system including servo-hydraulic actuators, PID controller and experimental substructure. For RT operation of the HS a system capable of prioritizing the most critical tasks are required to impose a tight jitter tolerance. This is achieved through a RT target like an e.g. cRIO RT target or speedgoat – x86 which provides deterministic and RT performance for data acquisition and control systems.

The accuracy and stability of a HS configuration is highly dependent of the experimental errors induced on the shared boundary including transfer system dynamics, compliance in the transfer system driven by slack and deformations in the load train, inertia effects induced by the mass of the load train, communication delay, sensor miscalibration, measurement noise and random truncations in the A/D and D/A conversion. To assess the sensitivity of the HS configuration presented in figure 5.16 to any of these systematic errors – a virtual HS is conducted by handling the entire simulation numerically. Through this virtual HS each error at the shared boundary can be adjusted to fit the expected system performance and the corresponding response of the HS in terms of performance and stability can be evaluated [21], [22].

The fidelity of the numerical substructure exhibits a major factor in representing the true structural behaviour through RTHS [61]. For a FE-model including the 26m outer section of the SSP34m wind turbine blade, this implies a computational heavy numerical model formulated in e.g. a commercial FE-software like ANSYS, Abaqus, etc.

Furthermore, the external load configuration, which is generated by i.a. wind, is dependent of the structural response of the blade meaning that the external load needs to be updated throughout the HS using Computational Fluid Dynamics (CFD) software. The numerical substructure consumes therefore extensive computational resources, which may require an extended integration time. Within conventional RTHS, where the numerical and experimental substructure is running at an identical rate, this may compromise the ability to represent the underlying dynamics of the system given that the shared boundary has to follow a continuous time history with a frequency of operation, which is 10-25 times higher than the mode of interest [37]. To enhance the ability to handle the computational heavy numerical models within RTHS, a communication loop capable of executing the numerical and experimental substructure at two different rates could be of interest – referred to here as mrRTHS [44], [61], [65].

The shared boundary which represents the partitioning between the numerical and experimental substructure is cf. figure 5.15 described by a discrete point covering three dofs including translation in the x (edge wise) and y (flap wise) direction along with rotation around the z-axis. This is a major simplification given that the shared boundary ideally includes an infinite number of contact points, yielding a complex displacement distribution in the coupling between the two substructures. A better representation of the shared boundary may be achieved by refining the shared boundary into multiple boundary introduction zones – however it would be with the cost of a significant increase of complexity in the transfer system. From figure 5.10 and 5.11 it was found that the shared boundary represented in figure 5.15 combined with the boundary introduction zone of 6m made a sound representation of the experimental substructure relative to the reference in terms of global displacement and cross sectional shear distortion.

This page is intentionally left blank

6. Conclusion and future directions

With the aim of spreading the HS technique within other application areas, a single-component HS were introduced capable of operating a shared boundary with a continuous edge or plane instead of a clearly defined hinge as seen within conventional HS. Therefore, a HS platform capable of performing substructural testing within the QS and RT regime for structural assessment of large composite structures has been developed and demonstrated.

By compliance in the transfer system driven by slack and deformations in the load train and boundary introduction zone, an experimental error is induced at the shared boundary within single-component HS. This error was handled in the QS and RT regime through a compensator named high precision tracking compensator. In the QS regime the compensator were operating the shared boundary with a predefined error tolerance by allowing multiple adjusting correction steps within a single time step. The technique was verified through a three point bending test on a GFRP beam with an error tolerance of $\pm$0.01mm and $\pm$20$\mu\varepsilon$ with the shared boundary monitored through DIC and internally mounted FBG's respectively. The compensator was also verified through a cantilever GFRP beam with a shared boundary defined by a discrete point with three dofs including in-plane translation and rotation. Here the discrepancy between the desired and achieved displacement for the horizontal, vertical and rational dof at the shared boundary were reduced by 69%, 87% and 89% respectively in the QS regime even though that no error tolerance were defined. In the RT regime, improvements in the range of 3% to 84% were achieved for a sinusoidal wave with a frequency of 0.074Hz and 2.96Hz respectively. The communication delay between the DIC system and LabVIEW were here identified to 160ms, which corresponded to nearly 50% of a full period for a frequency of 2.96Hz. Therefore, to enhance the capability of the high precision tracking compensator through DIC in the RT regime, it is required to a) accurately predicting the achieved displacement ahead in time or b) establish a faster communication protocol. The weight contribution governed by the load introduction rig itself and added boundary introduction zone proved to compromise the underlying dynamics of the system. Therefore, an inertia compensator were designed capable of erasing the inertia forces induced by the test rig and boundary introduction zone. For a shared boundary with a single dof translation with a frequency of 0.74 and 2.96Hz the achieved reduction of the inertia contribution were 22.23% and 83.77% respectively. The acceleration of the shared boundary was here derived directly from the desired displacement, which is a vulnerable and inexact procedure. A more reliable and precise approach would be to include an accelerometer capable of feeding the current acceleration directly into the control loop of the RTHS in RT.

A communication loop capable of accommodating single-component HS within the QS and PsD regime were presented – operated through the LabVIEW environment. To reduce the complexity in verifying the capability of the overall system architecture for QS single-component HS a conventional application were analysed including a simple frame structure with a shared boundary defined by a discrete point with a single dof. Through a linearly increasing external load a discrepancy between the HS and reference were found to 0.57% of the peak-to-peak displacement at the shared boundary. Also a single-component application were tested on the overall system architecture through a GFRP beam which were clamped in both ends and partitioned by a discrete point with three dofs including in-plane translation and rotation. With an external displacement forming a triangular waveform with a peak-to-peak amplitude of 6.5mm the single-component HS was evaluated in the QS regime. Here a sound correlation between the reference and single-component HS were identified with a maximum deviation of 2.1% relative to the reference.

Due to the increased complexity of the numerical model within single-component HS an mrRTHS strategy were implemented capable of operating the numerical and experimental substructure at two different rates to optimize the computational resources while maintaining good actuator control. As a key component within mrRTHS the rate-transitioning link was implemented allowing the numerical substructure to be executed at a larger time interval than used within the experimental substructure. Here three different methods from the literature were presented including two polynomial extrapolation algorithms and a third approach based on linearly predicted acceleration. Furthermore, a new AMRI approach was developed and the tracking performance compared with the three existing

methods. Here it was proven that the AMRI method leaded to significant smaller errors than the already known algorithm – especially for higher SFR's. Furthermore, it was demonstrated that the mrRTHS architecture were leading to a smaller global error than the conventional RTHS approach where the fidelity of the numerical substructure were reduced to meet the RT constraints. Through a LabVIEW RT-target the overall system architecture of the mrRTHS configuration were demonstrated on a conventional application to reduce the complexity in verifying the system architecture. Through a third order polynomial algorithm an SFR of 5 and 10 were achieved with a transfer system operated with a constant frequency of 1kHz. For a SDOF mass-spring-damper system an RMS error of 7.45% and 7.67% were achieved between the mrRTHS and reference for an SFR of 5 and 10 respectively. For the MDOF system a RMS error of 2.50% and 5.41% were identified. By reducing the operation rate of the main loop by 50% an equivalent reduction of the computational resources were achieved. These savings in computational resources came with the trade-off of a 4% and 60% increase in the error between the mrRTHS and reference for the SDOF and MDOF configuration respectively. The mrRTHS approach was also demonstrated on a cantilever GFRP beam with a shared boundary containing a single discrete point with three dofs including in-plane translation and rotation. For the translational dofs at the shared boundary an RMS error of 19.37% to 21.59% in the horizontal direction and 15.01% and 16.23% in the vertical direction were achieved between the mrRTHS and reference. The rotation at the shared boundary exhibited an RMS error of 56.84% to 67.99% given that the commanded rotation defined by the numerical substructure was erroneously reduced by a factor of $\pi/180$. However, the overall system performance proved successful which was an important milestone in the effort of performing a successful single-component mrRTHS on a composite structure.

As an applied case study for an upcoming single-component HS on a large composite structure, a structural assessment of an SSP34m wind turbine blade was conducted to evaluate the high stresses in the leading edge region during service. Distortion of the cross section in transverse shear has according to the related literature proven to increase the leading edge stresses in the max-chord section of an SSP34m wind turbine blade. Therefore, a substructural setup for experimental assessment of the wind turbine blade region of interest were designed through a case study to obtain a better understanding of the phenomena. Here it was identified through a FE-simulation that the inner 8m root section of the SSP34m wind turbine blade was capable of physically replicating the cross sectional shear distortion. Furthermore, a load introduction zone of 6m were added to erase the distortion induced by the load train, entailing that the entire experimental substructure covered the inner 14m root section of the wind turbine blade. A fatigue rated multi-axial structural test setup were designed capable of accommodating the 14m inner root section of the wind turbine blade. Finally an initial HS architecture and strategy were presented to form the basis for an upcoming single-component HS on the SSP34m wind turbine blade.

Throughout this PhD thesis, the external load has been restricted only to cover a discrete point with a predefined squared, ramped or sinusoidal loading history. However, the HS technique holds the potential to apply a much more advanced external load configurations like winds, waves, traffic loads, gravity, etc. Within fluid dynamics, the external load is dependent on the structural response entailing that the external load needs to be updated throughout the HS using CFD software.

The presented single-component HS communication loop has been restricted to include a single discrete point, which has proven to be adequate for the presented case studies. However, for more advanced shared boundaries, multiple discrete loading points may be required to enforce the desired displacements at the shared boundary. However, that will require a much more advanced HS communication loop in terms of transfer system, compensators, etc.

7. Bibliography

[1] F. M. Jensen, B. G. Falzon, J. Ankersen and H. Stang, “Structural Testing and Numerical Simulation of a 34m Composite Wind Turbine Blade,” *Composite Structures,* vol. 76, no. 1-2, pp. 52 - 61, 2006.

[2] F. M. Jensen, “Ultimate Strength of a Large Wind Turbine Blade,” Department of Civil Engineering, Technical University of Denmark, Kgs. Lyngby, Denmark, 2008.

[3] P. Brondsted, H. Lilholt and A. Lystrup, “Composite Materials for Wind Power Turbine Blades,” *Annual Review of Materials Research,* vol. 35, pp. 505-538, 2005.

[4] C.-L. Hung and F.-K. Chang, "Bearing Failure of Bolted Composite Joints. Part II: Model and Verification," *Journal of Composite Materials,* vol. 30, no. 12, pp. 1359-1400, 1996.

[5] R. Karakuzu, B. M. Icten and Ö. Tekinsen, "Failure Behavior of Composite Laminates with Multi-Pin Loaded Holes," *Journal of Reinforced Plastics and Composites,* vol. 29, no. 2, pp. 247-253, 2010.

[6] B. F. Sørensen, Danish Centre for Composite Structures and Materials for Wind Turbines (DCCSM), 24 02 2016. [Online]. Available: http://www.dccsm.dk/Overview. [Accessed 31 03 2016].

[7] X. Shao, A. M. Reinhorn and M. V. Sivaselvan, "Real-time Hybrid Simulation Using Shake Tables and Dynamic Actuators," *Journal of Structural Engineering,* vol. 137, no. 7, pp. 748-760, 2011.

[8] O. S. Bursi, A. Gonzalez-Buelga, L. Vulcan, S. A. Neild and D. J. Wagg, "Novel Coupling Rosenbrockbased algorithm for real-time dynamic substructure testing," *Earthquake Engineering and Structural Dynamics,* vol. 37, no. 3, pp. 339-360, 2008.

[9] K. Takanashi and M. Nakaschiman, “Japanese Activities on ON-LINE Testing,” *Journal of Engineering Mechanics,* vol. 113, no. 7, pp. 1014-1032, 1987.

[10] M. S. Williams, "Real-time hybrid testing in structural dynamics," in *The 5th Australasian Congress on Applied Mechanics*, Brisbane, Australia, 2007.

[11] S. A. Mahin, P.-S. B. Shing, C. R. Thewalt and R. D. Hanson, “Pseudodynamic test method. Current status and future directions,” *Journal of Structural Engineering New York, N. Y,* vol. 115, no. 8, pp. 2113-2128, 1989.

[12] P. B. Shing, M. Nakashima and O. S. Bursi, “Application of pseudodynamic test method to structural research,” *Earthquake Spectra,* vol. 12, no. 1, pp. 26-56, 1996.

[13] M. Nakashima, H. Kato and E. Takaoka, "Development of real-time pseudo dynamic testing," *Earthquake Engineering and Structural Dynamics,* vol. 21, no. 1, pp. 79-92, 1992.

[14] M. Nakashima and N. Masaoka, "Real time on-line test for MDOF systems," *Earthquake Engineering and Structural Dynamics,* vol. 28, no. 4, pp. 393-420, 1999.

[15] T. L. Karavalis, J. M. Ricles, R. Sause and C. Chen, "Experimental evaluation of the seismic performance of steel MRFs with compressed elatsomer dampers using large-scale real-time hybrid simulation," *Engineering Structures,* vol. 33, no. 6, pp. 1859-1869, 2011.

[16] M. Ito, Y. Murata, K. Hoki and M. Nakashima, "Online Hybrid Test on Buildings with Stud-Type Damper Made of Slitted Steel Plates Stifferened by Wood Panels," *Procedia Engineering,* vol. 14, pp. 567-571, 2011.

[17] A. Jacobsen, T. Hitaka and M. Nakashima, "Online test of building frame with slit-wall dampers capable of condition assessment," *Journal of Constructional Steel Research,* vol. 66, no. 11, pp. 1320-1329, 2010.

[18] C. Chen, J. M. Ricles, T. L. Karavasillis, Y. Chae and R. Sause, "Evaluation of a real-time hybrid simulation system for performance evaluation of structures with rate dependent devices subjected to seimic loading," *Engineering Structures,* vol. 35, pp. 71-82, 2012.

[19] Y. Z. Lin and R. E. Christenson, "Comparison of Real-time Hybrid Testing with Shake Table Test for an MR Damper Controlled Structure," in *Americam Control Conference*, St. Louis, Missouri, USA, 2009.

[20] J. E. Carrion, B. F. Spencer and B. M. Phillips, "Real-Time Hybrid Testing of a Semi-Actively Controlled Structure with an MR Damper," in *American Control Conference*, St. Louis, Missouri, USA, 2009.

[21] A. Maghareh, S. J. Dyke, A. Prakash and J. F. Rhoads, "Establishing a Stability Switch Criterion for Effective RTHS Implementation," *Journal of smart Structures and Systems,* vol. 14, no. 6, pp. 1221-1245. doi:10.12989/sss.2014.14.6.1221, 2014.

[22] A. Maghareh, S. J. Dyke, A. Prakash and G. B. Bunting, "Establishing a predictive performance indicator for real-time hybrid simulation," *Earthquake Engineering & Structural Dynamics,* vol. 43, no. 15, pp. 2299-2318. doi:10.1002/eqe.2448, 2014.

[23] J. H. Hoegh, J. P. Waldbjoern, J. Wittrup-Schmidt, H. Stang and C. Berggreen, "Quasi-static single-component hybrid testing of a composite structure with multi-axial control," *STRAIN,* vol. 51, pp. 459-473, 2015.

[24] J. H. Høgh, J. P. Waldbjørn, S. Andersen and C. Berggreen, "Compensation Methods in Real-Time Hybrid Simulation," *Strain,* Submitted for peer-review in 2016.

[25] C.-M. Chang, T. M. Frankie, B. F. Spencer and D. A. Kuchma, "Multiple Degrees of Freedom Positioning Correction for Hybrid Simulation," *Journal of Earthquake Engineering,* vol. 19, pp. 277-296, 2015.

[26] J. P. Waldbjoern, J. H. Hoegh, J. Wittrup-schmidt, M. W. Nielsen, K. Branner, H. Stang and C. C. Berggreen, "Strain and displacement controls by fibre bragg grating and digital image correlation," *Strain,* vol. 50, no. 3, pp. 262-273, 2014.

[27] X. Fayolle, S. Calloch and F. Hild, "Controlling testing machines with digital image correlation," *Experimental techniques,* vol. 31, no. 3, pp. 57-63, 2007.

[28] T. Siebert and M. J. Crompton, “Application of High Digital Image Correlation for Vibration Mode Shape Analysis,” in *Society of the SEM Annual Conference*, Indianapolis, Indiana USA, 2010.

[29] R. Guastavino and P. Göransson, “A 3D displacement measurement methodology for anisotropic porous cellular foam materials,” *Polymer Testing,* vol. 26, pp. 711-719, 2007.

[30] GOM, The GOM Scripting Language, Braunschweig, Germany: GOM, 2006.

[31] M. Kreuzer, Strain Measurement with Fiber Bragg Grating Sensors, Darmstadt, Germany: HBM.

[32] Ibsen Photonics, I-MON E-USB 2.0 Product Specification, Farum, Denmark: Ibsen Photonics A/S, 2009.

[33] J. Palaniappan, S. L. Ogin, A. M. Thorne, G. T. Reed, A. D. Crocombe, T. F. Capell, S. C. Tjin and L. Mohanty, “Disbond growth detection in composite–composite single-lap joints using chirped FBG sensors,” *Composites Science and Technology,* vol. 68, no. 12, pp. 2410-2417, 2008.

[34] C. K. Y. Leung, K. T. Wan and Y. Jiang, “Development of a Fibre Optic Crack Sensor for Concrete Structures”.

[35] H.-Y. Ling, K.-T. Lau, Z. Su and E. T.-T. Wong, “Monitoring mode II fracture behaviour of composite laminates using embedded fiber-optic sensors,” *Composites,* vol. 38, no. 4, pp. 488-497, 2007.

[36] Ibsen Photonics, Camera driver manual, Farum, Denmark: Ibsen Photonics A/S, 2011.

[37] S. J. Dyke, "Acceleration feedback control strategies for active and semi-active systems: modeling, alogrithm development and experimental verification," Ph.D. Dissertation, University of Notre Dame, IN, 1996.

[38] S. Consortium, "Syntax and style," *USA: SCPI Consortium,* 1999.

[39] GOM, "PONTUS Live streaming with SCPI protocol," GOM, [Online]. Available: https://support.gom.com/display/KNOWLEDGE/PONTUS+Live+streaming+with+SCPI+protocol. [Accessed 12 February 2016].

[40] A. Schellenberg and T. Y. Yang, "Open Fresco," [Online]. Available: http://openfresco.berkeley.edu/users/openfresco/. [Accessed 01 03 2016].

[41] A. M. Reinhorn, M. V. Sivaselvan, Z. Liang and X. Shao, "Real-time dynamic hybrid testing of structural systems," in *13th World Conference on Earthquake Engineering*, Vancouver, B.C., Canada, 2004.

[42] R. Bitter, T. Mohiuddin and M. Nawrocki, *LabVIEW Advanced Programming Techniques,* Florida, USA: CRC Press, 2001.

[43] J. E. Carrion and B. F. Spencer, "Model-based Strategies for Real-time Hybrid Testing," Newmark Structural Engineering Laboratory, University of Illinois at Urbana-Champaign, Urbana-Champaign, Illinois, USA, 2007.

[44] P. A. Bonnet, "The development of multi-axis real-time substructure testing," University of Oxford, Oxford, United Kingdom, 2006.

[45] J. Zhao, C. French, C. Shield and T. Posbergh, "Considerations for the development of real-time dynamic testing using servo-hydraulic actuation," *Earthquake engineering and structural dynamics,* vol. 32, pp. 1773-1794, 2003.

[46] A. Gilat, MatLAB An Introduction With Applications, Ohio: John Wiley and Sons, Inc., 2005.

[47] S. M. Afazov, "Modelling and simulation of manufacturing process chains," *CIRP journal of Manufacturing Science and Technology,* vol. 6, no. 1, pp. 70-77, 2013.

[48] LabVIEW, "Working with m-file Scripts in NI LabVIEW for Text-based Signal Processing, Analysis and Math," [Online]. Available: ftp://ftp.ni.com/pub/devzone/LV_Online_Eval/daq_ic/mathscript_getting_started.pdf. [Accessed 01 03 2016].

[49] LabVIEW, "System Exec VI," [Online]. Available: http://zone.ni.com/reference/en-XX/help/371361J-01/glang/system_exec/. [Accessed 02 03 2016].

[50] MTS, LabVIEW Programming Libraries: Model 793.00 Software, MTS Systems Corporation, 2009.

[51] T. Horiuchi, M. Inoue, T. Konno and Y. Namita, "Real-time hybrid experimental system with actuator delay compensation and its application to a piping system with energy absorber," *Earthquake Engineering and Structural Dynamics,* vol. 28, pp. 1121-1141, 1999.

[52] M. I. Wallace, D. J. Wagg and S. A. Nield, "An adaptive polynomial based forward prediction algorithm for multi-actuator real-time dynamic substructuring," *Proceedings of the royal society A,* vol. 461, pp. 3807-3826, 2005.

[53] T. Horiuchi and T. Konno, "A new method for compensating actuator delay in real-time hybrid experiments," *Phil. Trans. Royal Soc. London (series A),* vol. 359, pp. 1893-1909, 2001.

[54] B. M. Phillips and B. F. Spencer, "Model-based servo-hydraulic control for real-time hybrid simulation," Newmark Structural Engineering Laboratory, University of Illinois at Urbana-Champaign, Urbana-Champaign, Illinois, USA, 2011.

[55] I. ANSYS, "ANSYS Mechanical APDL Theory Reference," ANSYS, Inc., Canonsburg, PA, USA, 2013.

[56] A. M. Legendre, New Methods for the Determination of the Orbits of Comets, Paris: F. Didot, 1805.

[57] J. P. Waldbjoern, J. H. Hoegh, H. Stang, C. C. Christian, J. Wittrup-Schmidt and K. Branner, "Hybrid Testing of Composite Structures with Single-Axis Control," in *Proceedings of the 19th International Conference on Composite Materials* , Montréal, 2013.

[58] D. Ferry, A. Maghareh, G. Bunting, A. Prakash, K. Agrawal, C. Lu and S. Dyke, "On the performance of a highly parallelizable concurrency platform for real-time hybrid simulation," in *The 6'th World Conference on Structural Control and Monitoring*, Barcelona, Spain, 2014.

[59] V. Saouma, G. Haussmann, D. H. Kang and W. Ghannoum, "Real time hybrid simulation of a non ductile reinforced concrete frame," *Journal of Structural Engineering,* vol. 140, no. 2, 2014.

[60] H. Kobayashi and K. Tamura, "Experimental study on the validity of real-time hybrid vibration experiments with a 2-dimensional and 3-degree-of-freedom model," in *World Conference of Earthquake Engineering*, Auckland, New Zealand, 2000.

[61] A. Maghareh, J. P. Waldbjoern, S. J. Dyke and A. Prakash, "Adaptive multi-rate interface: development and experimental verification of an interface for multi-rate real-time hybrid simulation," *Earthquake Engineering and Structural Dynamics,* Accepted for publication - december 2015.

[62] S. Andersen and P. N. Poulsen, "Nonlinear Real-time Simulations Using a Taylor Basis," *International Journal for Numerical Methods in Engineering,* Submitted for peer-review in 2015.

[63] S. Andersen and P. N. Poulsen, "Reduction Method for Kinematic Nonlinear Real-time Simualtions," *International Journal for Numerical Methods in Engineering,* Submitted for peer-review in 2015.

[64] T. Horiuchi, M. Nakagawa, M. Sugano and T. Konno, “Development of real-time hybrid experiment system with actuator delay compensation,” in *Proc. 11th World conference on Earthquake engineering* , Acapulco, 1996.

[65] J. P. Waldbjoern, A. Maghareh, G. Ou, S. J. Dyke and H. Stang, "Multi-rate Real Time Hybrid Simulation operated on a flexible LabVIEW real-time platform," *Smart Structures and Systems,* Submitted for peer review (2015).

[66] Bladena, “Reliability of wind turbine blades,” [Online]. Available: http://www.bladena.com/getattachment/Publications/RELIABILITY-OF-WIND-TURBINE-BLADES.pdf.aspx. [Accessed 26 01 2016].

[67] ANSYS, "SOLID186," [Online]. Available: http://inside.mines.edu/~apetrell/ENME442/Documents/SOLID186.pdf. [Accessed 26 01 2016].

[68] ANSYS, "MPC184," [Online]. Available: http://www.helpdoc-online.com/SCS0001EN1A40P8191~ANSYS-10.0-Documentation-en~MPC184-Multipoint-Constraint-Rigid-Link-and-Rigid-Beam-Element.htm. [Accessed 26 01 2016].

[69] ANSYS, "MASS21," [Online]. Available: http://www.ansys.stuba.sk/html/elem_55/chapter4/ES4-21.htm. [Accessed 26 01 2016].

[70] J. P. Waldbjørn, S. Andersen, J. H. Høgh, J. W. Schmidt and C. Berggreen, "Single-component Multi-rate Real-time Hybrid Simulation pilot test on a composite structure," *To be desided,* 2016.

[71] G. Ellis, Control system design guide, San Diego, CA: Academic Press, 2000.

This page is intentionally left blank

8. Appendices

8.1. Appended journal papers

8.1.1. Appendix A: **paper I**

"Strain and Displacement Controls by Fibre Bragg Grating and Digital Image Correlation"
Authors: Jacob P. Waldbjørn, Jacob H. Høgh, Jacob Wittrup-Schmidt, Michael W. Nielsen, Kim Branner, Henrik Stang and Christian Berggreen
Published in: Strain (2014) 50, 262-273

8.1.2. Appendix B: **paper II**

"Quasi-Static Single-Component Hybrid Simulation of a Composite Structure with Multi-Axis Control"
Authors: Jacob H. Høgh, Jacob P. Waldbjørn, Jacob Wittrup-Schmidt, Henrik Stang and Christian Berggreen
Published in: Strain (2015) 51, 459-473

8.1.3. Appendix C: **paper III**

"*Multi-rate Real Time Hybrid Simulation operated in a flexible LabVIEW real-time platform"*
Authors: Jacob P. Waldbjørn, Amin Maghareh, Ge Ou, Shirley J. Dyke and Henrik Stang
Submitted in: Smart Structures and Systems (2015)

8.1.4. Appendix D: **paper IV**

"Adaptive multi-rate interface: development and experimental verification for real-time hybrid simulation"
Authors: Amin Maghareh, Jacob P. Waldbjørn, Shirley Dyke, Arun Prakash and Ali Ozdaqli
Accepted for publication in: Earthquake engineering and structural dynamics (2016)

8.1.5. Appendix E: **paper V**

"Single-Component Multi-Rate Real Time Hybrid Simulation Pilot Test on a Composite Structure"
Authors: Jacob P. Waldbjørn, Sebastian Andersen, Jacob H. Høgh, Jacob Wittrup-Schmidt and Christian Berggreen
Submitted in: Strain (2016)

8.1.6. Appendix F: **paper VI**

"Compensation Methods in Real-Time Hybrid Simulation"
Authors: Jacob H. Høgh, Jacob P. Waldbjørn, Sebastian Andersen and Christian Berggreen
Submitted in: Strain (2016)

8.2. Appended conference papers

8.2.1. Appendix G: **paper VII**

"Hybrid Testing of Composite Structures with Single-Axis Control"
Authors: Jacob P. Waldbjørn, Jacob H. Høgh, Henrik Stang, Christian Berggreen, Jacob Wittrup-Schmidt and Kim Branner
Presented in: The 19th international conference on composite materials

8.3. Associated journal papers

8.3.1. Appendix H: **paper VIII**

"Life cycle strain monitoring in glass fibre reinforced polymer laminates using embedded fibre bragg grating sensors from manufacturing to failure"

Authors: Michael W. Nielsen, Jacob Wittrup-Schmidt, Jacob H. Høgh, Jacob P. Waldbjørn, Jesper H. Hattel, Tom L. Andersen and Christen M. Markussen

Published in: journal of composite materials (2013) 0, 1-17

Appendix A

50 YEARS of strain
strain
An International Journal for Experimental Mechanics

Strain and Displacement Controls by Fibre Bragg Grating and Digital Image Correlation

J. Waldbjørn*, J. Høgh†, J. Wittrup-Schmidt*, M. W. Nielsen‡, K. Branner§, H. Stang* and C. Berggreen†

*Department of Civil Engineering, Technical University of Denmark, Brovej Building 118, 2800, Kgs. Lyngby, Denmark
†Department of Mechanical Engineering, Technical University of Denmark, Nils Koppels Alle, Building 403, 2800, Kgs. Lyngby, Denmark
‡Department of Mechanical Engineering, Technical University of Denmark, Produktionstorvet Building 425, 2800, Kgs. Lyngby, Denmark
§Department of Wind Energy, Technical University of Denmark, Frederiksborgvej 399, 4000 Roskilde, Denmark

ABSTRACT: Test control is traditionally performed by a feedback signal from a displacement transducer or force gauge positioned inside the actuator of a test machine. For highly compliant test rigs, this is a problem since the response of the rig influences the results. It is therefore beneficial to control the test based on measurements performed directly on the test specimen. In this paper, fibre Bragg grating (FBG) and Digital Image Correlation (DIC) are used to control a test. The FBG sensors offer the possibility of measuring strains inside the specimen, while the DIC system measures strains and displacement on the surface of the specimen. In this paper, a three-point bending test is used to demonstrate the functionality of a control loop, where the FBG and DIC signals are used as control channels. The FBG strain control was capable of controlling the test within an error tolerance of 20 $\mu m\,m^{-1}$. However, the measurement uncertainty offered by the FBG system allowed a tolerance of 8.3 $\mu m\,m^{-1}$. The DIC displacement control proved capable of controlling the displacement within an accuracy of 0.01 mm.

KEY WORDS: *digital image correlation, displacement control, fibre Bragg grating, fibre reinforced plastic, three-point bending*

Introduction

Mechanical testing is commonly controlled by a proportional-integral-derivative (PID) controller using the feedback signal from a load cell or a gauge positioned in the actuator of the testing machine e.g. linear variable differential transducer (LVDT). However, the compliance of the load train will in this case affect the results, and it is therefore more accurate to control the test by measurements performed directly on the specimen e.g. by a clip gauge [1], where the strain from the gauge is fed into the PID control loop as an analogue signal. Other measurement techniques have also been used to control tests e.g. digital image correlation [2]. In these efforts, the signal from the external measurements has not been used in the PID controller, instead, an outer control loop was designed to correct the displacement/strain applied by the PID controller in the inner control loop. These methods might be useful when testing specimens with complex geometry and/or test rigs with joints and bearings. In such cases, the desired strain state is not easily obtained, since the displacement measured by the LVDT at the actuator is not the same as the displacement in the specimen, and it is therefore possible to obtain higher accuracy if measurements are performed directly on the specimen and feed into the control loop. The effect of the compliance of the load train is thereby omitted.

FBG sensors are gauges inside optical fibres capable of measuring strains by changes in a reflected light beam. Due to the small diameter and environmental robustness of the fibre optic sensor, it can be embedded into several types of materials e.g. laminated/sandwich composites and concrete, without affecting the mechanical properties [3] of the test specimen. This has made the FBG technology widespread within the field of mechanical engineering covering manufacturing techniques, material/component testing, structural health monitoring (SHM) and damage assessment and support control systems. By embedding/attaching FBG sensors to a structure during manufacturing, it is possible to monitor the process-induced temperature and residual strains as they develop [4–6]. Within material/component testing, the FBG sensor provides accurate and local measurement capabilities of internal stress distribution, stress concentrations and vibrations [7, 8]. Furthermore, FBG sensors can detect cracks and delamination, which are key information in glass fibre reinforced polymer (GFRP) testing [9, 10]. Also, in SHM, the FBG sensors are used for the observation of the in-service structural performance due to ageing and degradation caused by the environment. In this case, the sensors can be used to monitor the integrity of the structure [11–15]. The environmental robustness and high resolution of the FBG sensors enable high precision control suitable for systems in which geometry or harsh environmental conditions do not allow the use of other sensor technologies [16]. When performing tests where a certain strain state is difficult to obtain due to a complex test rig/geometry, it is beneficial to use FBG sensors for control, since they can measure strains directly on the specimen or even inside.

DIC is a technique capable of calculating strains and displacement on a surface on the basis of digital images. Within the field of mechanical and civil engineering, the DIC technology is widespread within multiple categories e.g. material characterization (Young's modulus, Poisson's

doi: 10.1111/str.12089

ratio, elasto-plastic behaviour, etc.), component testing, fracture mechanics and high speed testing for dynamic and high strain rate measurements. With the ability to identify both local and global strain distribution and perform measurements in the plastic regime, the DIC technology has proven to be a useful tool within material testing [17–20]. The DIC technique inherently has no limit of size, and it has been applied for varying length scales covering a few square millimetres up to multiple square metres [21–23]. In fracture mechanics, the DIC technique is able to deliver information about crack propagation, which can be used for the determination of important fracture mechanic parameters [24, 25]. The DIC technique has the ability of high rate image acquisition, which makes it suitable for dynamic measurements [26–28] or even blast tests where it has been used for image acquisition in the range of megahertz [29]. The DIC system is capable of delivering high resolution 3D full field measurements, which are easily integrated in the testing environment. When dealing with a complex specimen geometry and/or load train, the measurement technique represents a substitute to a large number of analogue gauges including extensometers, potentiometers and strain gauges. Thus, with the aim of performing real-time measurements from multiple positions on the test object surface, the DIC technique is implemented in this work for static displacement control.

This paper documents a series of three-point bending tests controlled by a feedback signal acquired from the test specimen by DIC and FBG measurements for displacement and strain controls, respectively. This is performed by a control loop that operates and acquires data from a test station, FBG interrogation system and DIC system. The displacement is applied by the test station using a servo-hydraulic actuator operated by a PID controller. The FBG measurements are obtained by emitting light through two optical fibres, each containing three FBG sensors. The optical fibres are embedded into the GFRP beams during manufacturing, one at the top and one at the bottom of the beam. The reflected light is analysed by an interrogator and converted to strain. The DIC measurements are performed by a stereoscopic camera system, capable of tracking the displacement of the specimen surface by image matching and photogrammetry. The experiments are performed within the linear elastic regime for five GFRP beams with a predefined error tolerance to document the functionality of the control loop.

Principle of Fibre Bragg Grating

An FBG is a short segment of several thousand organised layers with varying refractive indices written into a single mode fibre. When a broad band light beam strikes the interface between each layer in the FBG, the light is reflected and refracted cf. Fresnel equation [29]. When the grating period is equal to the wavelength, each single interface reflection is reflected in the phase magnifying the energy level by positive interference forming a narrow band spectral peak. The remaining reflected spectra are out of the phase with the grating period and therefore erased. By straining the FBG, a shift of the peak reflectivity is generated as illustrated in Figure 1, which is convertible to multiple physical quantities including strain, temperature and vibrations. [30].

Knowing the initial wavelength λ_0, the wavelength change $\Delta\lambda$ and the temperature change ΔT of the specimen, the strain is calculated from Equation (1).

$$\frac{\Delta\lambda}{\lambda_0} = \varepsilon k_\varepsilon + k_t \Delta \mathrm{T} \tag{1}$$

where the gauge factors k_ε and k_t are provided by the FBG manufacturer. The identification of the narrow band light reflected by the FBG is performed by an interrogation monitor, which converts the incident light to an array of discrete digital intensity data.

Principal of Digital Image Correlation

The DIC technique is a non-contact, full field measurement method based on grey-value digital images [31]. The system has two imaging sensors tracking the shape, motion and displacement of an object surface in three dimensions [27]. Figure 2 illustrates a DIC setup with a commercial system, capable of acquiring images of the specimen surface, which are subsequently analysed by the DIC software, [32].

DIC utilise two techniques to acquire data: image matching and photogrammetry [31]. Image matching identifies the position of each measurement point in the two camera images. This is done by dividing the first camera image into squared facets containing multiple pixels. For each facet, a suitable transformation matching the homologous area in the second camera image is derived tracking each successive image with sub-pixel accuracy. The surface must have a stochastic speckle pattern in order

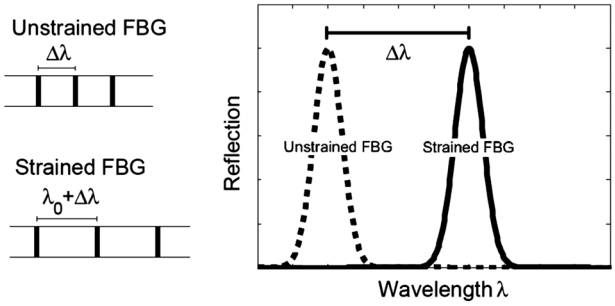

Figure 1: The change in peak reflectivity as a function of the grating period

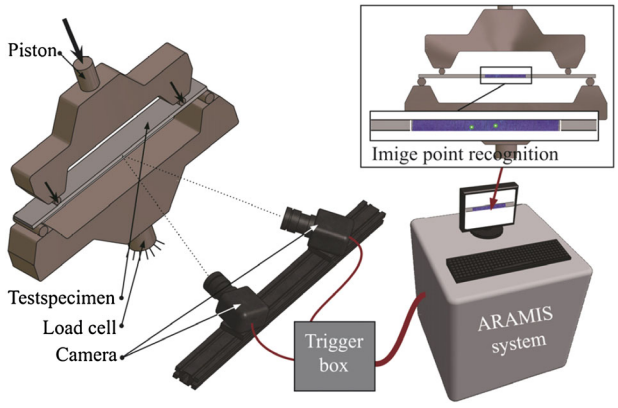

Figure 2: A four-point bending test with the commercial DIC system; ARAMIS

for the facets to be uniquely identifiable. Photogrammetry performs a transformation between the geometric properties of the measurement surface in the photographic image. This technique relies on a calibration to determine the imaging parameters for each camera (intrinsic) and the relative position and orientation of the cameras with respect to each other (extrinsic) [32]. The outcome is a 3D full field component shape and surface displacement field, along with the components of a plane strain tensor.

Test Setup

The test specimen is loaded in a four-column MTS 810 test machine with a T-slot strong table and an axial servo-hydraulic actuator with a static stroke of ±33.00 mm. The servo-hydraulic actuator is an MTS model 244.22 with a load capacity of 100 kN. The oil flow through the actuator is controlled by an MTS servo valve, model 252.24C-04 with a capacity of 38 L min^{-1}. Two feedback transducers are mounted in conjunction with the actuator: an internal LVDT and a load cell model MTS 661.19E-04 with a capacity of 25 kN. The actuator is operated, and the transducer signal is acquired by an MTS FlexTest60 PID controller. The loading nose and support rollers are 40 and 25 mm in diameter, respectively, cf. Figure 3, and the support rollers are able to move horizontally. Electrical resistance strain gauges are mounted on the specimens of the type SR-4 general purpose strain gauges from Vishay Micro-Measurements. The gauge resistance is 120.0Ω ± 0.3% and gauge length 6.99 mm for all specimens, while the gauge factor is 2.075 ± 0.5% for beams 1 and 3 and 2.035 ± 0.5% for the remaining. The optical fibres embedded in the specimens are silica fibres provided by FOS&S. Each fibre contains three draw tower gratings (FBG sensors) with a gauge length of 4.00 mm and an Ormocer coating (cladding diameter of 125 μm). The sensitivity coefficients k_ε and k_T are equal to 7.75E-7 μm m^{-1} and 6.27E-6 K^{-1}, respectively. The signal is acquired by a stand-alone interrogator type: I-MON 512 E-USB with a wavelength range of 1510–1595 nm cf. [33]. The surface is painted with a stochastic black speckle pattern on a white background, and three measurements points (MP) are selected, cf. Figure 3. The displacement of the measurement points is tracked by the commercial DIC system of the type ARAMIS from the company Geseltshaft für Optische Messtechnik (GOM). The camera resolution is 4 megapixels (2352 × 1728 pixels) with 20 mm focal length Titanar lenses. The images are divided into facets of 15 × 15 pixels, with a shift of 13 pixels. The cameras were calibrated to an intersection deviation of 0.024 pixels, with a 250 × 200 mm ARAMIS calibration panel to obtain a measurement area of 330 mm width and 330 mm height. The accuracy of the DIC setup is evaluated by a micrometre of the type: Mitutoyo — series 164 and range 0–50 mm. The micrometre offers an accuracy and resolution

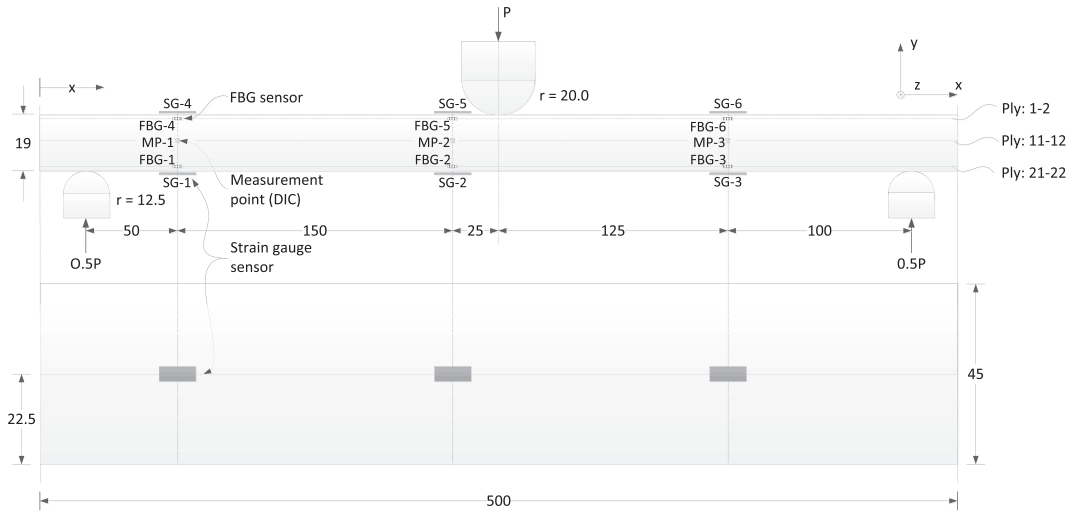

Figure 3: Dimensions of the test setup and specimen along with numbering and location of various sensors

© 2014 Wiley Publishing Ltd | ***Strain*** (2014) **50**, 262–273
doi: 10.1111/str.12089

of 3 μm and ±1 μm, respectively, and is mounted to a linear motion system type: THK-RSR7W. The dimensions of the three-point bending setup and test specimen along with numbering of the FBG sensors, electrical resistance strain gauges and the DIC measurement points (MPs) are displayed in Figure 3.

The entire test setup, with the specimen inserted into the three-point bending rig with the mounted gauges, is presented in Figure 4.

Specimen properties

The test specimen is a GFRP beam with 22 plies of uni-directional (UD) fibre mats of the type L1200/G50F-E06-A, from Devold AMT, with a nominal area weight of 1246 g m^{-2}. The matrix is a thermoset epoxy resin of the type Airstone 760E mixed with Airstone 776H hardener, from Dow Chemicals Company. Five GFRP beams were produced by vacuum infusion with a fibre orientation in the *x*-direction (see Figure 3) and fibre volume fraction of 55% [34]. The stiffness and strength properties of the beams are calculated by the rule-of-mixture on the basis of UD mechanical properties listed in Table 1 [35].

The load capacity at first ply failure (FPF) is estimated on the basis of the max stress failure criterion [35]. This yields a corresponding force of $F_{FPF} = 8.00$ kN. The Young's modulus of the specimen has been determined experimentally to 40.21 GPa.

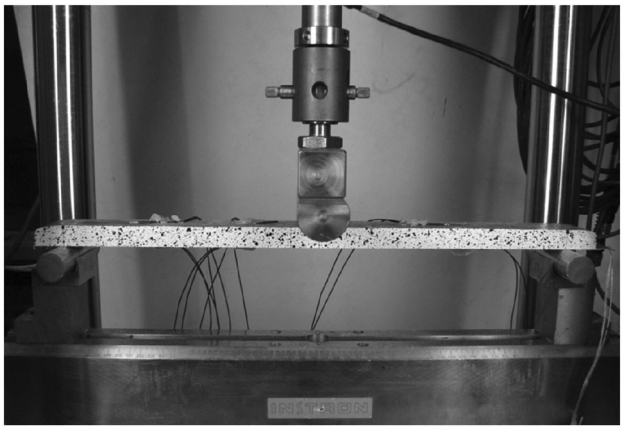

Figure 4: The three-point bending setup with a GFRP beam applied strain gauges, speckle pattern and FBG sensors

Control Loop

The control loop enables static displacement control operated by a feedback signal acquired from the test specimen using DIC or FBG measurements. This control system follows the architecture of a single input-single output feedback control loop [36]. This test configuration is implemented in LabVIEW 8.6, and the implemented test algorithm includes two independent systems: the displacement controlled actuator and the external data acquisition (DAQ) system. The displacement controlled hydraulic actuator is operated through an MTS FlexTest 60 servo controller [37] by the TCP/IP port using a dynamic link library (DLL) [38]. The external DAQ system includes the DIC and FBG measurements. The control loop is executed in a state-machine framework [39] according to the flowchart illustrated in Figure 5.

The control loop is initiated by feeding a displacement input to the servo controller (1) operated by a feedback signal from the LVDT in the actuator. In (2), the actuator is moved towards the end level in a monotonic motion with a predefined time rate. When the defined displacement is reached, the data from the servo controller: LVDT and load cell signals along with the external measurements: FBG and DIC are acquired by (3) and (4), respectively. The displacement input is compared with the response of the specimen, and a deviation is derived. If the deviation is within the error tolerance, the control loop is ready to receive the next user defined displacement input in (6). If the deviation exceeds the error tolerance, the actuator is moved in the direction necessary to reduce the error with a magnitude equal to the deviation. This is carried out by repeating the entire loop from (1) – (5) until a deviation below the error tolerance is obtained.

FBG system—control loop communication

A real-time communication between the I-MON 512E interrogator and the LabVIEW is established through the USB port by a dynamic link library (DLL) [40]. These DLL files are implemented directly in the LabVIEW environment, while all the data analyses are hard-coded in the LabVIEW according to [41]. The functions in the control sequence are presented in a flow chart diagram in Figure 6.

In Figure 6, the communication is initiated in (1), which identifies and configures a communication between the LabVIEW and the I-MON interrogator. The data are collected in a block mode setup separated in three tasks: acquire a single image, convert the analogue signal to an

Table 1: Mechanical properties of a UD-glass fibre ply

E_1 (GPa)	E_2 (GPa)	G_{12} (GPa)	υ_{12} (−)	$\hat{\sigma}_{1t}$ (MPa)	$\hat{\sigma}_{1c}$ (MPa)	$\hat{\sigma}_{2t}$ (MPa)	$\hat{\sigma}_{2c}$ (MPa)	$\hat{\tau}_{12}$ (MPa)
40	9.8	2.8	0.3	1100	600	20	140	70

doi: 10.1111/str.12089

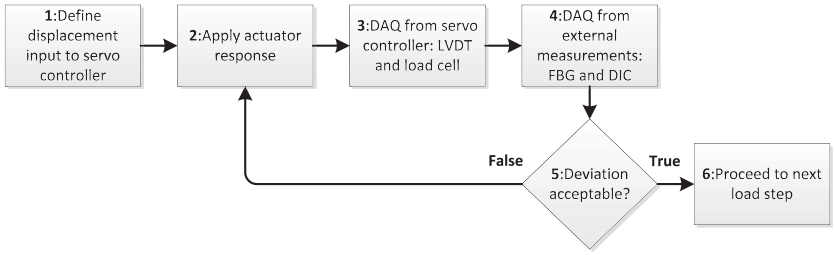

Figure 5: Control loop algorithm operating and acquiring data from servo controller, FBG interrogator and DIC system

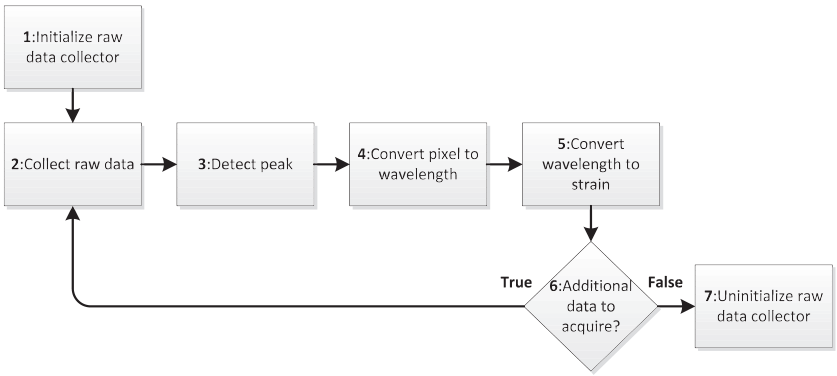

Figure 6: Communication procedure between control loop algorithm and FBG interrogator

array of discrete intensity data and transfer the data from the PCB buffer to the LabVIEW software. The data acquisition is performed in (2) with a predefined cycle time for each iteration. The photoelectrical signal is generated by the linear image sensor consisting of 512 elements. Each element represents one pixel in the image sensor, while the appertaining integer describes the individual pixel response generated by the incident light. The locations of the pixels representing the reflection peak, generated by the reflection spectra of the multitude FBG sensors, are identified in (3). The function pinpoints the individual pixels exceeding the pixel response, defined by a threshold parameter. By a Gaussian fit routine, the location of the peak is determined by including a predefined number of neighbouring pixels in the analysis. In (4), the relation between the pixels on the linear image sensor and the optical wavelength is described by a fifth degree polynomial [33]. A compensation for temperature drift in the interrogator is included by a correction equation [33]. All calibration coefficients are acquired through the USB port from the electronically erasable programmable read-only memory (EEPROM). The relation between the wavelength and strain, present in each FBG included in the system, is outlined in (5) cf. Equation (1). If no additional measurements from the I-MON interrogator are required (6), the programme is stopped (7). This is done by releasing the main PCB internal image data buffer, USB camera, and finally, the USB device and DLL.

Strain control by FBG

The FBG strain control is performed by using strain data from the FBG sensors to obtain an equivalent displacement at the loading point. This is inserted as a displacement input in the control loop cf. Figure 5. The strains at the location of the FBG sensors are converted to a displacement by Bernoulli–Euler beam theory, Navier's stress relation and Hooke's law.

$$\frac{d^2u}{dx^2} = -\frac{M}{EI}z, \qquad \sigma = \frac{M}{I}z, \qquad \sigma = E\varepsilon \tag{2}$$

This yields two relations between displacement and strain for the three-point bending load case

$$u_{max} = \frac{1}{24}\frac{L^3\varepsilon(x)}{xz} \text{ for } x \leq \frac{L}{2} \tag{3}$$

$$u_{max} = \frac{1}{24}\frac{L^3\varepsilon(x)}{(L-x)z} \text{ for } x \geq \frac{L}{2} \tag{4}$$

where x is the position in the x-direction cf. Figure 3, u_{max} is the deflection at centre position, L is the length between the support points, z is the distance from the neutral axis to the FBG sensors in the y-direction and $\varepsilon(x)$ is the strain in the x-direction at the position x. The displacement input at the loading point is derived as the average deflection of all six FBG sensors embedded in the specimen cf. Figure 3.

doi: 10.1111/str.12089

DIC system—control loop communication

The GOM IVIEW software is an extension to the ARAMIS measurement system capable of acquiring single measurement points on the specimen surface in real time [17]. From each measurement point, the 3D coordinates are obtained and fed to the LabVIEW program through a TCP/IP connection. The TCP/IP communication and image processing, performed by IVIEW, is handled in a Python macro with commands from the GOM package [42]. The steps in the communication between the two systems are presented by the flowchart in Figure 7.

In Figure 7, the communication between LabVIEW and DIC is initiated by opening a TCP/IP port in (1). When this communication is established and verified, the LabVIEW application sends a trigger signal to (2) initiating the image acquisition with a predefined frame rate. The coordinates for each measurement point are calculated real time and fed to an internal image buffer. LabVIEW is requesting image data in (3) by generating a trigger signal. This trigger signal is fed through the TCP/IP connection to (4) transferring the data stored in the buffer to (5). When all the data are transferred, the image data buffer is overwritten with new image data while waiting for the next trigger signal by (3). When all the requested data are acquired and the LabVIEW application is terminated, the TCP/IP connection is closed by (7).

Displacement control by DIC

DIC displacement control is carried out using the displacement signals from the measurement points on the surface, cf. Figure 3, to obtain an equivalent displacement at the loading point. These data are inserted as a displacement input for the control loop cf. Figure 5. The relation between the maximum displacement and displacement at a given coordinate x is again derived from the Bernoulli–Euler beam theory.

$$u_{max} = \frac{u(x)}{3\left(\frac{x}{L} - \frac{4}{3}\left(\frac{x}{L}\right)^3\right)} \quad for\ x \leq \frac{L}{2} \tag{5}$$

$$u_{max} = \frac{u(x)}{4\left(\left(1 - \frac{x}{L}\right)\left(\frac{2x}{L} - \frac{1}{4} - \left(\frac{x}{L}\right)^2\right)\right)} \quad for\ x \geq \frac{L}{2} \tag{6}$$

where $u(x)$ is the displacement in the y-direction at position x. The displacement input is obtained by averaging the u_{max} calculated from each of the three measurement points.

Results

A GFRP specimen is tested within the linear elastic regime in a three-point bending rig cf. Figure 4 with a ramped displacement rate of $1\,\mathrm{mm\,s^{-1}}$. The setup is operated by a feedback signal from the test specimen by using FBG and DIC measurements for static strain and displacement control, respectively.

FBG sensor strain control

Static strain control by FBG is utilised to limit the deviation between the displacement input and FBG measurements, within a given error tolerance. The magnitude of this tolerance is given on the basis of the measurement uncertainty and repeatability [43] offered by the FBG system. The repeatability has a standard uncertainty of $0.0994\,\mu\mathrm{m\,m^{-1}}$ from a sample of 160 measurements for each FBG, acquired under constant conditions with a frequency of 970 Hz. The stand-alone interrogation monitor measures wavelengths with an accuracy of ±10 pm cf. [33], which corresponds to $\pm 8.3\,\mu\mathrm{m\,m^{-1}}$ cf. Equation (1). The error tolerance is defined to $\pm 20\,\mu\mathrm{m\,m^{-1}}$, which is equal to approx. ±0.69% of the peak strain, cf. Figure 8. A displacement input with a triangular waveform is applied including 91 iterations forming five peaks. The peak-to-peak amplitude of the displacement input is $2900\,\mu\mathrm{m\,m^{-1}}$ between plies 21–22 at the loading point, see Figure 3. The displacement input is validated by FBG measurements,

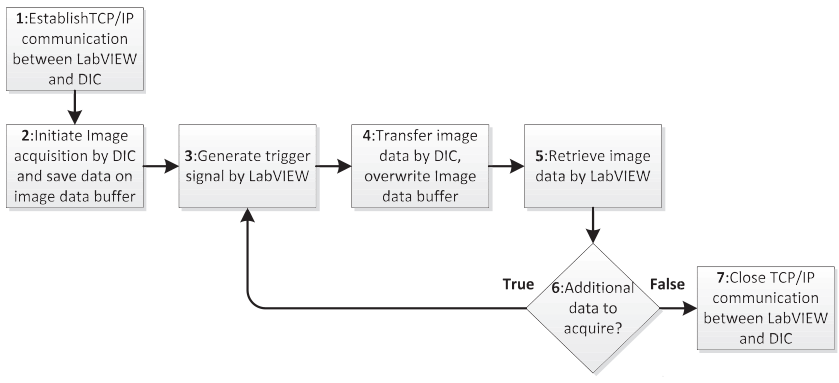

Figure 7: Communication procedure between: control loop algorithm and DIC system

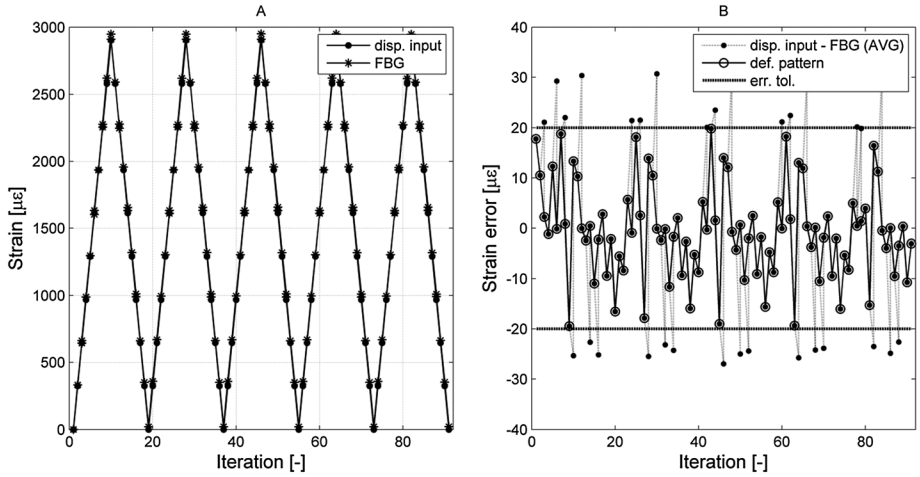

Figure 8: Strain control by FBG (A) displacement input and FBG and (B) discrepancy between displacement input and FBG

which are calculated by converting the strain data from each FBG sensor to obtain an equivalent strain between plies 21–22 at the centre of the beam and take the average of all six measurements. Operated by a feedback signal from the FBG measurements, the prescribed displacement input along with the appurtenant FBG measurement is presented in Figure 8A. Furthermore, the deviation between the displacement input and FBG measurement is available in Figure 8B.

In Figure 8B, multiple violations of the error tolerance are observed. The system reacts by adjusting the position of the actuator in the direction necessary to reduce of the error. The resulting displacement pattern operated within the error tolerance is marked with circles in Figure 8B. The discrepancy between the displacement input and each of the six FBG measurements is presented in Figure 9.

Except FBG 2 and FBG 5, a linear dependent discrepancy between the displacement input and FBG reading is observed in Figure 9. This could indicate an unexpected variation of the inter-ply location of the embedded optical fibre. However, other effects including stress concentrations generated by the support rollers /loading nose and imperfections in the specimen also have an influence. The average time elapsed between each iteration is approx. 3.5 s. Three tests are accomplished on the same test specimen. The number of adjustments, needed to maintain a deviation within the error tolerance for each test is presented in Table 2.

To validate the output from the FBG sensors, six strain gauges are attached to the specimen: three at the top in compression and three at the bottom in tension cf. Figure 3. With the assumption of having a linear variation of the strain in the ply stack thickness (*y*-direction), the measurements from the FBG are compared directly with the strain gauge. This is done by multiplying the strain gauge measurement with the factor *n*, which is the distance from the neutral axis (plies 11–12) to the position of the FBG (plies 21–22) divided by half the beam thickness. A load–strain curve is presented in Figure 10 for specimen 1, including the strain in the FBG and appertaining strain gauge multiplied by an *n* factor of 0.91.

Except SG-3/FBG-3 and SG-1/FBG-1, a small deviation between the FBG and strain gauge is detected. However, a systematic error between the FBG and appurtenant strain gauge is detected for all six cases with a confidence interval of 95%. To accept the hypothesis of having a random error between the FBG and appurtenant strain gauge, the factor *n* is adjusted. The results are presented in Table 3 for five different test specimens.

The empty cells in Table 3 refer to a lack of data due to malfunctioning of strain gauges during testing.

DIC displacement control

Static strain control by DIC is performed to restrict the discrepancy between the displacement input and DIC measurements within a predefined error tolerance. The magnitude of the error tolerance is given on the basis of the measurement uncertainty and repeatability [43] offered by the DIC system. The repeatability is determined from a sample of 100 measurements for each measurement point, acquired under unchanged conditions to have a standard uncertainty of 2.91 μm. The measurement uncertainty is determined as the discrepancy between the displacement measured at a measurement point by the DIC system and a micrometre. With 10 samples equally distributed over a displacement range of 0–6 mm, the measurement uncertainty is 0.01 mm. From the given measurement uncertainty and repeatability, an error tolerance of ±0.01 mm is defined, which is equal to 0.17% of the peak displacement. A displacement input with a triangular waveform is assigned including 91 iterations forming five peaks. The peak-to-peak amplitude of the displacement

doi: 10.1111/str.12089

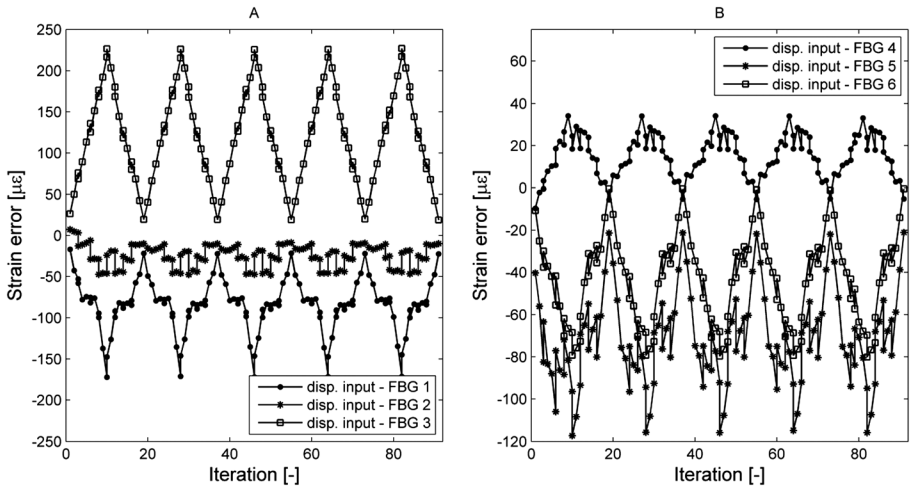

Figure 9: Discrepancy between displacement input and each FBG: (A) FBG 1–3 and (B) FBG 4–6

Table 2: Number of adjustments required in strain control by FBG for each test

Test number (–)	Number of adjustments (–)
1	28
2	26
3	24

input is 5.87 mm at the loading point of the specimen. The displacement input is validated by DIC measurements, which are generated by converting the displacement from each stage point to an equivalent displacement at the loading point and take the average of all three measurements. Operated by a feedback signal from the DIC measurements, the prescribed displacement input along with the appurtenant DIC measurement is presented in Figure 11A. Furthermore, the deviation between the displacement input and DIC measurement is available in Figure 11B.

In Figure 11B, the discrepancy between the displacement input and DIC measurements exceeds the error tolerance multiple times. The system reacts by moving the actuator with a magnitude equal to the respective displacement error. The resulting displacement pattern operated within the error tolerance is marked with circles. The discrepancy between the displacement input and each of the three DIC measurements is presented in Figure 12.

In Figure 12, a linear dependent discrepancy between the displacement input and DIC measurement is observed. The discrepancy increases when enlarging the distance between the loading nose and measurement point in the *x*-direction (see Figure 3). This tendency may be due to the assumptions

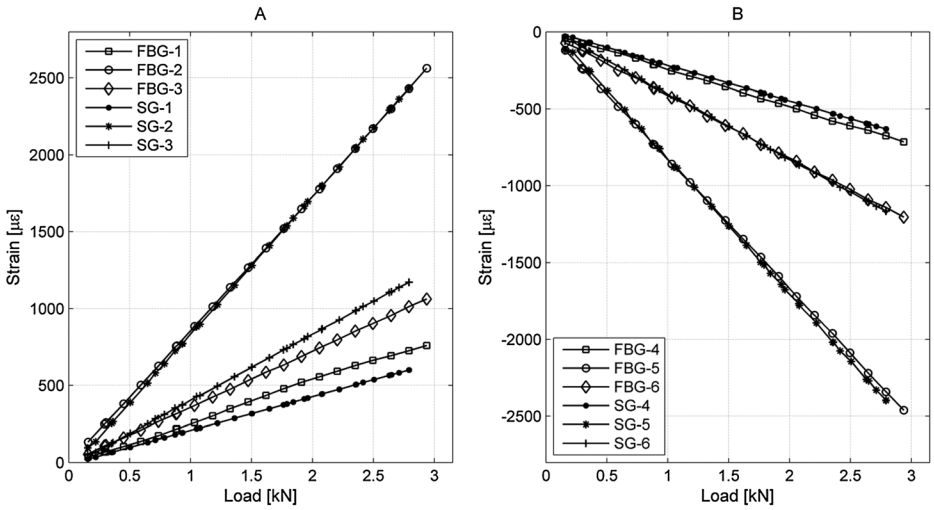

Figure 10: Load–strain curve for each individual FBG and SG: (A) bottom fibres in tension and (B) top fibres in compression

doi: 10.1111/str.12089

Table 3: Factor n to eliminate the deviation between the FBG and appurtenant strain gauge

Test specimen (–)	SG1 (–)	SG2 (–)	SG3 (–)	SG4 (–)	SG5 (–)	SG6 (–)
1	1.01	0.92	0.83	1.14	0.93	0.77
2	0.98	0.93	-	1.00	0.86	0.74
3	1.13	0.89	0.77	0.97	0.87	0.87
4	0.94	-	0.86	0.72	0.79	0.95
5	0.85	-	0.88	1.00	-	0.83

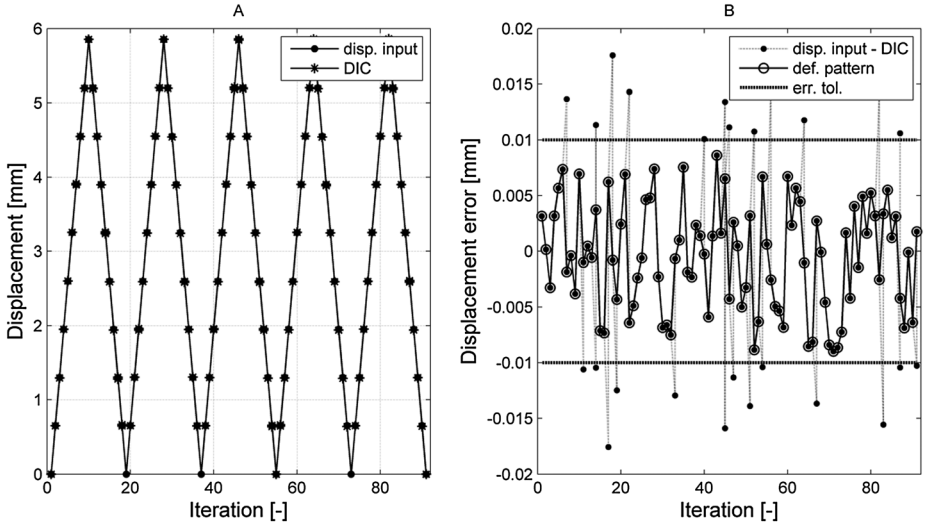

Figure 11: Strain control by DIC: (A) displacement input and DIC and (B) deviation between displacement input and DIC

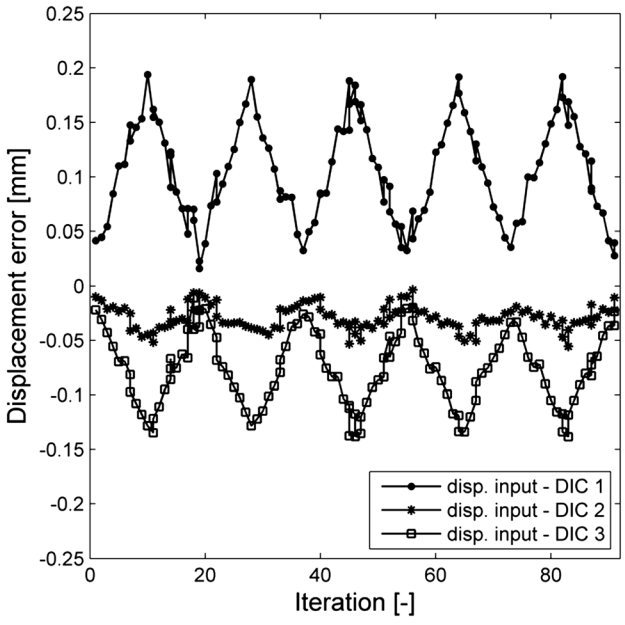

Figure 12: Discrepancy between displacement input and each DIC measurement

concerning the displacement shape of the beam, not being fulfilled. The average time elapsed between each iteration is approx. 3.5 s, and three tests are accomplished on the same test specimen. The number of adjustments needed to maintain a deviation within the error tolerance for each test is presented in Table 4.

Discussion

Control loop

In this investigation, the control loop was successfully demonstrated using two different measurement techniques: FBG and DIC for strain and displacement controls, respectively. Each time the discrepancy between the displacement input and the actual response of the specimen exceeded the error tolerance, the system reacted by moving the actuator with a magnitude equal to the respective displacement error. When the discrepancy was within the error tolerance, the next displacement input was applied in the subsequent iteration.

doi: 10.1111/str.12089

Table 4: Number of adjustments required in displacement control by DIC for each test

Test number (−)	Number of adjustments (−)
1	25
2	17
3	20

The control loop operated with an iteration frequency of 0.29 Hz for the given system, this frequency could be enhanced by using better hardware to operate the control loop. However, changing the system architecture from a state-machine framework to a cascade feedback loop would be another opportunity allowing a full dynamic response of the system [2]. However, given that the sampling rate of the external measurements is lower than the bandwidth of the PID controller, multiple iterations are made without knowing whether the error tolerance is exceeded. This means that, depending on the bandwidth of the external measurement system and PID controller, a number of iterations that are performed between each correlation are executed.

FBG sensor strain control

The control loop was successfully demonstrated for strain control with an error tolerance of $\pm 20\,\mu m\,m^{-1}$, which generated a total of 24–28 correlating adjustments with a total of 91 iterations cf. Figure 8A. According to Figure 8B, it is expected that the number of correlating adjustments is increased if the error tolerance is decreased and vice versa. With a measurement uncertainty and repeatability of $\pm 8.3\,\mu m\,m^{-1}$ and $0.0994\,\mu m\,m^{-1}$, respectively, an error tolerance of $\pm 20\,\mu m\,m^{-1}$ was accepted. However, decreasing the error tolerance to the level of the measurement uncertainty would be an opportunity.

The FBG measurements were compared with strain gauges as a reference, and a systematic error was detected for all six FBGs. This is mainly caused by a combination of two effects: the stress concentrations generated by the support rollers / loading nose and imperfections in the specimen. However, other effects also affect the FBG signal [30]. When comparing the strain acquired by the FBG system with the measurements from the strain gauges, some mismatches are detected cf. Figure 10 and Table 3. This could be explained by stress concentrations along with variations of the distance between the neutral axes to the FBG sensor. However, when $n \geq 1$, cf. Table 3, the FBG sensor appears to be positioned at the same level or above the appurtenant strain gauge. This indicates that the stress concentrations have a significant impact on the FBG measurements rather than variations of the FBG position. To support that theory, previous research with similar specimens showed that the optical fibres were found to be situated at the same inter-ply region [34].

The strain data from the FBG measurement are converted to an equivalent displacement by the Bernoulli–Euler beam theory. An error of that reconstructed displacement will be present due to the number of strain sensors, position of the strain sensors and uncertainty of the strain sensor signal [16]. That error could be erased by calibrating the FBG signal against the surface displacement as a function of the induced forces. However, that solution is only valid when staying within the linear elastic response.

DIC displacement control

The control loop was successfully demonstrated for displacement control with an error tolerance of ±0.01 mm, which generated a total of 17–25 correlating adjustments with a total of 91 iterations, Figure 11. According to Figure 11, it is expected that the number of correlating adjustments is increased if the error tolerance is decreased and vice versa. With a measurement uncertainty and repeatability of 0.01 mm and 2.91 μm, respectively, an error tolerance of ±0.01 mm was selected.

The static displacement control uses three measuring points to reduce the signal noise and the influence of local effects e.g. stresses concentrations, material defects and geometrical imperfections. However, when multiple measurement points are included, it is necessary to make assumptions concerning the displacement shape of the beam that might not be fulfilled. This could be avoided by oversampling a single measurement point, but this approach will only improve the repeatability, not the bias.

In [2], the standard displacement uncertainty is calculated to $\rho_u = 0.0421$ pixels for a facet size of 15 × 15 pixels and shift of 15 pixels. In this study, the standard displacement uncertainty is calculated to 3.3021 μm for a facet size of 15 × 15 pixels and shift of 15 pixels. This is converted to pixels by the measurement height of 330 mm and camera height resolution of 1728 pixels, thereby, 5.236 pixels/mm. With a displacement deviation of 2.91 μm, the resolution is 0.015pixels. This is 2.8 times higher pixel resolution than found in [2].

Conclusion

Five GFRP beams were loaded in the linear elastic regime in a three-point bending test configuration controlled by feedback signals from DIC and FBG measurements for displacement and strain control, respectively, obtained directly on or inside the specimen. The test configuration was obtained using a control loop algorithm, operating

and acquiring data from the servo-hydraulic controller, FBG interrogator and DIC system. It was demonstrated that such a test configuration is beneficial when a given stress state is required as a control parameter in connection with e.g. a complex test rig, loading configuration or specimen geometry. With the precision and accuracy offered by the DIC and FBG system, the test setup was capable of operating within an error tolerance of 0.01 mm and 20 $\mu m\,m^{-1}$ for displacement and strain controls, respectively.

ACKNOWLEDGEMENTS

The authors would like to acknowledge the financial support from the Danish Centre for Composite Structures and Materials (DCCSM) funded by the Danish Council for Strategic Research within Sustainable Energy and Environment (Grant 09-067212).

REFERENCES

1. Mallat, A. and Alliche, A. (2011) A modified tensile test to study the behaviour of cementitious materials. *Strain* **47**, 499–504.
2. Fayolle, X., Galloch, S. and Hild, F. (2007) Controlling testing machines with digital image correlation. *Exp. Tech.* **31**, 57–63.
3. Udd, E. (1996) Fiber optic smart structures. *IEEE* **84**, 60–67.
4. Khoun, L., Oliveira, R. D., Michaud, V. and Hubert, P. (2011) Investigation of process-induced strains development by fibre Bragg grating sensors in resin transfer moulded composites. *Composites* **42**, 274–282.
5. Molimard, J., Vacher, S. and Vautrin, A. (2010) Monitoring LCM Process by FBG sensor under birefringence. *Strain* **47**, 364–373.
6. Hsieh, M. Y., Tsai, L., Chiang, C. C., Lin, C. L. and Fang, B. L. (2012) Curing residual strain monitoring in different layer of Gr/Epoxy laminated composites using embedded optical fiber Bragg grating sensors. *SPIE* **8409**, 1–8.
7. Mitzutani, Y. and Groves, R. M. (2011) Multi-functional measurements using a single FBG sensor. *Exp. Mech.* **51**, 1489–1498.
8. Zhang, H., Ghandehari, M. and Sidelev, A., *et al*. (2011) Monitoring the hysteresis effects in a strain-stress curve of carbon fiber reinforced laminates by FBG technology. *SPIE* **7753**, 1–4.
9. Palaniappan, J., Ogin, S. L., Thorne, A. M., Reed, G. T., Crocombe, A. D., Capell, T. F., Tjin, S. C. and Mohanty, L. (2008) Disbond growth detection in composite–composite single-lap joints using chirped FBG sensors. *Compos. Sci. Technol.* **68**, 2410–2417.
10. Ling, H.-Y., Lau, K.-T., Su, Z. and Wong, E. T.-T. (2007) Monitoring mode II fracture behaviour of composite laminates using embedded fiber-optic sensors. *Composites* **38**, 488–497.
11. Gebremichael, Y. M., Li, W. and Meggitt, B. T., *et al*. (2005) A field deployable, multiplexed Bragg grating sensor system used in an extensive highway bridge monitoring evaluation tests. *IEEE Sens. J.* **5**, 510–519.
12. Kerrouche, A., Boyle, W. J. O., Sun, T., Grattan, K. T. V., Schmidt, J. W., Täljsten, B. (2009) Enhanced FBG sensor-based system performance assessment for monitoring strain along a prestressed CFRP rod in structural monitoring. *Sens. Actuators, A* **151**, 127–132.
13. Kerrouche, A., Boyle, W. J. O., Gebremichael, Y., Sun, T., Grattan, K. T. V., Täljsten, B. and Bennitz, A. (2008) Field tests of fibre Bragg grating sensors incorporated into GFRP for railway bridge strengthening condition monitoring. *Sens. Actuators, A* **148**, 68–74.
14. Gebremichael, Y. M., Li, W. and Boyle, W. J. O., *et al*. (2005) Integration and assessment of fibre Bragg grating sensors in an all-fibre reinforced polymer composite road bridge. *Sens. Actuators, A* **118**, 78–85.
15. Kerrouche, A., Leighton, J., Boyle, W. J. O., Gebremichael, Y. M., Sun, T., Grattan, K. T. V. and Täljsten, B. (2008) Strain measurement on a rail bridge loaded to failure using a fiber Bragg grating-based distributed sensor system. *Sens. Actuators, A* **8**, 2059–2065.
16. Mueller, U. C., Zeh, T., Koch, A. W. and Baier, H. (2006) Fiber optic Bragg grating sensors for high-precision structural deformation control in optical systems. *SPIE* **6167**, 127–132.
17. Guastavino, R. and Göransson, P. (2007) A 3D displacement measurement methodology for anisotropic porous cellular foam materials. *Polym. Test.* **26**, 711–719.
18. Owolabi, G. M. and Singh, M. N. K. (2009) A comparison between two analytical models that approximate notch-root elastic-plastic strain-stress components in two-phase, particle-reinforced, metal matrix composites under multiaxial cyclic loading: experiments. *Int. J. Fatigue* **28**, 918–925.
19. Jones, A., Shaw, J. and Wineman, A. (2006) An experimental facility to measure the chemorheological response of inflated elastomeric membranes at high temperature. *Exp. Mech.* **46**, 579–587.
20. Moser, R. and Lighter, J. G. (2007) Using three-dimensional digital imaging correlation techniques to validate tire finite-element model. *Exp. Tech.* **31**, 29–36.
21. Helm, J. D., Sutton, M. A. and McNeill, S. R. (2003) Deformations in wide, center-notched, thin panels, Part I: three-dimensional shape and deformation measurements by computer vision. *Opt. Eng.* **42**, 1293–1305.
22. Vialettes, P., Siguier, J.-M., Guigue, P., Karama, M., Mistou, S., Dalverny, O., Granier, S. and Petitjean, F. (2006) Experimental and numerical simulation of super-pressure balloon apex section: mechanical behavior in realistic flight conditions. *Adv. Space Res.* **37**, 2077–2081.
23. Leblanc, B., Niezrecki, C., Avitabile, P., Chen, J., Sherwood, J. and Hughes, S. (2011) Full-field inspection of a wind turbine blade using three-dimensional digital image correlation. *SPIE* **7979**, 2077–2081.
24. Luo, P. F. and Huang, F. C. (2000) Application of stereo vision to the study of mixed-mode crack-tip deformations. *Opt. Lasers Eng.* **33**, 349–368.
25. Corr, D., Accardi, M., Graham-Brady, L. and Shah, S. (2007) Digital image correlation analysis of interfacial debonding properties and fracture behavior in concrete. *Eng. Fract. Mech.* **74**, 109–121.
26. Pan, B. and Li, K. (2011) A fast digital image correlation method for deformation measurement. *Opt. Lasers Eng.* **49**, 841–847.

doi: 10.1111/str.12089

27. Siebert, T. and Crompton, M. J. (2010) Application of high digital image correlation for vibration mode shape analysis. In: *Society of the SEM Annual Conference*, Indianapolis, Indiana USA.
28. Siebert, T., Becker, T., Splitthof, K. and Neumann, I. (2007) High-speed digital image correlation: error estimations and applications. *Opt. Eng.* **46**, 51004/1-7.
29. Arora, H., Hooper, P. A. and Dear, J. P. (2011) Dynamic response of full-scale sandwich composite structures subject to air-blast loading. *Composites Part A* **42**, 1651–1662.
30. Chan, T. H., Yu, L., Tam, H. Y., Ni, Y. Q., Liu, S. Y., Chung, W. H. and Cheng, L. K. (2006) Fiber Bragg grating sensors for structural health monitoring of Tsing Ma bridge: background and experimental observation. *Eng. Struct.* **28**, 648–659.
31. Kreuzer, M. (2013) Strain Measurement with Fiber Bragg Grating Sensors. HBM, Darmstadt, Germany
32. Sutton, M. A., Orteu, J.-J. and Schreier, H. W. (2009) Image Correlation for Shape, Motion and Deformation Measurements, Springer, New York, U.S.A.
33. GOM, ARAMIS. (2006) User Manual - Software. GOM, Braunschweig, Germany.
34. Ibsen Photonics. (2009) I-MON E-USB 2.0 Product Specification. Ibsen Photonics A/S, Farum, Denmark.
35. Nielsen, M. W., Wittrup-Schmidt, J., Hattel, J., Høgh, J. H., Waldbjørn, J. P., Andersen, J. and Markussen, T. L. (2014) Life cycle strain monitoring in glass fibre reinforced polymer laminates using embedded fibre Bragg grating sensors from manufacturing to failure. *Composites Materials, to be published* **48**, 365–381.
36. Zenkert, D. and Battley, M. (2006) Composite Lightweight Structures, DK-2800 Kgs. Technical University of Denmark, Lyngby, Denmark
37. Svrcek, W. Y., Mahoney, D. P. and Young, B. R. (2007) Fundamentals of single input-single output systems. In: Fundamentals of Single Input-Single Output Systems in A Real-Time Approach to Process Control. John Wiley & Sons Ltd., Chichester, UK.
38. MTS. (2004) FlexTest SE & GT Digital Servocontrollers. MTS Systems Corporation, Minnesota, U.S.A.
39. MTS. (2009) LabVIEW Programming Libraries: Model 793.00 Software. MTS Systems Corporation, Minnesota, U.S.A.
40. Bitter, R., Mohiuddin, T. and Nawrocki, M. (2001) LabView Advanced Programming Techniques. CRC Press, Boca Rotan, Florida, USA.
41. Ibsen Photonics. (2011) Camera driver manual. Ibsen Photonics A/S, Farum, Denmark.
42. Ibsen Photonics. (2011) User Manual, Ibsen Photonics A/S, Farum, Denmark.
43. GOM. (2006) The GOM Scripting Language. GOM, Braunschweig, Germany.

This page is intentionally left blank

Appendix B

strain
An International Journal for Experimental Mechanics

Quasi-Static Single-Component Hybrid Simulation of a Composite Structure with Multi-Axis Control

J. Høgh*, J. Waldbjørn†, J. Wittrup-Schmidt†, H. Stang† and C. Berggreen*

*Department of Mechanical Engineering, Technical University of Denmark, Kgs. Lyngby, Denmark
E-mail: jhho@mek.dtu.dk
†Department of Civil Engineering, Technical University of Denmark, Kgs. Lyngby, Denmark

Abstract: This paper presents a quasi-static hybrid simulation performed on a single component structure. Hybrid simulation is a substructural technique, where a structure is divided into two sections: a numerical section of the main structure and a physical experiment of the remainder. In previous cases, hybrid simulation has typically been applied to structures with a simple connection between the numerical model and physical test, e.g. civil engineering structures. In this paper, the method is applied to a composite structure, where the boundary is more complex i.e. 3 degrees of freedom. In order to evaluate the validity of the method, the results are compared to a test of the emulated structure – referred to here as the reference test. It was found that the error introduced by compliance in the load train was significant. Digital image correlation was for this reason implemented in the hybrid simulation communication loop to compensate for this source of error. Furthermore, the accuracy of the hybrid simulation was improved by compensating for communication delay. The test showed high correspondence between the hybrid simulation and the reference test in terms of overall deflection as well as displacements and rotation in the shared boundary.

KEY WORDS: *composite structure, high-precision control, multi-axial control, single-component hybrid simulation, substructural testing*

Introduction

The ambition to improve the structural and operational performance of large structures within the industry of wind energy [1] has resulted in extensive research regarding large scale- and high performance composite structures. In these efforts, testing has primary been focusing on two scales: full scale and coupon testing [2]. Full scale testing provides valuable knowledge of the structural behaviour but is time consuming and expensive to perform due to the large scale of the structure [1]. The structure is typically tested in simple load configuration which is a significant simplification of the actual loads to which the structure is exposed during service. In order to investigate the material characteristics of the individual materials in the composite structure, coupon testing is conducted [3]. Such tests are performed on specially designed specimens, resulting in idealised stress- and strain states, and as a consequence, they do not account for the complex stress states and interactions between the different materials in the joints, bearings and other critical details throughout the structure.

To address shortcomings in full scale and material testing within the industry of wind energy, the hybrid simulation concept is introduced as a sub-modelling technique. For an SSP34m wind turbine blade (SSP Technology, Stenstrup, Denmark), the 0–13 m segment was identified as the critical section of interest [1, 2]. For that reason, the hybrid simulation concept could be implemented as an alternative to full-scale testing – providing the capability to isolate and experimentally test that section for which a reliable model may not be available. The remainder of the emulated structure is assumed to be well understood and is for that reason handled in a numerical model – capable of handling advanced load cases covering both static and dynamic effects. As a consequence, neither cost-intensive full-scale experiments nor demanding theoretical evaluation procedure is required to reveal the response of the experimental substructure, when exposed to the effect of the remaining structure. The coupling between the numerical and experimental substructure is governed through the interface between the two components referred to here as the shared boundary. During the test, a pre-defined external displacement is applied to the numerical substructure which is equivalent to the loads acting on the structure during service. The corresponding response is computed through a commercial finite element (FE) software and imposed on the experimental substructure using actuators. The forces required to deform the experimental substructure – referred to here as the restoring force – are retrieved and fed back to the numerical substructure to compute the next displacement corresponding to the next time step. This communication is established through an algorithm, referred to here as the hybrid simulation communication loop.

The hybrid simulation technique originated in the late 1960's, where it was used for simulation of the structural response to an earthquake as an alternative to shake table test [4]. Since then, the research within hybrid simulation has mainly been focused on seismic protection of building structures [5, 6]. Here, the numerical and experimental substructure has been two separate – typically simply connected – structural components referred to here as multi-component hybrid simulation. For this application, the load bearing structure has been simulated

doi: 10.1111/str.12157

in a numerical model, while damping fixtures has been tested experimentally e.g. elastomer [7], stud types [8, 9] and magneto-rheological [10, 11]. However, to close the gap between full scale and material testing within the industry of wind energy, the hybrid simulation concept is implemented for a single component structure – referred to here as single component hybrid simulation. This concept only deviates from the traditional multi-component hybrid simulation by the complexity of the shared boundary which for the single component hybrid simulation consists of an edge instead of e.g. a clearly defined hinge as presented in [12, 13]. This comprises an infinite number of contact points yielding a complex force/displacement distribution in the coupling between the two substructures. The operation of the shared boundary justifies the need for advanced measuring techniques to ensure a high degree of accuracy in the displacement imposed on the shared boundary of the experimental substructure [14, 15]. To the author's knowledge, only a single publication is published concerning single-component hybrid simulation [16]. Here, the concept is introduced, and the system demonstrated on a composite beam with the shared boundary covering a discrete point with a single degrees-of-freedom (DOF).

The scope of this paper is to perform a single-component hybrid simulation – here with special attention paid to the operation of the shared boundary between the numerical and experimental substructure. The emulated structure consists of a composite beam, clamped in both ends and loaded by a single point load. The shared boundary is described as a discrete point with three DOF. Digital image correlation (DIC) is implemented as a method of adjusting the quasi-static imposed displacements on the shared boundary, to fit the command signal received by the numerical model – referred to here as a *DIC compensator*. Furthermore, compensation of communication delay is conducted through linear regression – referred to here as a *communication delay compensator*. A parametric study is conducted where the effect of DIC compensation and communication delay compensation is investigated. Finally, the optimal configuration of these two parameters is identified and demonstrated on an applied case. For verification of the single-component hybrid simulation technique, a test of the emulated structure is conducted – referred to here as the reference test. Here, a point load is applied to the specimen and the global response monitored in multiple measurement point (MP) to compare with the global response of the hybrid simulation.

Hybrid simulation setup

The reference structure consists of a beam which is clamped in both ends and loaded by an external displacement D_{ext} cf. Figure 1. This configuration is studied to reduce the complexity in verifying the hybrid simulation communication loop capabilities and operation of the shared boundary. The material properties of the reference structure are determined by coupon testing cf. Table 1.

The reference structure is separated in a numerical- and experimental substructure. Two slits are located in the compression flange to yield a geometrical non-linear response of the experimental substructure due to buckling, cf. Figure 1. Each substructure along with the coupling between them is illustrated in Figure 2.

The shared boundary between the two substructures is defined by a discrete point with three DOF: translation in the *x*- and *y*-direction along with rotation around the *z*-axis – referred to here as *f*.

Experimental substructure (section A)

The experimental substructure consists of a 648-mm long thin-walled glass fibre reinforced polymer (GFRP) beam produced by Fibre Pultrusion. The closed rectangular cross section has a width and height of 140 mm and 60 mm, respectively, while the corresponding material thickness is 5 mm and 6 mm cf. Figure 1. Two slits at the centre of the compression flange are initiated in order to include non-linear behaviour. These slits are located 112 mm from each other, each with a length and width of 240 and 4 mm, respectively. The experimental substructure is loaded as a cantilever beam, with the free edge as the shared boundary between the two substructures cf. Figure 2. The in-plane material properties of the tensile/compression flange are presented in Table 1, determined in accordance with D3039/D3039M–08 [17] and D5379/D5379M–12 [18].

The tensile stress–strain relation in both the 1- and 2-direction is demonstrated linear elastic until failure. For the longitudinal tensile specimen, a clear relation between the laminate stiffness and position in the width of the tension/compression flange (2-direction) is observed. The lowest stiffness is found at the centre of the tensile/compression flange while increasing when moving towards the corner of the cross section. This tendency is most likely caused by variances in the fibre content along the width of the tension/compression flange. The 1-direction is the first in-plane direction, corresponding to the *x*-direction in Figure 2. The 2-direction corresponds to the second in-plane direction (2-direction corresponds to the *z*-direction for the flanges and *y*-direction for the sides in Figure 2).

The specimen is in both ends clamped to the rig through a rectangular steel profile cf. Figure 5. Installation plates of steel are positioned on each side of the test specimen for supporting and to avoid critical stress concentrations in the interface between the test specimen and rectangular steel profile. Everything is tightened together by 18 bolts to establish a stiff friction connection between the rectangular steel profile and test specimen, see Figure 3.

doi: 10.1111/str.12157

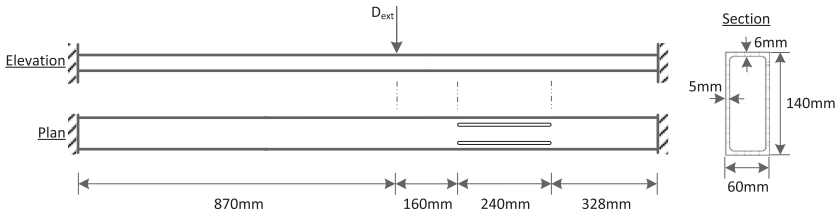

Figure 1: Reference structure representing the overall dimensions, external displacement and boundary conditions

Table 1: In-plane tensile moduli, shear modulus and Poisson's ratio

Specimen [-]	E_1 [GPa]	E_2 [GPa]	ν_{12} [-]	ν_{21} [-]	G_{12} [GPa]	G_{21} [GPa]
1	34.79	10.09	0.23	0.07	3.49	3.10
2	25.48	9.24	0.23	0.08	3.64	2.75
3	21.68	9.31	0.22	0.09	3.56	3.03
4	20.89	10.17	0.21	0.07	3.18	3.38
5	23.65	10.52	0.24	0.09	3.59	2.85
6	32.41	9.91	0.22	0.07	3.08	3.25
7	39.63	10.49	0.25	0.08	3.39	–
8	–	–	–	–	3.33	–
Average	28.36	9.96	0.23	0.08	3.41	3.06
Standard deviation	7.25	0.52	0.01	0.01	0.20	0.24
Coefficient of variance [%]	25.57	5.18	5.89	11.45	5.90	7.75

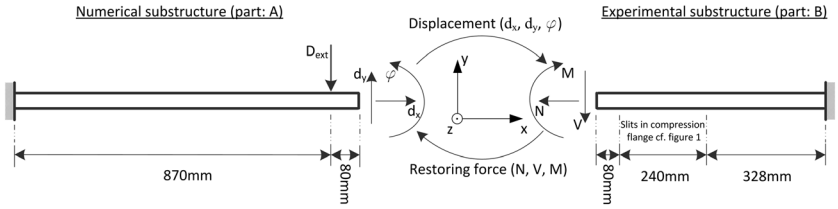

Figure 2: The reference structure separated in: (A) numerical substructure and (B) experimental substructure

Numerical substructure (section B)

The numerical substructure is simulated in ANSYS 15.0 (ANSYS, Inc, Canonsburg, PA, USA) in a three-dimensional (3D) FE-model, using isoparametric quadrilateral eight-node shell elements of the type: shell281 [19], with a Reissner–Mindlin formulation for the displacement field. Each side of the shell element includes a node in the corner and middle. These elements have six DOF in each node: translation and rotation in the *x*-, *y*-, and *z*-direction. The model has 2256 elements, and orthotropic material properties are assigned according to Table 2. The laminate is assumed transversely isotropic hence G13 = G12, G12 = G21, G13 = G31 and G23 = G32. The G23 has negligible effect on in-plane stiffness and therefore set equal to G12 for simplicity. The same assumption is made for the Poisson's ratio.

The external displacement is applied to the numerical structure as a nodal displacement along a line 870 mm from the clamped support, cf. Figure 1.

The restoring force is applied to the structure at the position of 950 mm from the support, cf. Figure 2. The vertical- and horizontal forces and moment are applied as nodal loads. The nodal loads are distributed statically and work equivalent to the uniformly distributed forces and moments in the structure.

The clamped supports of the FE model are designed as presented in Figure 4 with a width, height and thickness of $160 \times 280 \times 10$ mm and isotropic material properties.

doi: 10.1111/str.12157

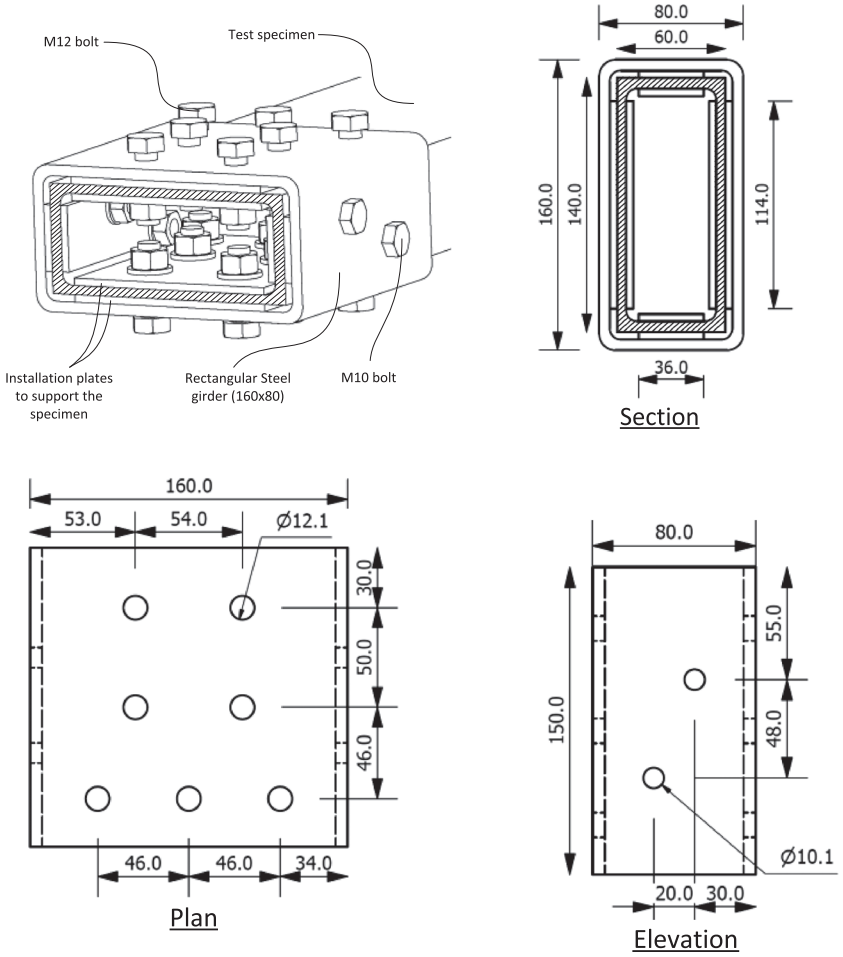

Figure 3: Clamped support of the experimental substructure displaying plan, section and elevation view

Table 2: Orthotropic material properties used in the finite element model

E_x [GPa]	E_y [GPa]	E_z [GPa]	G_{xy} [GPa]	G_{yz} [GPa]	G_{xz} [GPa]	υ_{xy} [-]	υ_{yz} [-]	υ_{xz} [-]
28.36	9.96	9.96	3.235	3.235	3.235	0.155	0.155	0.155

To ensure an identical stiffness of the numerical and experimental clamped support, an FE model of the reference structure is created. Here, the Young's modulus, E, of the support in the FE model is adjusted to fit the root rotation of the composite beam measured in the test of the reference structure. This rotation is measured by DIC in MPs 12, 13 and 14 cf. Figure 7. The correct rotation occurred with a Young's modulus of 170 GPa.

Experimental test setup

The experimental test setup is handled in a suitably stiff frame structure, re-configurable to handle both the reference test, see Figure 7, and experimental substructure of the hybrid simulation, see Figure 5. Fabricated steel interface plates are mounted to the frame structure to accommodate the swivel base of up to three servo-hydraulic actuators named A, B and C. Actuator A is an Material Testing Systems (MTS) model: 244.12 which provide a force capacity of ±25 kN with a static and dynamic stroke of 182.9 mm and 152.4 mm, respectively. The actuator is operated by a servo valve model: MTS 252.23G-01 with a capacity of 19 L min^{-1}. The displacement of the actuator is monitored by a linear variable differential transducer (LVDT) and the force measured by an MTS load cell model: 661.19E-04 with a capacity of ±25 kN. Actuators B and C are

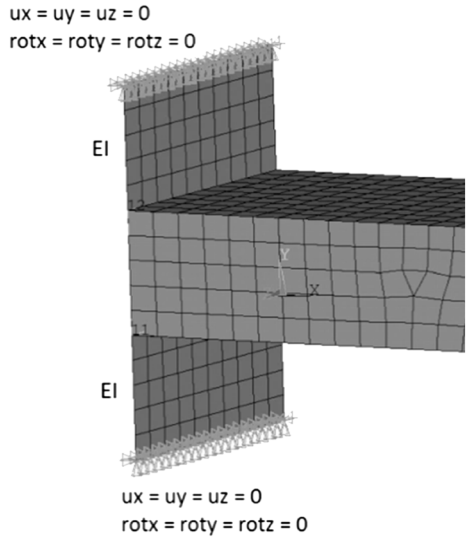

Figure 4: The clamped support of the finite element model

an MTS model: 242.01 which provide a force capacity of ±5 kN with a static and dynamic stroke of 114.3 and 101.6 mm, respectively. The actuator is operated by a servo valve model: MTS 252.21G-01 with a capacity of 4 L min^{-1}. The displacement of the actuator is monitored by an LVDT and the force measured by an MTS load cell model: 661.19E-01 with a capacity of ±5 kN. The actuators are operated through an MTS TestStar II proportional-integral-derivative (PID) – controller with a three-channel configuration. The system is connected to a hydraulic power unit operating at 3000 psi pressure.

Experimental substructure of the hybrid simulation

The experimental substructure of the hybrid simulation consists of the cantilever GFRP beam loaded in the stiff frame structure, described above, by three actuators A, B and C cf. Figure 5. The response of the GFRP beam is monitored on both sides by two individual 3D – DIC systems named: DIC 1 and DIC 2. The camera setup and performance of the DIC system are presented in Table 3.

From the DIC measurements, the displacement of the shared boundary and remainder of the experimental substructure are tracked through five MPs on each side cf. Figure 5. Given that the MPs for DIC 1 are tracked real-time, no full field data is available from this system, due to software limitations. Both sides of the GFRP beam applied a high contrast by a random speckle pattern of white background with black dots. The surface is illuminated with an even and high intensity. The compression and tension flanges are monitored through three strain gauge measurements (SGs) on each side cf. Figure 5. The electrical strain gauges are of the type SR-4 general purpose strain gauges from Vishay Micro-Measurements (951 Wendell Blvd., Wendell, NC 27591, USA).

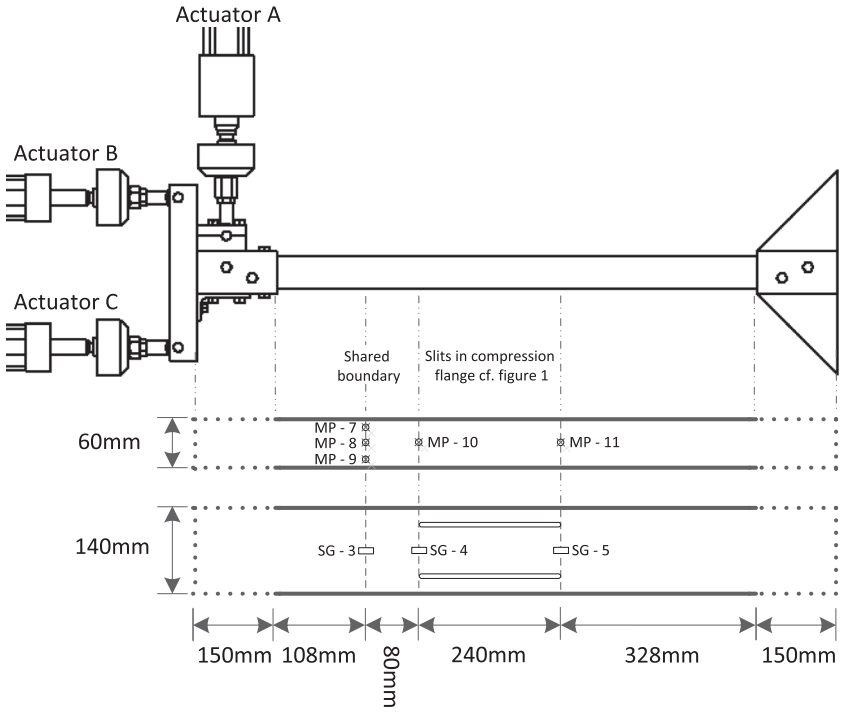

Figure 5: Experimental substructure including test rig and specimen with measurement point (MP) and strain gauge measurement (SG)

doi: 10.1111/str.12157

Table 3: Setup and performance of the 3D-DIC system

	Hybrid simulation		Reference test	
Configuration label	DIC 1	DIC 2	DIC 3	DIC 4
Side of beam	1	2	1	2
Technique used	3D image correlation	3D image correlation	3D image correlation	3D image correlation
Subset	20 pixel	20 pixel	20 pixel	20 pixel
Shift	13 pixel	13 pixel	13 pixel	13 pixel
Camera	4M 1 in CCD chip	2M 2/3 in CCD chip	4M 1 in CCD chip	2M 2/3 in CCD chip
Lens	20 mm	8 mm	20 mm	8 mm
Field of view	960 mm × 960 mm	590 mm × 590 mm	960 mm × 960 mm	590 mm × 590 mm
	2048 × 2048 pixel	1600 × 1200 pixel	2048 × 2048 pixel	1600 × 1200 pixel
Measurement points	24 818	11 360	24 818	11 360
Displacement				
Spatial resolution	20 pixel	20 pixel	20 pixel	20 pixel
Resolution, σ standard deviation				
In-plane	5.1 μm × 3.5 μm	6.6 μm × 3.4 μm	4.1 μm × 3.4 μm	5.6 μm × 3.2 μm
Out-of-plane	21.7 μm	17.2 μm	17.8 μm	17.0 μm

3D-DIC, three-dimensional-digital image correlation; CCD, charge-coupled device.

The gauge resistance is 120.0 Ω ± 0.3% and gauge length 6.00 mm with a gauge factor of 2.075 ± 0.5% for all specimens. The test configuration along with position and numbering of the DIC and SG is presented in Figure 5.

The three DOF of the shared boundary is monitored through three MPs named: MP 7, MP 8 and MP 9 cf. Figure 5. The shared boundary is located 108 mm from the rectangular steel profile to erase any strain concentrations initiated by the clamped support. A numerical analysis of the setup verified that the concentrations were diminished for a load introduction zone longer than 100 mm. Through DIC compensation, the quasi-static imposed displacements at the shared boundary are adjusted to fit the command signal received by the numerical model [14]. The full setup of the test configuration including hydraulic actuators, specimen mounted in the test rig, strain gauges and DIC camera is presented in Figure 6.

Reference test

The reference test consists of the GFRP beam, cf. Figure 1, which is clamped in both ends and loaded in the stiff frame structure described above, by the servo-hydraulic actuator A cf. Figure 7. The response of the GFRP is likewise monitored on both sides by two individual 3D – DIC systems named: DIC 3 and DIC 4. The camera setup and performance of the DIC system are presented in Table 3. From the DIC measurements, the displacement of the shared boundary and remainder of the reference structure are tracked through 14 MPs on each side cf. Figure 7. The compression and tension flanges are monitored through five SGs on each side cf. Figure 7. The electrical strain gauges are of the same type and specifications as the ones used in the experimental substructure of the hybrid simulation. The full test configuration along with position and numbering of the DIC and SG is presented in Figure 7.

The specimen is in both ends clamped cf. Figure 7. Details of the clamping support are given in Figure 3. The full setup of the test configuration including the hydraulic actuator, specimen mounted in the test rig and DIC camera is presented in Figure 8.

Hybrid simulation communication loop

The quasi-static hybrid simulation communication loop provides the capability to experimentally test a substructure of interest while simulating the remainder in a numerical model on an extended time scale. The software is partitioned in a numerical and experimental portion, connected through a digital to analogue–analogue to digital interface. The software is operated in a producer/consumer architecture [20] through LabVIEW 13.0. The outline of the dataflow in the hybrid simulation communication loop is presented in Figure 9.

The interface between the numerical and experimental substructure is generated through a NI9205 and NI9263 LabVIEW board. Product specifications including accuracy and precision are stated in [21] and [22].

An external displacement is applied to the numerical FE-model **(1)** further clarified in Figure 2. The FE-model is defined by the ANSYS parametric design language (APDL-script) and executed in batch mode through the Windows command prompt. The displacement $\underline{d}_{com}(i)$ at the shared boundary for the current load step, i, is extracted in three DOF: translation in the x- and y-direction along with rotation around the z-axis, cf. Figure 2 and Equation [2].

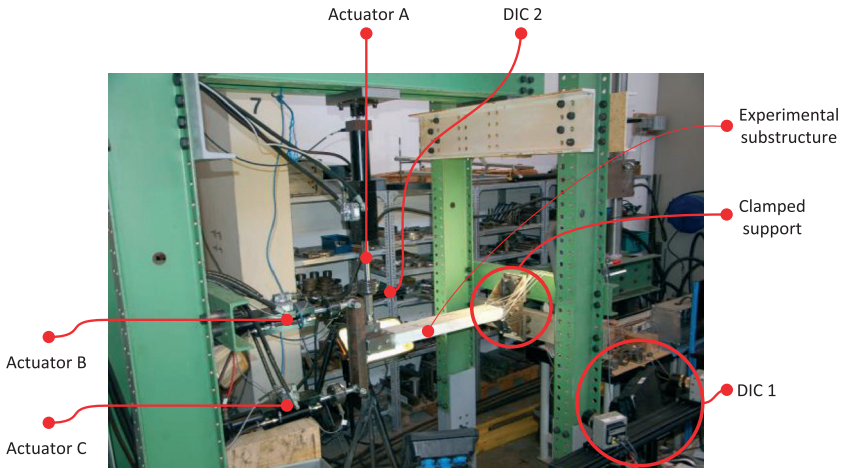

Figure 6: The multi-axial single-component hybrid simulation setup with glass fibre reinforced polymer beam, strain gauges and speckle pattern. DIC, digital image correlation

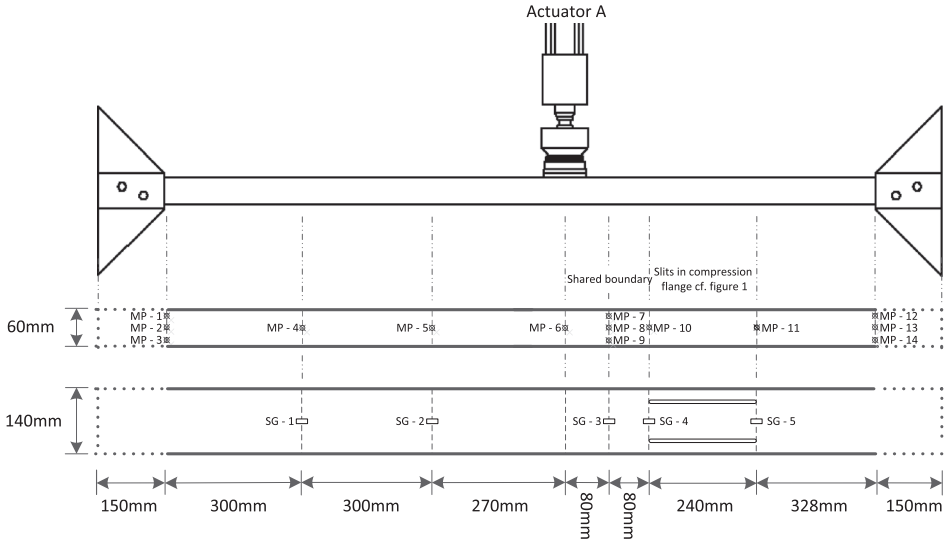

Figure 7: The test of the reference structure including test rig and specimen with measurement points (MPs)

To eliminate the effect of compliance in the load train, a *DIC compensator* is applied. The in-plane displacement of the shared boundary is tracked by DIC in **(2)** through three MPs named: MP7, MP8 and MP9 cf. Figure 5. The measured displacement is compared with the previous displacement $\underline{d}_{com}(i-1)$ and the deviation, $\underline{d}_{err}(i)$, derived in Equation [3]. This deviation is added to $\underline{d}_{num}(i)$ to find the compensated displacement at the current load step $\underline{d}_{com}(i)$, Equation [4]. $\underline{d}_{num}(i)$, $\underline{d}_{com}(i)$ and $\underline{d}_{err}(i)$ contains *x*- and *y*-translation and *z*-rotation in the format of Equation [2]. This compensator is similar to the one used in [14] except here; only the subsequent command signal is updated instead of iterating several times for every step. The corresponding displacement of actuators A, B and C, $\underline{d}_{act}(i)$ Equation [1] is derived through a trigonometric algorithm following the assumption of rigid body motion in **(3)**.

$$\underline{d}_{act}(i) = [d_A(i)\ d_B(i)\ d_C(i)] \tag{1}$$

$$\underline{d}(i) = [d_x(i)\ d_y(i)\ \varphi(i)] \tag{2}$$

$$\underline{d}_{err}(i) = d_{com}(i-1) - d_{num}(i-1) \tag{3}$$

$$\underline{d}_{com}(i) = \underline{d}_{num}(i) + \underline{d}_{err}(i) \tag{4}$$

In **(3)** Figure 9, the coordinates of actuators A, B and C loading points to the *i*'th step ($x_m(i)$ and $y_m(i)$) are found by superposition of the translational displacement, $d_x(i)$ and $d_y(i)$, and the position from the rotational contribution,

doi: 10.1111/str.12157

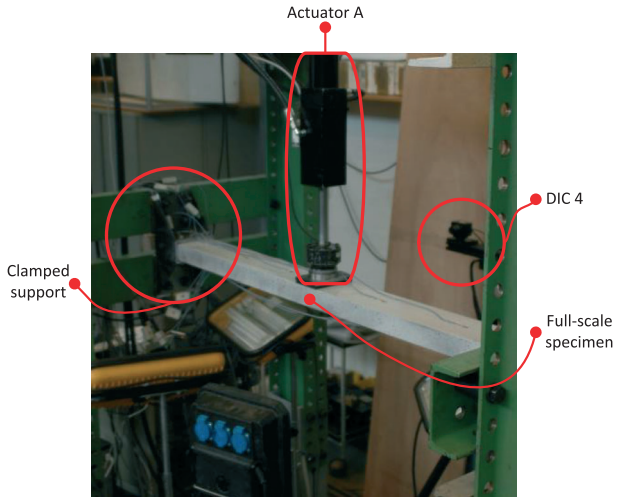

Figure 8: The reference test with glass fibre reinforced polymer beam, strain gauges and speckle pattern. DIC, digital image correlation

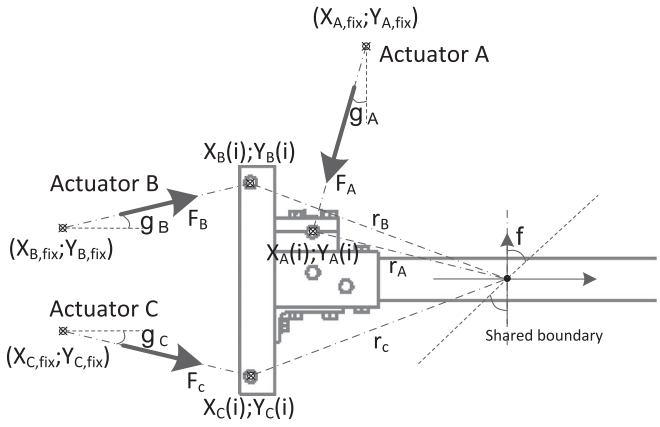

Figure 10: Notation for the calculation of the actuators A, B and C displacements

$x_{m,\varphi}$ and $y_{m,\varphi}$, assuming rigid body motion of the test rig, cf. Equations (5)–(6). The m denotes the actuators A, B or C.

$$x_m(i) = x_{m,\varphi}(i) + d_x(i) \text{ for } m = \text{A, B, C} \tag{5}$$

$$y_m(i) = y_{m,\varphi}(i) + d_y(i) \text{ for } m = \text{A, B, C} \tag{6}$$

The rotational contribution to the translation, $x_{m,\varphi}$ and $y_{m,\varphi}$, is found by a trigonometric relation between the rotation of the shared boundary, φ, and the actuator loading point position in the previous load step, $x_m(i-1)$ and $y_m(i-1)$, cf. Equations (7)–(8). Here, r_m, is the distance from the shared boundary to the actuator loading point, cf. Figure 10.

$$x_{m,\varphi}(i) = r_m \cos\left(\arccos\left(\frac{x_m(i-1)}{r_m}\right) + \varphi\right) \text{ for } m = \text{A, B, C} \tag{7}$$

$$y_{m,\varphi}(i) = r_m \sin\left(\arcsin\left(\frac{y_m(i-1)}{r_m}\right) + \varphi\right) \text{ for } m = \text{A, B, C} \tag{8}$$

The actuator displacement in load step i, $\underline{d}_{act}(i)$, is found from the distance between the actuator fix point, $x_{m,fix}$ and $y_{m,fix}$, and actuator loading point position, $x_m(i)$ and $y_m(i)$, cf. Equation [9].

$$\underline{d}_{act}(i) = \begin{bmatrix} \sqrt{\left(x_A(i) - x_{A,fix}\right)^2 + \left(y_A(i) - y_{A,fix}\right)^2} \\ \sqrt{\left(x_B(i) - x_{B,fix}\right)^2 + \left(y_B(i) - y_{B,fix}\right)^2} \\ \sqrt{\left(x_C(i) - x_{C,fix}\right)^2 + \left(y_C(i) - y_{C,fix}\right)^2} \end{bmatrix}^T \tag{9}$$

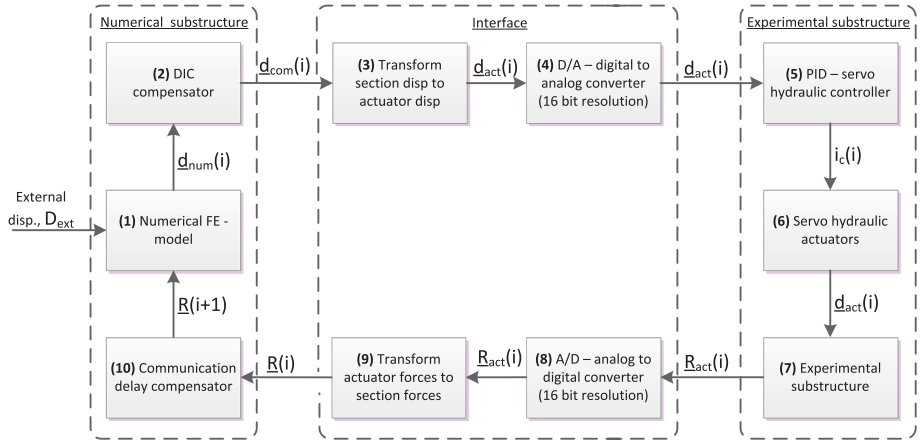

Figure 9: Dataflow in the quasi-static hybrid simulation communication loop. DIC, digital image correlation; FE, finite element; PID, proportional-integral-derivative

Through **(4)**, the current compensated displacement $\underline{d}_{com}(i)$ is transferred to a digital PID controller in **(5)** operated in displacement mode. Here, an electrical command signal $\underline{i}_c(i)$ is generated and passed to the servo valves in **(6)** causing the actuator to move $\underline{d}_{act}(i)$ and apply reaction forces on the test specimen. These actuator forces $R_{act}(i)$ is obtained by load cells in **(7)** and transformed to section forces $R(i)$ through a trigonometric relation in **(9)**, assuming rigid body motion. The relation is derived from Figure 10 and presented in Equations (12)–(14).

$$\underline{R}_{act}(i) = [R_A(i)\ R_B(i)\ R_C(i)] \tag{10}$$

$$\underline{R}(i) = [R_V(i)\ R_H(i)\ M(i)] \tag{11}$$

$$R_V = R_A\cos(\gamma_A) + R_B\sin(\gamma_B) + R_C\sin(\gamma_C) \tag{12}$$

$$\begin{aligned} R_H &= R_A\sin(\gamma_A) + R_B\cos(\gamma_B) + R_C\cos(\gamma_C) \\ M &= R_A\big(\cos(\gamma_A)(x_A(i) - x(i)) + \sin(\gamma_A)\big(y(i) - y_A(i)\big)\big) \end{aligned} \tag{13}$$

$$\begin{aligned} &+R_B\big(\cos(\gamma_B)\big(y(i) - y_B(i)\big) + \sin(\gamma_B)(x_B(i) - x(i))\big) \\ &+R_C\big(\cos(\gamma_C)\big(y(i) - y_C(i)\big) + \sin(\gamma_C)(x_C(i) - x(i))\big) \end{aligned} \tag{14}$$

In a hybrid simulation, the restoring force from the experimental substructure is one step behind the numerical simulation [23] – referred to here as communication delay. This is compensated for by a *communication delay compensator*. In **(10)**, the restoring force for the upcoming load step $\underline{R}(i+1)$ is extrapolated by the three or four previous sets of external displacement D_{ext} and restoring forces $R(i)$. This extrapolation is done by a function ψ, using least-square linear regression [24]

$$\begin{aligned} R_V(i+1) = \psi(&R_V(i-n), D_{ext}(i-n), R_V(i-n+1), \\ &D_{ext}(i-n+1), \ldots, R_V(i), D_{ext}(i)) \text{ for } n = 3, 4 \end{aligned} \tag{15}$$

$$\begin{aligned} R_V(i+1) = \psi(&R_V(i-n), D_{ext}(i-n), R_V(i-n+1), \\ &D_{ext}(i-n+1), \ldots, R_V(i), D_{ext}(i)) \text{ for } n = 3, 4 \end{aligned} \tag{16}$$

$$\begin{aligned} M(i+1) = \psi(&M(i-n), D_{ext}(i-n), M(i-n+1), \\ &D_{ext}(i-n+1), \ldots, M(i), D_{ext}(i)) \text{ for } n = 3, 4 \end{aligned} \tag{17}$$

Test result

A GFRP beam is tested in a quasi-static single component hybrid simulation setup presented in Figure 2 and Figure 5. A test of the emulated structure is conducted for verification purposes cf. Figure 1 and Figure 7. The system is loaded with a ramped deformation pattern in the range: 0.0 mm to 6.5 mm which is equivalent to a vertical reaction force of 0.0 to 5.0 kN. The load is applied through 20, 40 and 60 steps per period cf. Figure 11 at a rate of approximately 9 s step^{-1}.

In order to verify that both the reference test and hybrid simulation setup do not introduce out-of-plane displacements e.g. twisting, both sides of the GFRP beam are monitored in the MPs stated in Table 4. In here, side 1 is monitored by DIC 1 and 3, while side 2 is monitored by DIC 2 and 4, cf. Figure 6, Figure 8 and Table 3

The numerical substructure represented in Table 4 is not considered, since no out-of-plane deformations are observed. It is noted that the out-of-plane displacements are of a magnitude equal to the measurement precision cf. Table 3 and therefore insignificant. A deviation of vertical and horizontal displacement between sides 1 and 2 is clearly identified for the hybrid simulation, probably induced by misalignment of the load train. The same effect is also identified in the reference test; however, the magnitude is significantly smaller. The deviation between the vertical and horizontal displacement of both sides of the specimen is proportional to the load.

Digital image correlation compensator

By the use of 60 steps per loading period, the difference between enabling and disabling DIC compensation is investigated, cf. Equations (1)–(4).

From Figure 12A, the displacement distribution of the hybrid simulation reveals a significant lack of bending stiffness relative to the reference test along with a discontinuity in the shared boundary of 33% due to compliance in the load train. However, when using the DIC system to compensate for these effects, the reference test and hybrid simulation correlate significantly better with a maximum deviation of 2.6% relative to the reference test cf. Figure 12B. The DIC compensator slowed the programme by 50 ms step^{-1}.

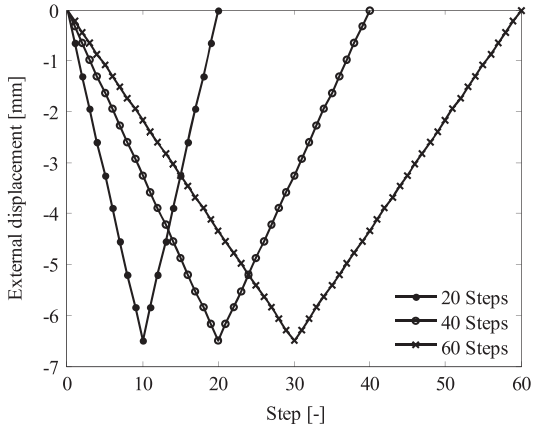

Figure 11: Ramped external displacement pattern for a single period

Table 4: Error for in-plane displacement between sides 1 and 2 and out-of-plane displacements at 5 kN

		Numerical substructure			Experimental substructure			Mean
		MP 4	MP 5	MP 6	MP 8	MP 10	MP 11	–
Reference test	Side 1 vertical [mm]	−2.96	−5.34	−6.29	−6.05	−5.60	−3.48	–
	Side 2 vertical [mm]	−2.94	−5.46	−6.36	−6.13	−5.67	−3.49	–
	Deviation vertical [mm]	0.01	0.12	0.07	0.08	0.07	0.01	0.060
	Side 1 horizontal [mm]	0.138	0.133	0.128	0.144	0.137	0.117	–
	Side 2 horizontal [mm]	0.124	0.157	0.133	0.146	0.118	0.126	–
	Deviation horizontal [mm]	0.014	0.024	0.005	0.002	0.019	0.009	0.012
	Out-of-plane displacement [mm]	0.05	0.04	0.04	0.04	0.03	0.02	–
Hybrid simulation	Side 1 vertical [mm]	–	–	–	−6.04	−5.64	−3.59	–
	Side 2 vertical [mm]	–	–	–	−6.25	−5.83	−3.76	–
	Deviation vertical [mm]	–	–	–	0.21	0.19	0.17	0.190
	Side 1 horizontal [mm]	–	–	–	0.080	0.100	0.100	–
	Side 2 horizontal [mm]	–	–	–	0.100	0.112	0.121	–
	Deviation horizontal [mm]	–	–	–	0.020	0.012	0.021	0.018
	Out-of-plane displacement [mm]	–	–	–	0.02	0.00	0.04	–

MP, measurement point.

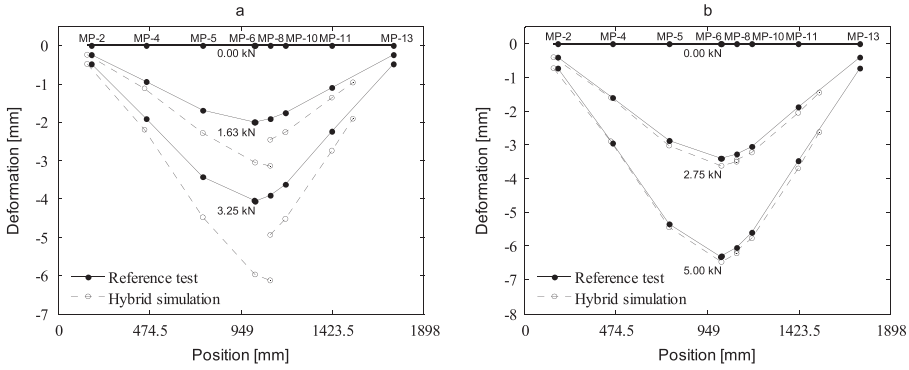

Figure 12: Displacement distribution of glass fibre reinforced polymer beam: (A) digital image correlation (DIC) compensation disabled and (B) DIC compensation enabled. MP, measurement point

The deviation between the numerical and experimental substructure is presented in Figure 13 including vertical, horizontal and rotational error at the shared boundary. For all three DOF, the effect of DIC compensation is significant.

Communication delay compensator

With 20 steps per loading period, compensation of the communication delay is performed through linear regression of the restoring force, Equations (15)–(17). Two different compensator schemes are implemented: 'no comp' where the restoring force to the current external displacement is set equal to the previous and 'linear' where the restoring force is extrapolated by least-square linear regression from the previous three or four MPs.

From Figure 14A, the displacement distribution of the hybrid simulation reveals a lack of bending stiffness with a maximum deviation of 9.3%, relative to the reference test. However, when a 4-point linear compensator is implemented, the reference test and hybrid simulation correlate with a maximum deviation of 4.6% relative to the reference test cf. Figure 14B.

The deviation between the compensated and given restoring force is presented in Figure 15 for vertical, horizontal and moment error. For all three DOF, the effect is significant within the first 11 steps. However, when the external displacement changes direction, instability is introduced by the compensator which will converge during a number of steps. Within the first half loading period, the averaging error in all three DOFs is presented for 20, 40 and 60 steps per period in Table 5.

doi: 10.1111/str.12157

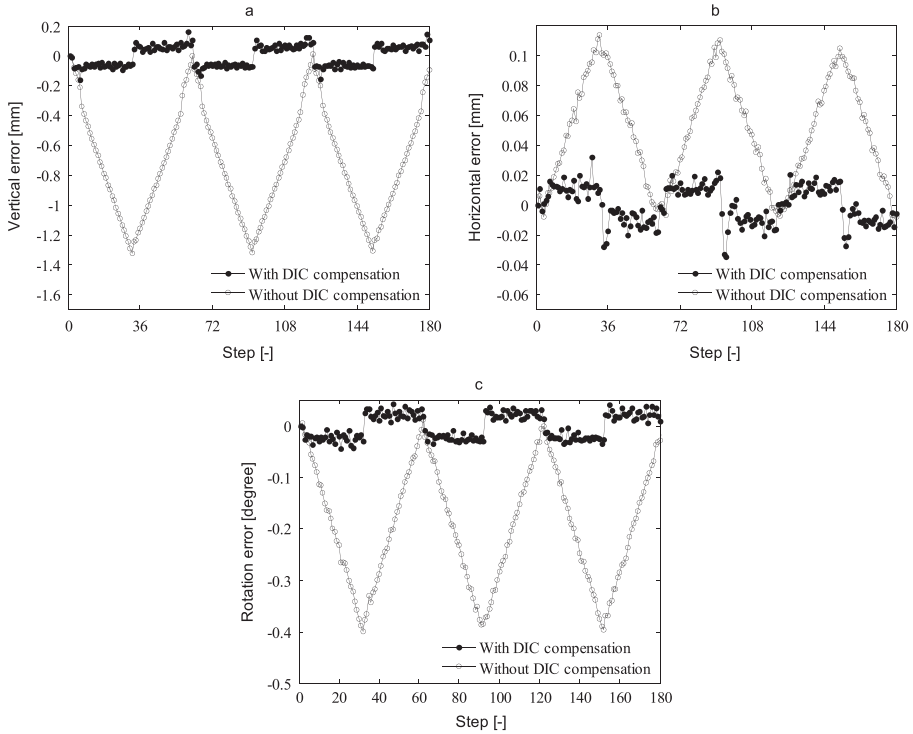

Figure 13: Deviation between cmd and feedback signal at shared boundary: (A) vertical, (B) horizontal and (C) rotation. DIC, digital image correlation

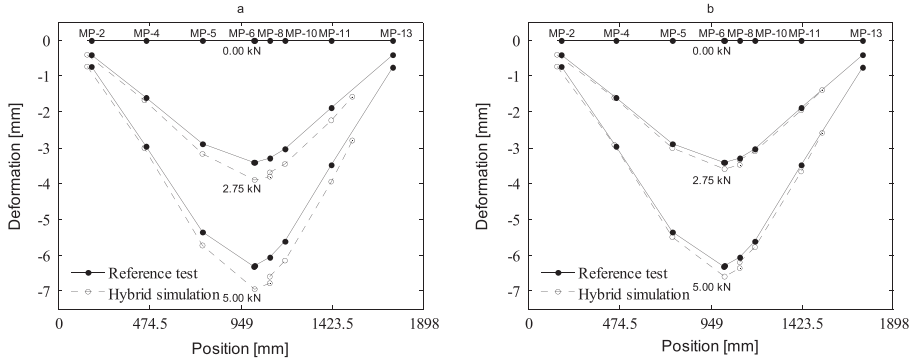

Figure 14: Displacement distribution with 20 sub-steps per period: (A) no compensator and (B) 4-point linear compensator. MP, measurement point

From Table 5, the deviation between the compensated and given restoring force decreases significantly when using a linear compensator within the first half loading period.

Combined effect of compensators

By the use of a 4-point linear compensator Equations (15)–(17), 60 steps per loading period and DIC compensation Equations (1)–(4), the hybrid simulation method is compared with the reference test including strain and displacement measurements.

In Figure 16, the displacement distribution in the reference test and hybrid simulation is shown, measured in the MPs stated in the top part of the graph. The maximum deviation between the reference test and hybrid simulation is 2.1% relative to the reference test.

The vertical and horizontal displacement and rotation of the shared boundary are measured through MP 7, MP 8 and MP 9 for both the reference test and hybrid simulation of the experimental and numerical substructure cf. Figure 17. A good correlation between the hybrid simulation and reference test is identified in terms of vertical and rotational stiffness of the shared boundary. In the horizontal direction, a deviation in stiffness is identified between the reference test and hybrid simulation. In Figure 17C, an offset between the reference test, numerical- and experimental substructure

doi: 10.1111/str.12157

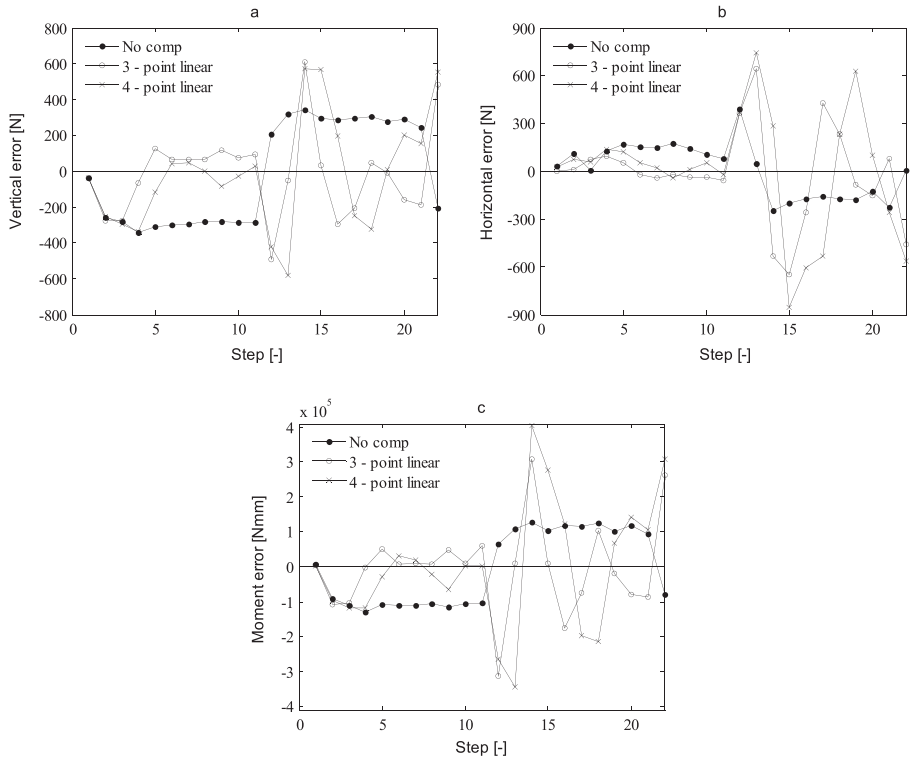

Figure 15: Deviation between predicted and given restoring force at 20 steps per period: (A) vertical, (B) horizontal and (C) moment

Table 5: Average vertical, horizontal and rotational error at first half loading period

Steps per period	Compensator type	Average vertical error [*N*]	Relative deviation [%]	Average horizontal error [*N*]	Relative deviation [%]	Average moment error [Nmm]	Relative deviation [%]
20	Non	−269	–	113	–	−98 900	–
	3-point linear	−41	15.4	22	19.5	−19 465	19.7
	4-point linear	−94	34.9	45	39.8	−35 563	35.9
40	Non	−141	–	66	–	−52 286	–
	3-point linear	−22	15.6	11	16.7	−8457	16.2
	4-point linear	−25	17.7	11	16.7	−9334	17.9
60	Non	−96	–	50	–	−35581	–
	3-point linear	−21	21.9	11	22.0	−7931	22.3
	4-point linear	−11	11.5	7	14.0	−4084	11.5

is identified. In the reference test, this offset is likely due to contact issues in the loading nose. Since the numerical and experimental substructure represents the command (cmd) and feedback signal, respectively, this offset may be due to compliance in the load train.

The strain distribution of the top and bottom flange is compared between the reference test and hybrid simulation through a number of strain gauges mounted on the experimental substructure; see Figure 5 and Figure 6.

For SG-3t, SG-4t and SG-5t represented in Figure 18B, some non-linear effects are observed due to the initiated slits in the top flange of the GFRP beam. The relative maximum deviation between the reference test and hybrid simulation is here found to be 47% for SG-3t, 17% for SG-4t and 6.2% for SG-5t, relative to the reference test.

All strain gauges in the bottom flange reveal a linear response. For SG-3b, SG-4b and SG-5b represented in Figure 5B, the maximum deviation between the reference

doi: 10.1111/str.12157

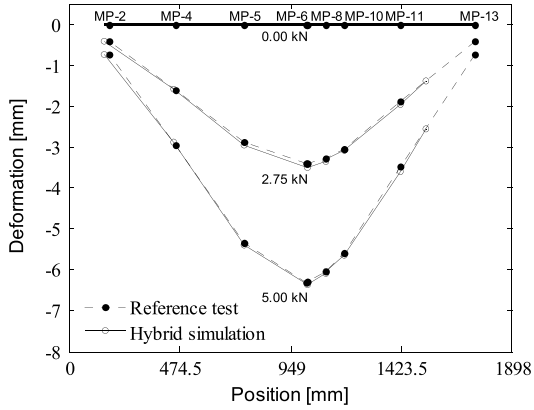

Figure 16: Displacement distribution of glass fibre reinforced polymer beam including test, hybrid simulation and finite element-model. MP, measurement point

test and hybrid simulation is found to be 2.3%, 0.7% and 2.4%, respectively, relative to the reference test.

Discussion

The overall response of the hybrid simulation was coinciding with the reference test within maximum 2.1%, when using a 4-point linear compensator and DIC compensation for displacement adjustment. This proved the hybrid simulation setup was capable of performing an accurate simulation of the compliance behaviour of the composite beam. Some discrepancies between the two were observed, and these will be discussed in the following. The main topics are as follows: discrepancies between the two sides of the beam, the strains in the top and bottom flanges and the effects of the compensator schemes.

A discrepancy between the deflections of the two sides of the beam was observed. For the reference test, the deviation was in average 60 μm and 12 μm for the vertical and horizontal displacements. For the hybrid simulation, the deviation was 190 μm and 18 μm for vertical and horizontal displacements, cf. Table 4. This indicates some out-of-plane effects in the test rig connecting the actuators to the specimen. One can argue whether to fix the actuators against out-of-plane movements to minimise these errors. However, all specimens have some out-of-plane imperfections that might introduce the observed out-of-plane displacements, and if the test rig is constraining this, it might initiate undesired damage to the specimen and load train instead of letting it distort freely.

The deviation in strains between the hybrid simulation and the reference test was maximum 47% – found on the top-flange, closest to the loading nose. This deviation is most likely caused by stress concentrations introduced by

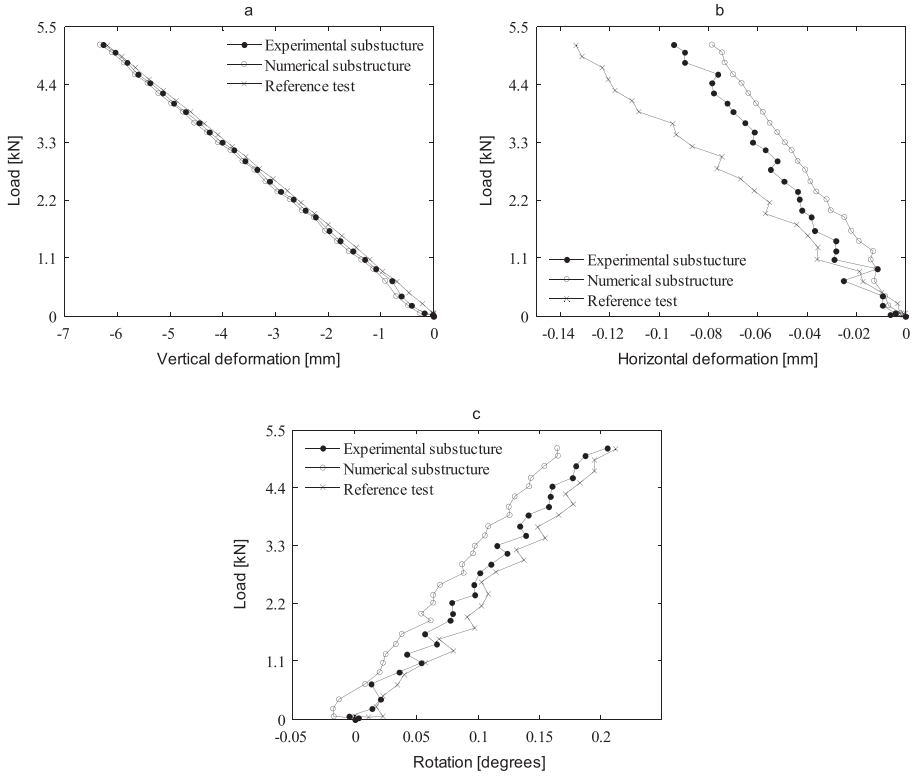

Figure 17: Displacement of the shared boundary: (A) vertical, (B) horizontal and (C) rotation

doi: 10.1111/str.12157

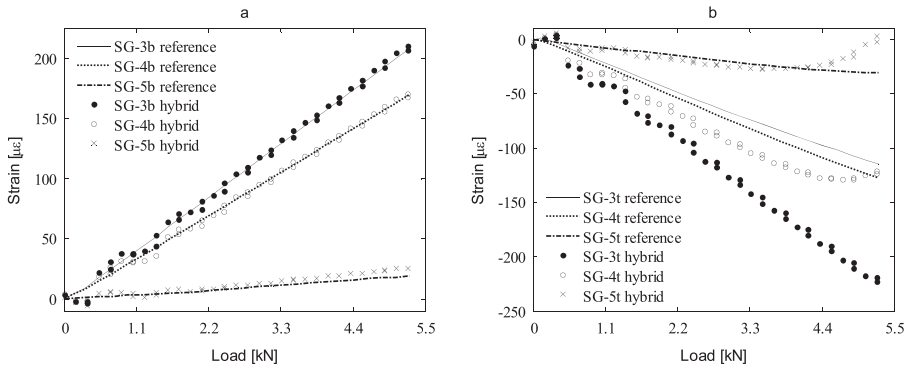

Figure 18: Strain gauge measurements at the experimental substructure: (A) bottom flange and (B) top flange. SG, strain gauge measurement

the point load applied in the reference test. The two remaining strain gauges at the top-flange indicated a non-linear strain induced by buckling (cf. Figure 18B) in the hybrid simulation, which was not the case in the reference test. It is not clear why buckling was introduced before in the hybrid simulation than in the reference test. However, buckling is induced by small imperfections in the geometry, layup, cutting of the slit etc., and these might vary greatly from specimen to specimen. However, the different buckling behaviour is not important in relation to the performance of the hybrid simulation, since this primarily depends on the ability of obtaining the correct overall response and transferring the DOF correctly in the shared boundary.

The emulated structure was designed to yield a non-linear response of the restoring force from the experimental substructure. Although non-linear strains were observed, cf. Figure 18, they were not large enough to yield a non-linear relation between the restoring force and the applied displacement. This implies that the compensators were only investigated in the linear regime. However, the *DIC compensator* is only dependent on the compliance of the load train and will therefore most likely be adequate for non-linear experimental substructure as well.

The DIC compensation technique showed a significant improvement of the beam's overall deflection, with a deviation between the reference test and hybrid simulation going from 33 to 2.6%, cf. Figure 12 while slowing the step speed by 50 ms. This is because the deformations and slack in the test fixture, see Figure 5, are not accounted for when disabling the DIC compensation. This also means that the error between the numerical and experimental substructure in the shared boundary could be decreased by 89% for rotations and 87% for vertical- and 69% for horizontal displacements, cf. Figure 13. This proved that using DIC in an outer control loop to operate the shared boundary is an efficient strategy.

The accuracy of the hybrid simulation was improved through compensation of communication delay. This was done by linear regression, using 3 and 4 previous data points. The 4-point compensator was capable of improving the overall deflection response of the beam from 9.3 to 4.6% cf. Figure 14. The accuracy of compensator was evaluated by comparing the predicted restoring force with the actual restoring force, cf. Figure 15 and Table 5. For both force and moment, the compensator improved the accuracy for the first half period of the loading sequence. But when the external displacement changes direction, the accuracy of the compensator diminished. The loss of accuracy is most likely caused by hysteresis effects in the specimen and test setup.

Conclusion

A static single-component hybrid simulation of a composite beam was performed, and the results were compared to the reference test. In these tests, high correspondence between the hybrid simulation and the reference test was observed, when comparing the overall displacement response along the shared boundary cf. Figure 16 and Figure 17. This verifies the hybrid simulation as a substructural testing technique for the given configuration. This also shows that comparing the hybrid simulation with a reference test is a powerful tool when evaluating hybrid simulation; however, in larger structures, this is not feasible.

In order to increase the accuracy of the physical specimen's stiffness response, communication delay was compensated through linear extrapolation of the previous restoring force as function of external displacement. This increased the accuracy by 2.1%. Furthermore, the deviation between the numerical- and experimental substructure was improved by adjusting the displacement through DIC compensation. This technique improved the accuracy of the vertical, horizontal displacement and rotation by 87, 69 and 89%, respectively. This DIC compensator also improved the accuracy of the overall displacement shape from 33 to 2.6%. This method was introduced because of the high compliance of the load train. The higher

doi: 10.1111/str.12157

compliance and complexity in the load train are due to the test is a single component test that requires a more comprehensive test rig to apply the desired actions in the shared boundary. This is in general not the case in multi-component hybrid simulation where the shared boundary is simple with few DOF.

ACKNOWLEDGEMENTS

The authors would like to acknowledge the financial support from the Danish Centre for Composite Structures and Materials (DCCSM) funded by the Danish Council for Strategic Research within Sustainable Energy and Environment (grant 09-067212). Furthermore, the authors acknowledge Fiberline Composites, Barmstedt Allé 5, 5500 Middelfart, DK, for the donation of the GFRP test specimens.

REFERENCES

1. Jensen, F. M., Falzon, B. G., Ankersen, J., and Stang, H. (2006) Structural testing and numerical simulation of a 34m composite wind turbine blade. *Compos. Struct.* **76**, 52–61.
2. Jensen, F. M. (2008) Ultimate strength of a large wind turbine blade. Department of Civil Engineering, Technical University of Denmark, Kgs. Lyngby.
3. Brondsted, P., Lilholt, H., and Lystrup, A. (2005) Composite materials for wind power turbine blades. *Annu. Rev. Mater. Res.* **35**, 505–538.
4. Takanashi, K., and Nakaschiman, M. (1987) Japanese activities on ON-LINE testing. *J. Eng. Mech.* **113**, 1014–1032.
5. Chen, C., Ricles, J. M., Karavasilis, T. L., Chae, Y., and Sause, R. (2012) Evaluation of a real-time hybrid simulation system for performance evaluation of structures with rate dependent devices subjected to seismic loading. *Eng. Struct.* **35**, 71–82.
6. Bonelli, A., and Bursi, O. S. (2004) Generalized-alpha methods for seismic structural testing. *Earthquake Eng. Struct. Dyn.* **33**, 1067–1102.
7. Karavalis, T. L., Ricles, J. M., Sause, R., and Chen, C. (2011) Experimental evaluation of the seismic performance of steel MRFs with compressed elastomer dampers using large-scale real-time hybrid simulation. *Eng. Struct.* **33**, 1859–1869.
8. Ito, M., Murata, Y., Hoki, K., and Nakashima, M. (2011) Online hybrid test on buildings with stud-type damper made of slitted steel plates stiffened by wood panels. *Procedia Eng.* **14**, 567–571.
9. Jacobsen, A., Hitaka, T., and Nakashima, M. (2010) Online test of building frame with slit-wall dampers capable of condition assessment. *J. Constr. Steel Res.* **66**, 1320–1329.
10. Lin, Y. Z. and Christenson, R. E. (2009) Comparison of real-time hybrid testing with shake table test for an MR damper controlled structure. *American Control Conference*, pp. 5228-5233.
11. Carrion, J. E., Spencer Jr., B. F. and Phillips, B. M. (2009) Real-time hybrid testing of a semi-actively controlled structure with an MR damper. in *American Control Conference*, Hyatt Regency Riverfront, St. Louis, MO, USA.
12. Shao, X., Reinhorn, A. M., and Sivaselvan, M. V. (2011) Real-time hybrid simulation using shake tables and dynamic actuators. *J. Struct. Eng.* **137**, 748–760.
13. Chen, C., Ricles, J. M., Marullo, T. M., and Mercan, O. (2009) Real-time hybrid testing using unconditionally stable explicit CR integration algorithm. *Earthquake Eng. Struct. Dyn.* **38**, 23–44.
14. Waldbjørn, J., Høgh, J., Wittrup-Schmidt, J., Nielsen, M., Branner, K., Stang, H., and Berggreen, C. (2013) Strain and deformation control by fibre Bragg grating and digital image correlation. *Strain.* **50**, 262–273.
15. Fayolle, X., Galloch, S., and Hild, F. (2007) Controlling testing machines with digital image correlation. *Exp. Tech.* **31**, 57–63.
16. Waldbjørn, J., Høgh, J., Berggreen, C., Wittrup-Schmidt, J. and Branner, K. (2013) Hybrid testing of composite structures with single-axis control. in *The 19th International Conference on Composite Materials*, Montreal, Canada.
17. ASTM (2011) Standard test method for tensile properties of polymer matrix composite materials. West Conshohocken, Pennsylvania, United States of America: ASTM International.
18. ASTM (2014) Standard Test Method for Shear Properties of Composite Materials by the V-Notched Beam Method. ASTM International, West Conshohocken, Pennsylvania, United States of America.
19. ANSYS Inc. (2013) ANSYS Mechanical APDL Theory Reference. ANSYS Inc., Canonsburg, PA, USA.
20. Bitter, R., Mohiuddin, T., and Nawrocki, M. (2001) LabView Advanced Programming Techniques. CRC Press, Boca Rotan, Florida, USA.
21. N. Instruments (2009) »http://www.ni.com/pdf/manuals/373781e.pdf,« National Instruments, 8. [Online] accessed the November 12, 2014.
22. N. Instruments (2008) »http://www.ni.com/pdf/manuals/374188d.pdf,« National Instruments, 2. [Online] accessed the November 12, 2014.
23. Juan, E. C. and Billie, F. S. J. (2007) Model-based strategies for real-time hybrid testing. Urbana-Champaign: Illinois Digital Environment for Access to Learning and Scholarship - Dept. of Civil and Environmental Engineering.
24. Legendre, A.-M. (1805) New Methods for the Determination of the Orbits of Comets (in French). F. Didot, Paris.
25. Mahin, S. A., Shing, P.-S. B., Thewalt, C. R., and Hanson, R. D. (1989) Pseudodynamic test method. Current status and future directions. *J. Struct. Eng. N. Y.* **115**, 2113–2128.
26. Shing, P. B., Nakashima, M., and Bursi, O. S. (1996) Application of pseudodynamic test method to structural research. *Earthq. Spectra* **12**, 26–56.

doi: 10.1111/str.12157

Appendix C

Multi-rate Real Time Hybrid Simulation operated on a flexible LabVIEW real-time platform

Jacob P. Waldbjoern*[1], Amin Maghareh[2a], Ge Ou[2b], Shirley J. Dyke[2c] and Henrik Stang[1d]

[1] *Department of Civil Engineering, Technical University of Denmark, Brovej 118, Kgs. Lyngby, Denmark*
[2] *Lyles School of Civil Engineering, Purdue University, 550 Stadium Mall Drive, West Lafayette, IN 47907-2051, USA*

(Received keep as blank , Revised keep as blank , Accepted keep as blank)

Abstract. This paper represents a real-time hybrid simulation (RTHS) strategy where the numerical and experimental substructures are executed at two different rates to optimize computational resources while maintaining good actuator control. The concept is referred to here as multi-rate real-time hybrid simulation (mrRTHS) which is operated on a Laboratory Virtual Engineering Workshop (LabVIEW) real-time target and demonstrated through a single and multiple degree-of-freedom (SDOF) and (MDOF) mass-spring-damper system. The numerical substructure generates a displacement signal with a coarse time step of Δt. Using the current and three previous displacement data points, a finer control signal is defined with a time step of δt, using a third order polynomial algorithm – referred to here as the polynomial fitting extrapolator. Both the numerical substructure and polynomial fitting extrapolator is executed with a sampling rate of Δt by an on-board single-core processor - referred to here as the digital signal processor (DSP). Through a field programmable gate array (FPGA) the control signal is compensated and transmitted to the transfer system through an I/O module with a sampling rate of 1 kHz (i.e. $\delta t = 0.001$sec). The ratio between Δt and δt are an integer - referred to here as the execution ratio. For an execution ratio of 1:5 and 1:10 the system performance is evaluated against a numerical model of the emulated structure – referred to here as the reference. For the SDOF system, a root-mean-square (RMS) error of 7.45% and 7.67% is identified between the mrRTHS and reference for an execution ratio of 1:5 and 1:10 respectively. For the MDOF system, a RMS error of 2.50% and 5.41% is obtained. When changing the execution ratio from 1:5 to 1:10 an approximately 50% reduction of the required computational resources on the DSP is achieved.

Keywords: Real-time hybrid simulation; hardware-in-the-loop; performance evaluation; experimental substructure; numerical substructure; field programmable gate array

---

*Corresponding author, Ph.D. Student, E-mail: jpwa@byg.dtu.dk
[a] Ph.D. Student, E-mail: amaghare@purdue.edu
[b] Ph.D. Student, E-mail: gou@purdue.edu
[c] Professor, E-mail: sdyke@purdue.edu
[d] Professor, E-mail: hs@byg.dtu.dk

1. Introduction

Hybrid simulation is a substructuring technique where a structure of interest is emulated by combining the advantages of numerical modeling with those of experimental testing Shao *et al.* (2011), Bursi *et al.* (2008). Here, the numerical substructure typically includes the majority of the emulated structure which represents either predictable mechanical behavior or is considered uncritical for the analysis conducted. The remainder of the emulated structure is of special interest and is for that reason physically replicated to reveal the effects of e.g. viscoelasticity, buckling, rate dependent properties or other non-linear effects. As a consequence, neither cost-intensive full-scale experiments nor demanding theoretical evaluation procedures are required to reveal the response of the emulated structure Takanashi and Nakaschiman (1987), Carrion and Spencer (2007). The coupling governed through the interface between the numerical and experimental substructure – referred to here as the shared boundary – is achieved by maintaining compatibility and equilibrium at the interface. During the test, a predefined external load is applied the numerical substructure and the corresponding response computed. Through a communication loop, the displacement at the shared boundary is acquired and applied to the experimental substructure through a servo-hydraulic transfer system. The forces required to meet the boundary conditions between the numerical and experimental subassemblies – referred to here as the restoring force – are fed back to the numerical substructure to reveal the response of the emulated structure. The experimental and numerical substructure, communication loop and servo-hydraulic transfer system is combined to form the hybrid simulation.

The research within hybrid simulation has primary been focusing on testing of seismic protection of building structures on either a real-time or extended time-scale Mahin *et al.* (1989), Shing *et al.* (1996), Nakashima *et al.* (1992), Nakashima and Masaoka (1999). Here, the shared boundary between the numerical and experimental substructure typically consists of a set of discrete points with a few degrees-of-freedom (dofs) referred to here as multi-component hybrid simulation. For this application, the load bearing structure is simulated in a numerical model while damping fixtures are tested experimentally including: elastomer Karavalis *et al.* (2011), stud types Ito *et al.* (2011), Jacobsen *et al.* (2010) and magneto-rheological Chen *et al.* (2012), Lin and Christenson (2009), Carrion *et al.* (2009). However, multi-component hybrid simulation is becoming a mature, reliable technology, which opens the opportunity to spread the hybrid simulation technique to other application areas including: large-scale composite structures Williams (2007).

The ambition to improve the structural and operational performance in the wind energy industry Jensen *et al.* (2006) has resulted in extensive research within large-scale and high performance composite structures. In these efforts, testing has primary been focusing on two scales: full scale and coupon material testing Jensen (2008). Full scale testing provides valuable knowledge of the structural behavior; however it requires large laboratory facilities and typically entails significant simplifications of the load configurations applied, compared to the actual loads to which the structure is exposed during service. On the other hand, material characteristics are normally provided through small scale testing performed on specially designed standardized specimens. This approach does not require large laboratory facilities; however it introduces idealized stress and strain states in the test specimens and as a consequence, does not account for the material behavior under complex stress states and interactions between the different materials and joints, bearings and other critical details throughout the structure.

To address shortcomings in full scale and material testing, the hybrid simulation concept is

implemented for large scale composite structures – referred to here as single component hybrid simulation. Single component hybrid simulation is a substructuring technique, capable of evaluating the global response of the emulated structure under the influence of local effects and when exposed to advanced load configurations Waldbjoern *et al.* (2013). However the single component hybrid simulation technique highly complicates the numerical and experimental substructure due to the complex geometry and material characterization. Furthermore, the shared boundary is continuous along the edge which leads to transferring of response in – ideally – an infinite number of contact points, potentially yielding a complex force/displacement distribution in the coupling between the two substructures. Previous research has been carried out within the field of single component hybrid testing on a composite structure with the shared boundary covering; a single discrete point with multiple and single axis control Waldbjoern *et al.* (2013), Hoegh *et al.* (2015). However, both studies only cover the quasi-static regime the relevance of which is somewhat limited given that the significance of structural dynamics is becoming increasingly important as lighter, cheaper, higher and larger structures become more frequent. As a consequence, static testing and analysis have only limited relevance for structures exposed to dynamic loads including wind, earthquake, traffic from vehicles and pedestrians, etc.

Real time hybrid simulation (RTHS) is a useful technique to evaluate the performance of structural dynamics Chen and Ricles (2008). Roughly, the RTHS communication loop can be separated in to two tasks including solving the numerical substructure and operating the shared boundary. Due to the inherent dynamics in the experimental substructure, the shared boundary needs to follow a continuous time history of displacement, velocity or acceleration with a frequency of operation which is 10-25 times higher than the mode of interest Dyke (1996). In conventional RTHS the numerical substructure and shared boundary is operated sequentially at an identical rate. However, given the increased complexity of the numerical substructure within single component hybrid simulation, this execution frequency can be difficult to achieve with the available onboard computational resources due to the implementation of e.g. non-linear effects along with numerous degrees of freedom. Furthermore, the use of commercial FE-software could be of interest Waldbjoern *et al.* (2013), Hoegh *et al.* (2015) which may require access through a network to a remote computer. For all these reasons, the numerical substructure may require an extended integration time, compromising the ability to represent the underlying dynamics of the system. To optimize available computational resources and enhance flexibility to the RTHS architecture, the numerical substructure and shared boundary are executed at two different rates – referred to here as multi-rate real-time hybrid simulation (mrRTHS).

The mrRTHS strategy has been presented previously in the literature by Nakashima and Masaoka (1999), Nakashima (2001). Here, both the numerical substructure and shared boundary are handled through a single core processor using the programming language C. Other platforms capable of handling e.g. Matlab commands exist; however the C language provides the most computationally efficient approach. Continuous real-time loading of the shared boundary is provided through a combined extrapolation and interpolation procedure, inducing a communication delay equivalent to the integration time of the numerical substructure. Furthermore, an irregular step is identified between the last extrapolated points and consecutive interpolated one, as discussed in Bonnet (2006). Alternatives to the mrRTHS exist including parallel real-time computing techniques Maghareh *et al.* (2015). This parallelization of the real-time system enables higher simulation frequency of the numerical model by allowing multiple threads to execute simultaneously across multiple processors Ferry *et al.* (2014).

The scope of this paper is to implement and demonstrate an mrRTHS strategy to extend the

boundaries of existing RTHS systems by optimizing the computational resources. This strategy is operated through a Laboratory Virtual Engineering Workshop (LabVIEW) real-time target capable of providing deterministic and real-time performance for data acquisition and control systems. The numerical substructure is discretized through an explicit state-space representation with a coarse time step of Δt. By the current and 3 previous displacement data points, a finer control signal is generated with a time step of δt, using a third order polynomial algorithm – referred to here as the polynomial fitting extrapolator. Both the numerical substructure and polynomial fitting extrapolator is executed with a sampling rate of Δt by an on-board single-core processor – referred to here as the digital signal processor (DSP). Through a field programmable gate array (FPGA) the control signal is compensated through a feedforward (FF) compensator and transmitted to the transfer system through an I/O module with a time step of δt. Thus the tasks related to the numerical substructure and shared boundary is dedicated its own processor to allocate computationally independent and separated resources. The ratio between Δt and δt is an integer - referred to here as the execution ratio. The mrRTHS strategy is demonstrated through a single and multiple degree-of-freedom (SDOF) and (MDOF) mass-spring-damper system in order to reduce the complexity in verifying the software capabilities when handling the test response and theory. The system characterization is identified and a suitable delay compensation scheme implemented to account for communication delay and dynamics in the transfer system. The mrRTHS communication loop is tested and verified against a numerical model of the emulated structure – referred to here as the reference.

2. mrRTHS communication loop

2.1 Configuration for mrRTHS

The overall architecture of the mrRTHS communication loop includes a transfer system and two loops named main- and outer-loop, which are handled in a producer/consumer configuration Bitter *et al.* (2001). The outline of the dataflow in the mrRTHS communication loop is separated in 9 units labeled from **(1)** to **(9)** presented in Fig. 1.

The mrRTHS communication loop is operated through a CompactRIO 9074 (cRIO – 9074) NI (2014) including the FPGA and 400MHz onboard single-core processor – referred to here as the Digital Signal Processor (DSP). The FPGA offers high reliability and determinism given that all logics are compiled to the physical hardware, and for that reason, does not utilize any overarching operating systems. However, this comes with the tradeoff of having a relatively small amount of memory available on the FPGA, implying a limited complexity of the on-board algorithm. The interface between the mrRTHS communication loop and transfer system is handled through a digital to analog (NI9263) NI (2009) and analog to digital (NI9205) NI (2008) I/O module. The cRIO – 9074 and I/O modules combine to form the real time target.

The main-loop is operated through the DSP with a coarse time step of Δt. Here the numerical substructure in **(1)** computes the next step displacement signal $d_{num}(t)$ based on the external load and last available restoring force $F_{res}(t\text{-}i)$. Through the current and previous data points provided by **(1)**, the predicted system response after the communication delay is identified as the displacement signal $d_{pred}(t)$ in **(2)**. Between each data point provided by **(2)** the displacement signal is resampled through extrapolation $d_{exp}(t+i)$ in **(3)** with the time increment δt for $i \in [0;\Delta t]$. The delay compensation in **(2)** and polynomial fitting extrapolator in **(3)** are both handled by a 3rd order

polynomial algorithm, further described in section 3.2.

The outer-loop is operated through the FPGA with an execution rate of 1 kHz (i.e. δt = 0.001sec) allowing the shared boundary to handle frequencies of up to 100 Hz Dyke (1996). Here the actuator displacement after the delay/lags, associated with the dynamics of the transfer system, is predicted to generate the command displacement $d_{com}(t)$ through a FF compensator in **(4)**. Further details of the FF compensator in **(4)** are given in section 3.1. From the data points provided by **(4)** an equivalent DC voltage $V_{com}(t)$ is generated in **(5)** to operate the transfer system. The corresponding restoring force $V_{res}(t)$ are acquired from the transfer system and converted to a digital signal in **(9)**.

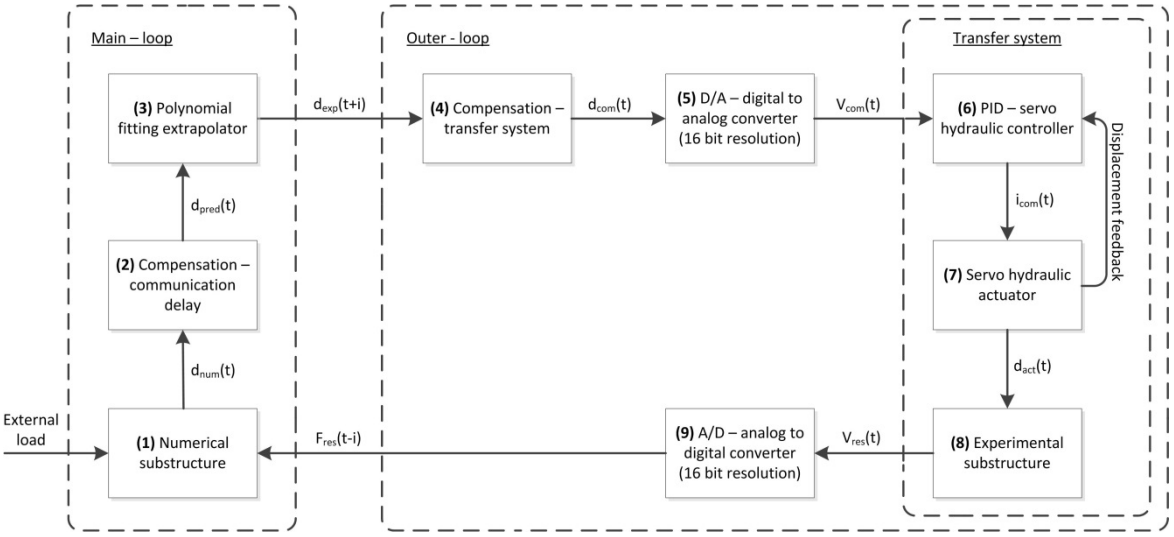

Fig. 1 Schematic block diagram representing the overall architecture for the mrRTHS communication loop

The transfer system is operated by transmitting the real-time command signal $V_{com}(t)$ to a digital proportional-integral-derivative (PID) controller model: Shore Western SC6000 in **(6)**. To prevent data loss due to under sampling, the execution rate of the transfer system F_{PID} is set equal to or higher than the outer-loop (i.e. 1 kHz $\leq F_{PID}$). Through the PID controller, an electrical current $I_{com}(t)$ is generated to operate a Schenck-Pegasus 162M servo-valve with a capacity of 15 GPM at 3000psi in **(7)**. The servo valve is connected to a Shore Western 910D-77-6-4-348 actuator with a 152.4mm (6.0 inch) stroke and 4.89kN (1.1kip) force capacity. The actuator displacement $d_{act}(t)$ is measured through an internal LVDT model: G.L Collins, LMT-711P34 and the associated restoring force monitored by a Omega S-beam load cell model: LCM101-2K (S/N 245518) with a capacity of ±8.89kN (±2 kips). The experimental substructure in **(8)** consists of a spring with the stiffness k_e, further defined in Table 1. The standard uncertainty of the repeatability offered by the transfer system is given by: $8.5 \cdot 10^{-3}$mm and 6.81N. The repeatability is identified from a sample of 100000 measurements, acquired under constant conditions with a sampling frequency of 1 kHz.

2.2 Communication interface between main- and outer-loop

The interface between the main- and outer-loop is handled through a dual channel Direct Memory Access (DMA) First-In-First-Out (FIFO) configuration Ashasi-Sorkhabi and Mercan (2014). Here the data received from the extrapolator algorithm in **(3)** and restoring force in **(9)** is buffered and exchanged between the two loops cf. Fig. 1. A schematic of the main- and outer-loop switching logic are outlined in Fig. 2, separated in an initiating, running and completion sequence. The initiating and completion sequence represents the first and last main-loop time step respectively. The running sequence represents the switching logic for the remaining duration of the mrRTHS. For demonstration purposes, only a couple of main-loop time steps are represented cf. Fig. 2.

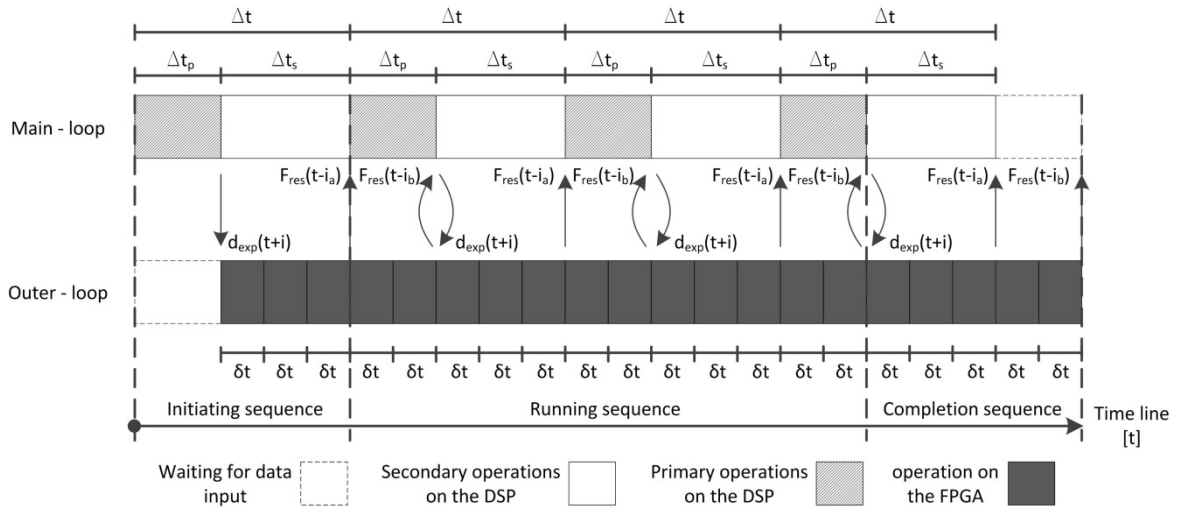

Fig. 2 Schematic of the main- and outer-loop switching logic for an execution ratio of 1:5

The numerical substructure, communication delay compensator and extrapolated displacement signal $d_{exp}(t+i)$ are computed in the main-loop through primary operations for the duration of Δt_p and buffered in the DMA FIFO. When the primary operations of the DSP are completed, the secondary tasks include: file manipulation, TCP/IP communication, etc. is handled for the duration of Δt_s. The total time step of the main loop Δt is identified as the sum of Δt_p and Δt_s cf. Fig. 2. In parallel the FPGA is emptying and processing the received displacement signal while buffering the corresponding restoring force $F_{res}(t-i)$ in the DMA FIFO with a time increment of δt for $i \in [0;\Delta t]$. Given that $\Delta t_p > 0$, a communication delay is included given that only $F_{res}(t-i_a)$ for $i_a \in [\Delta t_p;\Delta t]$ is available in the DMA FIFO when the next displacement signal is computed. While the primary operation in the main-loop is completing, the remaining restoring forces $F_{res}(t-i_b)$ in the DMA FIFO for $i_b \in [0;\Delta t_p]$ is acquired and the next extrapolated displacement signal $d_{ext}(t+i)$ returned for the upcoming main-loop iteration. The duration of Δt_p is regulated by the available computational resources of the DSP and the complexity of the primary operations in the main-loop algorithm.

2.3 Communication interface between main- and outer-loop

The main framework for the mrRTHS platform is divided into 5 units labeled from **(1)** to **(5)** in Fig. 3. Here, the host application in **(1)** operates the user interface along with data storage and external load. This is done through a master computer (personal computer) which typically comprises ample onboard memory and computational resources. Through a TCP/IP communication, the master computer continuously transmits the predefined external load and user defined inputs, while receiving feedback to and from **(2)** in the main-loop. This configuration is required due to the limited on-board memory available on the cRIO – 9074.

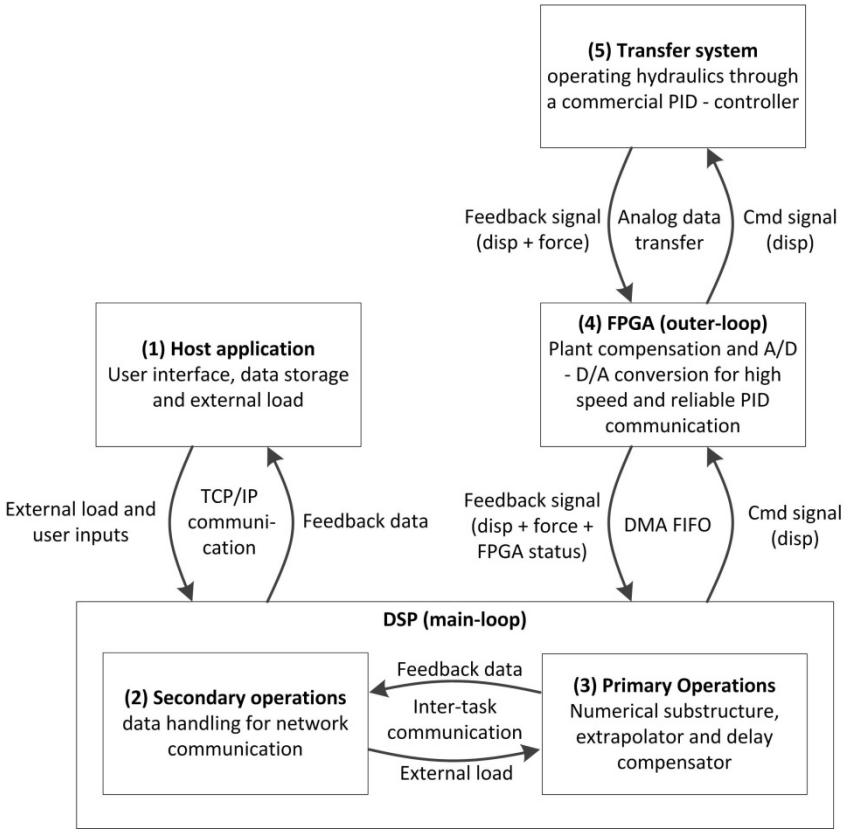

Fig. 3 The main framework of the mrRTHS software

The main-loop is divided into a secondary **(2)** and primary **(3)** portion, both operated by the DSP as outlined in Fig. 3. The interface between **(2)** and **(3)** are provided through a producer/consumer configuration Bitter *et al.* (2001), where **(2)** consists of two separate while loops: a) producer loop that transmits the feedback data to **(1)** and b) consumer loop that receives the external load from **(1)**. The primary operation by **(3)** is handled through a single while loop which both transmits the feedback data and receive the external load to and from **(2)**. To reduce jittering and optimize the computational resources of the DSP, each of the three while loops in the

main-loop are assigned the following order of priority: a) deterministic loop in **(3)**, b) consumer loop in **(2)** and c) producer loop in **(2)**. By prioritizing each task, it is ensured that the secondary operations in **(2)** are halted whenever computational resources are needed for primary operations in **(3)**. Furthermore, the flow of external load is prioritized ahead of feedback data.

The outer-loop is handled in **(4)** operated by the FPGA as outlined in Fig. 3. Here the interface between the main-loop and outer-loop is established through the DMA FIFO as clarified in section 2.2. The displacement signal from the numerical model is transmitted from **(3)** to **(4)** for further processing and the feedback signal returned for monitoring of the system response. Given the fast execution rate and high reliability of the FPGA, interlocks are here implemented to prevent damage to the transfer system and its surroundings. The transfer system is operated through the I/O modules which offer a high speed and reliable analogue data transfer. Here the displacement signal is transmitted from **(4)** to **(5)** and corresponding feedback data received including measured displacement and restoring force.

3. System characterization

3.1 Actuator dynamics

The dynamics of the entire transfer system including servo-hydraulic actuator, PID controller and experimental substructure, represent a significant source of time delay/lags in the RTHS communication loop Carrion and Spencer (2007). Thus, compensation is crucial to ensure accuracy and stability of the RTHS Horiuchi *et al.* (1996). To understand the system behavior in a wide range of frequencies and amplitudes, open loop system identification is performed through a band-limited white noise with a frequency ranging from 0 to 15Hz and a root-mean-square (RMS) of 0.25mm. Based on an obtained data series of 300000 measurements, acquired with a sampling rate of 1 kHz, the system identification in the frequency domain are given in Fig. 4.

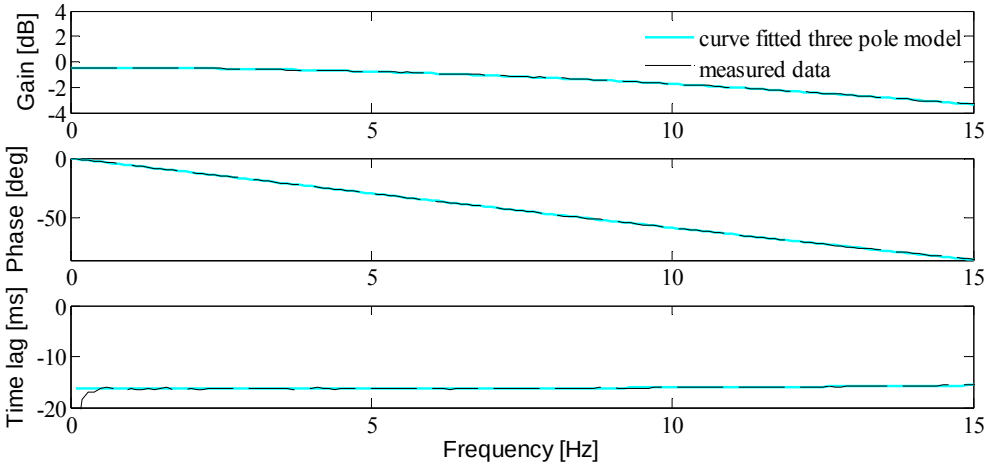

Fig. 4 System identification in the frequency domain – open loop transfer function

The magnitude is demonstrating an undershooting in the entire bandwidth, which is nearly constant in the range: 0-4Hz. In the remaining frequency domain, the magnitude starts to roll off as a function of the frequency. The phase of the dynamic system is nearly linear throughout the entire bandwidth, resulting in a constant time lag of approximately 16.4ms. A three pole model is found sufficient to accurately represent the dynamics over the entire frequency range: 0-15Hz cf. Fig. 4. The curve fitted continuous transfer function $G_a(s)$ is presented in the frequency domain *s* in Eq. (1).

$$G_a(s) = \frac{5.163 \cdot 10^6}{s^3 + 530.8s^2 + 8.899 \cdot 10^4 s + 5.44 \cdot 10^6} \tag{1}$$

To cancel the dynamics of the transfer system over the frequency range of interest, a FF compensator is implemented Ellis (2000). For an SDOF system where only a single eigenfrequency of 1.00Hz is present cf. Table 1, a direct inverted first order compensator is deemed sufficient. The discrete first order direct inverted compensator $K_a(z)$ is presented in the *z*-domain by Eq. (2).

$$K_a(z) = \frac{\alpha z - (\alpha - 1)}{z} \tag{2}$$

Here α is calibrated so that the measured and desired displacement correlate in the frequency range of interest. This calibration process is conducted through an open loop sinusoidal reference signal. For the MDOF system the eigenfrequency ranges from 1.77 – 7.71Hz cf. Table 1, meaning that a higher order transfer function is required to ensure good performance in the entire frequency range of interest. Given that a three pole model accurately represents the dynamics of the transfer system cf. Fig. 4, a discrete third order inverted compensator Phillips and Spencer (2011) is implemented in the time domain *t* - presented by Eq. (3).

$$K_a(t) = a_0 r(t) + a_1 \dot{r}(t) + a_2 \ddot{r}(t) + a_3 \dddot{r}(t) \tag{3}$$

Here, the coefficients a_0 through a_3 are given by Eq. (1) and the dots denote differentiation of the desired displacement *r* with respect to time *t*. The closed loop performance of the first and third order compensators is outlined in Fig. 11 and 13, respectively.

3.2 Communication delay and extrapolation

Both communication delay and extrapolation are handled through an algorithm capable of predicting the desired displacement. Various forward prediction schemes have been investigated for the use in mrRTHS Maghareh *et al.* (2015). In this study, the polynomial fitting extrapolator (third order polynomial algorithm) is selected for further analysis due to the minimal computational resources needed to run the algorithm, making it well suited for real time analysis. By the use of the current and 3 previous data points provided with a time step of ΔT, the control signal is extrapolated with a predefined time step *t* in Eq. (4).

$$d_{\exp} = \sum_{i=0}^{N} a_i d_i \tag{4}$$

Here N, d_i and a_i represent the order of the algorithm (i.e. N = 3), the current and 3 previous data points with the time step $\triangle$T and polynomial coefficients generated through the Lagrange formula, respectively. For a fully independent relation between t and $\triangle$T, the polynomial coefficients a_i are given by Eqs. (5)-(8) cf. Bonnet (2006).

$$a_0 = \frac{t}{\Delta T}\left(\frac{11}{6} + \frac{t}{\Delta T} + \frac{1}{6}\left(\frac{t}{\Delta T}\right)^2\right) \tag{5}$$

$$a_1 = -\frac{t}{\Delta T}\left(3 + \frac{5}{2}\frac{t}{\Delta T} + \frac{1}{2}\left(\frac{t}{\Delta T}\right)^2\right) \tag{6}$$

$$a_2 = \frac{t}{\Delta T}\left(\frac{3}{2} + 2\frac{t}{\Delta T} + \frac{1}{2}\left(\frac{t}{\Delta T}\right)^2\right) \tag{7}$$

$$a_3 = -\frac{t}{\Delta T}\left(\frac{1}{3} + \frac{1}{2}\frac{t}{\Delta T} + \frac{1}{6}\left(\frac{t}{\Delta T}\right)^2\right) \tag{8}$$

Compensation of the communication delay $d_{pred}(t)$ is achieved for $t = \Delta t_p$ cf. Fig. 2. Here, d_i is the current and 3 previous data points provided by the numerical substructure $d_{num}(t)$. The extrapolated displacement signal $d_{exp}(t+i)$ is generated with a time step of $t = \delta t$ for $i \in [0;\Delta t]$ and d_i the current and 3 previous data points provided by $d_{pred}(t)$.

The performance of the polynomial fitting extrapolator is investigated through a chirp sinusoidal wave with a linearly increasing frequency ranging from 0 to 10 Hz for the duration of 10 seconds and constant amplitude of 3.81mm. The signal is generated with two different sampling rates including: 100Hz and 1 kHz named under sampled and desired signal respectively. With an execution ratio of 1:10, the under sampled signal is resampled through extrapolation $d_{exp}(t)$ and compared with the desired signal – referred to here as desired cf. Fig. 5.

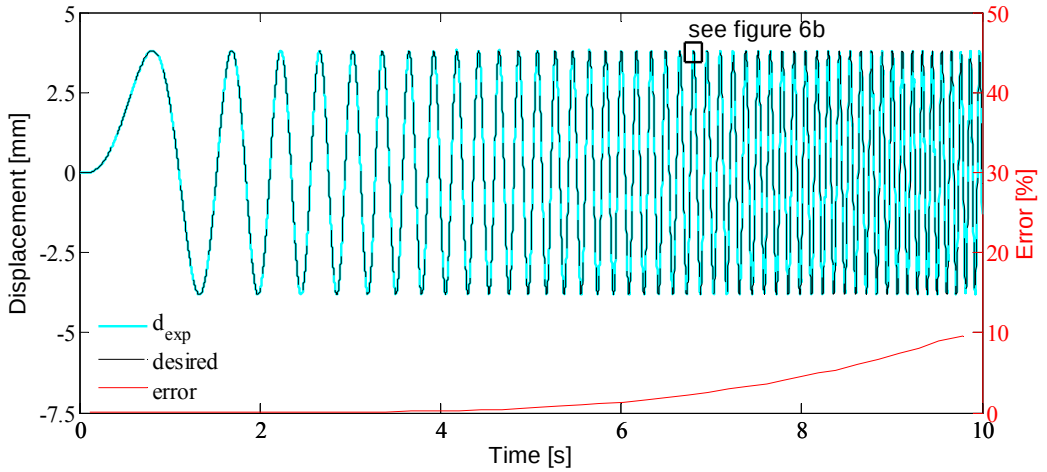

Fig. 5 Extrapolation performance with a chirped sine wave in the domain 0-10Hz and execution rate 1:10

Here the error is presented as the relative deviation between the extrapolated $d_{exp}(t)$ and desired signal cf. Eq. (9). To smooth the presented error output, only the peak error within each displacement period is presented.

$$Error(t) = \frac{\left| d_{\exp}(t) - desired(t) \right|}{\max\left(\left| desired(t) \right| \right)} \cdot 100 \tag{9}$$

The same approach is used for other execution ratios, and the corresponding error presented in Fig. 6(a). From Fig. 5 and 6a the error between the extrapolated and desired signal is related to the execution ratio and frequency (acceleration). In Fig. 6(b), a detail of the desired signal and corresponding extrapolated signal is presented. Here, the error between the extrapolated and desired signal is gradually increasing as a function of time. For that reason, an irregular step (discontinuity) is bound to happen between the last extrapolated point $d_{exp}(t)$ and consecutive displacement signal $d_{pred}(t)$.

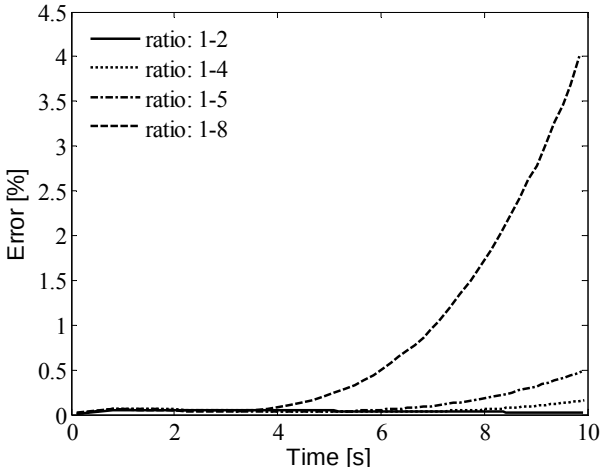

(a) Error between the desired and extrapolated signal

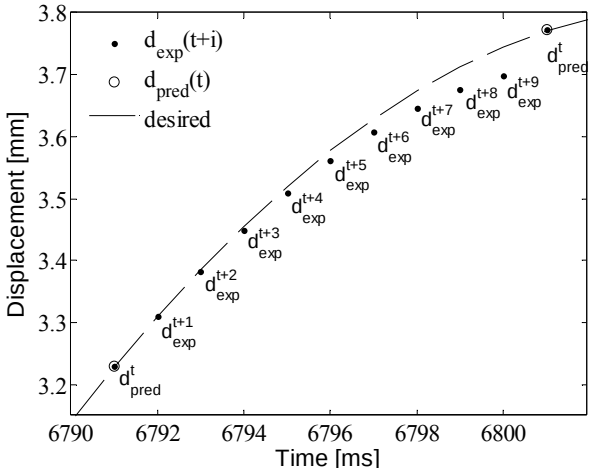

(b) Correlation details

Fig. 6 Chirped sine wave in the domain 0-10Hz

Increasing the order of the polynomial fitting extrapolator improves the performance in the higher frequency domain; however this comes with the trade-off of increased: a) vulnerability to system noise and b) required computational resources. Thus, we chose not to increase the order of the polynomial any further.

4. Emulated structure and shared boundary

The emulated structure consists of an SDOF and MDOF mass-spring-damper system loaded by the external load g_{acc} cf. Fig. 7(a) and 7(b). The spring stiffness k_e is represented as the experimental substructure while the remainder of the emulated structure is discretized through an explicit state-space representation. The shared boundary is further clarified in Fig. 7(c).

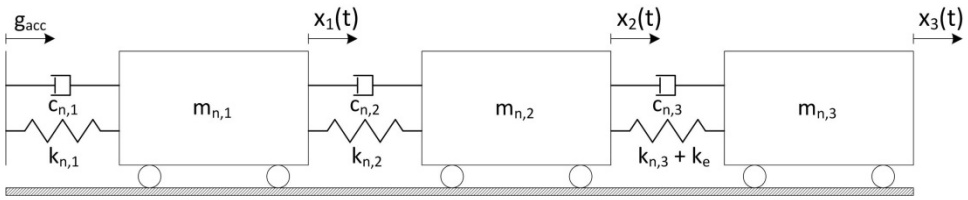

(a) MDOF system

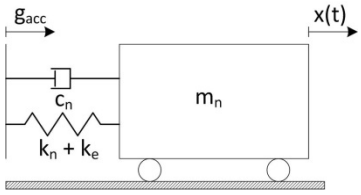

(b) SDOF system

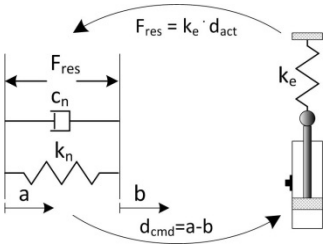

(c) Details of the shared boundary

Fig. 7 Schematic of the emulated structure and shared boundary

To conduct a successful mrRTHS, global stability and performance are the major issues. In Maghareh *et al.* (2014a) and Maghareh *et al.* (2014b), predictive stability and performance indicators (PSI and PPI) have been developed to assess the sensitivity of an RTHS configuration to any phase discrepancy at the shared boundary resulting from transfer system dynamics and computation/communication delays. These metrics predict how transfer system dynamics and computation/communication delays, which are significant sources of systematic experimental error in RTHS, distort RTHS responses and how the corresponding error propagates through the entire simulation and may de-stabilize the system. Thus, PPI and PSI are used here to design a successful RTHS configuration from a stability and performance perspectives. Using PSI and PPI, the design of a successful RTHS is provided in Fig. 8. On the basis of the PSI and PPI indicators outlined in Fig. 8, SDOF and MDOF mrRTHS configurations are defined as presented in Table 1.

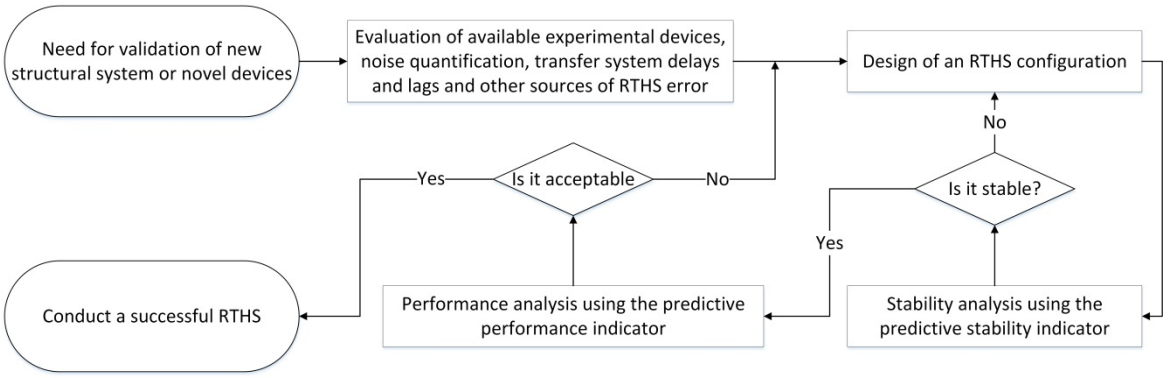

Fig. 8 Design flow of a successful real-time hybrid simulation

Table 1 Structural parameters of the numerical and experimental substructures for the mrRTHS

Structure [-]	Module [-]	m_n [kg]	c_n [N·sec/m]	k_n [kN/m]	k_e [kN/m]	Mode [-]	Modal period [Hz]	Mode damping [%]
MDOF	1	440	880	275	-	1	1.77	1.78
	2	440	880	275	-	2	4.96	4.99
	3	440	880	165	110	3	7.17	7.21
SDOF	1	630	2370	110	110	1	1.00	2.99

5. Test results

The mass-spring-damper systems are tested in SDOF and MDOF configurations for the duration of 70 sec. Here the mrRTHS architecture is evaluated using the normalized relative error between the mrRTHS and reference presented in Eq. (10).

$$Error(t) = \frac{|mrRTHS(t) - REF(t)|}{\max(|REF(t)|)} \cdot 100 \tag{10}$$

The system is loaded by the Chichi earthquake – referred to here as the external load g_{acc}. The external load is showed in Fig. 9 for both the SDOF and MDOF mrRTHS. The magnitude of the load is adjusted to achieve a maximum displacement of the shared boundary of approximately 3.81mm.

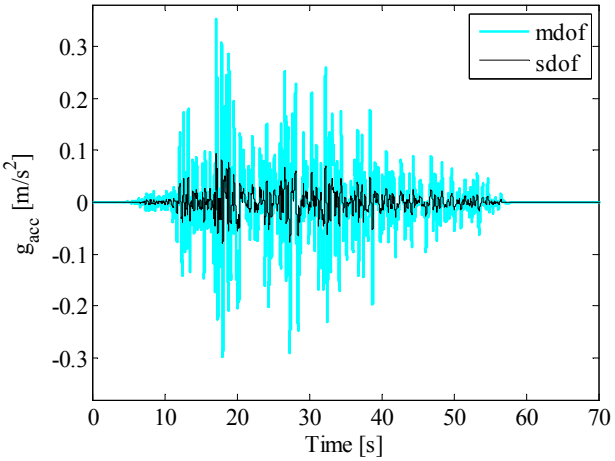

Fig. 9 Chichi earthquake applied on the SDOF and MDOF system

The stiffness ratio between k_n and k_e at the shared boundary is set to 50% and 66% for the SDOF and MDOF configurations, respectively cf. Table 1.

The performance of the mrRTHS architecture is demonstrated in both cases for an execution

ratio of 1:5 and 1:10 with the outer loop running at a constant rate of 1kHz (i.e. $\delta t = 0.001$sec).

5.1 SDOF mrRTHS

For the SDOF mass-spring-damper system, the relative displacement x(t) (see Fig. 7(b)) is presented for the mrRTHS and reference for an execution ratio of 1:5 and 1:10 in Fig. 10. The corresponding relatively error between the mrRTHS and reference are determined cf. Eq. 10. The time step of the primary operation of the main loop Δt_p is 1ms. The computational complexity of the main-loop causes the DSP to operate at 69% and 35% of the full capacity for an execution ratio of 1:5 and 1:10, respectively. For that reason, by reducing the sampling frequency of the main loop by 50%, an equivalent reduction of the computational resources on the DSP is achieved. From Fig. 10, the relationship between the amplitude of the displacement x(t) and relative error between the mrRTHS and reference is identified. Here, it appear that an increasing amplitude amplifies the error. When the external load ceases after approximately 55 sec cf. Fig. 9, the freely oscillating system will gradually decay with a frequency equal to the modal period. However, due to actuator dynamics and communication delay, the damping of the mrRTHS is lower than the reference, causing the error to gradually magnify during the free oscillation period.

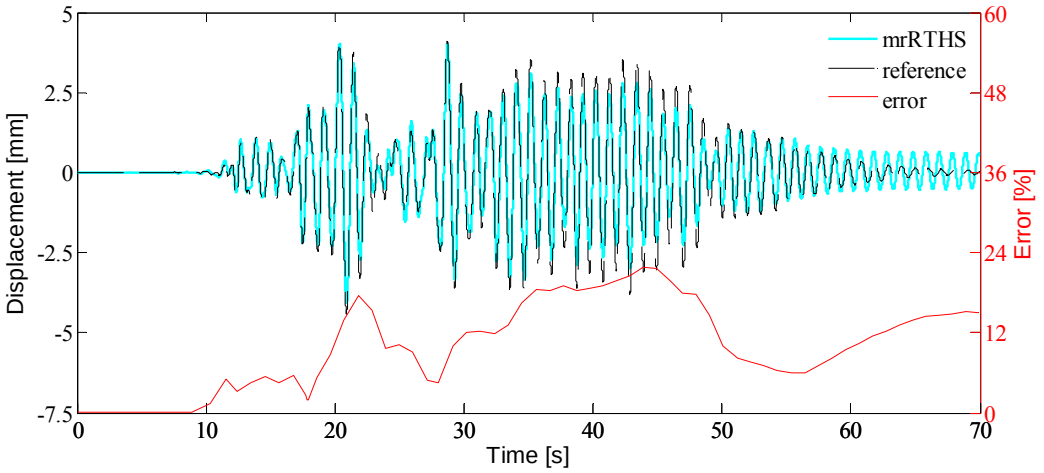

(a) Execution ratio 1:5

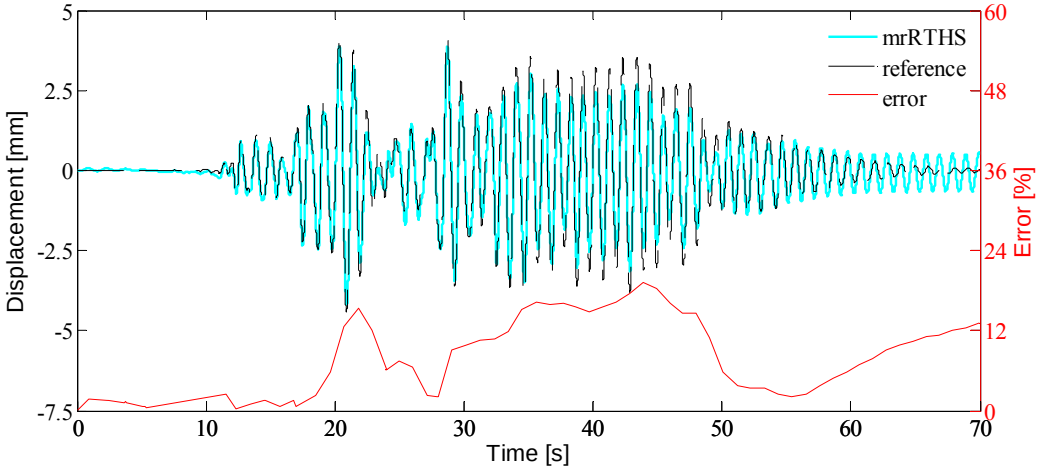

(b) Execution ratio 1:10

Fig. 10 Displacement response and error for the SDOF system

The corresponding actuator performance in the time domain for both execution ratios are presented in Fig. 11. Here, a sound correlation between the desired and measured displacement of the actuator is identified, indicating that the single-order FF compensator is adequate for the given application.

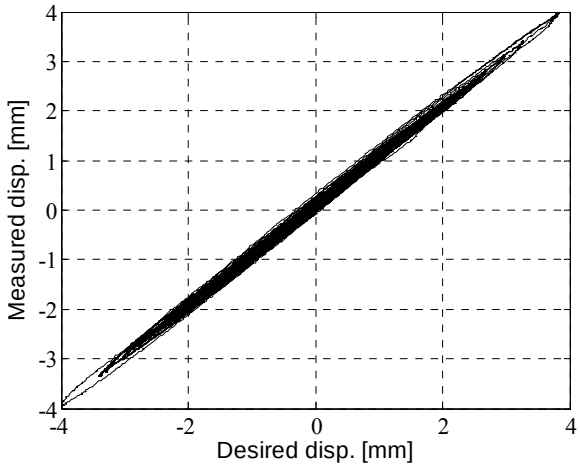

(a) Execution ratio 1:5

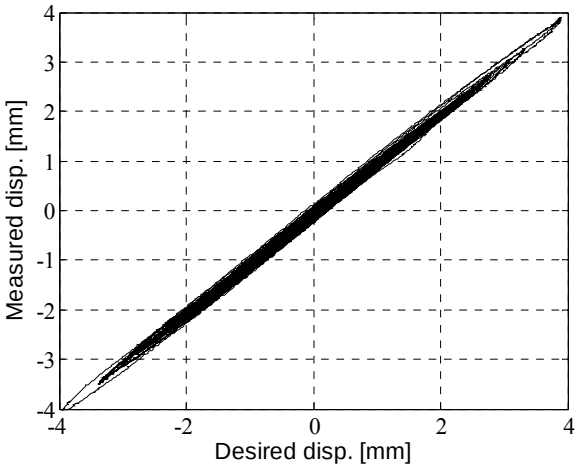

(b) Execution ratio 1:10

Fig. 11 Time domain comparison of actuator performance with the single-order FF controller

In Table 2, the RMS and peak error between the mrRTHS and reference are presented for execution ratios of 1:5 and 1:10. To isolate the error induced by the extrapolation algorithm through the communication delay compensator and extrapolation procedure, the experimental substructure is substituted by a numerical model – referred to here as numerical mrRTHS. With this modification, the experimental errors including transfer system dynamics, sensor miscalibration, measurement noise and random truncations in the analogue-to-digital (AD) conversion of the signal are eliminated.

Table 2 RMS and peak error obtained through SDOF mrRTHS and numerical mrRTHS

Execution ratio [-]	mrRTHS RMS error [%]	Num. mrRTHS RMS error [%]	mrRTHS peak error [%]	Num. mrRTHS peak error [%]
5	7.45	1.10	20.64	3.21
10	7.67	1.15	21.82	3.33

From Table 2, approximately 15% of the RMS and peak error are generated by the extrapolation procedure for both execution ratios, meaning that other sources of errors – also present in conventional RTHS – comprise the remaining 85% of the total error. Furthermore, by increasing the execution ratio from 1:5 to 1:10, a 50% reduction of the computational resources of the DSP is achieved, with the tradeoff of increasing the error between the mrRTHS and reference by approximately 4%.

5.2 MDOF mrRTHS

For the MDOF mass-spring-damper system, the displacement $x_3(t)$ relative to the ground (see Fig. 7(a)) are presented for the mrRTHS and reference for execution ratios of 1:5 and 1:10 in Fig. 12. Note that the displacement of the shared boundary - given by $x_3(t)$-$x_2(t)$ cf. Fig. 7(a) - is on the

same order as the displacement of the SDOF system. The corresponding relatively error between the mrRTHS and reference are determined cf. Eq. 10. The time step of the primary operation of the main loop Δt_p is for the MDOF configuration 2ms due to the enhanced complexity of the numerical substructure. Furthermore the work load of the DSP is 75% and 38% of the full capacity for execution ratios of 1:5 and 1:10. For that reason, by reducing the frequency of the main loop by 50% an equivalent reduction of the computational resources on the DSP is achieved. From Fig. 12, the relation between the amplitude of the displacement $x_3(t)$ and relatively error between the mrRTHS and reference is found to be identical to the SDOF system. However, due to the increased magnitude of displacement, the error is reduced relative to the SDOF system cf. Eq. (10).

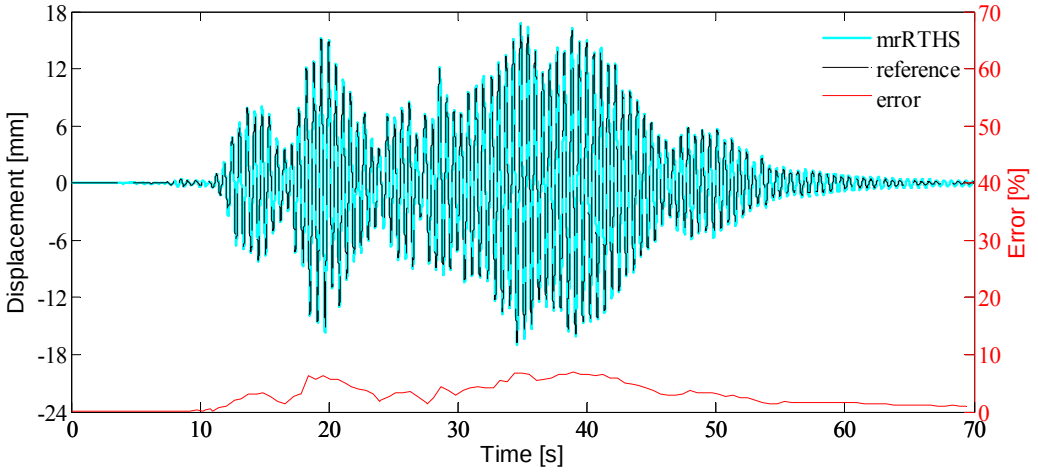

(a) Execution ratio 1:5

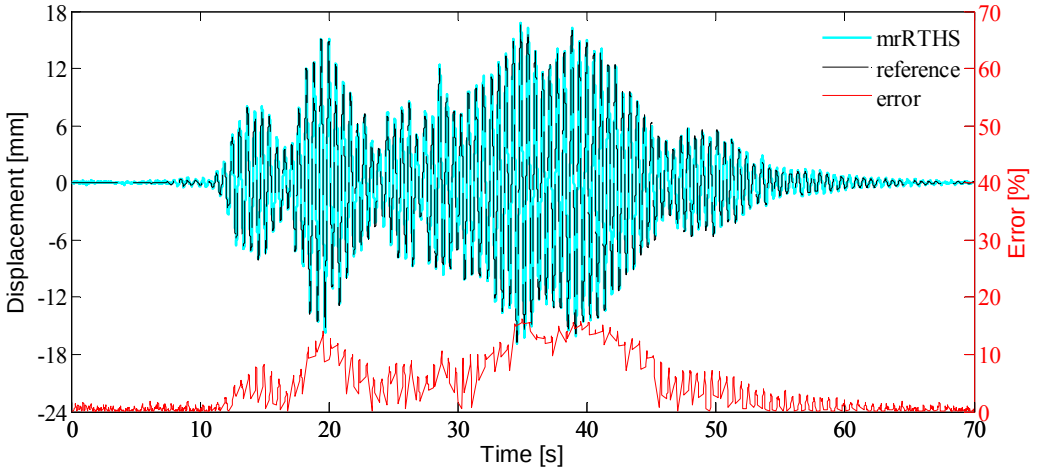

(b) Execution ratio 1:10

Fig. 12 Displacement response and error for the MDOF system

The corresponding actuator performance in the time domain for both execution ratios are presented in Fig. 13. Here a sound correlation between the desired and measured displacement of the actuator is identified for an execution ratio of 1:5, indicating that the third-order FF compensator is adequate for the given application. However when the execution ratio is increased to 1:10 some major inconsistencies between the desired and measured displacement is observed. This outcome is probably caused by the instability induced by the irregular step between the last extrapolated point $d_{exp}(t)$ and consecutive displacement signal $d_{pred}(t)$, see Fig. 6(b). This instability does likewise appear in the error represented in Fig. 12(b). In Table 3 the RMS and peak error between the mrRTHS and reference along with the numerical mrRTHS and reference are presented for execution ratios of 1:5 and 1:10.

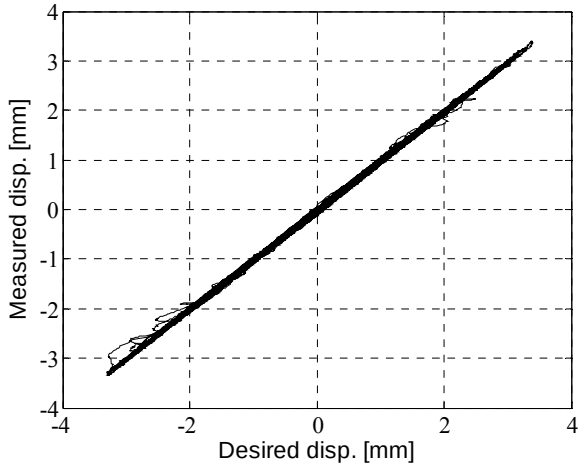

(a) Execution ratio 1:5

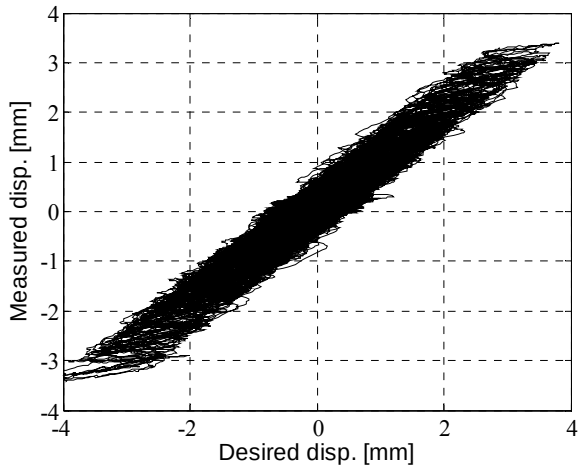

(b) Execution ratio 1:10

Fig. 13 Time domain comparison of actuator performance with the third-order FF controller

Table 3 RMS and peak error obtained through MDOF mrRTHS and numerical mrRTHS

Execution ratio [-]	mrRTHS RMS error [%]	Num. mrRTHS RMS error [%]	mrRTHS peak error [%]	Num. mrRTHS peak error [%]
5	2.50	0.70	7.14	2.07
10	5.41	1.77	16.05	5.12

From Table 3, approximately 30% of the RMS and peak error is generated by the extrapolation procedure for both execution ratios, meaning that other sources of error – also present in conventional RTHS – comprise the remaining 70% of the total error. It is noted that this error is identified to be 15% for the SDOF system. However due to the increase in frequency, the error induced by the extrapolation procedure will increase cf. Fig. 6(a). When the execution ratio is increased from 1:5 to 1:10, a 50% reduction of the computational resources is achieved; however this comes with a 60% increase in the error between the mrRTHS and reference. Compared with the SDOF system, this is a significant increase in the error induced by the extrapolation procedure. A reduction of this error could be achieved by using a different or higher order polynomial fitting extrapolator.

6. Dicussion

The polynomial fitting extrapolator is implemented to handle both the communication delay and extrapolation procedure in the main loop. This algorithm consumes very little computational resources, making it suitable for real time hybrid simulation, especially for low-cost execution. However, for an increasing execution ratio and/or sampling frequency, the error induced by the polynomial fitting extrapolator leads to a reduced correlation between the mrRTHS and reference cf. Fig. 6(a). Increasing the order of the polynomial fitting extrapolator enables the algorithm to handle higher frequencies; however, that comes with an enhanced vulnerability to system noise and required computation resources. Other applicable extrapolation algorithms exists including least-square polynomial fitting, linearly predicted acceleration scheme and multi-rate linear compensation cf. Maghareh *et al.* (2015). From Maghareh *et al.* (2015) the performance of the least-square polynomial fitting is found identical to the polynomial fitting extrapolator while the linearly predicted acceleration scheme only exhibits improved performance for an execution ratio below 1:5. The multi-rate linear compensator provides significantly better performance relative to the polynomial fitting extrapolator for both execution ratios of interest; however this performance comes with the cost of significantly higher computational resources.

Between each data point provided by the numerical substructure, a finer displacement signal is generated through extrapolation. This approach provides a relatively short communication delay equivalent to the duration of the primary operations on the DSP Δt_p which is 1-2ms in the applied case. Other publications concerning mrRTHS combine extrapolation/interpolation to generate the displacement signal handled in the outer loop cf. Nakashima and Masaoka (1999), Nakashima (2001) and Bonnet (2006). Through this method, extrapolation is performed until the numerical model is computed and the next displacement signal identified – which is equivalent to the duration of Δt_p in the applied case. The remaining portion of the finer displacement signal, equivalent to the duration of Δt_s in the applied case, is generated by interpolation. The communication delay is for that reason given by the time step of the main loop, which in the applied case is 10ms. Pure extrapolation provides for that reason a reduced communication delay

relative to the combined extrapolation/interpolation procedure. However, given that the error is gradually increasing during each extrapolation sequence cf. Fig. 6(b), and an irregular step is bound between the last extrapolated point and consecutive displacement signal; a limited number of extrapolation points would be preferable.

To ensure continuous real-time loading of the shared boundary, displacement signals must be available in the outer-loop at all times. For the applied configuration of the main- and outer-loop switching logic, the number of extrapolated points is deemed consistent throughout the entire duration of the mrRTHS. For that reason, only explicit numerical models which exhibit a consistent and predictable integration time can be handled in this configuration to satisfy the explicit deadlines in the switching logic between the main- and outer-loop. To allow implicit numerical models, the number of extrapolated points has to vary depending on the current integration time. This could be achieved by making an estimate of the number of extrapolated points, followed by either erasing or adding additional extrapolated points if the integration time of the numerical model is shorter or longer than estimated.

7. Conclusion

An mrRTHS configuration was implemented on a LabVIEW real-time target model: cRIO – 9074, capable of operating the numerical and experimental substructure at two different rates to optimize computational resources while maintaining good actuator control. The system proved that by reducing the execution rate of the numerical substructure by 50% an equivalent reduction of the computational resources on the DSP were achieved. This proves the mrRTHS configuration as an effective method in optimizing the computational resources, extending the capabilities of existing RTHS systems.

The mrRTHS was demonstrated through an SDOF and MDOF mass-spring-damping system and the performance evaluated against the corresponding reference. For the SDOF configuration relative RMS errors of 7.45% and 7.67% were identified between the mrRTHS and reference for an execution ratio of 1:5 and 1:10, respectively. The same RMS errors were identified to 2.50% and 5.41% for the MDOF configuration. Due to the magnification of the amplitude for the MDOF configuration relative to the SDOF system, a reduction of the RMS error was identified. By reducing the frequency of the main loop with 50% an equivalent reduction of the computational resources on the DSP were achieved. These savings in computational resources came with the tradeoff of a 4% and 60% increase in the error between the mrRTHS and reference for the SDOF and MDOF configurations, respectively.

The error induced by the polynomial fitting extrapolator was found to include an irregular step between the last extrapolated point and consecutive displacement signal. This discontinuity introduced some chattering in the system which became distinct for the MDOF system with an execution ratio of 1:10. To isolate the error induced by the polynomial fitting extrapolator operated in the main loop, the experimental substructure was replaced by the numerical model. From this analysis, it was found that 85% and 70% of the RMS error between the mrRTHS and reference were generated by other experimental errors for the SDOF and MDOF configuration, respectively. This indicates that other sources of error including: transfer system dynamics, sensor miscalibration, measurement noise and random truncations in the analogue-to-digital (AD) conversion, which likewise appear in conventional RTHS, are attributed for the majority of the error between the mrRTHS and reference.

Acknowledgments

The authors would like to acknowledge the financial support from: i) the Danish Centre for Composite Structures and Materials (DCCSM) funded by the Danish Council for Strategic Research within Sustainable Energy and Environment (Grant: 09-067212), ii) COWI foundation, iii) Otto Moensted Foundation and IV) U.S. NSF under grant no. NSF-1136075. Furthermore the authors acknowledge the Bowen Laboratory in the Lyles School of Civil Engineering, Purdue University for supplying laboratory facilities and technical support.

References

Ashasi-Sorkhabi, A. and Mercan, O. (2014), "Development, implementation and verification of a user configurable platform for real-time hybrid simulation", *Smart Structures and Systems*., **14**(6), 1151-1172

Bitter, R., Mohiuddin, T. and Nawrocki, M. (2001), *LabVIEW Advanced Programming Techniques*, CRC Press, Florida, USA.

Bonnet, P.A. (2006), "The development of multi-axis real-time substructure testing", Ph.D. Dissertation, University of Oxford, Oxford, United Kingdom

Bursi, O.S., Gonzalez-Buelga, A., Vulcan, L., Neild, S.A. and Wagg, D.J. (2008), "Novel coupling rosenbrockbased algorithm for real-time dynamic substructure testing", *Earthquake Engineering and Structural Dynamics*, **37**(3), 339-360

Carrion, J.E., Spencer, B.F. and Phillips, B.M. (2009), "Real-Time Hybrid Testing of a Semi-Actively Controlled Structure with an MR Damper", *American Control Conference*, St. Louis, Missouri, USA, June

Carrion, J.E. and Spencer, B.F. (2007), "Model-based Strategies for Real-time Hybrid Testing", *Newmark Structural Engineering Laboratory*, University of Illinois at Urbana-Champaign, Urbana-Champaign, Illinois, USA

Chen, C., Ricles, J.M., Karavasillis, T.L., Chae, Y. and Sause, R. (2012), "Evaluation of real-time hybrid simulation system for performance evaluation of structures with rate dependent devices subjected to seimic loading", *Engineering Structures*, **35**(1), 71-82

Chen, C. and Ricles, J.M. (2008), "A General Approach for Analysis of Actuator Delay Compensation Methods for Real-time Testing", *The 14th World Conference on Earthquake Engineering*, Beijing, China, October

Dyke, S.J. (1996), "Acceleration feedback control strategies for active and semi-active systems: modeling, algorithm development and and experimental verification", Ph.D. Dissertation, University of Notre Dame, Notre Dame, Indiana, USA

Ellis, G. (2000), *Control System Design Guide*, Academic Press, San Diego, Califonia, USA

Ferry, D., Maghareh, A., Bunting, G., Prakash, A., Agrawal, K., Lu, C. and Dyke, S.J. (2014), "On the performance of a highly parallelizable concurrency platform for real-time hybrid simulation", *The 6th World Conference on Structural Control and Monitoring*, Barcelona, Spain, July

Hoegh, J.H., Waldbjoern, J.P., Wittrup-Schmidt, J., Stang, H. And Berggreen, C.C. (2015), "Quasi-static single-component hybrid testing of a composite structure with multi-axial control", *Strain*, submitted

Horiuchi, T., Nakagawa, M., Sugano, M. and Konno, T. (1996), "Development of real-time hybrid experiment system with actuator delay compensation", *Proc. 11th World Conference e on Earthquake Engineering*, Acapulco, Mexico, June

Ito, M., Murata, K., Hoki, K. and Nakashima, M. (2011), "Online Hybrid Test on Buildings with Stud-Type Damper Made of Slitted Steel Plates Stifferened by Wood Panels", *Procedia Engineering*, **14**(1), 567-571

Jacobsen, A., Hitaka, T. and Nakashima, M. (2010), "Online test of building frame with slit-wall dampers

capable of conddtion assessment", *Constructional Steel Research*, **66**(11), 1320-1329
Jensen, F.M., Falzon, B.G., Ankersen, J. and Stang, H. (2006), "Structural Testing and Numerical Simulation of a 34m Composite Wind Turbine Blade", *Composite Structures*, **76**(1-2), 52-61
Jensen, F.M. (2008), "Ultimate Strength of a Large Wind Turbine Blade", Ph.D. Dissertation, Technical University of Denmark, Kgs. Lyngby, Denmark
Karavalis, T.L., Ricles, J.M., Sause, R. and Chen, C. (2011), "Experimental evaluation of the seismic performance of steel MRFs with compressed elastomer dampers using large-scale real-time hybrid simulation", *Engineering Structures*, **33**(6), 1859-1869
Lin, Y.Z. and Christenson, R.E. (2009), "Comparison of Real-time Hybrid Testing with Shake Table Test for an MR Damper Controlled Structure", *American Control Conference*, St. Louis, Missouri, USA, 2009
Maghareh, A., Waldbjoern, J.P., Dyke, S.J. and Prakash, A. (2015), "Adaptive multi-rate interface: development and experimental verification of an interface for multi-rate real-time hybrid simulation", *Earthquake Engineering and Structural Dynamics*, submitted
Maghareh, A., Dyke, S.J., Prakash, A. and Bunting, G.B. (2014a), "Establishing a predictive performance indicator for real-time hybrid simulation", *Earthquake Engineering and Structural Dynamics*, **43**(15), 2299-2318
Maghareh, A., Dyke, S.J., Prakash, A. and Rhoads, J.F. (2014b), "Establishing a Stability Switch Criterion for Effective RTHS Implementation", *Smart Structures and Systems*, **14**(6), 1221-1245
Mahin, S.A., Shing, P.S.B., Thewalt, C.R. and Hanson, R.D. (1989), "Pseudodynamic test method. Current status and future directions", *Structural Engineering*, **115**(8), 2113-2128
Nakashima, M. and Masaoka, N. (1999), "Real-time on-line test for MDOF systems", *Earthquake Engineering and Structural Dynamics*, **28**(4), 393-420
Nakashima, M., Kato, H. and Takaoka, E. (1992), "Development of real-time pseudo dynamic testing", *Earthquake Engineering and Structural Dynamics*, **21**(1), 79-92
Nakashima, M. (2001), "Development, potential and limitations of real-time online (pseudo-dynamic) testing", *Philosophical Transactions of the Royal Society A: Mathematical, Physical and Engineering Science*, **373**(2035), 1851-1867
NI. (2009), "http://www.ni.com/pdf/manuals/373781e.pdf", Website link, Accessed: 12.11-2014
NI. (2008), "http://www.ni.com/pdf/manuals/374188d.pdf", Website link, Accessed: 12.11-2014
NI. (2014), "http://www.ni.com/pdf/manuals/375874b.pdf", Website link, Accessed: 12.11-2014
Phillips, B.M. and Spencer, B.F. (2011), "Model-based servo-hydraulic control for real-time hybrid simulation", Research Report, Newmark Structural Engineering Laboratory, University of Illinois at Urbana-Champaign, Urbana-Champaign, Illinois, USA
Shao, X., Reinhorn, A.M. and Sivaselvan, M.V. (2011), "Real-time Hybrid Simulation Using Shake Tables and Dynamic Actuators", *Structural Engineering*, **137**(7), 748-760
Shing, P.B., Nakashima, M. and Bursi, O.S. (1996), "Application of pseudo dynamic test method to structural research", *Earthquake Spectra*, **12**(1), 29-56
Takanashi, K. and Nakaschiman, M. (1987), "Japanese Activities on ON-LINE Testing", *Engineering Mechanics*, **113**(7), 1014-1032
Waldbjoern, J.P., Hoegh, J.H., Stang, H., Berggreen, C.C., Wittrup-Schmidt, J. and Branner, K. (2013), "Hybrid Testing of Composite Structures with Single-axis Control", *The 19th International Conference on Composite Materials*, Montréal, Canada, July
Williams, M.S. (2007), "Real-time hybrid testing in structural dynamics", *The 5th Australasian Congress on Applied Mechanics*, Brisbane, Australia, December

Appendix D

Earthquake Engineering & Structural Dynamics
The Journal of the International Association for Earthquake Engineering

EARTHQUAKE ENGINEERING & STRUCTURAL DYNAMICS
Earthquake Engng Struct. Dyn. 2016; **45**:1411–1425
Published online 11 February 2016 in Wiley Online Library (wileyonlinelibrary.com). DOI: 10.1002/eqe.2713

Adaptive multi-rate interface: development and experimental verification for real-time hybrid simulation

Amin Maghareh[1,*,†], Jacob P. Waldbjørn[2], Shirley J. Dyke[1,3], Arun Prakash[1] and Ali I. Ozdagli[1]

[1]*Lyles School of Civil Engineering, Purdue University, West Lafayette, U.S.A.*
[2]*Department of Civil Engineering, Technical University of Denmark, Copenhagen, Denmark*
[3]*School of Mechanical Engineering, Purdue University, West Lafayette, U.S.A.*

SUMMARY

Real-time hybrid simulation (RTHS) is a powerful cyber-physical technique that is a relatively cost-effective method to perform global/local system evaluation of structural systems. A major factor that determines the ability of an RTHS to represent true system-level behavior is the fidelity of the numerical substructure. While the use of higher-order models increases fidelity of the simulation, it also increases the demand for computational resources. Because RTHS is executed at real-time, in a conventional RTHS configuration, this increase in computational resources may limit the achievable sampling frequencies and/or introduce delays that can degrade its stability and performance. In this study, the Adaptive Multi-rate Interface rate-transitioning and compensation technique is developed to enable the use of more complex numerical models. Such a multi-rate RTHS is strictly executed at real-time, although it employs different time steps in the numerical and the physical substructures while including rate-transitioning to link the components appropriately. Typically, a higher-order numerical substructure model is solved at larger time intervals, and is coupled with a physical substructure that is driven at smaller time intervals for actuator control purposes. Through a series of simulations, the performance of the AMRI and several existing approaches for multi-rate RTHS is compared. It is noted that compared with existing methods, AMRI leads to a smaller error, especially at higher ratios of sampling frequency between the numerical and physical substructures and for input signals with high-frequency content. Further, it does not induce signal chattering at the coupling frequency. The effectiveness of AMRI is also verified experimentally.

Received 18 March 2015; Revised 6 January 2016; Accepted 7 January 2016

KEY WORDS: real-time hybrid simulation; RTHS; multi-rate RTHS; mrRTHS; adaptive multi-rate interface; AMRI

1. INTRODUCTION

As civil engineering structures evolve to meet the needs of future generations, there is an increasing demand to address ongoing challenges such as demonstrating the effectiveness of performance-based design, considering soil-structure interaction, and utilizing new materials capable of reducing earthquake impact [1]. These challenges justify the need for extending and evolving our experimental capabilities for evaluating structural response and performance in a suitable and cost-effective manner. The necessity to assess the dynamic performance of rate-dependent structural components and recent advances in systems with hard real-time computing capabilities have led researchers to conduct real-time hybrid simulation (RTHS). In RTHS, the interface interaction between the substructures is enforced by servo-hydraulic actuators or a shake table, which acts as a transfer system. This transfer

*Correspondence to: Amin Maghareh, Intelligent Infrastructure Structure Systems Laboratory, Purdue University, West Lafayette, IN, U.S.A.
†E-mail: amaghare@purdue.edu

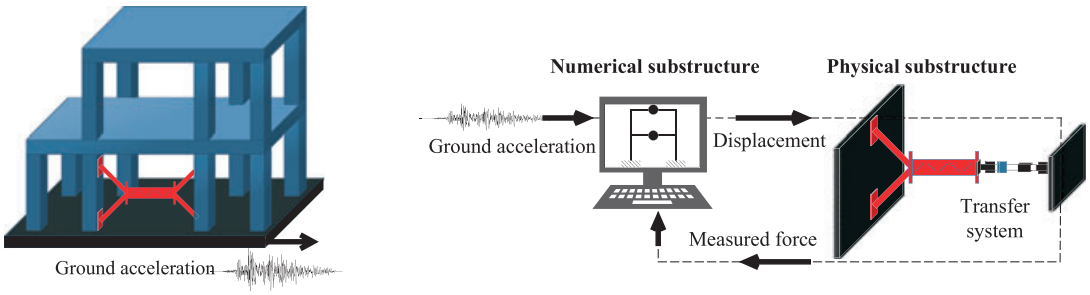

(a) Reference structure (b) Real-time hybrid simulation

Figure 1. A typical real-time hybrid simulation of a civil structure.

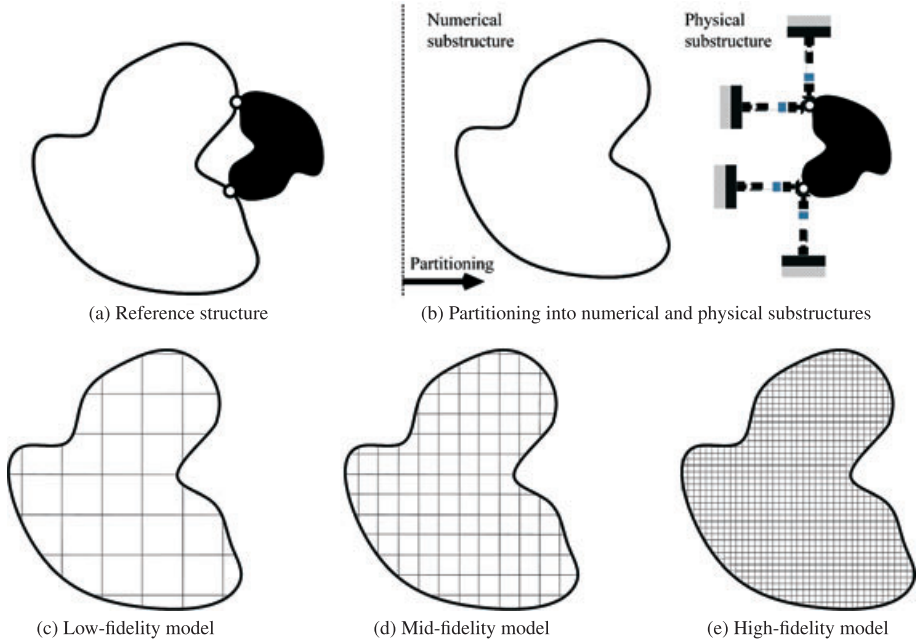

(a) Reference structure (b) Partitioning into numerical and physical substructures

(c) Low-fidelity model (d) Mid-fidelity model (e) High-fidelity model

Figure 2. RTHS partitioning and different modeling choices for the numerical substructure.

system must be controlled properly to ensure that all interface boundary conditions and equilibrium are satisfied in real-time. Figure 1 depicts a real-time hybrid simulation of a two-story structure where a hydraulic actuator is used as transfer system.

The power of hybrid simulation (HS) and real-time hybrid simulation lies in its promise to accelerate the rate at which research in hazard engineering is conducted. In the past decade, an increasing number of researchers have utilized HS methods as an alternative to quasi-static or shake table testing. Many projects have used RTHS to investigate a variety of topics related to earthquake engineering [2–6] and, recently, some related to energy [7], soil-structure interaction [8], and wind engineering [9]. Moreover, researchers are beginning to rely on HS or RTHS to assess local and global responses and to consider various aspects related to design guidelines and codes [10–15], further details of these studies are provided in [16].

In conventional RTHS, global stability and performance dictate the sampling frequency [17], and it is usually chosen to be an integer multiple of the digital servo-controller's sampling frequency, such as 1024 Hz [18]. In RTHS, the time required to solve a computationally demanding numerical model (Figure 2(e)) could certainly be much greater than the maximum time interval required to ensure stability and performance for the transfer system control. Therefore, low-order or mid-order numerical models (Figure 2(c) and Figure 2(d)), which usually do not require such large integration time are

DOI: 10.1002/eqe

adopted by researchers. Idealized models that are limited in their ability to represent the underlying dynamics of the numerical substructure may not be suited to the purpose intended for the simulation. To overcome this challenge, two approaches are available: real-time high-performance computing (RT-HPC) and multi-rate real-time hybrid simulation (mr-RTHS).

Real-time high-performance computing has the potential to enable execution of computationally demanding numerical models in RTHS. However, currently there are very few openly available platforms that are suitable for writing and executing real-time parallel computations [19]. Most current real-time systems only support sequential processing, in which a real-time workload may use only one processor core at a time, or multi-processing, in which a real-time workload may use multiple independent processor cores. Recently, a computational platform based on a federated scheduling model that exploits both intra-task and inter-task parallelism, was developed to enable execution of high fidelity numerical models within the real-time constraints of RTHS [20].

The concept of mr-RTHS was first developed by Nakashima and Masaoka because of the computing/processing limitations in the late 1990s [21]. In their RTHS setup, a novel sub-stepping technique was developed so that the physical substructure is continuously loaded. Their computer executes two tasks: (i) the task of creating the target displacement by solving the equations of motion with an integration time interval of ΔT; and (ii) the task of creating successive displacement signals with a smaller time interval of Δt (i.e., to ensure smooth actuator motion) and sending the signals to the digital servo-controller. The computation of the numerical substructure was executed at each main integration time step, ΔT, while a smooth command signal generation task was executed at each sub-step, Δt. The two tasks were computationally independent and separated. The sub-stepping technique, combined with the use of priority based multi-tasking, produced a smooth command signal for the physical substructure [21]. This work was later pursued by Bonnet [22] who introduced a new multi-tasking strategy.

In mr-RTHS, the computations associated with the simulation of the numerical substructure (or a portion of it) are executed at a larger time interval than what is used for the physical substructure while still executing them both in real-time and ensuring geometric compatibility between them at all instants of time. Executing the numerical substructure at a larger time interval allows more time for a computationally demanding model to execute its computations and thereby enables it to meet the constraint of real-time execution, albeit at a lower rate of execution than the physical substructure. The discrepancy between the rates of execution for the numerical and physical substructures is addressed through a rate-transitioning method that ensures geometric compatibility between them. An effective rate-transitioning method is not only necessary for implementing mr-RTHS but also for ensuring its stability and performance.

In this paper, we develop a new rate-transitioning and compensation technique (Adaptive Multi-rate Interface), which enables researchers to implement multi-rate RTHS. This approach facilitates the use of complex, high-fidelity numerical models. To evaluate the performance of different rate-transitioning techniques, an evaluation procedure is adopted, and the effectiveness of the Adaptive Multi-rate Interface is compared with three existing rate-transitioning techniques in a set of simulations designed to assess the performance of the transfer system's ability to track the desired command. Finally, the Adaptive Multi-rate Interface is experimentally validated in a multi-degree-of-freedom mr-RTHS.

2. RATE-TRANSITIONING TECHNIQUES

Currently, three methods are available that facilitate multi-rate RTHS using rate transitioning. Rate transitioning is needed to provide a continuous control signal to the physical substructure at the intermediate points. The first two methods are based on polynomial extrapolation, and the third method is based on linearly predicted acceleration. Herein, we define some recurring symbols in this study:

ΔT: coarse time interval (rate at which the numerical substructure is executed)
Δt: sub-interval (rate at which the physical substructure is executed)
SFR: sampling frequency ratio ($\Delta T/\Delta t$)

DOI: 10.1002/eqe

2.1. Existing methods

Method I: This method was developed by Bonnet, see [22]. In this method, the control signal is extrapolated through a compensation method developed by Horiuchi *et al.* in [23,24] using current and previous data points from the numerical substructure. For an Nth-order polynomial fit, a number of $N+1$ data points are needed in the following equation:

$$d_{exp} = \sum_{i=0}^{N} a_i d_i, \tag{1}$$

where d_{exp}, d_i, and a_i are the control signal with a time step of Δt, the current and previous displacements with a time increment of ΔT, and polynomial coefficients generated through the Lagrange polynomials, respectively. The original prediction scheme in [23] assumes identical time increment for d_{exp} and d_i. For that reason, Bonnet reformulated a more general expression for a_i, allowing a fully independent time increment for d_{exp} and d_i using a third order polynomial fitting scheme,

$$a_1 = \frac{\Delta t}{\Delta T}\left[\frac{11}{6} + \frac{\Delta t}{\Delta T} + \frac{1}{6}\left(\frac{\Delta t}{\Delta T}\right)^2\right] \tag{2a}$$

$$a_2 = -\frac{\Delta t}{\Delta T}\left[\frac{3}{1} + \frac{5}{2}\frac{\Delta t}{\Delta T} + \frac{1}{2}\left(\frac{\Delta t}{\Delta T}\right)^2\right] \tag{2b}$$

$$a_3 = \frac{\Delta t}{\Delta T}\left[\frac{3}{2} + 2\frac{\Delta t}{\Delta T} + \frac{1}{2}\left(\frac{\Delta t}{\Delta T}\right)^2\right] \tag{2c}$$

$$a_4 = -\frac{\Delta t}{\Delta T}\left[\frac{1}{3} + \frac{1}{2}\frac{\Delta t}{\Delta T} + \frac{1}{6}\left(\frac{\Delta t}{\Delta T}\right)^2\right]. \tag{2d}$$

Method II: The second polynomial method was established by Wallace *et al.* using least-square polynomial fitting, see [25]. As in Method I, the command signal is extrapolated using the current and previous data points computed in the numerical substructure. A polynomial of order N with coefficients a_i, where $i \in \{0, \cdots, N\}$, is fit using least-squares,

$$y = a_0 + a_1 x + \cdots + a_N x^N. \tag{3}$$

Given N data points $\{(x_0, y_0) \cdots (x_{N-1}, y_{N-1})\}$, the polynomial coefficients can be computed using the following equation:

$$\begin{pmatrix} 1 & 0 & \cdots & 0 \\ 1 & -\Delta T & \cdots & \Delta T^{N-1} \\ \vdots & \vdots & \ddots & \vdots \\ 1 & -(N-1)\Delta T & \cdots & [-(N-1)\Delta T]^{N-1} \end{pmatrix} \begin{pmatrix} a_0 \\ a_1 \\ \vdots \\ a_N \end{pmatrix} = \begin{pmatrix} y_0 \\ y_1 \\ \vdots \\ y_{N-1} \end{pmatrix} \tag{4}$$

and X_p is the forward prediction vector given by

$$X_p = \begin{bmatrix} 1 & p\Delta T & \cdots & p^N \Delta T^N \end{bmatrix}, \tag{5}$$

where p is the number of time intervals to be predicted and the predicted point d_{exp} is computed as

$$d_{exp} = X_p [a_0 \cdots a_N]^T. \tag{6}$$

DOI: 10.1002/eqe

Method III: A third method by Horiuchi and Konno is based on the assumption that there is a linear acceleration as a function of time, see [26]. The extrapolated command signal for a sub-interval Δt is given by

$$d_{exp} = d_0 + \Delta t \dot{d}_0 + \frac{1}{3}\Delta t^2 \ddot{d}_0 + \frac{1}{6}\Delta t^2 \ddot{d}_{exp}, \tag{7}$$

where $\ddot{d}_{exp}$ is the predicted acceleration after Δt given by

$$\ddot{d}_{exp} = 2\ddot{d}_0 - \ddot{d}_1. \tag{8}$$

This calculation requires the current velocity and acceleration. However, only the velocity and acceleration from the previous time interval are available. Thus, Horiuchi and Konno proposed a method to overcome this issue, see [26].

Although these techniques are effective at low sampling frequency ratios (about 1–5), at higher sampling frequency ratios (SFR $>$ 5), they may either lead to a significant signal chattering at the coupling frequency or even instabilities. Therefore, a new technique is proposed and shown to be effective at high sampling frequency ratios as well as at low sampling frequency ratios. Furthermore, with the proposed technique, no additional time-delay compensation is required.

2.2. Adaptive multi-rate interface

Building on the successes of the techniques discussed in the previous sections, the adaptive multi-rate interface (AMRI) is developed here to allow the numerical substructure being executed at a larger time interval than what is used for the physical substructure and thereby providing more time for a computationally demanding model to finish its computations. In this method, after selecting a set of orthonormal bases, such as polynomial or exponential, sampling frequency ratio between the numerical and physical substructures, and compensation time, a finer control signal is generated by the AMRI at the rate of Δt. Herein, we define some of the AMRI's parameters

- X: input signal at coarse time interval ΔT
- Y: output signal at sub-interval Δt
- SFR: sampling frequency ratio ($\Delta T/\Delta t$)
- a: number of α coefficients for compensation
- b: number of previous points used for compensation
- k: number of orthogonal bases used for interpolation
- r: number of points used for interpolation
- p: compensation coefficient, $p\Delta T$ is time to be compensated.

In the AMRI, $a + b + p - 1$ displacement input points (current point: $\{X_n\}$ and previous points: $\{X_{n-p-b-a+2}, \ldots, X_{n-2}, X_{n-1}\}$) with the coarse time interval ΔT are used to generate SFR displacement output points with the sub-interval rate Δt. For a better understanding of how the proposed rate-transitioning scheme functions, the AMRI computations are divided into two sequential steps: compensation and rate transitioning.

Compensation: In this step, a time-varying discrete transfer function is used to compensate and predict the command signal,

$$C(z) = \alpha_1 \times z^{-p} + \alpha_2 \times z^{-p-1} + \cdots + \alpha_a \times z^{-p-a+1}, \tag{9}$$

where $p\Delta T$ is the time to be compensated, $p \in \{1, 2, 3 \ldots\}$ and z is the complex variable in the Z-domain. In Equation (9), the coefficients $\{\alpha_1, \alpha_2, \ldots, \alpha_M\}$ are obtained at each time interval by solving the following least-squares equation

DOI: 10.1002/eqe

$$\begin{pmatrix} X_{n-p-b+1} & X_{n-p-b} & \cdots & X_{n-p-b-a+2} \\ \vdots & \vdots & \ddots & \vdots \\ X_{n-p} & X_{n-p-1} & \cdots & X_{n-p-a+1} \end{pmatrix}_{b\times a} \times \begin{pmatrix} \alpha_1 \\ \alpha_2 \\ \vdots \\ \alpha_a \end{pmatrix} = \begin{pmatrix} X_{n-b+1} \\ X_{n-b+2} \\ \vdots \\ X_n \end{pmatrix}. \tag{10}$$

Although in the experimental verification we employ this compensation technique, several other compensation methods available in the literature could also be used here, such as [27]. After obtaining the α values, the next p points $\{X_{n+1}, \ldots, X_{n+p}\}$ are extrapolated using Equation (11).

$$\begin{pmatrix} X_{n-p+1} & X_{n-p} & \cdots & X_{n-p-a+2} \\ \vdots & \vdots & \ddots & \vdots \\ X_n & X_{n-1} & \cdots & X_{n-a+1} \end{pmatrix}_{p\times a} \times \begin{pmatrix} \alpha_1 \\ \alpha_2 \\ \vdots \\ \alpha_a \end{pmatrix} = \begin{pmatrix} X_{n+1} \\ X_{n+2} \\ \vdots \\ X_{n+p} \end{pmatrix} \tag{11}$$

Rate-transitioning: In this step, Chebyshev polynomials of the first kind are used as a set of orthonormal bases for interpolation and rate transitioning from ΔT to Δt. The Chebyshev polynomials of the first kind are defined by the following recurrence relation

$$\begin{cases} T_1(s) = 1 \\ T_2(s) = s \\ T_{i+1}(s) = 2sT_i(s) - T_{i-1}(s). \end{cases} \tag{12}$$

These polynomials must be adjusted to be within a general range of $[a, b]$, where, $a = (p+r-1)\Delta T$ and $b = p\Delta T$. For this adjustment, $s = \frac{2x-(a+b)}{b-a}$ where x corresponds to a variable in the range [-1, 1]. The first five polynomials are shown in Figure 3. Next, the following linear equation is solved to obtain $\{\beta_1, \beta_2, \ldots, \beta_k\}$

$$\begin{pmatrix} T_1[(p+1-r)\Delta T] & \cdots & T_k[(p+1-r)\Delta T] \\ \vdots & \ddots & \vdots \\ T_1[(p)\Delta T] & \cdots & T_k[(p)\Delta T] \end{pmatrix}_{r\times k} \times \begin{pmatrix} \beta_1 \\ \beta_2 \\ \vdots \\ \beta_k \end{pmatrix} = \begin{pmatrix} X_{n-r+p+1} \\ \vdots \\ X_n \\ \vdots \\ X_{n+p} \end{pmatrix}. \tag{13}$$

Using the β coefficients, the command signal at the coarse time interval Δt can be computed as follows

$$Y(h) = \beta_1 T_1(h) + \beta_2 T_2(h) + \cdots + \beta_k T_k(h), \tag{14}$$

where $h \in \{(n+p-1)\Delta T, (n+p-1)\Delta T + \Delta t, (n+p-1)\Delta T + 2\Delta t, \cdots, (n+p)\Delta T\}$.

Tuning factor: In addition, a tuning factor is defined to enable the researcher to effectively set the compensation time while tuning the transfer system. The tuning factor can be monitored in real-time or used as a post-experiment tracking performance assessment measure. It is based on a dimensionless index that is computed in equation 15.

DOI: 10.1002/eqe

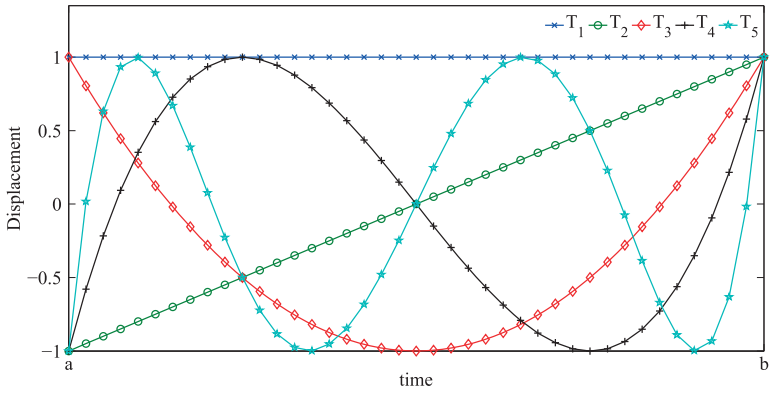

Figure 3. First 5 adjusted Chebyshev polynomials for the general range [a, b].

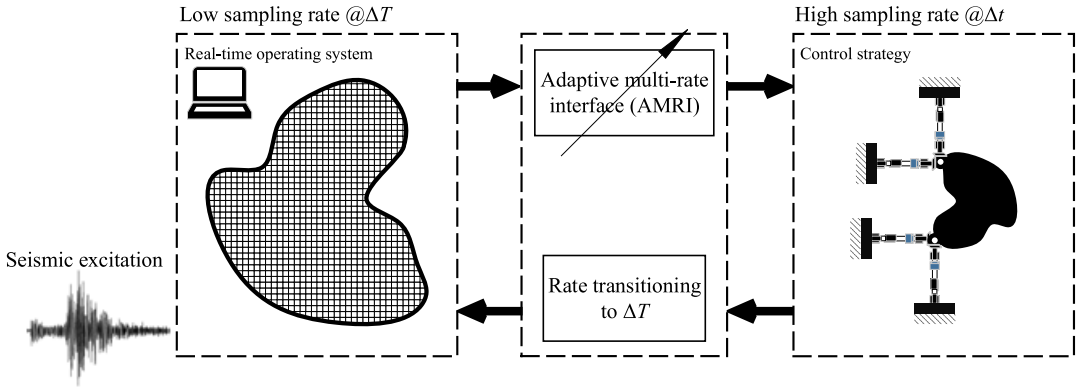

Figure 4. Use of AMRI to implement mr-RTHS.

$$TF_i = \frac{\| \left[x^d_{i+n-p-a-b+2} \cdots x^d_{i+n-p} \right] - \left[x^m_{i+n-a-b+2} \cdots x^m_{i+n} \right] \|_2}{\| \left[x^m_{i+n-a-b+2} \cdots x^m_{i+n} \right] \|_2}, \quad (15)$$

where x^d and x^m refer to the desired and measured displacement signals, respectively. The proposed method allows researcher to set (and tune) the required compensation time (i.e., $p \times \Delta T$). The tuning factor is defined in a way that the closer the p-value line to the reference line, which is the x-axis ($TF = 0$) and corresponds to a perfect correlation between the desired and measured signals, determines what p value should be selected.

AMRI framework: Here, Figure 4 shows a simplified framework in which the AMRI can be used in implementation of mr-RTHS. Also, the data flow diagram in the AMRI is provided in Figure 5 (with SFR = 4). Figure 5 demonstrates how the command displacement and measured force signals are exchanged among the numerical substructure, transfer system control, physical substructure, and memory within each fixed length time step.

3. VERIFICATION OF THE ADAPTIVE MULTI-RATE INTERFACE

3.1. Simulated case studies

Tracking performance evaluation of the transfer system is a necessary preliminary step in RTHS. To evaluate the performance of the AMRI, three case studies of transfer system tracking dynamics are simulated (Figure 6). In these three simulated studies, the input signal to the AMRI is sampled at a

DOI: 10.1002/eqe

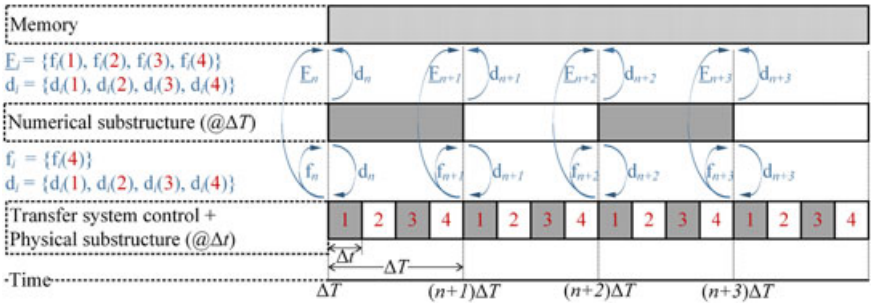

Figure 5. Schematic of AMRI for SFR = 4.

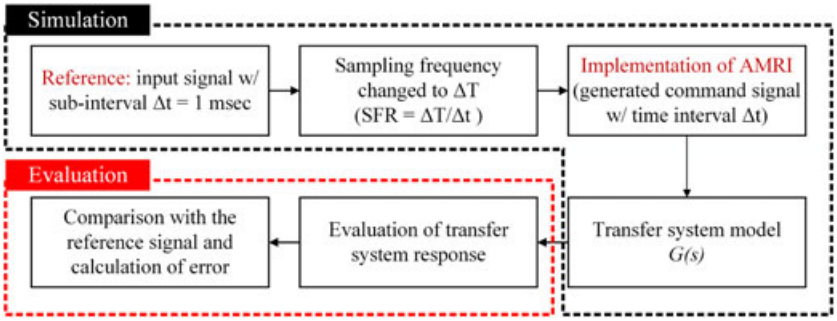

Figure 6. Procedure used to evaluate performance of AMRI for various reference signals (case studies I–III).

larger time interval (ΔT), which indicates an additional time is provided for executing a complex, high-fidelity numerical model. The transfer system model (servo-hydraulic actuator), identified in the Intelligent Infrastructure Systems Laboratory at Purdue University, is used in this study where transfer function of the plant from command to measured displacement is given by

$$G(s) = \frac{4.52 \times 10^9}{s^4 + 577s^3 + 3.68 \times 10^5 s^2 + 6.28 \times 10^7 s + 4.93 \times 10^9}. \tag{16}$$

Case study I: In this study, the desired signal is band-limited white noise with a cut-off frequency at 15 Hz. The sampling frequency ratio is set to be 5, such that the transfer system is running at 1000 Hz. It is shown in Figure 7 that the tracking performance using the Adaptive Multi-rate Interface is smooth and 5 ms delay is well compensated. Using the proposed tuning factor, the AMRI allows the researcher to set and tune the required compensation time (Figure 7(c)). Here, $p = 2$ is the best choice. In addition, in Figure 7(d), coefficients of the adaptive compensation method are shown. A normalized tracking error is computed as

$$NE\% = \frac{max\left(\left|X_i^{sim}(t) - X_i^{ref}(t)\right|\right)}{max\left(\left|X_i^{ref}(t)\right|\right)} \times 100, \tag{17}$$

where X_i^{sim} and X_i^{ref} refer to the transfer system model response at $t = i\,\Delta t$ and the reference response at $t = i\,\Delta t$, respectively. It has been found that $NE\%$ is smaller than 1%.

DOI: 10.1002/eqe

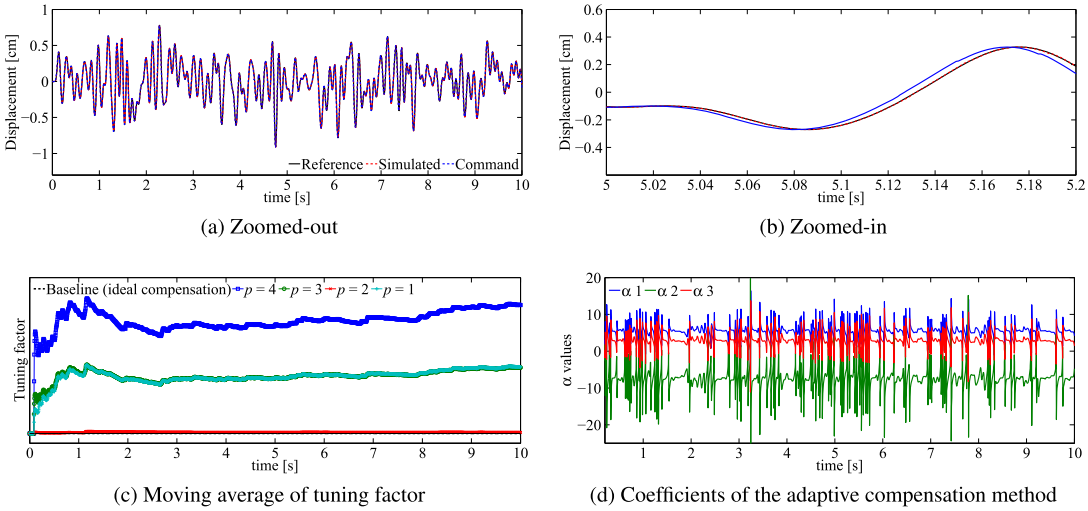

(a) Zoomed-out

(b) Zoomed-in

(c) Moving average of tuning factor

(d) Coefficients of the adaptive compensation method

Figure 7. Simulation results of transfer system tracking.

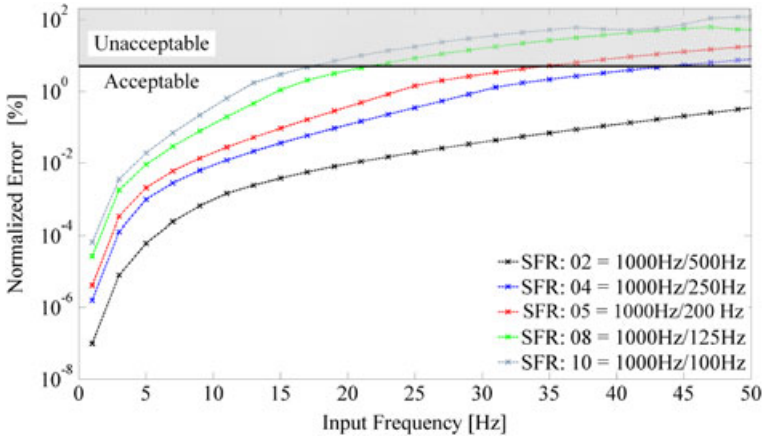

Figure 8. Determining acceptable/unacceptable ranges for a specific multi-rate implementation error.

Case study II: Two significant strengths of the AMRI are its effective performance for input signals with high-frequency content and large sampling frequency ratios. To evaluate the performance of the proposed interface, a series of simulated case studies are implemented in which the input is a sinusoidal signal with various frequencies between 1-49 Hz and sampling frequency ratios of 2, 4, 5, 8, and 10. The corresponding normalized tracking errors using Equation (17) are shown in Figure 8.

The simulation results shown in Figure 8 allow the researcher to have a better understanding of the error stemming from the multi-rate implementation of a real-time hybrid simulation using the AMRI. In this analysis, the frequency spectrum of the command signal is assumed to be known. For instance, the shaded region in Figure 8 results in less than 5% transfer system tracking error using the AMRI rate-transitioning scheme. Moreover, Figure 8 shows that in the majority of cases, the normalized error is less than 1%.

Case study III: Finally, to systematically compare the performance of the three existing methods (method I–III) and the AMRI, a set of actuator tracking simulations are conducted with one time step (ΔT) compensation and various sampling frequency ratios of 2, 5, 8, and 10. In these simulations, the desired displacement is a chirp signal (0–15 Hz).

DOI: 10.1002/eqe

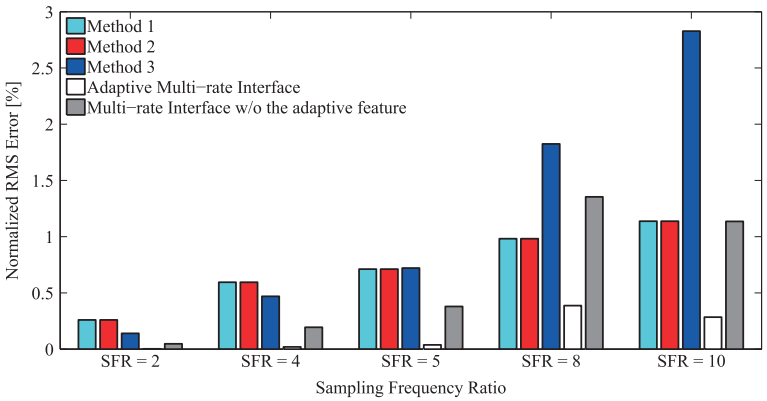

Figure 9. Tracking performance of different rate-transitioning methods.

A normalized tracking error is computed as

$$NRMSE\% = \frac{\sqrt{\frac{1}{n-1}\sum_{i=1}^{n}\left(X_i^{sim} - X_i^{ref}\right)^2}}{max\left(|X_i^{ref}|\right)} \times 100, \tag{18}$$

where NRMSE stands for normalized root mean square error. The errors are presented in Figure 9.

The results show that the Adaptive Multi-rate Interface exhibits significantly smaller error due to the sampling frequency rate transition for all sampling frequency ratios when compared with the existing methods (i.e., methods I–III). The Multi-rate Interface without the adaptive feature is not as effective as the Adaptive Multi-rate Interface, especially at higher sampling frequency ratios and input signals with high-frequency content. Method I and method II exhibit identical performance in the simulated cases. Method III performs better than method I and II for smaller sampling frequency ratios but is not effective for larger sampling frequency ratios.

3.2. RTHS case studies

In RTHS and in the case of a highly computationally demanding numerical substructure subject to hard real-time constraints, three approaches may be considered: (i) utilizing a real-time high-performance platform, such as a multicore real-time target machine, to drive the numerical substructure while meeting the stringent real-time constraints; (ii) obtaining a low-fidelity numerical substructure using the existing model reduction techniques; and (iii) using a multi-rate RTHS strategy to run the numerical substructure at a slower rate while the physical substructureis run at a higher rate.

In this section, the objective is to implement approaches (i), (ii), and (iii) and experimentally verify the effectiveness of the AMRI. Thus, three real-time hybrid simulations are implemented.

Experiment 1: approach (i) is adopted and RTHS with a high-fidelity numerical substructure running at 1024 Hz is implemented on high-performance xPC (Speedgoat) real-time target system.

Experiment 2: approach (ii) is adopted and RTHS with a low-fidelity numerical substructure running at 1024 Hz is implemented on a regular xPC real-time target machine.

Experiment 3: approach (iii) is adopted and multi-rate RTHS, with a high-fidelity numerical substructure at 256Hz and physical substructure at 1024 Hz (SFR = 4), is implemented on a regular xPC real-time target machine.

Here, the excitation is the N–S component of the El Centro earthquake recorded at the Imperial Valley Irrigation District substation in El Centro, California, during the Imperial Valley, California

DOI: 10.1002/eqe

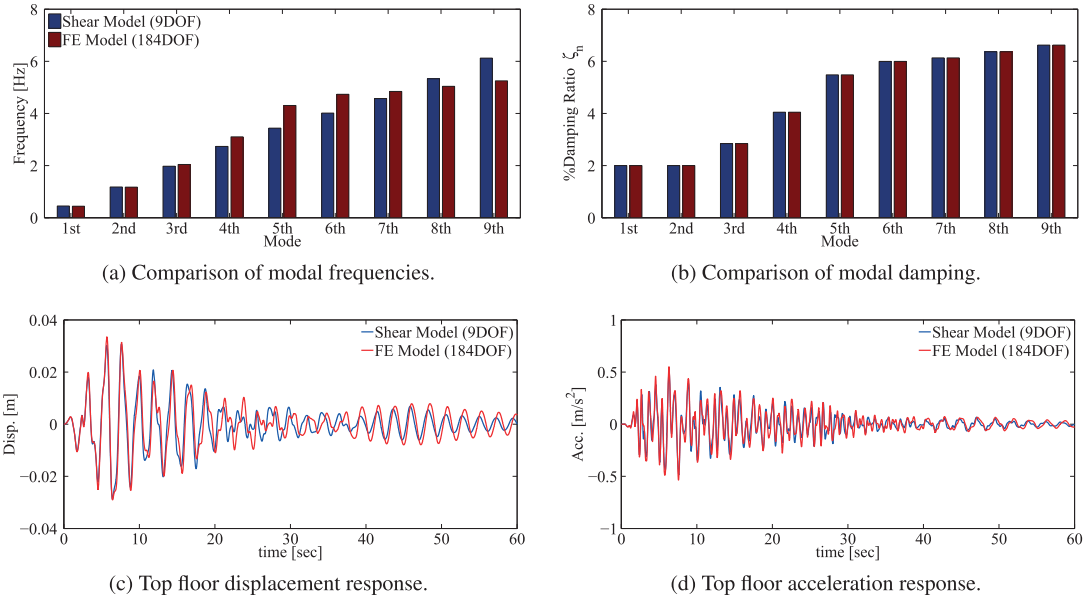

(a) Comparison of modal frequencies.

(b) Comparison of modal damping.

(c) Top floor displacement response.

(d) Top floor acceleration response.

Figure 10. Comparison of top floor responses obtained from the two numerical models.

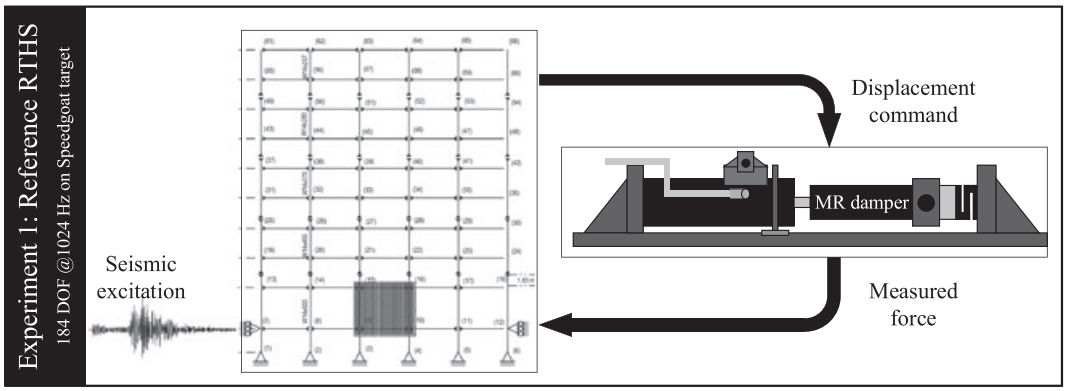

Figure 11. Reference, conventional RTHS with 1024-Hz sampling rate and FEM numerical substructure.

earthquake of 18 May 1940 scaled to PGA = $0.28\,m/s^2$. In these experiments, the numerical substructure is the nine-story structure designed by Brandow and Johnston Associates (1996) for the SAC phase II steel project. The nine-story structure is well studied as one of the benchmark control structures for seismically excited nonlinear buildings proposed in [28]. Two models with different levels of refinement are used for the numerical substructure: a 184 degree-of-freedom finite element model constructed using RT-Frame2D open-source software available at [29] and a 9 degree-of-freedom shear model with similar dynamic characteristic at [30]. The seismic responses and some modal characteristics of the two models are compared (Figure 10). Figure 10 shows that the low-fidelity 9DOF shear model is able to capture the dominant dynamics of the more refined finite element model.

Experiment 1 (reference): In this RTHS, we designate the response from the real-time hybrid simulation of the nine-story structure where the numerical model is chosen to be a detailed finite element model (184DOF) running at 1024 Hz. Because of the computational demands of the modeling choice, the numerical substructure cannot be implemented on a regular xPC real-time target machine, and real-time high-performance xPC (Speedgoat) target system is used instead. In this RTHS,

DOI: 10.1002/eqe

the physical substructure is a scaled MR-damper placed on the first floor (between node 9 and node 16), see Figure 11. The response of this experiment is chosen as the reference response.

Experiment 2 (conventional RTHS): In the second RTHS, the 9DOF low-fidelity numerical model is adopted and RTHS is conducted at 1024-Hz sampling rate on a regular xPC real-time target machine. The physical substructure is a scaled MR-damper placed on the first floor (Figure 12).

Experiment 3 (mr-RTHS): Finally, a multi-rate RTHS using the AMRI where the numerical model is chosen to be the detailed finite element model (184DOF) executed at 256 Hz on a regular xPC real-time target machine. The physical substructure is also a scaled MR-damper placed on the first floor (between node 9 and node 16), see Figure 13. The control system and the physical substructure are executed at 1024 Hz (SFR = 4). In the use of the AMRI, an adaptive compensation technique is implemented. Corresponding coefficients for the adaptive compensation technique are provided in Figure 14. It should be mentioned that, if properly implemented, the use of an adaptive technique to extrapolate and compensate in the AMRI leads to a smooth command displacement. However, if a proper technique is not adopted, an undesirable signal chattering in the command displacement can cause instability and unbalance force in the system.

The results of these experiments are provided in Figure 15. Because of the modeling choice for the numerical substructure (184DOF) and executing at 1024 Hz, the response of Experiment 1 is chosen as the reference response. The results demonstrate that the mr-RTHS technique enables researchers

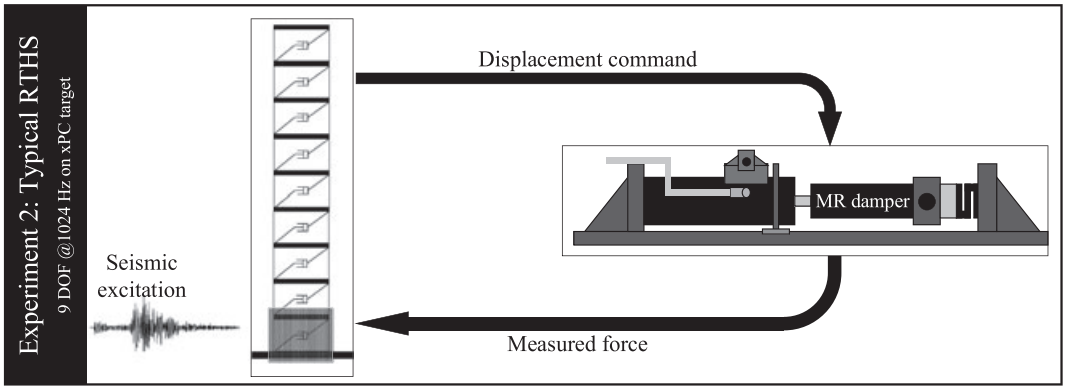

Figure 12. Typical RTHS with 1024-Hz sampling rate and shear model numerical substructure.

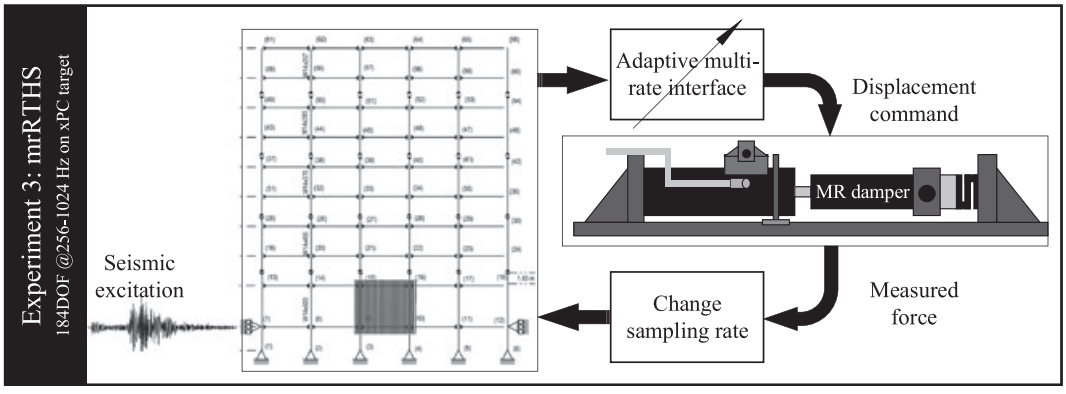

Figure 13. Multi-rate RTHS with sampling ratio 4 (@256-1024Hz).

DOI: 10.1002/eqe

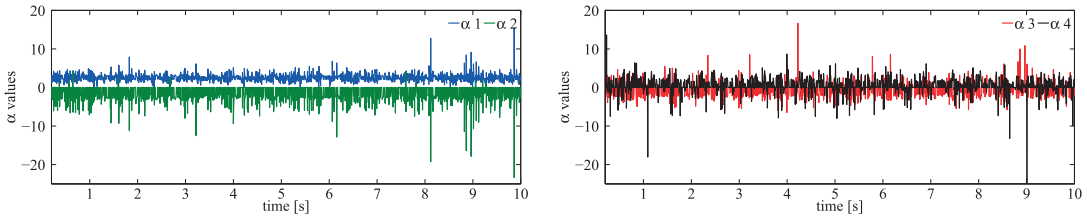

(a) (b)

Figure 14. Coefficients of the adaptive compensation method in mr-RTHS.

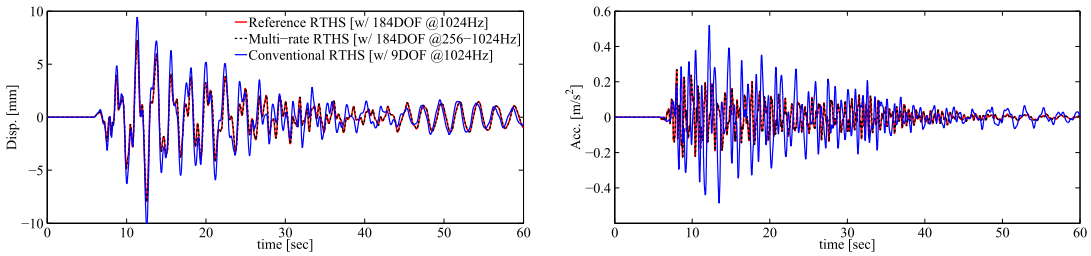

(a) Comparison of first floor displacements.

(b) Comparison of first floor accelerations.

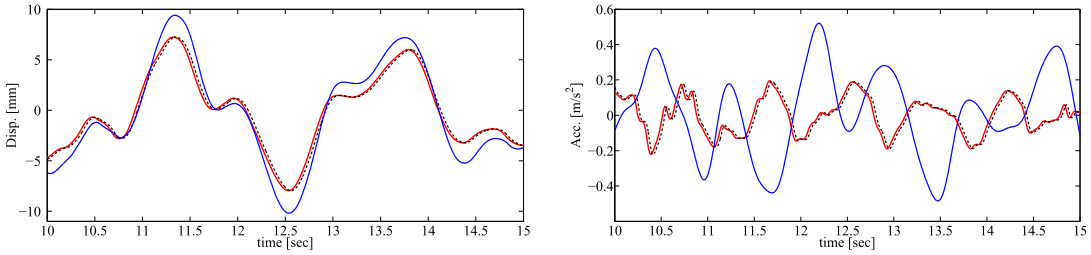

(c) Comparison of first floor displacements (zoomed in).

(d) Comparison of first floor accelerations (zoomed in).

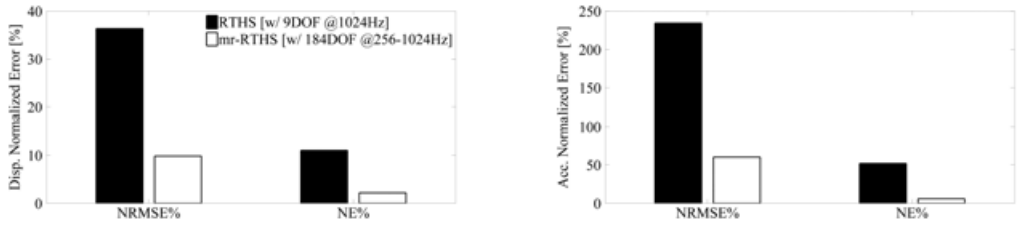

(e) Comparison of displacement error at first floor.

(f) Comparison of acceleration error at first floor.

Figure 15. Comparison of RTHS and mr-RTHS responses.

to successfully implement high-fidelity experiments using a commonly available real-time target system. Referring to the three approaches for implementation of high-fidelity RTHS, approach (i) is the most desirable one. However, it requires a high-performance real-time hardware. The mr-RTHS response successfully matches the reference response (displacement and acceleration). In this experimental example, the use of a low-fidelity numerical substructure causes considerable displacement and acceleration errors (Figures 15(a)–(d)). Modeling idealization error in the numerical substructure can considerably degrade the global RTHS response. As is also evident from Figures 10(a)–(b), the low-fidelity model is able to capture the dominant dynamics of the high-fidelity model. However, this insignificant modeling mismatch leads to considerable displacement and acceleration errors in the RTHS response (Figures 15(a)–(d)). Comparing the response of the conventional RTHS with mr-RTHS using the AMRI (Figures 15(e)–(f)) demonstrates that, if properly implemented, mr-RTHS can significantly lower the propagation of error caused by modeling error in the numerical substructure

DOI: 10.1002/eqe

(NE% and NRMSE% in Equations (17) and (18)). The fact that the mr-RTHS response can successfully replicate the reference response provides valuable insight into use of RTHS for a broader range of problems. Concurrent use of high-performance real-time operating system and mrRTHS enables users to include high-fidelity numerical substructures with thousands of degrees of freedom in RTHS. Also, the proposed mrRTHS technique can be implemented on regular real-time operating systems to optimize the use of computational resources in RTHS.

4. CONCLUSIONS

A major factor that determines the ability of RTHS to represent realistic behavior of the reference system is the fidelity of the numerical substructure. However, in real-time hybrid simulation, due to stringent real-time constraints, high-fidelity complex models that require a significant time to solve are unsuitable. A multi-rate approach allows the computationally-demanding part of the numerical substructure to be executed at larger time intervals than what is used for the physical substructure while still executing them both in real-time and ensuring compatibility between them at all time. Thus, the multi-rate technique enables the computationally demanding model to meet the constraint of real-time execution.

In this study, a new rate-transitioning and compensation technique, the Adaptive Multi-rate Interface (AMRI), is developed. In a set of experiments, we show that mr-RTHS using AMRI is more effective and leads to a smaller global error than the alternative approach of reducing the order of numerical substructure to meet the real-time constraints. It is also demonstrated that modeling error in the numerical substructure can considerably degrade the global RTHS response. An apparently insignificant modeling mismatch may lead to considerable displacement and acceleration errors in the global response. To mitigate this error, a user can integrate AMRI in RTHS to implement a high-fidelity complex model as numerical substructure. Furthermore, a set of simulated transfer system tracking performance studies are implemented to systematically compare the performance of existing methods and the adaptive multi-rate interface. Compared with existing methods, AMRI leads to smaller errors, specifically at higher sampling frequency ratios $\Delta T/\Delta t$ and input signals with high-frequency content, generates a smooth and continuous command signal, and includes a built-in delay compensation feature.

ACKNOWLEDGEMENTS

This material is based upon work supported by the National Science Foundation under Grant No. CNS-1136075. The authors would also like to acknowledge the financial support from the Danish Centre for Composite Structures and Materials (DCCSM) funded by the Danish Council for Strategic Research within Sustainable Energy and Environment (Grant: 09-067212), COWI foundation, and Otto Moensted Foundation.

REFERENCES

1. Dyke SJ, Stojadinovic B, Arduino P, Garlock M, Luco N, Ramirez JA, Yim S. 2020 Vision for earthquake engineering research: report on an openspace technology workshop on the future of earthquake engineering 2010; **20**(5). (Available from: https://nees.org/resources/1636.)
2. Phillips BM, Spencer BF. Model-based multiactuator control for real-time hybrid simulation. *Journal of Engineering Mechanics* 2013; **139**(2):219–228.
3. Christenson R, Lin YZ, Emmons A, Bass B. Large-scale experimental verification of semiactive control through real-time hybrid simulation. *Journal of Structural Engineering* 2008; **134**(4):522–534.
4. Shao X, Reinhorn AM, Sivaselvan MV. Real-time hybrid simulation using shake tables and dynamic actuators. *Journal of Structural Engineering* 2011; **137**(7):748–760.
5. Bursi OS, Gonzalez-Buelga A, Vulcan L, Neild SA, Wagg DJ. Novel coupling Rosenbrock-based algorithms for real-time dynamic substructure testing. *Earthquake Engineering & Structural Dynamics* 2008; **37**(3):339–360.
6. Mercan O, Ricles JM. Experimental studies on real-time testing of structures with elastomeric dampers. *Journal of Structural Engineering* 2009; **135**(9):1124–1133.
7. Börner T, Alam M. Real time hybrid modeling for ocean wave energy converters. *Renewable and Sustainable Energy Reviews* 2015; **43**:784–795.
8. Wang Q, Wang J, Jin F, Chi F, Zhang C. Real-time dynamic hybrid testing for soil-structure interaction analysis. *Soil Dynamics and Earthquake Engineering* 2011; **31**(12):1690–1702.

DOI: 10.1002/eqe

9. Brodersen ML, Ou G, Hø gsberg J, Dyke SJ. Analysis of hybrid viscous damper by real time hybrid simulations. *Engineering Structures* submitted.
10. Dong B, Sause R, Ricles J, Ahn R, Chae Y, Marullo T, Novak G. Real-time Hybrid Simulation of a large-scale steel structure with Viscous Dampers-Phase 2. *Technical Report*, Network for Earthquake Engineering Simulation: Bethlehem, PA, USA, 2014.
11. Friedman AJ. Development and experimental validation of a new control strategy considering device dynamics for large-scale MR dampers using real-time hybrid simulation. *Ph.D. Thesis*, Purdue University, West Lafayette, IN, USA, 2012.
12. Jiang Z, Christenson R. A comparison of 200 kN magneto-rheological damper models for use in real-time hybrid simulation pre-testing. *Smart Materials and Structures* 2011; **20**(6):065011.
13. Kim SJ, Holub CJ, Elnashai AS. Experimental investigation of the behavior of RC bridge piers subjected to horizontal and vertical earthquake motion. *Engineering Structures* 2011; **33**(7):2221–2235.
14. Lin PC, Tsai KC, Wang KJ, Yu YJ, Wei CY, Wu AC, Tsai CY, Lin CH, Chen JC, Schellenberg AH, Mahin SA, Roeder CW. Seismic design and hybrid tests of a full-scale three-story buckling-restrained braced frame using welded end connections and thin profile. *Earthquake Engineering & Structural Dynamics* 2012; **41**(5):1001–1020.
15. Lignos DG, Moreno DM, Billington SL. Seismic retrofit of steel moment-resisting frames with high-performance fiber-reinforced concrete infill panels: large-scale hybrid simulation experiments. *Journal of Structural Engineering* 2014; **140**(3):04013072. (Available from: http://ascelibrary.org/doi/abs/10.1061/(ASCE)ST.1943-541X.0000877.)
16. Gomez D, Dyke SJ, Maghareh A. On the role of hybrid and real-time hybrid simulations in advancing the practice of earthquake engineering. *Smart Structures and Systems* 2014; **15**(3):913–929.
17. Maghareh A, Dyke SJ, Prakash A, Rhoads JF. Establishing a stability switch criterion for effective implementation of real-time hybrid simulation. *Smart Structures and Systems* 2014; **14**(6):1221–1245.
18. Chen C, Ricles JM. Improving the inverse compensation method for real-time hybrid simulation through a dual compensation scheme. *Earthquake Engineering & Structural Dynamics* 2009; **38**(10):1237–1255.
19. Ferry D, Li J, Mahadevan M, Agrawal K, Gill CD, Lu C. A real-time scheduling service for parallel tasks. *IEEE Real-Time and Embedded Technology and Applications Symposium (RTAS'13)*: Philadelphia, USA, 2013; 261–272.
20. Ferry D, Maghareh A, Bunting G, Prakash A, Agrawal K, Gill C, Lu C, Dyke SJ. On the performance of a highly parallelizable concurrency platform for real-time hybrid simulation. *6WCSCM*: Barcelona, Spain, 2014.
21. Nakashima M, Masaoka N. Real-time on-line Test for MDOF Systems. *Earthquake Engineering & Structural Dynamics* 1999; **28**(4):393–420.
22. Bonnet PA. The development of multi-axis real-time substructure testing. *Ph.D. Thesis*, University of Oxford, Oxford, UK, 2006.
23. Horiuchi T, Nakagawa M, Sugano M, Konno T. Development of a real-time hybrid experimental system with actuator delay compensation. *Proceedings of 11th World Conference Earthquake Engineering*: Acapulco, Mexico, 1996; 660.
24. Horiuchi T, Inoue M, Konno T, Yamagishi W. Development of a real-time hybrid experimental system using a shaking table (Proposal of experimental concept and feasibility study withs rigid secondary system). *JSME International* 1999; **42**(2):255–264.
25. Wallace MI, Wagg DJ, Neild SA. An adaptive polynomial based forward prediction algorithm for multi-actuator real-time dynamic substructuring. *Proceedings of the Royal Society A: Mathematical, Physical and Engineering Sciences* 2005; **461**:3807–3826.
26. Horiuchi T, Konno T. A new method for compensating actuator delay in real-time hybrid experiments. *Philosophical Transactions of the Royal Society A: Mathematical, Physical and Engineering Sciences* 2001; **359**:1893–1909.
27. Ahmadizadeh M, Mosqueda G, Reinhorn AM. Compensation of actuator delay and dynamics for real-time hybrid structural simulation. *Earthquake Engineering & Structural Dynamics* 2008; **37**(1):21–42.
28. Ohtori Y, Christenson RE, Spencer BF, Dyke SJ. Benchmark control problems for seismically excited nonlinear buildings. *Journal of Engineering Mechanics* 2004; **130**:366–385.
29. Castaneda-Aguilar N, Gao X, Dyke SJ. RT-Frame2D: A computational platform for the real-time hybrid simulation of dynamically-excited steel frame structures 2012. (Available from: https://nees.org/resources/realtimeframe2d.)
30. Maghareh A, Dyke SJ, Prakash A, Bunting G, Lindsay P. Evaluating modeling choices in the implementation of real-time hybrid simulation, *EMI/PMC 2012 Joint Conference of the Engineering Mechanics Institute and the 11th ASCE Joint Specialty Conference on Probabilistic Mechanics and Structural Reliability*: Notre Dame, USA, 2012; 550.

DOI: 10.1002/eqe

Appendix E

strain
An International Journal for Experimental Mechanics

Single-component Multi-rate Real Time Hybrid Simulation Pilot Test on a Composite Structure

Journal:	*Strain*
Manuscript ID	Draft
Manuscript Type:	Full Paper
Date Submitted by the Author:	n/a
Complete List of Authors:	Waldbjørn, Jacob; Technical University of Denmark, Department of Civil Engineering Andersen, Sebastian; Technical University of Denmark, Department of Civil Engineering Høgh, Jacob; Technical University of Denmark, Department of Mechanical Engineering Wittrup-Schmidt, Jacob; Technical University of Denmark, Department of Civil Engineering Berggreen, Christian; Technical University of Denmark, Department of Wind Energy
Keywords:	multi-rate real-time hybrid simulation, hardware-in-the-loop, performance evaluation, experimental substructure, numerical substructure, Taylor basis

Title:

Single-component Multi-rate Real Time Hybrid Simulation Pilot Test on a Composite Structure

Authors:

Jacob P. Waldbjoern[1], jpwa@byg.dtu.dk, phone: +45 40185431 (corresponding author)

Sebastian Andersen[1], seba@byg.dtu.dk

Jacob Herold Høgh[2], jhho@mek.dtu.dk

Jacob Wittrup Schmidt[1], jws@byg.dtu.dk

Christian Berggreen[2], cbe@mek.dtu.dk

Affiliations and addresses:

1. Department of Civil Engineering, Technical University of Denmark, Brovej 118, Kgs. Lyngby, Denmark
2. Department of Mechanical Engineering, Technical University of Denmark, Nils Koppels Allé 403, Kgs. Lyngby

Single-component Multi-rate Real-Time Hybrid Simulation Pilot Test on a Composite Structure

Jacob P. Waldbjoern[1], Sebastian Andersen[1], Jacob Herold Høgh[2], Jacob Wittrup Schmidt[1] and Christian Berggreen[2]

[1]Department of Civil Engineering, Technical University of Denmark, Kgs. Lyngby, Denmark

[2]Department of Mechanical Engineering, Technical University of Denmark, Kgs. Lyngby, Denmark

Keywords: *multi-rate real-time hybrid simulation, hardware-in-the-loop, performance evaluation, experimental substructure, numerical substructure, Taylor basis*

Abstract

This paper represents a single component multi-rate Real-Time Hybrid Simulation (mrRTHS) strategy for structural assessment of a cantilever Glass Fiber Reinforced Polymer (GFRP) beam loaded at the tip by a sinusoidal point load. This emulated structure is implemented as a simplified wind turbine blade in terms of geometry, scale and load – here with special attention paid to the root and max-chord section. For that reason the experimental substructure comprises the clamped end of the GFRP beam while the free end makes up the numerical substructure. The partitioning between the numerical and experimental substructure – referred to here as the shared boundary - includes a discrete point with 3 degrees-of-freedom (dof). The numerical substructure generates a displacement signal through a Taylor basis with a coarse time step of Δt = 20 msec to optimize computational resources. Using the current and three previous displacement data points, a finer control signal is generated with a time step of δt = 2 msec to ensure accurate actuator control in the transfer system. The hybrid simulation communication loop is operated through a Laboratory Engineering Workshop (LabVIEW) real-time target which combines an onboard reconfigurable Field-Programmable Gate Array (FPGA) and real-time single-core processor within the same chassis. A DIC and inertia compensator is implemented to account for the compliance and dynamics imposed by the load train in the transfer system. The structural response is investigated by mrRTHS for an execution frequency in the range: 0.074Hz – 2.96Hz for the sinusoidal point load. The system performance is evaluated against a numerical model of the emulated structure – referred to here as the reference. For the translational dofs at the shared boundary a root-mean-square (RMS) error of 19.37% to 21.59% in the x-direction and 15.01% to 16.23% in the y-direction is identified between the mrRTHS and reference. The rotation at the shared boundary exhibits an RMS error of 56.84% to 67.99%. This significant RMS error is induced in the mrRTHS given that the commanded rotation defined by the numerical substructure was erroneously reduced by a factor of $\pi/180$. However the overall system performance proved successful which is an important milestone in the effort of performing a successful single component mrRTHS on an e.g. wind turbine blade.

1. Introduction

Hybrid simulation is a substructuring technique where a structure of interest is emulated by combining the advantages of numerical modelling with those of experimental testing [1], [2]. The coupling governed through the interface between the numerical and experimental substructure – referred to here as the shared boundary – is achieved by maintaining the compatibility and equilibrium at the interface. During the test, a predefined external load is applied the numerical substructure and the corresponding response computed. Through a communication loop, the displacement at the shared boundary is acquired and applied to the experimental substructure through a servo-hydraulic transfer system. The forces required to deform the experimental substructure – referred to here as the reaction force – are fed back to the numerical substructure to reveal the response of the emulated structure. The experimental and numerical substructure, communication loop and servo-hydraulic transfer system combine to form the hybrid simulation.

The research within hybrid simulation has primary been focusing on testing of seismic protection of building structures on a real-time and extended time-scale [3], [4], [5], [6]. Here the shared boundary between the numerical and experimental substructure typically consist of a discrete point with a few degree-of-freedom (dof) referred to here as conventional hybrid simulation. For this application, the load bearing structure has been simulated in a numerical model while e.g. damping fixtures has been tested experimentally including: elastomer [7], stud types [8], [9] and magneto-rheological [10], [11], [12]. However conventional hybrid simulation is becoming a mature and reliable technology, which opens the opportunity to spread the hybrid simulation technique within other application areas [13].

Wind turbines are progressively used as a substitute to fossil fuels and the demand for larger and more energy producing turbines are needed. Thus demands for optimization yields test methods able to accurately determine the wind turbine blade response to major static and dynamic forces acting on the blade during service. The ambition to improve the structural and operational performance within the industry of wind turbines [14] has resulted in extensive research within large composite structures. In these efforts, testing has primary been focusing on two scales: structural and laminate scale testing [15]. However to address shortcomings in structural and laminate scale testing, the hybrid simulation concept is implemented as a substructural technique for large composite structures – referred to here as single component hybrid simulation.

Single component hybrid simulation is a substructuring technique, capable of evaluating the global response of the emulated structure when exposed to local effects and advanced load configurations. However the single component hybrid simulation technique highly complicates the numerical and experimental substructure due to the complex geometry and material characterization [16]. Furthermore, the transferring of response at the shared boundary is continues along the edge instead of e.g. a clearly defined hinge as mentioned above. The operation of the shared boundary justifies the need for advanced measuring techniques to ensure a high degree of accuracy in the displacement imposed on the shared boundary of the experimental substructure [17], [18]. Previous research has been done within the field of single component hybrid simulation on a composite structure with the shared boundary covering; a single discrete point with multiple and single axis control. However both publications only cover the quasi-static regime which is inadequate given the significance of strain rate and inertia effects on composite structures [19].

To include the dynamic effects on both the numerical and experimental substructure, Real Time Hybrid Simulation (RTHS) is implemented. RTHS includes critical time constraints throughout the entire system to ensure accuracy and stability of the experiment [20]. Given the increased complexity of the numerical substructure within single component hybrid simulation, this time constraints can be difficult to meet with the available on-board computational resources due to the implementation of e.g. non-linear effects along with higher order models. For that reason, the numerical substructure may require an extended integration time to be solved in real-time. However another principle aspect in the RTHS lies in the shared boundary, which needs to follow a continuous time history of displacement, velocity or acceleration [21]. Given that the output from the numerical substructure is discrete, fine time steps is required to ensure accurate actuator control. To optimize the available computational resources and enhance flexibility to the RTHS architecture, the numerical substructure and shared boundary is executed at different rates – referred to here as multi-rate Real-Time Hybrid Simulation (mrRTHS) [22].

The scope of this paper is to perform an experimental assessment of a cantilever thin-walled Glass Fibre Reinforced Polymer (GFRP) beam with a rectangular cross sectional geometry using single component mrRTHS. The cantilever beam is loaded at the tip by a sinusoidal point load representing a simplified wind turbine blade in terms of geometry, scale and loads. With the root and max-chord section as the area of special interest of the wind turbine blade [23] the clamped end of the GFRP beam is chosen as the experimental substructure while the free end makes up the numerical substructure. The partitioning between the numerical and experimental substructure is described by a discrete point with 3 dofs. The mrRTHS communication loop is operated through a Laboratory Virtual Engineering Workshop (LabVIEW) real-time target capable of providing deterministic and real-time performance for data acquisition and

control systems. Digital Image Correlation (DIC) is implemented as a method of adjusting the dynamically imposed displacement at the shared boundary, to fit the command signal received by the numerical model. Furthermore an inertia compensator is implemented to erase the dynamic effects implemented by the mass of the load train [24]. Compensation of communication delay and dynamics of the transfer system are conducted through a suitable compensator to ensure accuracy and stability in the communication loop. A so-called Taylor basis is applied in the numerical simulation of the mrRTHS, as this provides a computational efficient way of including the nonlinearities in the model, cf. [25], [26]. For verification of the single-component mrRTHS technique a numerical and experimental representation of the emulated structure is conducted – referred to here as the reference. Here a sinusoidal point load is applied the emulated structure and the global response monitored in multiple measurement points to compare with the global response of the mrRTHS.

2. Hybrid simulation setup

2.1. Emulated structure and partitioning

A cantilever beam is implemented as the emulated structure with the overall dimensions, external load and boundary conditions represented in figure 1. This configuration is studied to reduce the complexity and cost in verifying the mrRTHS communication loop for a wind turbine blade application in terms of geometry, scale and loads.

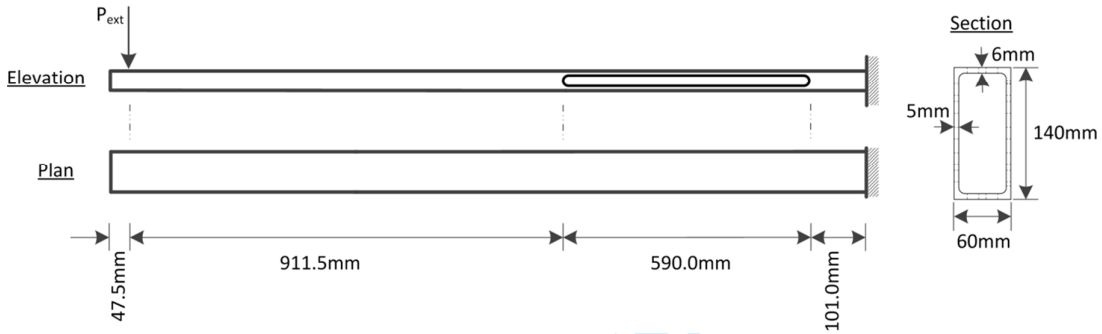

Figure 1: emulated structure representing the overall dimensions, external load and boundary conditions

The emulated structure is a 1650mm long thin-walled GFRP beam produced by fiber pultrusion. The in-plane stiffness properties of the GFRP beam are assumed identical to the properties identified in **[16]** given that the specimen used in both studies are from the same batch. The in-plane material properties are presented in table 1, determined in accordance with D3039/D3030M – 08 **[27]** and D5579/D5379M – 12 **[28]**. The 1-direction corresponds to the x-direction while the 2-direction corresponds to the z-direction for the compression/tension flanges and y-direction for the shear flanges in figure 2.

Table 1: In-plane stiffness properties and density for the GFRP composite

E_1 [GPa]	E_2 [GPa]	ν_{12} [-]	ν_{21} [-]	G_{12} [GPa]	G_{21} [GPa]	Dens [kg/m^3]
28.36	9.96	0.23	0.08	3.41	3.06	1825

The emulated structure is partitioned in a numerical and experimental substructure named: part A and part B respectively. In the experimental substructure a 590mm long and 40mm wide slit are initiated in both shear webs of the closed rectangular profile to weaken the shear stiffness – yielding a geometrical non-linear response. The shared boundary between the two substructures is defined by a discrete point with three dof including: translation in the x- and y-direction along with rotation around the z-axis – referred to here as d_x, d_y and θ respectively. The corresponding reaction force is defined by three dof including: normal and shear force along with a moment – referred to here as N, V and M respectively cf. figure 2.

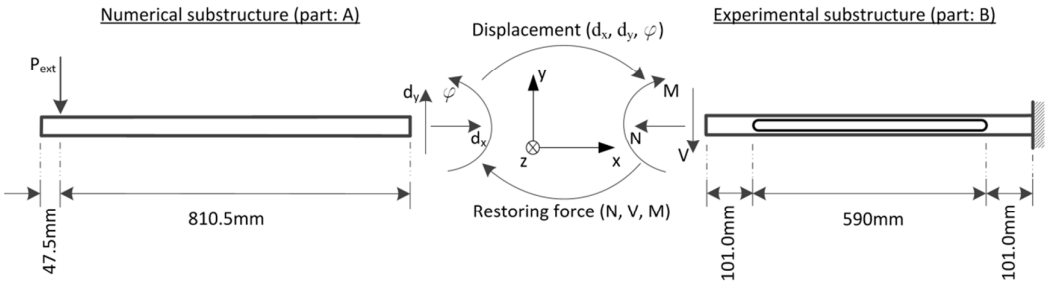

Figure 2: emulated structure and shared boundary between the numerical substructure (part A) and experimental substructure (part B)

2.2. Experimental test setup

The experimental test setup is handled in a reconfigurable stiff frame structure – capable of handle both the experimental substructure and reference structure. The clamped boundary of the GFRP beam is achieved through a rectangular steel profile which encloses the clamped end of the GFRP beam. Installation plates are fitted in between the GFRP beam and rectangular steel profile to ensure a tight fit and to avoid critical stress concentrations around the support. A stiff friction connection between the rectangular steel profile and GFRP beam is established through eighteen bolts. A more detailed description/representation of the design and dimensions of the clamped support are given in [16].

Experimental substructure (part: B)

The experimental substructure of the mrRTHS consist of a 1200mm long cantilever beam which is loaded in three dof by three actuators named: A, B and C cf. figure 3. Actuator A is a MTS model: 244.12 with a static and dynamic stroke of 182.9mm and 152mm respectively and force capacity of ±25kN. The actuator is operated by a 2 stage servo valve model: MTS 252.23G-01 with a capacity of 19l/min. The displacement of the actuator is measured by a Linear Variable Differential Transducer (LVDT) and the force obtained by an MTS load cell model: 661.19E-04 with a capacity of ±25kN. Actuator B and C is a MTS model: 242.01 with a static and dynamic stroke of 114.3 and 101.6mm respectively and force capacity of ±5kN. The actuators are operated by a 2-stage servo valve model: MTS 252.21G-01 with a capacity of 4l/min. All three actuators are operating at 3000psi pressure delivered by a hydraulic power unit (HPU). The Proportional Integral Derivative (PID) controller is a MTS model: TestStar II with a three channel configuration – controlled and monitored through the real-time target. The standard deviation of the repeatability offered by the transfer system is given in table 2. The repeatability is identified from a sample of 40000 measurements, acquired under constant conditions with a sampling frequency of 0.5 kHz.

Table 2: standard deviation (std.) of the repeatability offered by the transfer system

actuator label	act. A	act. B	act. C
std. displacemet [mm]	0.0103	0.0016	0.0017
std. force [N]	1.66	1.12	3.67

The response of the shared boundary is monitored through real time tracking of the three measurement points (MP's) applied on the shared boundary, see figure 3. This is achieved through a 3D DIC system of the type: ARAMIS 12M by Gesellschaft für Optische Messtechnik mbH (GOM). Through 24mm Titanar lenses a measurement volume of 200x150mm is achieved and calibrated using a 175x140mm calibration panel. The real-time tracking of the MP's are acquired, processed and transferred through an Ethernet port using the software: PONTUS live vs. 8. The in-plane and out-of-plane standard deviation of the repeatability offered by the DIC system is given by the average of MP-1, MP-2 and MP-3: dx = 0.419µm, dx = 4.157µm and dz = 0.777µm. The repeatability is identified from a sample of 10000 measurements, acquired under constant condition with a sampling frequency of 90 Hz. The MP's are illuminated with an even and high intensity to lower the shutter time as much as possible.

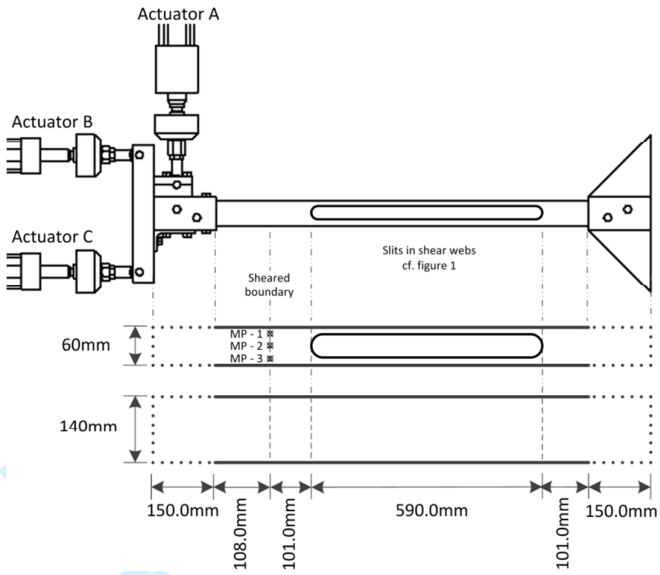

Figure 3: experimental substructure including: load train, support, specimen and MP's

A load introduction zone of 108mm is implemented between the shared boundary and the load introduction rig to erase any influence on the in-plane displacement field initiated by the rectangular steel profile. A numerical analysis of the setup verified that the influence was negligible for a load introduction zone longer than 100mm.

Experimental reference structure

A reference structure configuration is studied to reduce the complexity in verifying the mrRTHS communication loop capabilities and operation of the shared boundary. The experimental reference structure consists of an 1800mm long cantilever beam which is loaded in a single dof by actuator A cf. figure 4. The response of the loading point (MP - 4) is monitored through the LVDT and load cell on the actuator with the specifications further described in the previews section. The shared boundary is monitored through the 3D DIC system with the camera type, setup and performance as described in the previews section.

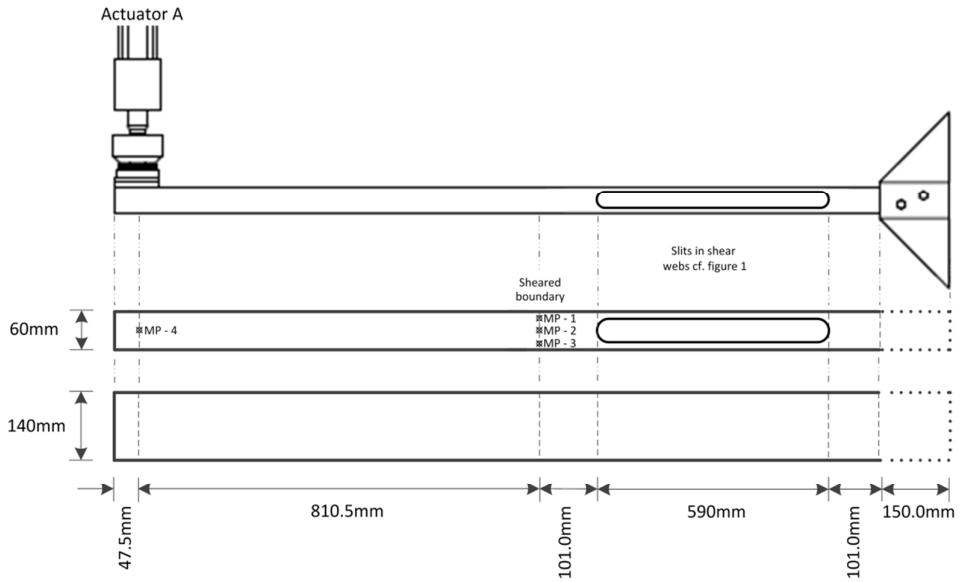

Figure 4: experimental reference structure including: load train, support, specimen and measurement points

The first and second natural frequency of the reference structure was experimentally identified to f_1 = 7.40Hz and f_2 = 47.3Hz through a vibration test further described in [24]. To access the first modal shape of the reference structure a modal analysis is performed through ANSYS 15.0 using isoparametric quadrilateral 8 node shell elements of the type: shell281. The model consists of 12841 elements and orthotropic material properties with the following extension to table 1: $E_2 = E_3$, all G-moduli are taken as the average of G_{12} and G_{21} i.e. ($G_{12}=G_{23}=G_{13}=3.235$) and all poisons ratio are taken as the average of ν_{12} and ν_{21} i.e. ($\nu_{12}=\nu_{23}=\nu_{13}=0.15$). The corresponding modal shape is presented in figure 5 with and eigenfrequency of f_1 = 8.90Hz.

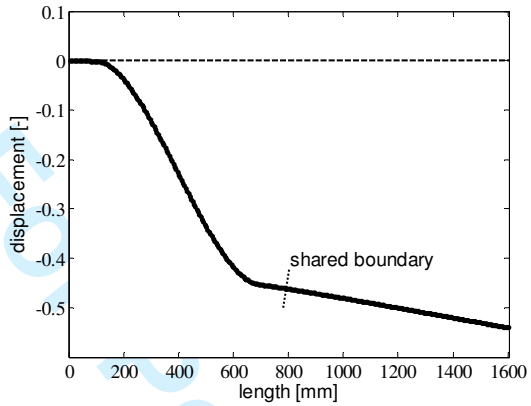

Figure 5: 1st modal shape of the cantilever beam generated by ANSYS

The increase of the Eigen frequency identified by the ANSYS model is caused by the clamped support which is modelled as infinitely stiff i.e. no rotation at the clamped end of the beam is allowed. This is not the case for the experimental reference structure where some rotation will be present in the clamped support **[16]**.

2.3. Numerical test setup

In the following is given a description of the numerical aspects of the hybrid simulation. First, the numerical substructure (part: A) is described. This part is used in the hybrid simulation. Next a finite element method (FEM) model of the full structure, used to verify the hybrid simulation, is described - referred to as the numerical reference structure.

The time integration is performed with the Central Difference Method (CDM), which is an explicit method, see e.g. [29]. This is chosen as it is simple to implement and does not require equilibrium iterations. The FEM model of the structure is modeled by two nodal plane Euler-Bernoulli beam elements with two translational dofs, v_{ix} and v_{iy}, and one rotational dof, θ_i, in each node, see figure 6. A detailed description of the element is presented in [25].

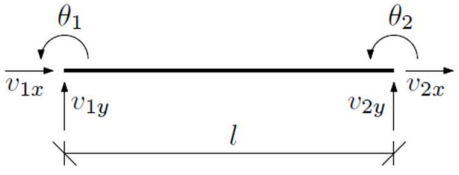

Figure 6: Plane Euler-Bernoulli Beam Element

Numerical substructure (part: A)

As described previously, the emulated structure consists of a numerical and experimental substructure. By distinguishing between the two substructures, the equations of motion (EOM) can be written as eq. (1).

$$\boldsymbol{M}_n\ddot{\boldsymbol{x}} + \boldsymbol{C}_n\dot{\boldsymbol{x}} + \boldsymbol{Q}_n + \boldsymbol{R} = \boldsymbol{F} \quad (1)$$

The matrices **M** and **C** represent the mass and damping matrices and the vectors **Q** and **F** the internal restoring forces and the external loading, respectively with the index n referring to the numerical substructure. Furthermore, **R** is a vector representing the inertia, damping and restoring forces of the experimental substructure, obtained by the actuators.

To reduce the computational resources required to execute the simulations in real time the EOM are projected onto a reduced basis. The basis applied in the given case is a so called Taylor basis, which combines a set of linear modes and their associated modal derivatives. The modal derivatives represent the higher order effects of the deformations introduced by the linear modes. These are important to include in nonlinear systems if effects such as membrane locking should be avoided. The Taylor basis is described in full detail in [25], [26]. In the given case the linear modes are determined from the linearized eigenvalue problem presented in eq. (2).

$$(\boldsymbol{K}_T - \omega_i^2\boldsymbol{M})\boldsymbol{\varphi}_i = \boldsymbol{0} \quad (2)$$

Here $\mathbf{K}_T$ is the tangent stiffness matrix, $\boldsymbol{\varphi}_i$ is the i'th linear modal vector and ω_i its associated frequency. The modal derivative of mode number i with respect to the reduced co-ordinates, s_j, is written as, $\frac{\partial \boldsymbol{\varphi}_i}{\partial s_j}$, and can be determined from eq. (3), see [25];

$$\left(\boldsymbol{K}_T - (\omega_i + \omega_j)^2\boldsymbol{M}\right)\frac{1}{2}\left(\frac{\partial \varphi_i}{\partial s_j} + \frac{\partial \varphi_j}{\partial s_i}\right) = \left[\frac{1}{m_j}\boldsymbol{\varphi}_j^T\left(\frac{\partial \boldsymbol{K}_S}{\partial s_k}\boldsymbol{\varphi}_j - \frac{\partial \boldsymbol{K}_S}{\partial s_j}\boldsymbol{\varphi}_k\right)\boldsymbol{M} - \frac{\partial \boldsymbol{K}_S}{\partial s_k}\right]\boldsymbol{\varphi}_j \quad (3)$$

Here $\mathbf{K}_s$ is the secant stiffness and m_j is the modal mass associated with mode j. It should be stressed that the modes determined from eq. (2) and (3) are based on the full structure which includes the full FE - model including both the physical and numerical substructure. The consequences and assumptions made when including the physical substructure in the modes is discussed in detail in chapter 5. The basis vectors are organized in the matrix $\boldsymbol{\phi}$. Projecting eq. 3 on the basis, the equations take the form presented in eq. 4.

$$\boldsymbol{\phi}^T(\boldsymbol{M}_n\boldsymbol{\phi}\ddot{\boldsymbol{s}} + \boldsymbol{C}_n\boldsymbol{\phi}\dot{\boldsymbol{s}} + \boldsymbol{Q}_n + \boldsymbol{R}) = \boldsymbol{\phi}^T\boldsymbol{F} \quad (4)$$

As shown in [25] and [26] the co-ordinates of the modal derivatives are given as a product of the linear mode co-ordinates. Thus, the number of unknowns corresponds to the number of linear modes only. Therefore, before solving the EOM in eq. (4) these are transformed into a linear set of equations - for details see [26].

Numerical damping of the magnitude 20% is included to damp out the high frequent response related to the included modes. This is done in order to stabilize the hybrid simulation. The damping is included in the linear mode through the principle of '*Superposition of Modal Damping Matrices'*, see e.g. [30]. As the linear modes and the modal derivatives are coupled, damping of the linear modes will have a damping effect on the modal derivatives as well.

A suitable time step increment is required to ensure precision and stability of the numerical substructure. An increasing natural frequency of interest comes with a reduced time step which requires additional onboard computational resources. In the given case the real-time target requires a time step magnitudes to be $\Delta t \geq 10^{-2}s$ to maintain real-time constraints. To meet this criteria only the first linear mode and its associated modal derivative can be included in the basis. Further modes would introduce higher frequencies and make the system turn unstable for a time step $\Delta t \geq 10^{-2}s$. The first linear mode and associated derivative is presented in Figure 7.

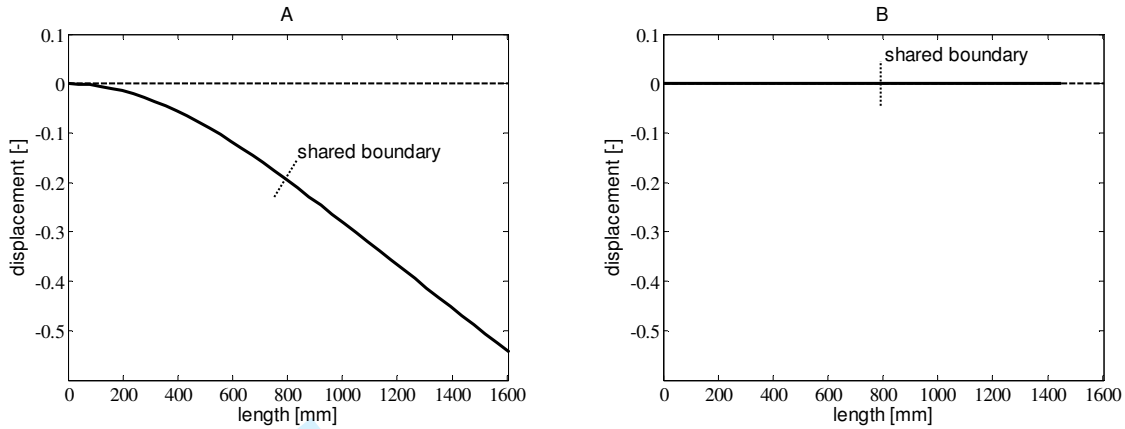

Figure 7: modal shape of the cantilever beam generated by plane Euler-Bernoulli elements: A) 1st linear mode and B) its associated derivative

Here the dashed and solid line outlines the initial and deformed position of the beam respectively. The linear mode is seen to be a bending mode and the modal derivative is a horizontal contraction. The horizontal deformation is kinematic nonlinear effect introduced when the beam is exposed to bending.

The linear bending mode in Figure 7 is significantly different from the first mode of the numerical reference structure presented in Figure 5. Thus, by only being able to include a single mode, displacement discontinuities at the shared boundary are expected.

Numerical reference structure

A full numerical model is organized in order to verify the output from the mrRTHS. The Euler-Bernoulli element, however, does not include the effect of shear flexibility. To account for this effect in the best way, the experimental substructure is modeled with a linear beam element in the numerical reference structure where the second moment of area I is scaled such that the deformations of the full FEM model attains the value (P,u) presented in Figure 12a in the quasi-static regime. The reference point chosen is (P,u) = (50 N, 10 mm), representing the linear regime of the experimental reference structure.

3. Overall testing strategy and equipment

3.1. Hardware

The overall hardware setup of the mrRTHS system is separated into four components including: 1) real-time target, 2) monitoring PC, 3) DIC system and 4) transfer system. A representation of the overall hardware setup and communication flow is illustrated in figure 8.

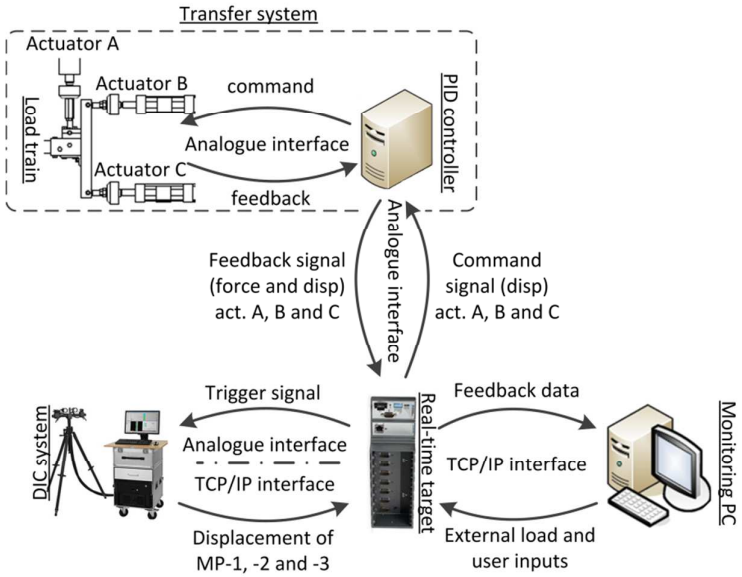

Figure 8: representation of the overall hardware setup

Here the real-time target consists of a CompactRIO 9074 (cRIO – 9074) [31] which is integrated to provide reliable, deterministic and real-time control and monitoring capabilities. The cRIO - 9074 system combines an onboard reconfigurable field-programmable gate array (FPGA) and 400MHz real-time single-core processor – referred to here as the Digital Signal Processor (DSP) – within the same chassis. An analogue interface between the DIC system, transfer system and cRIO – 9074 is handled through a digital to analogue (NI9263) [32] and analogue to digital (NI9205) [33] I/O module. The cRIO – 9074 and I/O module combine to form the real-time target.

The monitoring PC continuously transmits the predefined external load and user defined inputs, while receiving feedback data from the real-time target through Ethernet port 1. This configuration provides ample onboard memory and a Graphical User Interface (GUI) for the operator.

Through Ethernet port 2 in the real-time target the DIC system is connected. Here the in-plane displacement of the MP's on the shared boundary (see figure 3 and 4) are tracked in real-time and transferred to the real-time target through the Transmission Control Protocol/Internet Protocol (TCP/IP) interface. The communication delay - being the time from a displacement of the shared boundary occurs to the measurement is available to the real-time target - is quantified through an analogue trigger signal.

The transfer system consists of a load train driven by 3 servo hydraulic actuators named: A, B and C along with a PID controller cf. figure 3 and 8. The PID controller is operated and monitored by the real-time target through an analogue signal to ensure a reliable and real-time performance interface.

3.2. Communication loop and testing procedure

The main architecture of the mrRTHS communication loop is separated into three parallel processes named: 1) Main-loop, b) Outer-loop and c) transfer system. The outline of the dataflow in the mrRTHS communication loop is separated in 12 units labeled from **(1)** to **(12)** cf. figure 9.

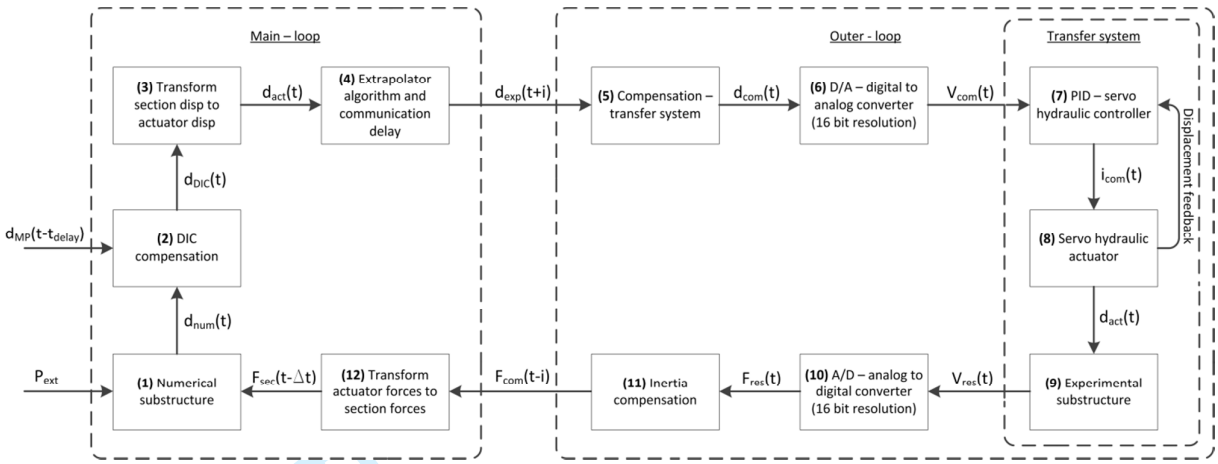

Figure 9: Schematic block diagram representing the overall architecture for the mrRTHS communication loop

The main-loop is operated in the time domain t through the DSP on the real-time target with a coarse time step of 50Hz (i.e. Δt = 0.020 sec) to save computational resources. Here the numerical substructure computes the next displacement signal $d_{num}(t)$ = [dx(t), dy(t), f(t)] in **(1)** based on the external load P_{ext} and last available reaction force $F_{sec}(t-\Delta t)$ = [N(t-Δt),V(t-Δt),M(t-Δt)]. For stability reasons **(1)** is executed with a numerical time step of 0.010 sec (100Hz) by using the same reaction force $F_{sec}(t-\Delta t)$ twice for each main-loop iteration – for further information see subchapter 2.3. The reaction forces from actuator A, B and C are transformed to section forces $F_{sec}(t-\Delta t)$ through a trigonometric relation in **(12)**, assuming rigid body motion [16]. To handle the effect of the compliance in the load train a DIC compensator is implemented in **(2)**. A schematic of the switching logic between the DIC compensator **(2)** and DIC – system are outlined in figure 10. Here the latest available in-plane displacement $d_{MP}(t-t_{delay})$ = [dx(t-t_{delay}), dy(t-t_{delay})] for each of the three measurement points on the shared boundary is transferred to the real-time target upon request. The real-time tracking rate achieved by the DIC system is 90Hz (dt = 0.011sec) with a time delay of t_{delay} = 160ms. The in-plane deformations $d_{MP}(t-t_{delay})$ are transformed to a 3 dof displacement on a discrete point with the format $d_{sec}(t-t_{delay})$ = [dx(t), dy(t), f(t)] by deriving the dx and dy translation as the average of the three measurement points while the rotation around the z-axis is determine by the angle between MP-1 and MP-3 [24]. Knowing the target displacement of the shared boundary $d_{num}(t-t_{delay})$, actual measured displacement $d_{sec}(t-t_{delay})$ and previews error $d_{error}(t-\Delta T)$ the current error can be derived as $d_{error}(t) = (d_{num}(t-t_{delay}) - d_{sec}(t-t_{delay})) + d_{error}(t-\Delta T)$. Tuning of the DIC compensation is conducted with the gain K_{gain} meaning that the current compensated displacement signal is given by $d_{DIC}(t) = K_{gain} \cdot d_{error}(t) + d_{num}(t)$. The compensated displacement $d_{DIC}(t)$ = [dx(t), dy(t), f(t)] is converted to an equivalent displacement for each of the three actuators $d_{act}(t) = [d_A(t),d_B(t),d_C(t)]$ through a trigonometric algorithm following the assumption of rigid body motion [16]. Through the current and previews data points provided for each of the three actuators by **(3)** the displacement signal is resampled through extrapolation $d_{exp}(t+i)$ in **(4)** with the time increment dt for iν[0;Δt]. Furthermore the predicted system response after the communication delay is identified as the displacement signal and included in the $d_{exp}(t+i)$ by superposition. The extrapolator and delay compensator in **(4)** are both handled by a 3rd order polynomial fitting algorithm, further described in subchapter 4.2.

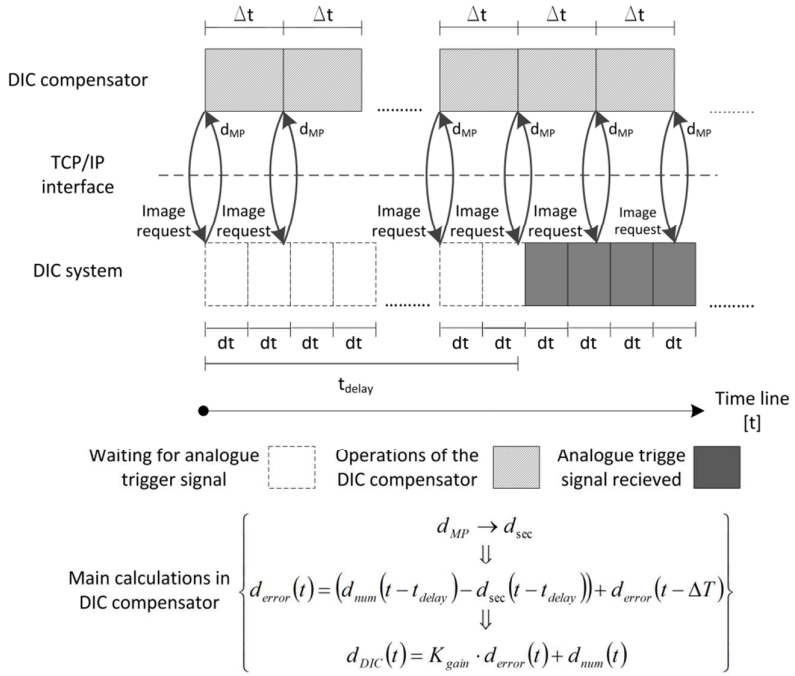

Figure 10: Schematic of the DIC compensator and DIC system switching logic and main calculations

The outer – loop is operated through the FPGA with an execution rate of 500Hz (i.e. $\delta t = 0.002$ sec) to generate a smooth command signal for the experimental substructure. Here the dynamics of the entire transfer system is handled through a direct inverted first order compensator in **(5)** for each of the three actuators. Further details of the compensator are given in subchapter 4.1. From the data points provided by **(5)** an equivalent analogue signal $V_{com}(t)$ is generated in **(6)** to operate the transfer system. The corresponding reaction force $V_{res}(t)$ are acquired from the transfer system and converted to a digital signal $F_{res}(t)$ by **(10)**. In order to compensate for the inertia effects induced by the load train – which acts as a lumped mass applied on the tip of an cantilever beam – an inertia force compensator is implemented in **(11)** [24]. Through the vertical displacement dy(t) of $d_{num}(t)$ an equivalent acceleration is derived. Knowing the mass of the load train and current acceleration the equivalent load can be derived from newton's second law. This force is subtracted from the current vertical load V from $F_{sec}(t-\Delta t)$ by obtaining the reaction force from the specimen.

The communication interface between the main- and outer-loop which is running with a sampling frequency ratio of ($\Delta t/\delta t = 10$) – referred to here as an execution rate of 1:10 - is handled through a producer/consumer configuration further specified in [34].

The transfer system is operated against the real-time analogue command signal $V_{com}(t)$ received from **(6)** with an execution frequency of 3 KHz. Through the PID controller in **(7)**, an electrical current $I_{com}(t)$ is generated and passed to the servo hydraulic actuators in **(8)** causing the actuators to move $d_{act}(t)$. The corresponding reaction forces induced on the load cells $V_{res}(t)$ is obtained from the experimental substructure in **(9)**.

4. System characterization

4.1. Transfer system dynamics

The dynamics of the transfer system represents a significant source of delay/lags in the mrRTHS communication loop – thus compensation is crucial to ensure accuracy and stability of the RTHS [35]. To handle the dynamics of each of the three actuators included in the transfer system over the frequency and amplitude range of interest a direct inverted

first order feed forward (FF) compensator is implemented. The discrete first order direct inverted compensator $K_i(z)$ is presented in the z-domain by eq. (5).

$$K_i(z) = \frac{\propto z-(\propto -1)}{z} \quad \text{for} \quad \text{i = actuator A, actuator B, actuator C} \tag{5}$$

Here $\propto$ is calibrated for each of the three actuators so that the measured and desired displacement correlate. This calibration process is conducted through an open loop chirped sinusoidal signal with a linearly increasing frequency ranging from 0 to 3 Hz for the duration of 40 seconds and constant peak-to-peak amplitude of 19.81mm, -1.46mm and 0.92mm for actuator A, B and C respectively. The amplitude is identified on the basis of the displacement of the shared boundary identified for the experimental reference (see table 3). The time domain comparison of the actuator performance is represented in figure 11.

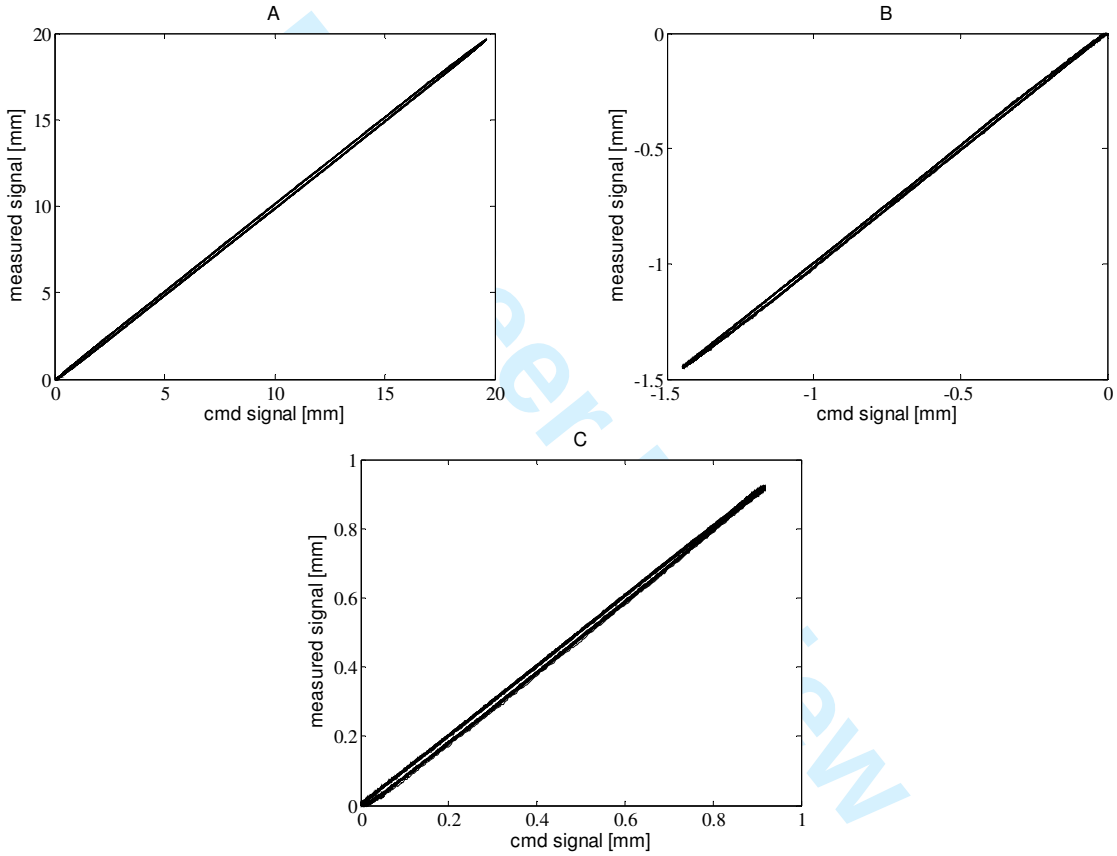

Figure 11: Time domain comparison of actuator performance with a single-order FF controller: a) act. A, b) act. B and c) act. C

Here a sound correlation between the desired and measured displacement of the actuator is identified, indicating that the single-order FF compensator is adequate for the given application.

4.2. Communication delay and extrapolation

Both the communication delay and extrapolation is handled through a forward prediction scheme of the type: third order polynomial fitting algorithm developed by [36]. Several of other prediction schemes have been investigated for the use in mrRTHS [22] – however the third order polynomial fit algorithm was identified as the best solution in terms of tracking performance and computational efficiency [34]. Through the use of the current and three previews data points provided by the numerical substructure with the time step $\triangle t$, the control signal is extrapolated with a predefined time step of δt in eq. (6).

$$d_{exp} = \sum_{i=0}^{N} a_i d_i \quad (6)$$

Here d_{exp} are the control signal with the time step Δt, d_i the current and three previous data points provided by the numerical substructure and a_i the polynomial coefficients generated through the Lagrange formula. For a fully independent relation between the main loop time step Δt and outer loop time step δt, the polynomial coefficients a_i are given by eq. (7) – (10) cf. [36].

$$a_0 = \frac{\delta t}{\Delta T}\left(\frac{11}{6} + \frac{\delta t}{\Delta T} + \frac{1}{6}\left(\frac{\delta t}{\Delta T}\right)^2\right) \quad (7)$$

$$a_1 = -\frac{\delta t}{\Delta T}\left(3 + \frac{5}{2}\frac{\delta t}{\Delta T} + \frac{1}{2}\left(\frac{\delta t}{\Delta T}\right)^2\right) \quad (8)$$

$$a_2 = \frac{\delta t}{\Delta T}\left(\frac{3}{2} + 2\frac{\delta t}{\Delta T} + \frac{1}{2}\left(\frac{\delta t}{\Delta T}\right)^2\right) \quad (9)$$

$$a_3 = -\frac{\delta t}{\Delta T}\left(\frac{1}{3} + \frac{1}{2}\frac{\delta t}{\Delta T} + \frac{1}{6}\left(\frac{\delta t}{\Delta T}\right)^2\right) \quad (10)$$

The tracking performance of the polynomial fitting extrapolator is investigated in [34] through a chirped sinusoidal open loop signal for an execution rate of 1:10. Here an error between the desired and extrapolated signal were identified to 0.10% for a frequency up to 3Hz. Given that the identified error is independent of the signal amplitude an error of 0.10% will be expected for all three actuators.

5. Test results and discussion

5.1. Response of the reference structure

The reference structure represented in figure 1 is tested in two configurations including an experimental and numerical representation. Initially the correlation of the global response between the numerical and experimental reference structure are investigated in the quasi-static regime cf. figure 12a. Here the force-displacement response of MP-4 for both reference structures is linear up to approximately 100N. Beyond this point the stiffness of the experimental reference structure decreases significantly with a local maximum of around P = 230 N. The response of the numerical reference structure seems to make a slight increase in the stiffness for a load P > 100N. It is expected that the behavior of the numerical reference structure exhibits a higher stiffness than the experimental reference structure given that the former does not include shear flexibility - as discussed previously. However, the softening behavior of the experimental reference structure cannot be attributed to the shear flexibility. The significant stiffness reduction is an effect originating from geometric nonlinearities where the flange at the shear slits is exposed to a local instability. This was furthermore visually verified during the quasi-static test presented in figure 12a.

To compare the global response of the experimental and numerical reference structure in the real-time regime the GFRP beam is loaded by a sinusoidal deformation P_{ext} with a peak-to-peak amplitude of 25mm and excitation frequency including: f_1 = 0.074Hz, f_2 = 0.74Hz, f_3 = 1.48Hz, f_4 = 2.22Hz and f_5 = 2.96Hz - equivalent to 1%, 10%, 20% 30% and 40% of the first natural frequency. From figure 12b the peak-to-peak reaction force decreases as a function of an increasing excitation frequency. This is explained by fact that more inertia is introduced into the system when the excitation frequency is increased. Furthermore, the experimental reference substructure seems to be more affected by the inertia effects than the numerical reference structure. This is most likely caused by the weight of the steel and rubber plate located between the load cell and GFRP beam – see figure 4. The peak to peak reaction force of the numerical reference structure is shifted and located slightly higher than in the experimental reference. This is in accordance with the force-displacement curve in Figure 12a, where a 25 mm displacement is seen to be outside the linear domain, indicating that the stiffness of the numerical reference is higher than the experimental reference.

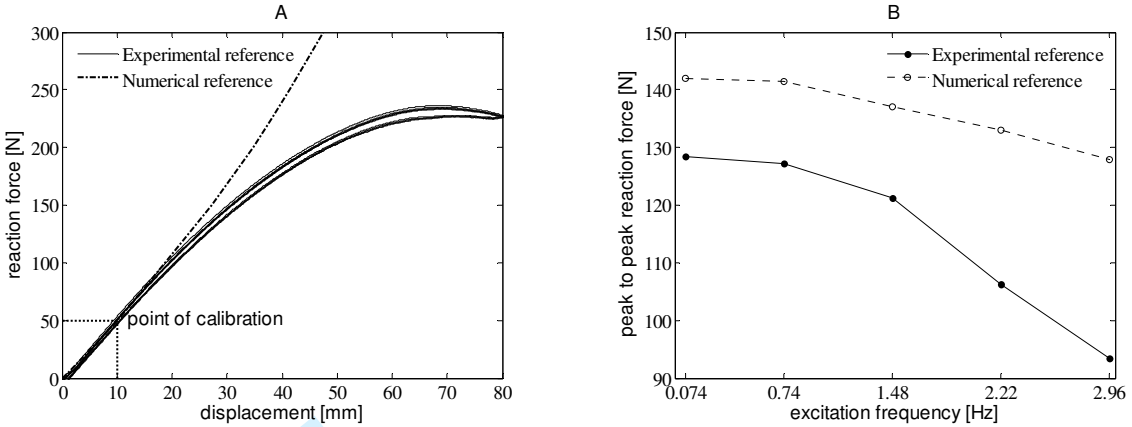

Figure 12: response of MP-4 in the reference structure: a) quasi-static response and b) peak-to-peak reaction force amplitude for a constant deformation of 25mm of MP-4

The displacement obtained at the shared boundary is represented in table 3 for a 25mm vertical displacement at MP-4. Here a large deviation between the numerical and experimental reference structure are present. The experimental reference is seen to experience the largest translations, whereas the largest rotation is found in the numerical reference. The significant deviations can be explained by the difference in the deformation shapes of the two reference structures – see figure 5 and 7. The deformation of the numerical reference is a pure bending deformation, as indicated in Figure 7a with a steady increase in both translations and rotation. The experimental reference structure, on the other hand, will experience a local deformation around the slits with large translations and rotations cf. figure 5. The rotation at the shared boundary required to reach 25 mm at MP-4, is therefore smaller than in the numerical reference.

Table 3: displacement of the shared boundary with a 25mm vertical displacement of MP-4

	dx [mm]	dy [mm]	£ [rad]
experimental reference	-0.563	-18.68	5.894e-3
numerical reference	-0.053	-8.10	18.91e-3
error [%]	90.58	56.64	220.8

Thus, by calibrating the numerical reference structure from the displacement at MP-4 as described in subchapter 2.3, discontinuities of the response at the shared boundary is inevitable introduced due to the lack of shear flexibility in the implemented element formulation.

5.2. Single component mrRTHS

The global response of the cantilever GFRP beam is evaluated in the real-time regime through a single component mrRTHS. Here the GFRP beam is loaded by a sinusoidal deformation P_{ext} with a peak-to-peak load of 130N with an excitation frequency including: $f_1 = 0.074$Hz, $f_2 = 0.74$Hz, $f_3 = 1.48$Hz, $f_4 = 2.22$Hz and $f_5 = 2.96$Hz - equivalent to 1%, 10%, 20% 30% and 40% of the first natural frequency. The mrRTHS is evaluated using a normalized error between the mrRTHS and numerical reference structure represented in eq. (11)

$$Error(t) = \frac{|mrRTHS(t) - REF(t)|}{max(|REF(t)|)} \cdot 100 \quad (11)$$

Due to global instability issues triggered by measurement noise and undesirable signal chattering induced by the extrapolator [22], [34] – a 75% reduction of the reaction force is introduced in the mrRTHS communication loop. An alternative approach would be to filter the generated displacement signal and/or the corresponding reaction force; however that was not possible due to the limited available computational resources offered by the real-time target.

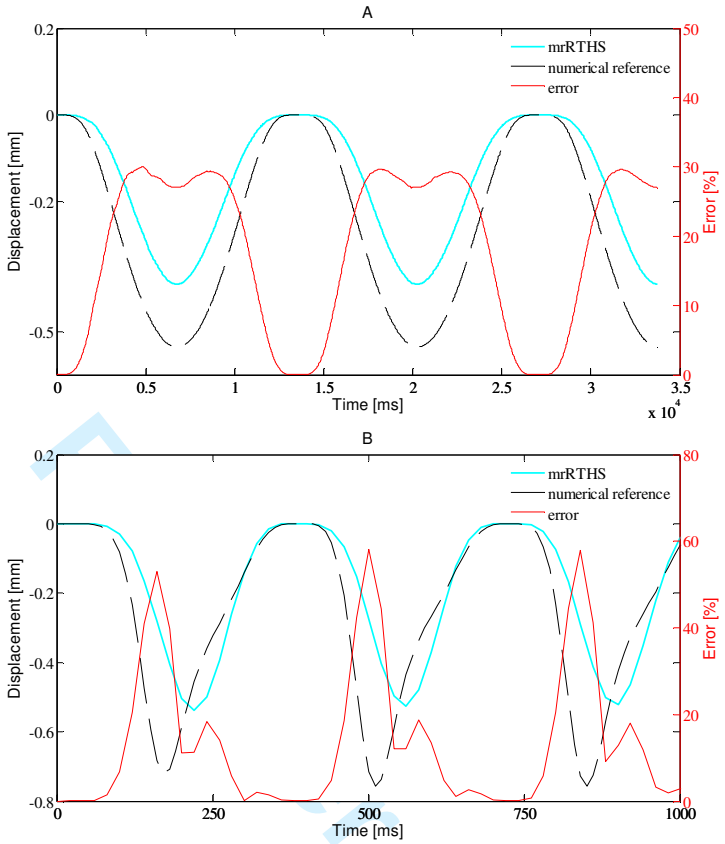

Figure 13: x-direction (dx) of the shared boundary for mrRTHS and reference including: a) f_1 = 0.074Hz and b) f_5 = 2.96Hz

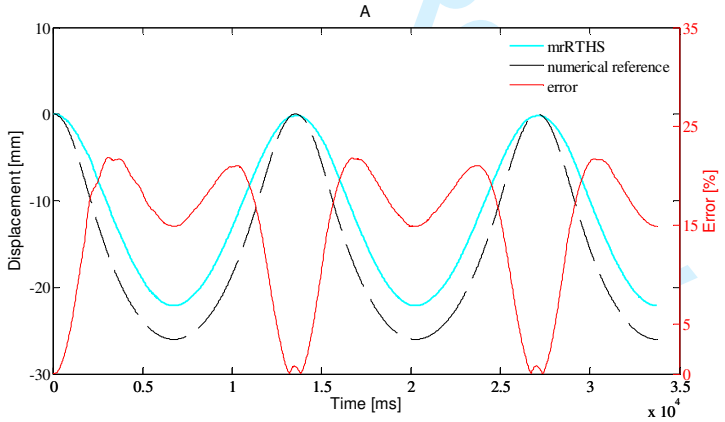

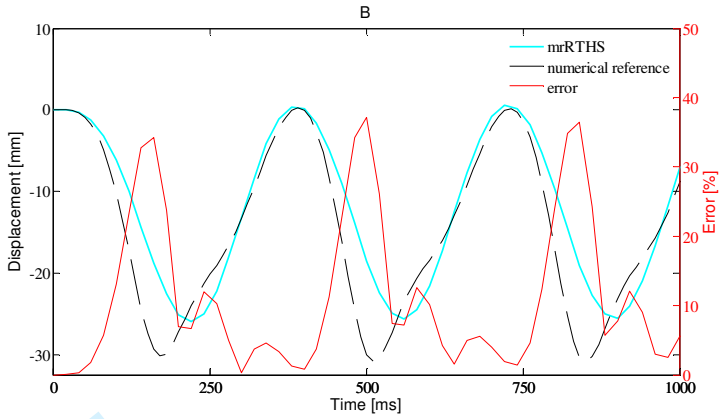

Figure 14: y-direction (dy) of the shared boundary for mrRTHS and reference including: a) f_1 = 0.074Hz and b) f_5 = 2.96Hz

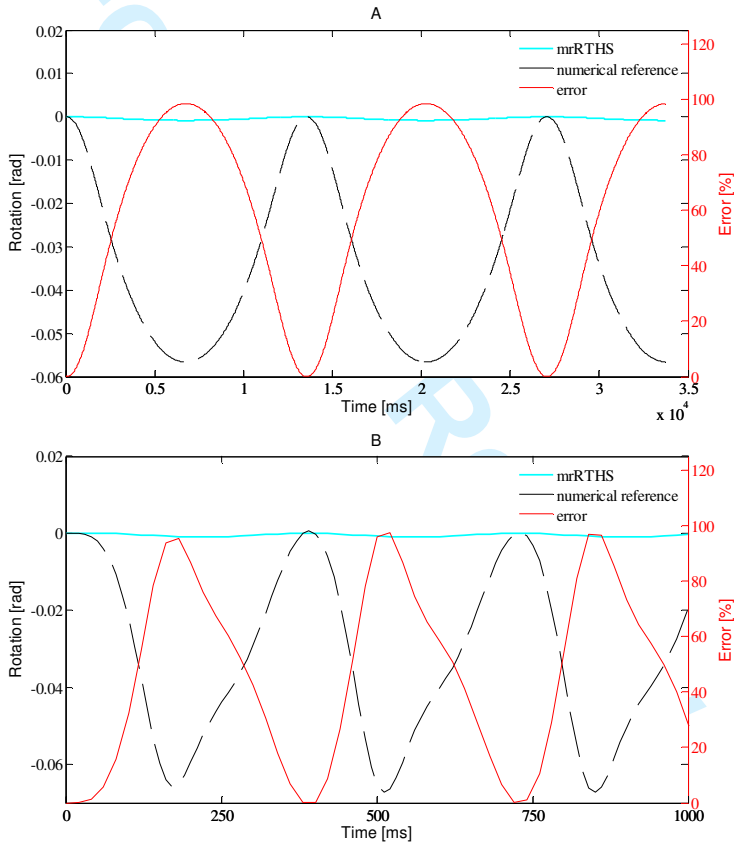

Figure 15: z-rotation (f) of the shared boundary for mrRTHS and reference including: a) f_1 = 0.074Hz and b) f_5 = 2.96Hz

In Figure 13 through 15 the in-plane displacement of the shared boundary for the two excitation frequencies f_1 = 0.074 Hz and f_5 =2.96 Hz are represented. The key results for the remaining frequencies (f_1 to f_4) are given in table 4. From the translations of the shared boundary in figure 13 and 14, the deformations in the mrRTHS are smaller than the numerical reference structure. Furthermore the reference responses are seen to be in phase for f_1. However in the f_5 case the numerical reference response is seen to be irregular. At the minima the numerical reference response is seen to be ahead of the mrRTHS response. However, this difference vanishes more or less between the local minima and maxima, as the reference response decreases its deformation speed. This is a dynamic effect, due to an increased influence of the bending mode. The bending mode has a natural frequency of 9 Hz for the numerical reference

structure. Thus, by increasing the excitation frequency from f_1 to f_5 - more energy in introduced into the mode. By increasing the damping of the system the effect was removed, confirming the consideration. For the remaining excitation frequencies represented in table 4 the peak error is increasing as a function of the frequency. However the root-mean-square (RMS) error is approximately constant supporting the fact that the irregularity seen at minima is very local along the time scale and does not influence the remaining wave shape. The difficulties in mimicking the dynamic effects through the mrRTHS method is most likely related to experimental errors including: transfer system dynamics, communication delay, sensor miscalibration, measurement noise and random truncations in the Analogue-to-Digital (AD) conversion of the communication interface between the real-time target and PID controller, etc. However the overall peak-to-peak displacement amplitude obtained for an increasing excitation frequency is increasing due to the dynamics in the system cf. table 4. The same effect is observed for the experimental and numerical reference structure cf. figure 12b.

Table 4: peak-to-peak displacement and error obtained through single component mrRTHS

direction		excitation frequency [Hz]				
		0.074	0.74	1.48	2.22	2.96
x-direction	peak-to-peak disp. ampl. [mm]	0.3906	0.4540	0.5123	0.5428	0.5394
	peak error [%]	30.03	30.26	46.98	56.75	58.05
	RMS error [%]	21.59	19.86	19.37	20.34	21.54
y-direction	peak-to-peak disp. ampl. [mm]	22.13	23.86	25.34	26.09	26.96
	peak error [%]	21.86	25.14	33.48	37.09	37.25
	RMS error [%]	16.23	15.32	15.01	15.06	15.64
z-rotation	peak-to-peak rot. ampl. [rad]	8.44e-4	9.09e-4	9.79e-4	10.25e-4	10.29e-4
	peak error [%]	98.51	98.46	98.40	98.78	98.81
	RMS error [%]	67.89	67.99	67.24	62.40	56.84

Considering the rotations of the shared boundary for the mrRTHS and reference structure in Figure 15, an evident difference appears. The rotation of the mrRTHS is seen to be significant smaller than the rotation in the reference structure. The reason for this is that the rotation introduced into the transfer system was erroneously reduced by a factor $\pi/180$, as if converted from degrees to radians. However, as the output from the numerical substructure is in radians, this reduction is meaningless. The rotations in the mrRTHS are therefore approximately zero compared to the rotations in the reference structure at the shared boundary. Due to the introduced rotation errors, a discussion of the results, are based primarily on the translation plots in Figure 13 and 14.

From the translational response in figure 13 and 14, a higher stiffness of the mrRTHS is unexpected – considering the results presented in figure 12 and table 3. However, two obvious reasons for the higher stiffness in the mrRTHS are given as the lack of rotations at the shared boundary and the applied modal basis. By restricting the rotation to be more or less zero when translations are imposed onto the shared boundary, a stiffer response is expected, compared to the case were the shared boundary were assigned a rotation which is a factor $180/\pi$ higher. Furthermore as only the first bending mode and its associated derivative are included in the applied basis, the local deformation in the region of the slits cannot be properly represented. Thus, by imposing the displacements of a pure bending mode onto the physical substructure, a further stiffness increase is expected.

The tracking performance between the mrRTHS (desired) and DIC (achieved) displacement of the shared boundary when using the DIC compensator is evaluated in table 5. Furthermore the correlation between the command signal (mrRTHS) and measured signal (DIC) are presented I figure 6 for an execution frequency of 0.074Hz.

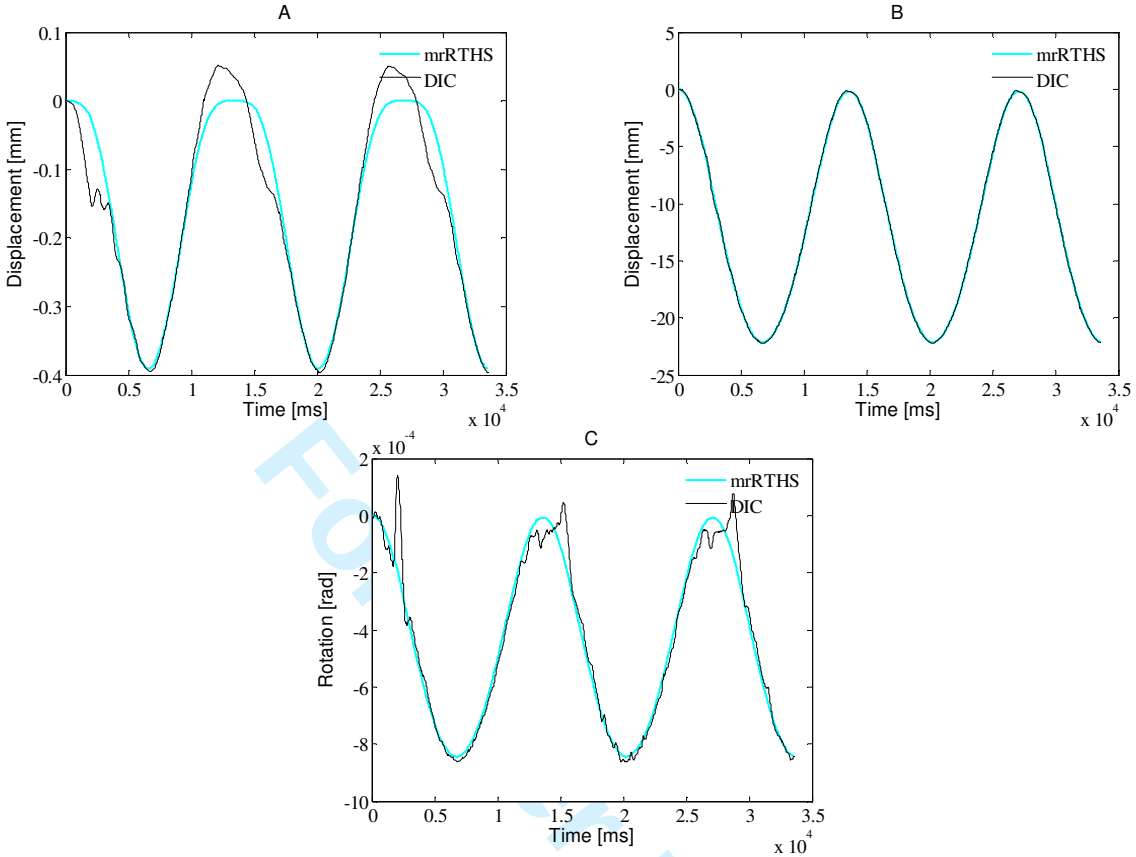

Figure 16: tracking performance of the shared boundary for mrRTHS including: a) x-direction, b) y-direction and c) z-rotation

Here a sound correlation between the desired and achieved displacement is achieved for an execution frequency of 0.074Hz. However for an increasing execution frequency the error is increasing as well due to the compliance of the test rig. This is expected due to the time delay of 160ms which is equivalent to 47.3% of a single period for an excitation frequency of 2.96 [24].

Table 5: error between the desired and achieved displacement of the shared boundary

direction		excitation frequency [Hz]				
		0.074	0.74	1.48	2.22	2.96
x-direction	peak error [%]	31.68	95.54	129.72	116.08	101.68
	RMS error [%]	9.19	30.85	40.45	26.94	22.14
y-direction	peak error [%]	2.31	9.97	16.81	32.15	31.56
	RMS error [%]	0.51	2.62	5.73	10.90	15.57
z-rotation	peak error [%]	39.74	38.54	57.38	68.22	68.85
	RMS error [%]	6.75	17.65	22.02	20.54	22.32

The missing ability to reach the target displacement due to compliance in the load train entails a reduced reaction force at the shared boundary – implying a reduced stiffness of the emulated structure.

6. Conclusion

A single component mrRTHS configuration was executed on a cantilever thin-walled GFRP beam with a rectangular cross sectional geometry loaded on the tip by a sinusoidal point load. This test configuration was chosen as a simplified substitute for a wind turbine blade in terms of geometry, scale and loads. Despite some inconsistencies

between the mrRTHS and reference the system proved successful which was an important milestone in the effort of conducting a successful single component mrRTHS on a wind turbine blade.

The mrRTHS was demonstrated on a single component structure and the performance evaluated against the corresponding reference. For the in-plane translational displacement in the shared boundary an RMS error of 19.37% to 21.59% and 15.01% to 16.23% were identified in the x- and y-direction respectively. For an increasing execution frequency of the external load a growing peak error between the mrRTHS and reference were identified. However, given that these peak errors were local along the time scale - this effect was not conclusive when measured as an RMS error. Furthermore, for an external load with constant amplitude the translational displacement were found to increase due to the inertia induced in the system. This effect was furthermore identified in the reference test presented in figure 12b. For the rotation around the z-axis a RMS errors of 56.84% to 67.99% was registered between the mrRTHS and refence. This very high error was due to the rotation received by the numerical substructure being erroneously reduced by a factor of $\pi/180$.

The error between the mrRTHS and corresponding reference in the in-plane translational displacement of the shared boundary was mainly triggered by the inconsistencies between the modal shape of the reference (see figure 5) and numerical substructure (see figure 7a). Furthermore having the rotation of the shared boundary being reduced by a factor of $\pi/180$ generated an increase of the stiffness in the mrRTHS representation outlined in figure 13 and 14. Other contributions to the identified error cover sensor miscalibration, transfer system dynamics, etc.

Due to instability issues in the mrRTHS communication loop the restoring force obtained by the experimental substructure was reduced to 15%. This instability was mainly triggered by undesirable signal chattering generated by the extrapolator. However other contributions to the instability were identified including the actuator dynamic and DIC compensator along with measurement noise and random truncations in the AD conversion. This instability could have been solved by e.g. filtering the command signal generated by the extrapolator – however due to the limited available computational resources offered by the real time target, this filter were not included in the mrRTHS communication loop.

7. Acknowledgement

The authors would like to acknowledge the financial support from the Danish Centre for Composite Structures and Materials (DCCSM) funded by the Danish Council for Strategic Research within Sustainable Energy and Environment (Grant: 09-067212). Furthermore, the authors acknowledge Fiberline Composites, Barmstedt Allé 5, 5500 Middelfart, DK, for the donation of the GFRP test specimens.

8. References

[1] X. Shao, A. M. Reinhorn and M. V. Sivaselvan, "Real-time Hybrid Simulation Using Shake Tables and Dynamic Actuators," *Journal of Structural Engineering,* vol. 137, no. 7, pp. 748-760, 2011.

[2] O. S. Bursi, A. Gonzalez-Buelga, L. Vulcan, S. A. Neild and D. J. Wagg, "Novel Coupling Rosenbrockbased algorithm for real-time dynamic substructure testing," *Earthquake Engineering and Structural Dynamics,* vol. 37, no. 3, pp. 339-360, 2008.

[3] S. A. Mahin, P.-S. B. Shing, C. R. Thewalt and R. D. Hanson, “Pseudodynamic test method. Current status and future directions,” *Journal of Structural Engineering New York, N. Y,* vol. 115, no. 8, pp. 2113-2128, 1989.

[4] P. B. Shing, M. Nakashima and O. S. Bursi, “Application of pseudodynamic test method to structural research,” *Earthquake Spectra,* vol. 12, no. 1, pp. 26-56, 1996.

[5] M. Nakashima, H. Kato and E. Takaoka, "Development of real-time pseudo dynamic testing," *Earthquake Engineering and Structural Dynamics,* vol. 21, no. 1, pp. 79-92, 1992.

[6] M. Nakashima and N. Masaoka, "Real time on-line test for MDOF systems," *Earthquake Engineering and Structural Dynamics,* vol. 28, no. 4, pp. 393-420, 1999.

[7] T. L. Karavalis, J. M. Ricles, R. Sause and C. Chen, "Experimental evaluation of the seismic performance of steel MRFs with compressed elatsomer dampers using large-scale real-time hybrid simulation," *Engineering Structures,* vol. 33, no. 6, pp. 1859-1869, 2011.

[8] M. Ito, Y. Murata, K. Hoki and M. Nakashima, "Online Hybrid Test on Buildings with Stud-Type Damper Made of Slitted Steel Plates Stifferened by Wood Panels," *Procedia Engineering,* vol. 14, pp. 567-571, 2011.

[9] A. Jacobsen, T. Hitaka and M. Nakashima, "Online test of building frame with slit-wall dampers capable of condition assessment," *Journal of Constructional Steel Research,* vol. 66, no. 11, pp. 1320-1329, 2010.

[10] C. Chen, J. M. Ricles, T. L. Karavasillis, Y. Chae and R. Sause, "Evaluation of a real-time hybrid simulation system for performance evaluation of structures with rate dependent devices subjected to seimic loading," *Engineering Structures,* vol. 35, pp. 71-82, 2012.

[11] Y. Z. Lin and R. E. Christenson, "Comparison of Real-time Hybrid Testing with Shake Table Test for an MR Damper Controlled Structure," in *Americam Control Conference*, St. Louis, Missouri, USA, 2009.

[12] J. E. Carrion, B. F. Spencer and B. M. Phillips, "Real-Time Hybrid Testing of a Semi-Actively Controlled Structure with an MR Damper," in *American Control Conference*, St. Louis, Missouri, USA, 2009.

[13] M. S. Williams, "Real-time hybrid testing in structural dynamics," in *The 5th Australasian Congress on Applied Mechanics*, Brisbane, Australia, 2007.

[14] F. M. Jensen, B. G. Falzon, J. Ankersen and H. Stang, “Structural Testing and Numerical Simulation of a 34m Composite Wind Turbine Blade,” *Composite Structures,* vol. 76, no. 1-2, pp. 52 - 61, 2006.

[15] F. M. Jensen, “Ultimate Strength of a Large Wind Turbine Blade,” Department of Civil Engineering, Technical University of Denmark, Kgs. Lyngby, Denmark, 2008.

[16] J. H. Hoegh, J. P. Waldbjoern, J. Wittrup-Schmidt, H. Stang and C. Berggreen, "Quasi-static single-component hybrid testing of a composite structure with multi-axial control," *STRAIN,* vol. 51, pp. 459-473, 2015.

[17] J. P. Waldbjoern, J. H. Hoegh, J. Wittrup-schmidt, M. W. Nielsen, K. Branner, H. Stang and C. C. Berggreen, "Strain and displacement controls by fibre bragg grating and digital image correlation," *Strain,* vol. 50, no. 3, pp. 262-273, 2014.

[18] X. Fayolle, S. Calloch and F. Hild, "Controlling testing machines with digital image correlation," *Experimental techniques,* vol. 31, no. 3, pp. 57-63, 2007.

[19] R. L. Sierakowski, "Strain rate effects in composites," *American Society of Mechanical Engineers,* vol. 50, no. 11, pp. 741-761, 1997.

[20] T. Horiuchi, M. Nakagawa, M. Sugano and T. Konno, "Development of real-time hybrid experiment system with actuator delay compensation," in *Proc. 11th World conference on Earthquake engineering* , Acapulco, 1996.

[21] S. J. Dyke, "Acceleration feedback control strategies for active and semi-active systems: modeling, alogrithm development and experimental verification," Ph.D. Dissertation, University of Notre Dame, IN, 1996.

[22] A. Maghareh, J. P. Waldbjoern, S. J. Dyke and A. Prakash, "Adaptive multi-rate interface: development and experimental verification of an interface for multi-rate real-time hybrid simulation," *Earthquake Engineering and Structural Dynamics,* Accepted for publication - december 2015.

[23] L. C. Overgaard, E. Lund and O. T. Thomsen, "Structural collapse of a wind turbine blade. part A: Static test and equivalent single layered models," *Composites: Part A,* vol. 41, pp. 257-270, 2010.

[24] J. H. Høgh, J. P. Waldbjørn, S. Andersen and C. Berggreen, "Compensation Methods in Real-Time Hybrid Simulation," *Strain,* Submitted for peer-review in 2016.

[25] S. Andersen and P. N. Poulsen, "Nonlinear Real-time Simulations Using a Taylor Basis," *International Journal for Numerical Methods in Engineering,* Submitted for peer-review in 2015.

[26] S. Andersen and P. N. Poulsen, "Reduction Method for Kinematic Nonlinear Real-time Simualtions," *International Journal for Numerical Methods in Engineering,* Submitted for peer-review in 2015.

[27] ASTM, "Standard Test Method for Tensile Properties of Polymer Matrix Composite Materials," ASTM International, West Conshohocken, Pennsylvania, United States of America, 2011.

[28] ASTM, "Standard Test Method for Shear Properties of Composite Materials by the V-Notched Beam Method," ASTM International, West Conshohocken, Pennsylnania, United States of America, 2014.

[29] R. D. Cook, D. S. Malkus, M. E. Plesha and R. J. Witt, Concepts and Applications of Finite Element Analysis, 4th edition, New York: John Wiley & Sons, 1974.

[30] A. K. Chopra, Dynamics of Structures: Theory and Application to Earthquake Engineering, Prentice-Hall, 1995.

[31] "http://www.ni.com/pdf/manuals/375874b.pdf," National Instruments, - 6 2014. [Online]. [Accessed 21 11 2014].

[32] "http://www.ni.com/pdf/manuals/373781e.pdf," National Instruments, - 8 2009. [Online]. [Accessed 12 11 2014].

[33] "http://www.ni.com/pdf/manuals/374188d.pdf," National Instruments, - 2 2008. [Online]. [Accessed 12 11 2014].

[34] J. P. Waldbjoern, A. Maghareh, G. Ou, S. J. Dyke and H. Stang, "Multi-rate Real Time Hybrid Simulation operated on a flexible LabVIEW real-time platform," *Smart Structures and Systems,* Submitted for peer review (2015).

[35] J. E. Carrion and B. F. Spencer, "Model-based Strategies for Real-time Hybrid Testing," Newmark Structural Engineering Laboratory, University of Illinois at Urbana-Champaign, Urbana-Champaign, Illinois, USA, 2007.

[36] P. A. Bonnet, "The development of multi-axis real-time substructure testing," University of Oxford, Oxford, United Kingdom, 2006.

[37] K. Takanashi and M. Nakaschiman, "Japanese Activities on ON-LINE Testing," *Journal of Engineering Mechanics,* vol. 113, no. 7, pp. 1014-1032, 1987.

[38] S. A. Mahin, P.-S. B. Shing, C. R. Thewalt and R. D. Hanson, "Pseudodynamic test method. Current status and future directions," *Journal of Structural Engineering,* vol. 115, no. 8, pp. 2113-2128, 1989.

[39] P. B. Shing, M. Nakashima and O. S. Bursi, "Application of pseudodynamic test method to structural research," *Earthquake Spectra,* vol. 12, no. 1, pp. 29-56, 1996.

[40] R. Bitter, T. Mohiuddin and M. Nawrocki, *LabVIEW Advanced Programming Techniques,* Florida, USA: CRC Press, 2001.

[41] G. Ellis, Control system design guide, San Diego, CA: Academic Press, 2000.

[42] B. M. Phillips and B. F. Spencer, "Model-based servo-hydraulic control for real-time hybrid simulation," Newmark Structural Engineering Laboratory, University of Illinois at Urbana-Champaign, Urbana-Champaign, Illinois, USA, 2011.

[43] M. Nakashima, "Development, potential, and limitations of real-time online (pseudo-dynamic) testing," *Philosophical Transactions of the Royal Society A: Mathematical, Physical and Engineering Sciences,* vol. 373, no. 2035, pp. 1851-1867, 2001.

[44] A. Ashasi-Sorkhabi and O. Mercan, "Development, implementation and verification of a user configurable platform for real-time hybrid simulation," *Smart Structures and Systems,* vol. 14, no. 6, pp. 1151-1172, 8 2014.

[45] D. Ferry, A. Maghareh, G. Bunting, A. Prakash, K. Agrawal, C. Lu and S. Dyke, "On the performance of a highly parallelizable concurrency platform for real-time hybrid simulation," in *The 6'th World Conference on Structural Control and Monitoring*, Barcelona, Spain, 2014.

[46] J. P. Waldbjoern, J. H. Hoegh, H. Stang, C. C. Berggreen, J. Wittrup-Schmidt and K. Branner, "Hybrid Testing of Composite Structures with Single-Axis Control," in *The 19th International Conference on Composite Materials*, Montréal, 2013.

[47] A. Maghareh, S. J. Dyke, A. Prakash and J. F. Rhoads, "Establishing a Stability Switch Criterion for Effective RTHS Implementation," *Journal of smart Structures and Systems,* vol. 14, no. 6, pp. 1221-1245. doi:10.12989/sss.2014.14.6.1221, 2014.

[48] A. Maghareh, S. J. Dyke, A. Prakash and G. B. Bunting, "Establishing a predictive performance indicator for real-time hybrid simulation," *Earthquake Engineering & Structural Dynamics,* vol. 43, no. 15, pp. 2299-2318. doi:10.1002/eqe.2448, 2014.

[49] C. Chen and J. M. Ricles, "A General Approach for Analysis of Actuator Delay Compensation Methods for Real-time Testing," in *The 14th World Conference on Earthquake Engineering*, Beijing, China, 2008.

This page is intentionally left blank

Appendix F

strain
An International Journal for Experimental Mechanics

Compensation Methods in Real-Time Hybrid Simulation

Journal:	*Strain*
Manuscript ID	Draft
Manuscript Type:	Full Paper
Date Submitted by the Author:	n/a
Complete List of Authors:	Høgh, Jacob; Technical University of Denmark, Department of Mechanical Engineering Waldbjørn, Jacob; Technical University of Denmark, Department of Civil Engineering Andersen, Sebastian; Technical University of Denmark, Department of Civil Engineering Berggreen, Christian; Technical University of Denmark, Department of Wind Energy
Keywords:	compensation method, composites, control, digital image correlation, finite element, hardware-in-the-loop, hybrid simulation, inertia force compensation, mRTHS, real-time

Title:

Compensation Methods in Real-Time Hybrid Simulation

Running Head Title:

Compensation Methods in RTHS

Authors:

Jacob H. Høgh (JHH)[1], jhho@mek.dtu.dk, phone: +45 45251967

Jacob P. Waldbjørn (JPW)[2], jpwa@byg.dtu.dk, phone: +45 40185431

Sebastian Andersen (SA)[2], seba@byg.dtu.dk, phone: +45 45255048

Christian Berggreen (CB)[1], cbe@mek.dtu.dk, phone: +45 45251373

Affiliations and Addresses:

1. Department of Mechanical Engineering, Technical University of Denmark, Kgs. Lyngby, Denmark, Nils Koppels Allé 403, 2800 Kgs. Lyngby, Denmark

2. Department of Civil Engineering, Technical University of Denmark, Kgs. Lyngby, Denmark Brovej 118, 2800 Kgs. Lyngby, Denmark

Compensation Methods in Real-Time Hybrid Simulation

Jacob Høgh[1], Jacob Waldbjørn[2], Sebastian Andersen[2] and Christian Berggreen[1]
[1]*Department of Mechanical Engineering, Technical University of Denmark*
[2]*Department of Civil Engineering, Technical University of Denmark*

Abstract

Hybrid simulation is a sub structural testing method where a structure's behaviour is obtained by combining a numerical simulation with a physical experiment. This paper presents compensation methods in real-time hybrid simulation in order to account for compliance and inertia forces of the load train in the physical experiment. The compensators are developed for hybrid simulation with a complex load train transferring several degrees of freedom in the shared boundary. The compensator accounting for the compliance of the load train utilizes digital image correlation in an outer control loop. The inertia compensator is applicable for test setups where the load train has considerable mass compared to the specimen. Both compensation methods proved valid for lower frequencies i.e. f < 1.48Hz, but due to communication lag and limitations in computational resources it was not possible to increase accuracy for loading frequencies higher than 2.96Hz hybrid simulation.

Keywords: compensation methods, digital image correlation, finite element model, hybrid simulation, real-time

Introduction

Hybrid simulation is a testing method where the main part of a structure is simulated while a subsection is tested in an experiment. The actions in the shared boundary between the simulation and experiment are fed between the two in an iterative process to simulate the behaviour of the entire structure [1]. The experiment is in this way implemented as a subroutine in the numerical calculation. Hybrid simulation is a well proven simulation method for structures with an overall linear response while a subsection behaves non-linearly. Hybrid simulation was developed during the 1970s for modelling structural behaviour in earthquake engineering [2]. Much effort has been made in earthquake engineering, especially for testing of damping systems for buildings [3], [4] and [5] or other earthquake protection [6], [7] and [8]. However, hybrid simulation has been applied to many different fields of engineering e.g. automobile [9], motor [10], robotics [11], space [12], train [13] and wind turbines [14] etc.

Much effort has been invested in developing and implementing explicit time integration schemes, e.g. central difference, operator splitting [15], direct integration algorithm [16], as well as implicit schemes, e.g. unconditionally stable implicit scheme [17], generalized alpha methods [18] and others. Furthermore, compensation methods to accommodate for the delay in the transfer system has been developed and implemented in hybrid simulation, e.g. feed-forward phase lead compensator and restoring force compensator [19], the improved adaptive inverse technique [20], prediction by third order polynomial fitted to previous displacement values [21], a discrete third order inverted compensator [22].

Hybrid simulation is therefore a well proven sub-structural testing method. However, in all the mentioned studies the focus has been on a fairly simple connection between the numerical model and the physical experiment, the so called shared boundary. This limits hybrid simulation to testing of structures where the shared boundary is made up of a hinge or other simple fixtures so that the actions from the experiment are easily translated to the numerical model and vice versa, this being the case when testing e.g. earthquake damper [23]. In

the study presented in this paper, the authors seek to broaden the application of hybrid simulation to structures with a more complex shared boundary between the numerical model and physical experiment. This being the case in structures where no clear mechanical connection is dividing the structure in the physical experiment and numerical model, formerly referred to as single component hybrid simulation [24]. In this type of testing the number of degrees of freedom in the shared boundary is in principal infinite and the transferring and monitoring of actions between numerical model and physical experiment therefore not trivial [25].

The main focus of this paper is to develop compensation methods for hybrid simulation of a structure with complex shared boundary. As mentioned before this setup requires a comprehensive load train and the compliance and inertia forces of this therefore becomes an issue during dynamic testing. The compliance problem is solved by measuring the displacements directly on the specimen and correcting the applied displacement in an outer control loop similar to the one developed in [26] except here, the displacements and rotations are measured by digital image correlation (DIC) and the trigonometric relation between the shared boundary and actuators different. The inertia force due to the mass of the load train is compensated for by measuring the accelerations, deriving the inertia forces and subtracting them from the restoring forces. The compensators are tested in a real-time hybrid simulation using the central difference method for time integration, a Lagrange polynomial [27] extrapolator for the command signal and an single order direct inverted compensator [28] to account for the transfer system delay. The hybrid simulation is conducted on a glass fibre reinforced polymer (GFRP) beam clamed in on end and free in the other.

Test Setup

The full structure selected for the analysis was a GFRP (Glass Fibre Reinforced Polymer) composite box girder clamped at one end and loaded vertically by an actuator at the tip. Two holes were made in the sides of the structure of length 590mm and height 45mm in order to weaken the shear stiffness thereby yielding non-linear stress strain behaviour due to large strains. The dimensions of the beam are presented in Fig. 1.

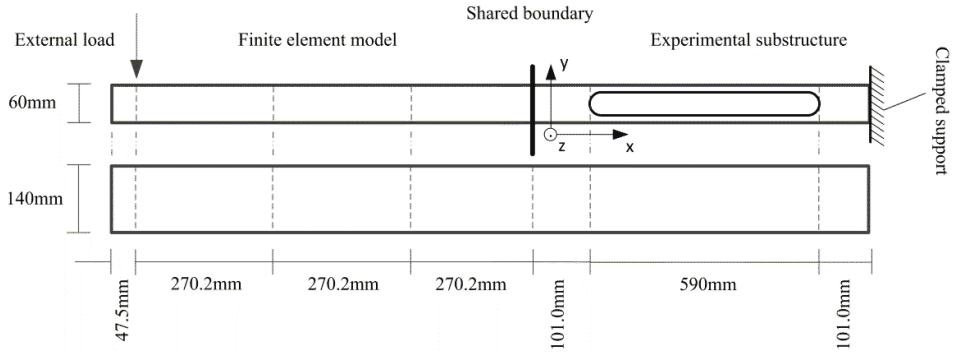

Fig. 1 The dimensions of the full structure that is separated in numerical model and Experimental subsection

In the hybrid simulation the experimental subsection consist of the beam from the clamped support and 792mm towards the tip, cf. Fig. 1. The remainder of the beam is modelled numerically and due to the lack of boundary conditions statically under determinate, however the model is restrained by the restoring forces from the experimental substructure iteratively fed into the finite element model. The experimental setup for the hybrid simulation is presented in Fig. 2 (a) and (b). The transition zone between the shared boundary and the load train of 108mm is selected in order to ensure that any stress concentrations from the load train, is not measured in the shared boundary by the DIC system.

a) b)

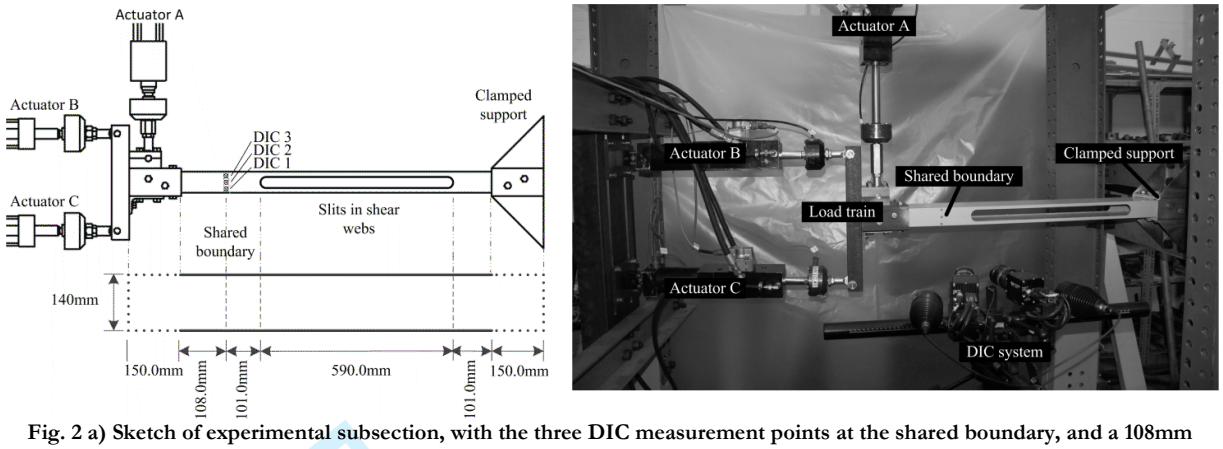

Fig. 2 a) Sketch of experimental subsection, with the three DIC measurement points at the shared boundary, and a 108mm transition zone between the experimental subsection and the load train b) picture of the experimental setup

Material Properties

The material properties of the structure have been determined for another specimen from the same batch of the pultruded GFRP beam, cf. [25]. The stiffness was determined in accordance with D3039/D3039M – 08 [29] and D5379/D5379M – 12 [30]. The 1 direction is longitudinal of the beam, 2-direction is in-plane perpendicular.

Table 1 Stiffness properties of the composite

E_1 [GPa]	E_2 [GPa]	ν_{12} [-]	ν_{21} [-]	G_{12} [GPa]	G_{21} [GPa]
28.36	9.96	0.23	0.08	3.41	3.06

The characteristic material strengths are specified in the Fiberline Composites A/S manual [31].

Table 2 Characteristic strengths of pultruded glass fiber beam

Property	-	Unit
Tensile 0°	240	MPa
Tensile 90°	50	MPa
Compression 0°	240	MPa
Compression 90°	70	MPa
Shear	25	MPa
Mass	1825	kg/m³

The dynamic properties of the structure are determined by a modal analysis of the reference structure. The natural frequencies were determined to: f_1 = 8.90Hz and f_2 = 52.59Hz, for the first and second vertical bending modes. The natural frequencies was later determined in a vibration test, where the full structure was stroke by a hammer and the accelerations was measured by an accelerometer connected to a vibration meter and logged by a A/D instrument. The frequencies was determined to f_1 = 7.40Hz and f_2 = 47.3Hz. The first natural frequency is used as a reference for the hybrid simulation hence the tests are performed with and external loading, cf. Fig. 1, with frequency at: 1%, 10%, 20%, 30% and 40% of the first natural frequency.

Test Equipment

The hybrid simulation program is running on a LabVIEW compact Rio board NI9073, that send command signals a PID (Proportional-Integral-Derivative) controller by LabVIEW output module NI9263 16bit resolution and 100kHz signal generation frequency [32]. The signals from the controller and DIC system is input by a

LabVIEW NI9205 module with 16bit of resolution and 250kHz acquisition frequency [33]. The PID controller is an MTS (Material Testing Systems, 14000 Technology Drive, Eden Prairie, MN USA 55344) TestStar II controller with three channels and 3.0kHz command signal generation. The hydraulic actuators are: one MTS ±25kN actuator with a ±25kN load cell and LVDT (Linear Variable Differential Transducer) with static and dynamic stroke of 182.9mm and 152.4mm, respectively, and two ±5kN actuators with ±5kN load cells and LVDTs with static and dynamic stroke of 114.3mm and 101.6mm, respectively.

The DIC (Digital Image Correlation) system used is ARAMIS 12M by GOM (Gesellschaft für Optische Messtechnik mbH, Mittelweg 7-8, 38106 Braunschweig, Germany). The DIC system is stereo system with two CCD (Charged-couple Device) chip 12 megapixel cameras: 4096pix x 3072pix, and 24mm focal length Titanar lenses. The system is setup 295mm from the specimen with 108mm between the cameras yielding a measuring volume of 200mm x 150mm, calibrated by a 175mm x 140mm calibration object. The DIC system runs the software PONTOS Live vs. 8 capable of performing point measurements, process and send data real-time, via Ethernet cable using UDP (User Datagram Protocol) and SCPI (Standard Commands for Programmable Instruments) protocol, cf. [34] and [35].

The vibration meter determining the Eigen frequencies of the specimen is a Vibration Meter Type 2511 [36] from Brüel & Kjær (Brüel og Kjær Sound & Vibration Measurement A/S, Skodsborgvej 307, 2850 Nærum, Denmark), measuring accelerations in the range: [0.3Hz ; 15kHz].

Finite Element Modelling

A finite element model to simulate the numerical substructure is organized. The model is made with plane Euler-Bernoulli elements containing two nodes with two transversal and one rotational degree of freedom in each node. Linear shape functions are used to model the horizontal element deformations and third order polynomials are used to model the transverse deformations and rotations. Full details about the element are given in [37]. The equations of motion in the numerical simulations are written on the form:

$$\boldsymbol{M}_n\ddot{\boldsymbol{x}} + \boldsymbol{C}_n\dot{\boldsymbol{x}} + \boldsymbol{Q}_n + \boldsymbol{R} = \boldsymbol{F} \quad (1)$$

Where $\mathbf{M}_n$ is the mass matrix, $\mathbf{C}_n$ the damping matrix, $\mathbf{Q}_n$ the internal restoring forces and $\mathbf{F}$ the external load. All of these refer to the numerical model, indicated by the subscript *n*. The vector $\mathbf{R}$ represents the inertia, damping and restoring forces of the physical substructure, measured by the actuators.

The numerical part is modelled with 20 beam elements and solved by use of the central difference method, which is an explicit time integration scheme, with a time step of $\Delta t = 10^{-2}$ s. However, in order to minimize the computational time, the equations of motion in eq. (1 are projected onto a reduced basis. In the present case is used a Taylor basis with one linear mode and one modal derivative, cf. [38] for details. However, as the Euler-Bernoulli element does not include shear flexibility, which has a significant influence on the response, the modes used in the Taylor basis introduce some discontinuities in, among other thing, the rotations at the common interface. The consequences of this are discussed in more detail in [38]. Furthermore a damping ratio of 20% is included in the first mode to remove the high frequency excitation of the modes.

Hybrid Simulation Setup – Multi Rate Approach

A substructural test of the GFRP composite box girder is conducted using a multi-rate real-time hybrid simulation (mrRTHS) approach. Here the numerical and experimental substructure is operated at two different

rates to optimize the available computational resources and enhance flexibility to the architecture of the hybrid simulation communication loop, [27], [39], [40]. The overall framework of the mrRTHS communication loop contains two loops named main- and outer-loop with an execution rate of $\Delta T = 0.020$ sec (50Hz) and $\delta t = 0.002$ sec (500Hz) respectively cf. Fig. 3.

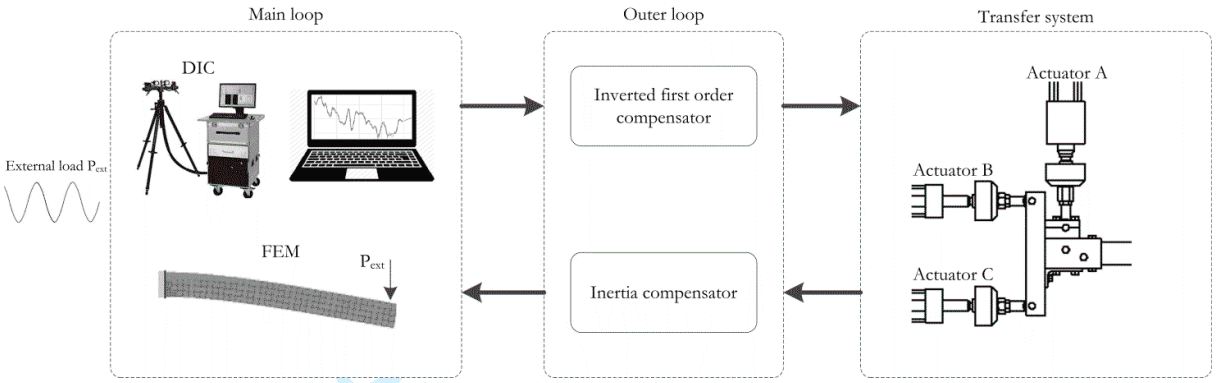

Fig. 3 Simplified schematic block diagram representing the overall architecture of the mrRTHS communication loop

The strategy is handled through the real-time target (National Instruments cRIO – 9074) which is capable of providing deterministic and real-time control and monitoring capabilities [41]. Through the main loop the numerical model is discretized using plane Euler-Bernoulli elements (see chapter: "Finite Element Modelling") to compute the next displacement signal based on the external load and last available restoring force received from the experimental substructure. Next the DIC Compensator (see chapter "Real-Time Digital Image Correlation Compensator") is implemented to enhance the tracking performance between the shared boundary on the experimental substructure and displacement signal. By the current and three previous displacement data points a finer control signal is generated with the time step δt, using a third order polynomial algorithm [42]. The numerical substructure, DIC compensator and extrapolator are executed with a sampling rate of ΔT by the 400MHz on-board single core processor which is embedded in the real-time target. Through the outer loop the control signal is compensated to account for actuator dynamics using an inverted first order compensator [43] and transmitted to the transfer system by an analogue signal with the time step δt. Here the transfer system consists of a PID controller and three servo hydraulic actuators named: A, B and C cf. Fig. 3. The restoring force from the experimental substructure is acquired and in order to remove the dynamic effects of the load train from the restoring force the Inertia Compensator (see subchapter "Real-Time Inertia Force Compensator") is implemented. The inverted first order compensator, communication interface between the real-time target and transfer system and Inertia Compensator is executed with an execution rate of δt by the Field Programmable Gate Array (FPGA) which – like the single core real-time processor - is embedded in the real-time target. Thus the main- and outer-loop is dedicated its own processor to allocate computationally independent and separate resources. The program was developed in [44].

Real-Time Digital Image Correlation Compensator

From previous research [25] it was documented that the compliance in the load train gave rise to a large error between the commanded displacement in the actuators and the displacements measured at the shared boundary directly on the specimen. A real-time digital image correlation compensator is therefore utilized in the hybrid simulation. The compensator is referred to as: *DIC Compensator*.

The displacement in the shared boundary is calculated by three measurement points, assuming linear cross sectional deformation. This allows for 1st order shear deformations of the cross section, cf. Timoshenko beam theory. The x- and y-displacement of the shared boundary is calculated as the average of the three points, while the rotation is calculated by the angle between the top and bottom point. The x, y and z- axis follows the coordinate system specified in Fig. 1. The u_x, u_y, u_z and φ_z are the displacements in the x-, y- and z-directions and rotation around the z-axis, respectively. The n denotes the DIC point number, cf. Fig. 2.

$$\boldsymbol{D} = [u_x\ u_y\ u_z\ \varphi_z] \tag{2}$$

$$u_x = \frac{\sum_1^N u_{x,n}}{N}, u_y = \frac{\sum_1^N u_{y,n}}{N}, u_z = \frac{\sum_1^N u_{z,n}}{N}, \qquad \text{for } n = 1,2,3 \tag{3}$$

$$\varphi_z = \text{Arctan}\left(\frac{u_{x,3} - u_{x,1}}{u_{y,1} - u_{y,3}}\right), \text{for} -\frac{\pi}{4} < \varphi_z < \frac{\pi}{4} \tag{4}$$

The DIC Compensator is applied in an outer control loop structure; cf. eq. (5) (the inner control loop being the PID loop for the LVDT and servo valve). The displacement commanded to the hybrid simulation program for the n'th iteration is named $\mathbf{D}_c(n)$. This is determined by the desired displacement with zero error, $\mathbf{D}_{c0}(n)$ added the error from the previous iteration $\mathbf{e}(n-1)$ multiplied by a proportional gain $\mathbf{K}_{DIC}$. The error in the previous iteration $e(n-1)$ is determined by the previous command signal $\mathbf{D}_c(n-1)$ and the feedback displacement measured with the DIC system $\mathbf{D}_{DIC}(n-1)$. It is noted that the displacement is a vector of horizontal and vertical displacements and rotations around the z-axis, $\mathbf{D} = [x\ y\ \varphi_z]$. The displacements and rotations are transformed into displacements in the actuators by a trigonometric relation [25].

$$\boldsymbol{D_c}(n) = \boldsymbol{K_{DIC}}\boldsymbol{e}(n-1) + \boldsymbol{D_{c0}}(n) \tag{5}$$

$$\boldsymbol{e}(n-1) = \boldsymbol{D_c}(n-1) - \boldsymbol{D_{DIC}}(n-1) \tag{6}$$

A similar approach has previously been applied hybrid simulation [26] using LVDTs to measure six degrees of freedom (three displacements and three rotations) instead of DIC. The accuracy of the DIC system is evaluated by the standard deviation of the noise of the measured displacements and rotation; cf. Table 3. The error was measured in a noise test with zero displacement applied the specimen.

Table 3 standard deviation (SD) of error of displacements and rotation

SD u_x [µm]	SD u_y [µm]	SD φ_z [°]	SD u_z [µm]
0.419	4.157	1.108e-3	0.777

The communication delay between the DIC system and the hybrid simulation program is 160ms from the data is measured by the cameras until the data is processed and arrives in the hybrid program. The specimen is loaded by a sinusoidal displacement and it is desirable to compensate for a difference between the command and feedback signal as close to the current value as possible, since the error between command and feedback might be must different at the peaks of the since wave than at the zero point. In Table 4 the percentage of the loading period is plotted for five frequencies for the delay of 160ms.

Table 4 the 160ms delay's portion of the sine period for 5 frequencies

Frequency [Hz]	Period [ms]	Delay relative to period [%]
0.074	13513	1.2
0.74	1351	11.8
1.48	676	23.7

2.22	450	25.6
2.96	338	47.3

Real-Time Inertia Force Compensator

In order to compensate for the inertia force from the mass of the load train an inertia force compensator is developed. In the remaining paper the compensator is referred to as; *Inertia Compensator*. The compensator calculates the inertia force of the load train by the mass and the acceleration derived from the double differentiated command signal. This force is subtracted the force measured in the load cells thereby obtaining the restoring force from the specimen.

$$F(t) = m\frac{d^2x}{dt^2} \tag{7}$$

The differentiation is performed by finite differencing.

$$F(t) = m\frac{d^2x}{dt^2} \cong m\frac{\Delta^2x}{\Delta t^2} = m\frac{x_2 - 2x_1 + x_0}{\Delta t^2} \tag{8}$$

The mass of the load train was determined, by a oscillation test, where the load train oscillates vertically at 2.96Hz with 9.25mm amplitude, to m = 25.68kg, without any specimen installed. The vibration test also shows whether the load train runs smoothly. The force as function of acceleration is plotted in Fig. 4. Ideally the trend should be linear; however a shift in the force is observed when the oscillations change direction. This shift is most likely caused by Coulomb damping due to friction in the swivels and hinges connecting the actuators to the load train and supports.

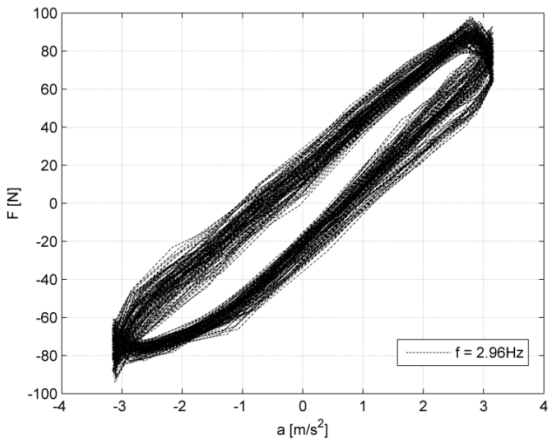

Fig. 4 Oscillations of the load train at 2.96Hz frequency and 9.25mm amplitude

In order to demonstrate the necessity of the Inertia Compensator the inertia force is calculated for the frequencies and amplitude used in the hybrid simulation. This is done by double differentiating the sinusoidal displacement function and finding the max acceleration and multiplying by the mass.

$$x(t) = A\sin(2\pi ft) \Longrightarrow \tag{9}$$

$$F_{max}(t) = -4A\pi^2mf^2 \tag{10}$$

The inertia force of the load train is compared to the section forces at the shared boundaries, i.e. if the inertia force of the load train is comparable to the restoring force of the specimen the inertia force required. The vertical restoring force from the specimen is determined by the external load applied the structure in the reference test. The forces are plotted in Fig. 5. It is observed that the inertia force is increasing for higher frequencies while the section force is decreasing towards the natural frequency of the composite beam. Fig. 5 shows the necessity for Inertia Compensation for tests at higher frequencies e.g. f > 0.5Hz.

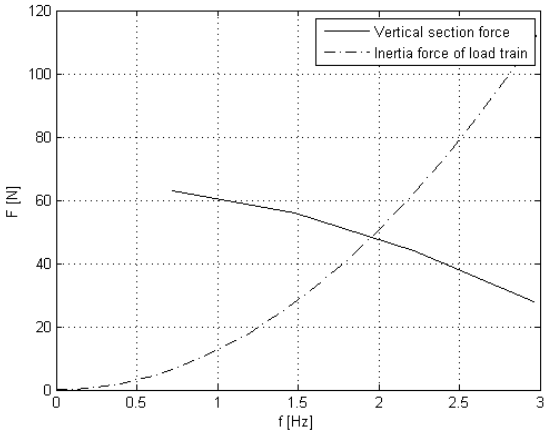

Fig. 5 Inertia force of a load train evaluated for the frequencies and amplitudes used in the hybrid simulation

Results

No Compensation

In order to evaluate the need for compensators in the hybrid simulation a hybrid simulation was run at different frequencies without DIC or Inertia Compensation. In Fig. 6 the x-, y- displacements and rotation around the z-axis in the shared boundary are plotted for a loading frequency of 0.074Hz. The standard deviation of the error between the command signal and feedback for all 5 frequencies are listed in Table 5. For evaluation of error the maximum amplitude of each DOF is listed in the table.

a) b)

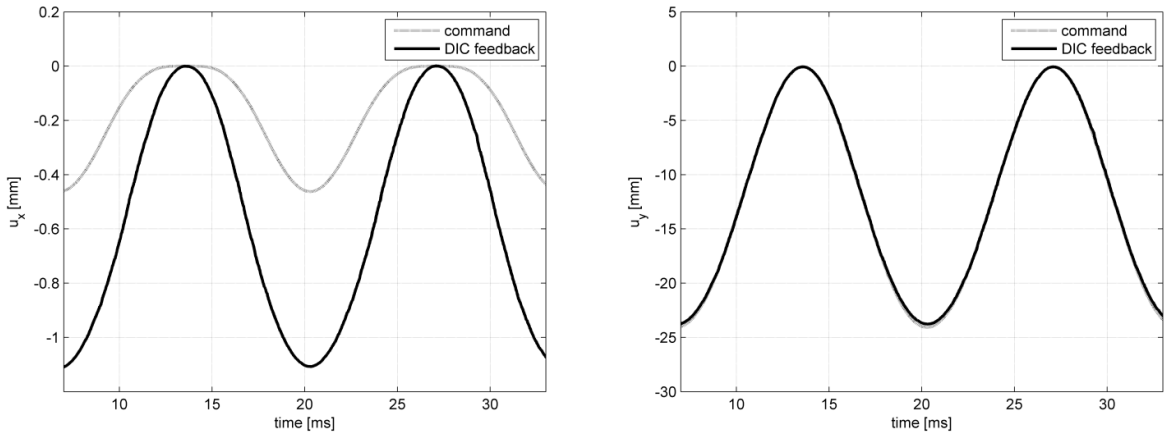

c)

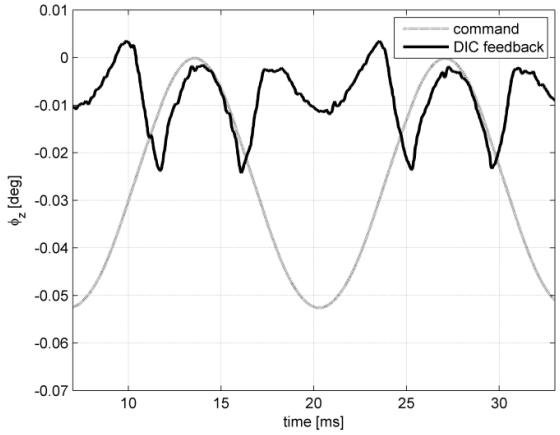

Fig. 6 Displacement of the shared boundary for a loading frequency of 0.074Hz, command and feedback for the three DOFs a) u_x, b) u_y c) φ_z

The results show poor correspondence between the command and feedback for the displacements and rotations except for y-displacements. However, for higher frequencies the y-displacement error also becomes considerably, e.g. at f = 2.96Hz the error is 24.5% of the amplitude.

Table 5 standard deviation (SD) of error between command and feedback and amplitude of command for comparison, no compensation

Frequency [Hz]	SD u_x [mm]	SD u_y [mm]	SD φ_z [deg]
0.074	0.2368	0.9339	0.0204
0.74	0.2313	1.4847	0.0203
1.48	0.2139	1.7797	0.0207
2.22	0.2175	4.7717	0.0234
2.96	0.1965	5.8946	0.0249
Amplitude of command signal	0.4626	24.0869	0.0526

DIC Compensator

In order to accommodate for the compliance of the test rig a DIC Compensator is applied. The DIC system measures the deformations in the shared boundary in three points and then calculates the overall x and y displacements and the rotation around the z axis. The command and DIC feedback signal is plotted in Fig. 7 In these tests the gain was set to K_{DIC} = [0.0075 ; 0.10] before the loop became unstable.

a) b)

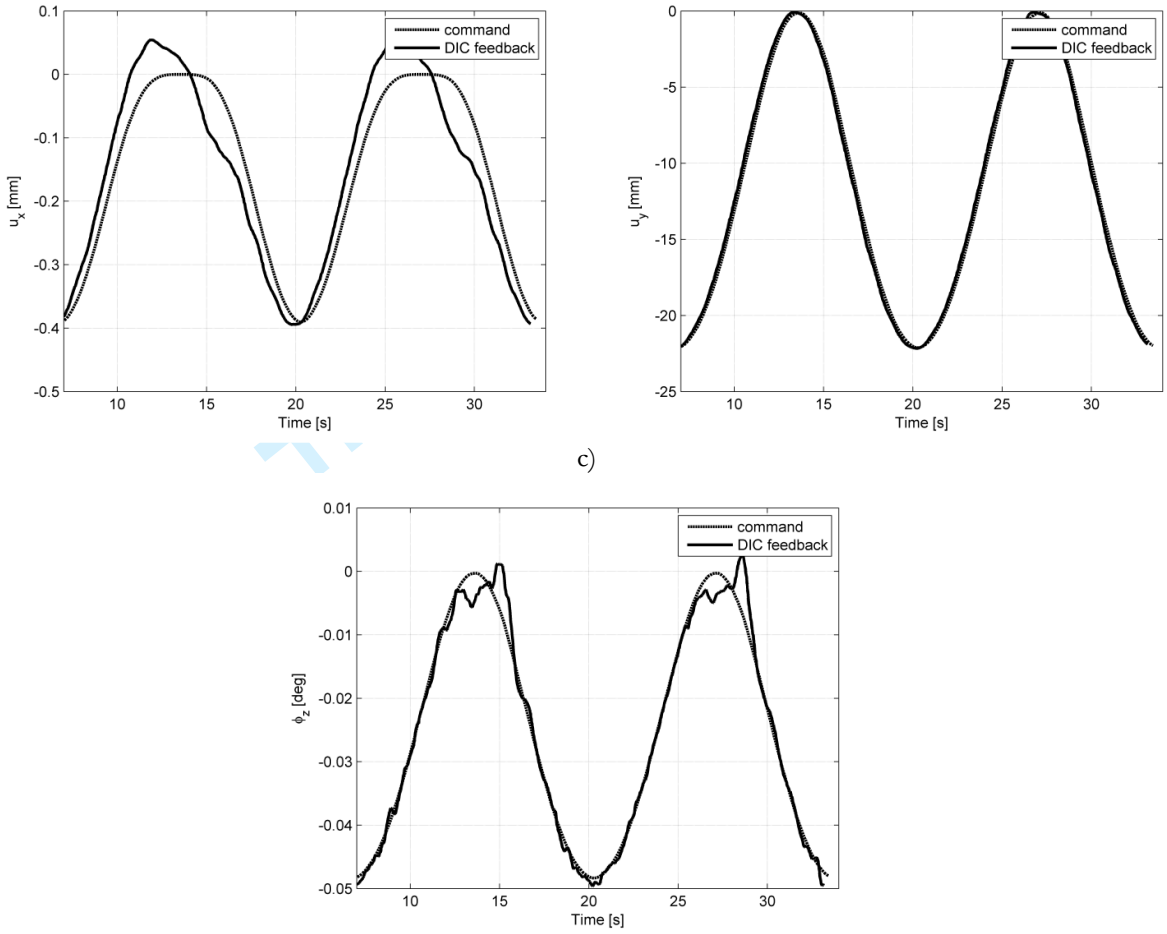

Fig. 7 Displacement of the shared boundary for a loading frequency of 0.074Hz, command and feedback for the three DOFs a) displacement u_x, b) displacement u_y c) rotation φ_z

Table 6 standard deviation of error between command and feedback, DIC compensation

Frequency [Hz]	SD u_x [mm]	SD u_y [mm]	SD φ_z [deg]
0.074	0.0403	0.5383	0.0038
0.74	0.2238	0.4940	0.0099
1.48	0.1899	1.3850	0.0130
2.22	0.1616	3.8033	0.0166
2.96	0.1680	5.7519	0.0203
Amplitude of command signal	0.4626	24.0869	0.0526

In Table 6 the standard deviation of the error between the command signal and feedback DIC measurements are presented for the five loading frequencies. In order to evaluate the error the amplitude of displacements are written for each DOF. It is observed that for 0.074Hz the error for all DOFs are less than 9% while for 2.96Hz the error is higher than 23%. The improvement by DIC compensation is evaluated by comparing the command versus feedback error when not using DIC compensation to the same error when using DIC compensation. The improvement in percent is plotted in Fig. 8. It is observed that the DIC Compensator improves the correlation between command and feedback signal for all frequencies for the displacements and rotation in the shared boundary. The improvement is decreasing for higher loading frequencies.

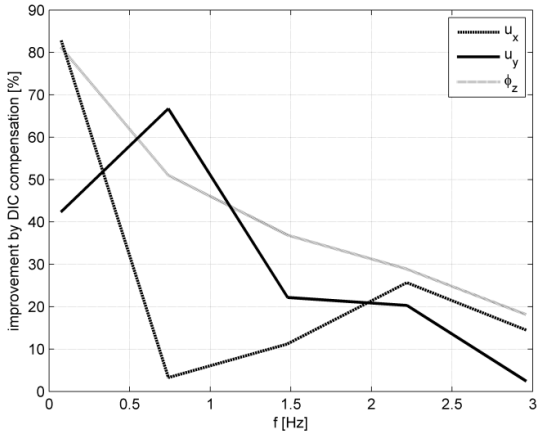

Fig. 8 Improvement by DIC compensation in terms of standard deviation of error between the command and feedback

Inertia Compensator

The inertia force is calculated by the acceleration which is determined by double differentiation of the displacement command signal, cf. eq. (8). In Fig. 9 the restoring force from the specimen is plotted with and without the Inertia Compensator for four frequencies; 0.74Hz, 1.48Hz, 2.22Hz and 2.96Hz.

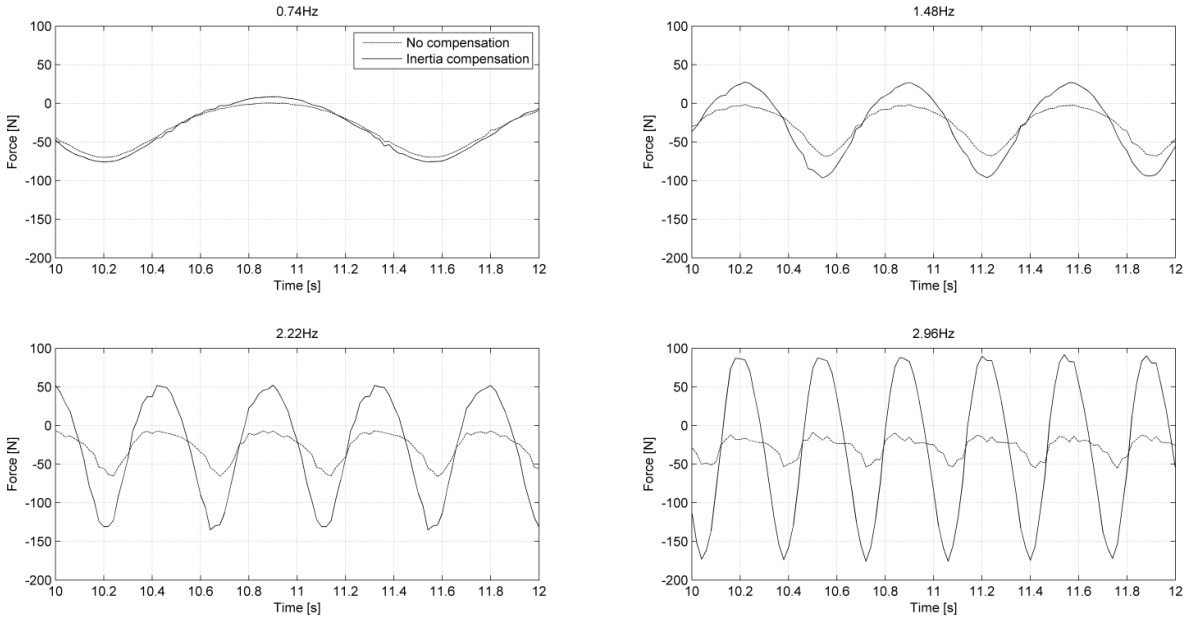

Fig. 9 The restoring force in the hybrid simulation with and without Inertia Compensation for four loading frequencies

It is observed that the inertia force of the load train is insignificant in the slow tests i.e. 0.074Hz and 0.74Hz, while at the highest frequency of 2.96Hz the force measured in the load cell is only 19.2% of the force acting on the specimen, cf. Table 7. The remaining force acting on the specimen is from the inertia force of the load train. The inertia force of the load train must therefore be included in the hybrid simulation for higher loading frequencies.

Table 7 comparison of force with and without compensation

Frequency [Hz]	Force Amplitude No Inertia Compensation [N]	Force Amplitude Inertia Compensation [N]	Uncompensated force as ratio of compensated force [%]
0.074	40.1	40.9	98.1
0.74	42.3	49.0	86.4
1.48	41.0	69.3	59.1
2.22	39.5	107.1	36.9
2.96	28.8	150.1	19.2

Due to compliance of the load train the displacement of the shared boundary was not as commanded by the hybrid testing program, cf. Table 6. This gave rise to an error in the inertia force, since this was calculated on the basis of the command signal. A hybrid simulation was therefore performed with both the Inertia Compensator and DIC Compensator utilized.

Combined Effect of Inertia- and DIC Compensator

Both compensators are applied the hybrid simulation for the five tested frequencies. The command and feedback signal is plotted in Fig. 10 for the shared boundary between the finite element model and the experimental subsection for the loading frequency of 0.074Hz. For the remaining four frequencies the standard deviation of the error between command and displacement is listed in Table 8.

a) b)

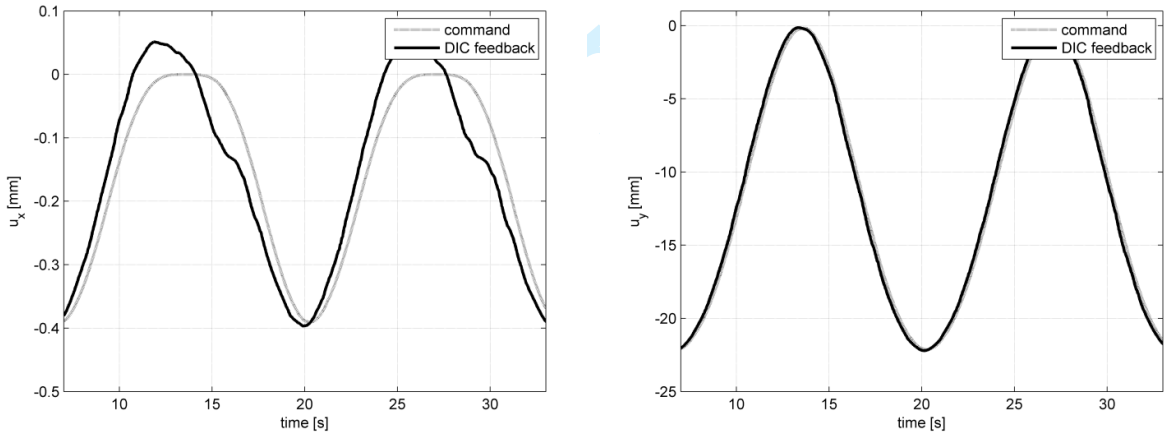

c)

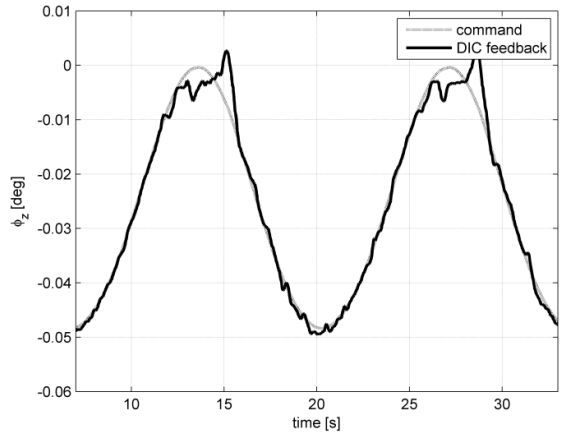

Fig. 10 command vs feedback displacements and rotation of the shared boundary for the three DOFs a) u_x, b) u_y c) φ_z

Table 8 standard deviation of error between command and feedback, inertia and DIC compensation

Frequency [Hz]	SD u_x [mm]	SD u_y [mm]	SD φ_z [deg]
0.074	0.0488	0.1118	0.0033
0.74	0.2239	0.6244	0.0100
1.48	0.1921	1.4533	0.0132
2.22	0.1642	4.0538	0.0173
2.96	0.1979	6.8682	0.0221
Amplitude of command signal	0.4626	24.0869	0.0526

When comparing the standard deviation of error with and without the Inertia Compensator and DIC Compensator, it is seen that using the Inertia Compensator together with DIC compensation increases the error slightly. This is most likely caused by the increasing noise in the test the double differentiation used in the inertia Compensator induces, cf. eq. (8). In Fig. 10 some oscillations of the rotation is observed which is due to the P-gain of the DIC Compensator, cf. eq. (5) and (6), is close to going instable.

Total errors: Communications lag from DIC, noise in measurements from DIC system cf. Table 3, high frequency vibrations in the specimen, noise due to finite differencing of the displacement signal, cf. eq. (8).

Discussion

Digital Image Correlation Compensator

The DIC Compensator shows good correlation between command and feedback for lower frequencies i.e. f < 1.48 Hz for displacements and rotation, cf. Fig. 8. However, at higher frequencies the improvement goes towards zero compared to no compensation, cf. Fig. 8. When observing the command vs feedback for the different frequencies it is seen that the lag between command and feedback becomes a bigger problem for higher frequencies, cf. Table 4. The problem occurs when attempting to compensate the command signal at the top of a peak with an error missing at the bottom of the valley of the sine wave. This problem could be solved by decreasing the communication delay between the DIC system and the hybrid simulation program. Alternatively, extrapolation methods could be applied the DIC Compensator to predict the error instead of using it directly. However, for the given tests this was not possible due to limited computational capacities of the hardware.

Another issue with the DIC Compensator was the P-gain approach applied to compensating the command signal, cf. eq. (5) and (6). Desirably the gain K_{DIC} should be set to approximately 1.0, however that caused the actuators to change position too violently which yielded noise in the restoring forces, which then led to instability of the hybrid simulation. Therefore the gain was set in the range of K_{DIC} = [0.0075 ; 0.10], due to these fairly low gains, together with the communication lag, the program was simply not able to reach the desired amplitudes at higher frequencies i.e. f > 1.48Hz.

Inertia Compensator

The results shows that the Inertia Compensator is crucial for running real time hybrid simulation with a load train with high mass compared to the specimen. The inertia force compensator shows that at higher frequencies > 1.48Hz the compensator must be included since the inertia force accounts > 40% of the force measured in the actuator.

The accuracy of the Inertia Compensator as it is designed depends on the accuracy of the feedback vs command signal, since the compensator uses commanded displacements to calculate inertia force of the load train. In the tests conducted it was possible to get a high degree of correlation between the command and feedback displacement for lower loading frequencies < 1.48Hz. In order to improve the accuracy of the inertia force it could be calculated by the feedback displacement instead of the command. However, this will result in a high degree of noise in the inertia force since it is calculated on the basis on double differentiated feedback displacements, which will always be noisier than a command signal. To get rid of the noise one could filter the displacements but that takes computational resources from running the hybrid simulation. In the tests conducted here this was not possible due to the capacity of the hardware and the degree of accuracy of the finite element model. The tests therefore shows that the best approach is to optimize the correlation between command and feedback displacement e.g. by DIC compensation or others and thereafter use the command signal to calculate the accelerations and thereby the inertia forces. In this way the Inertia Compensator is as accurate as possible while releasing as much computational resources for other tasks in the hybrid loop i.e. increase accuracy of the FEM model, time integration scheme etc.

It is noted that the Inertia Compensator is only applied vertical restoring force and not the horizontal force or moment. This is due to the horizontal inertia force and moment is insignificant to the loads applied the specimen due to the very small displacements and rotations even for large amplitude tests i.e. y > 20mm, x < 1mm, φ_z < 0.1°, at least for frequencies in the given range [0 ; 2.96Hz]. Furthermore the stiffness of the specimen in the longitudinal direction is much higher than in the vertical direction and eventual inertia forces from the load train has therefore much lower effects on the specimen.

Combined effect of Digital Image Correlation and Inertia Compensator

In order to achieve compensate for both compliance and inertia force of the load train both compensators was applied simultaneously, cf. Fig. 10. The DIC Compensator should ideally be able to increase the accuracy of the inertia Compensator since an error in the inertia compensator was the feedback displacement not following the command at higher frequencies i.e. 1.48Hz, cf. Table 5. The DIC Compensator should be able to solve this problem. The DIC Compensator did indeed improve the accuracy of the feedback signal for lower frequencies, however for higher frequencies little improvement was observed; cf. Table 6, due to the communication lag.

The main improvements to be made to the hybrid simulation setup presented, is to decrease communication lag between DIC system and hybrid simulation program by e.g. using another DIC system with less communication lag. Another improvement would be to increase the computational resources of the hybrid simulation program by utilizing other computational hardware. In this way high pass filtering could be applied to the load and DIC displacement feedback signals. The P-gain, cf. eq. (5) and (6), of the DIC Compensator could thereby be

increased without causing instability of the program, and lower errors between command and feedback be obtained. This would also improve the inertia compensator that uses the command signal.

Conclusion

This study shows the necessity for compensation methods in real time hybrid simulation in the case of high compliance and mass of the load train compared to the specimen tested. Two compensation methods are applied: DIC compensation, to account for compliance of the load train and Inertia Compensation to account for the mass of the load train. The DIC Compensator proved valid for all tested frequencies with higher improvement for lower frequencies. For higher frequencies i.e. f > 1.48Hz, the compensator is converging towards zero improvements, cf. Fig. 8. This is assumed to be due to the communication lag between the DIC system and hybrid program. The Inertia Compensator proved valid, however for higher frequencies i.e. f > 1.48Hz the error between the command and feedback displacements led to a too high error in the inertia compensator. The two compensators were implemented in the hybrid simulation program simultaneously in order to accommodate for the compliance of the load train and thereby also improve the accuracy of the inertia force in the inertia compensator. The combined effect of the compensators improved the accuracy of the hybrid simulation for low frequencies e.g. f < 1.48Hz. However, for higher frequencies the compensators need improvements before fully valid. The main improvements suggested are: minimizing the communication delay to the DIC system, filtering the noise from the Inertia Compensator and increasing the amount of computational resources in the CPU running the simulation. The latter would allow for smaller time steps and higher degree of filtering of the measurements before used in the compensators.

Acknowledgement

The authors acknowledge the funding by the Danish Centre for Composite Structures and Materials for Wind Turbine Blades (DCCSM), which is funded by the Danish Council for Strategic Research within Sustainable Energy and Environment (grant 09-067212). Furthermore the authors acknowledge Fiberline Composites A/S for providing the GFRP beams tested in the hybrid simulation.

References

[1] M. Nakashima, J. McCormick and T. Wang, "Chapter 1 Hybrid simulation: A historical perspective," in *Hybrid Simulation - Theory, Implementation and Applications*, London, UK, Taylor & Francis, 2008, pp. 3-14.

[2] K. Takanashi and M. Nakashima, "Japanese Activities on On-Line Testing," *Journal of Engineering Mechanics,* vol. 113, no. 7, pp. 1014-1032, 1987.

[3] Y. Chae, J. M. Ricles and R. Sause, "Large-scale rths of a three-story steel frame building with mr dampers," *Earthquake Engineering and Structural Dynamics,* vol. 43, no. 13, pp. 1915-1933, 2014.

[4] T. L. Karavalis, J. M. Ricles, R. Sause and C. Chen, "Experimental evaluation of the seismic performance of steel MRFs with compressed elastomer dampers using large-scale real-time hybrid simulation," *Engineering Structures,* vol. 33, pp. 1859-1869, 2011.

[5] J. E. Carrion, B. F. Spencer Jr. and B. M. Phillips, "Real-time hybrid testing of a semi-actively controlled structure with an MR-damper," in *American Control Conference*, St. Louis, MO, USA, 2009.

[6] M. Ito, Y. Murata, K. Hoki and M. Nakashima, "Online hybrid test on buildings with stud-type damper made of slitted steel plates stiffened by wood panels," in *12th East Asia-Pacific Conference on Structural*

Engineering and Construction, EASEC12, 2011.

[7] A. Jacobsen, T. Hitaka and M. Nakashima, "Online test of building frame with slit-wall dampers capable of condition assement," *Journal of Constructional Steel Research,* vol. 66, no. 11, pp. 1320-1329, 2010.

[8] S. Plude, R. Christenson, Z. Jiang and S. J. Kim, "Real-time hybrid simulation of a complex bridge model with mr dampers using the convolution integral method," *Smart Materials and Structures,* vol. 22, no. 10, 2013.

[9] K.-C. Lee, J.-W. Jeon, D.-H. Hwang, S.-H. Lee and Y.-J. Kim, "Development of Antilock Braking Controller Using Hardware In-the-Loop Simulatin and Field Test," in *The 30th Annual Conference of the IEEE Industrial Electronics Society*, Busan, Korea, 2004.

[10] C. Dufour, T. Ishikawa, S. Abourida and J. Bélanger, "Modern Hardware-In-the-Loop Simulation Technology for Fuel Cell Hybrid Electric Vehicles," in *2007 Vehicle Power and Propulsion Conference*, 2008.

[11] K. Osaki, A. Konno and M. Uchiyama, "Delay Time Compensation for a Hybrid Simulator," *Advanced Robotics,* vol. 24, pp. 1081-1098, 2010.

[12] H. Yan, Z. Ye, D. Cong, J. Han and H. Li, "Space docking hybrid simulation prototype experiment system," *Chinese Journal of Mechanical Engineering,* vol. 43, no. 9, pp. 51-56, 2007.

[13] A. Facchinetti and S. Bruni, "Hardware-in-the-loop hybrid simulation of pantograph-catenary interaction," *Journal of Sound and Vibration,* Vols. 2783-2797, p. 331, 2012.

[14] W. Song and W. Su, "A wind turbine hybrid simulation framework considering aeroelastic effects," in *Proceedings of the SPIE*, 2015.

[15] B. Wu, G. Xu, Q. Wang and M. Williams, "Operator-splitting method for real-time substructure testing," *Earthquake Engineering and Structureal Dynamics,* vol. 35, no. 3, pp. 293-314, 2005.

[16] C. Cheng and J. M. Ricles, "Development of Direct Integration Algorithms for Structural Dynamics Using Discrete Control Theory," *Journal of Engineering Mechanics,* vol. 134, no. 8, pp. 676-683, 2008.

[17] P.-S. B. Shing, M. T. Vannan and E. W. Carter, "Implicit time integration for pseudodynamic tests," *Earthquake Engineering and Structural Dynamics,* vol. 20, pp. 551-576, 1991.

[18] J. Chung and G. M. Hulbert, "A Time Integration Algorithm for Structural Dynamics with Improved Numerical Dissipation: The Generalized-alpha Method," *Journal of Applied Mechanics,* vol. 60, pp. 371-375, 1993.

[19] P.-C. Chen and K.-C. Tsai, "Dual compensation strategy for real-time hybrid testing," *Earthquake Engineering and Structural Dynamics,* vol. 42, no. 1, pp. 1-23, 2013.

[20] C. Chen, J. M. Ricles and T. Guo, "Improved Adaptive Inverse Compensation Technique for Real-Time Hybrid Simulatino," *Journal of Engineering Mechanics,* vol. 138, no. 12, pp. 1432-1446, 2012.

[21] T. Horuichi, M. Inoue, T. Konno and Y. Namita, "Real-time hybrid experimental system with actuator delay compensation and its application to a piping system with energy absorber," *Earthquake Engineering and Structural Dynamics,* vol. 28, no. 10, pp. 1121-1141, 1999.

[22] B. M. Phillips and B. F. Spencer, "Model-based servo-hydraulic control for real-time hybrid simulatino," Newmark Structural Engineering Laboratory, Urbana-Champaign, Illinois, USA, 2011.

[23] C. Chen, J. M. Ricles and T. L. Karavasilis, "Evaluation of a real-time hybrid simulation system for performance evaluation of structures with rate dependent devices subjected to seismic loading," *Engineering Structures,* vol. 35, pp. 71-82, 2012.

[24] J. Waldbjørn, J. Høgh, C. Berggreen, J. Wittrup-Schmidt and K. Branner, "Hybrid Testing of Composite Structures with Single-axis Control," in *The 19th International Conference on Composite Materials*, Montreal, Canada, 2013.

[25] J. Høgh, J. Waldbjørn, J. Wittrup-Schmidt, H. Stang and C. Berggreen, "Quasi-static single-component hybrid simulation of a composite structure with multi-axis control," *Strain,* vol. 51, pp. 459-473, 2015.

[26] B. F. Spencer, C.-M. Chang, T. M. Frankie and D. A. Kuchima, "Multiple Degrees of Freedom Positioning Correction for Hybrid Simulation," *Journal of Earthquake Engineering,* vol. 19, no. 2, pp. 277-296, 2015.

[27] P. A. Bonnet, The Development of Multi-axis Real-time Subrstructure Testing, Oxford: University of Oxford, 2006.

[28] G. Ellis, Control System Design Guide - A Practical Guide, San Diego, California, USA: Elsevier Academic Press, 1990.

[29] ASTM, Standard Test Method for Tensile Properties of Polymer Matrix Composite Materials, West Conshohocken, Pennsylvania, United States of America: ASTM International, 2011.

[30] ASTM, Standard Test Method for Shear Properties of Composite Materialsby the V-Notched Beam Method, West Conshohocken, Pennsylvania, United States of America: ASTM International, 2014.

[31] F. C. A/S, Konstruktionshåndbog, Kolding, Denmark: Fiberline Composites A/S, 2003.

[32] National Instruments, "National Instruments, NI 9263," National Instruments, 1 December 2015. [Online]. Available: http://sine.ni.com/nips/cds/view/p/lang/da/nid/208806. [Accessed 1 December 2015].

[33] National Instruments, "National Instruments, NI 9205," National Instruments, 1 December 2015. [Online]. Available: http://sine.ni.com/nips/cds/view/p/lang/da/nid/208800. [Accessed 1 December 2015].

[34] S. Consortium, Volume 1: Syntax and Style, USA: SCPI Consortium, 1999.

[35] GOM, "PONTOS Live streaming with SCPI protocol," GOM, 7 August 2015. [Online]. Available: https://support.gom.com/display/KNOWLEDGE/PONTOS+Live+streaming+with+SCPI+protocol. [Accessed 7 August 2015].

[36] Brüel & Kjær, Vibration Meter Type 2511, Brüel & Kjær, 1978.

[37] S. Andersen, "Reduction Method for Kinematic Nonlinear Real-time Simulation," *Journal for Numerical Methods in Engineering (in review).*

[38] J. Waldbjørn, J. Høgh and S. Andersen, "Multi-Rate Hybrid Simulation with Multi-axial Control," *To be submitted.*

[39] M. Nakashima og N. Masaoka, »Real time on-line test for MDOF systems,« *Earthquake Engineering and Structural Dynamics,* årg. 28, nr. 4, pp. 393-420, 1999.

[40] J. P. Waldbjoern, S. Andersem, J. H. Hoegh, J. W. Schmidt, C. Berggreen and H. Stang, "Single-component Multi-rate Real Time Hybrid Simulation pilot test on a composite structure," *To be published.*

[41] NI, »http://www.ni.com/pdf/manuals/375874b.pdf,« National Instruments, - 6 2014. [Online]. [Senest hentet eller vist den 21 11 2014].

[42] A. Maghareh, J. P. Waldbjoern, S. J. Dyke and A. Prakash, "Adaptive multi-rate interface: development and experimental verification of an interface for multi-rate real-time hybrid simulation," *Earthquake Engineering and Structural Dynamics,* Accepted for publication (2015).

[43] J. P. Waldbjoern, A. Maghareh, G. Ou, S. J. Dyke and H. Stang, "Multi-rate Real Time Hybrid Simulation operated on a flexible LabVIEW real-time platform," *Smart Structures and Systems,* Submitted for peer review (2015).

[44] J. P. Waldbjørn, S. Andersen, J. H. Høgh, J. Wittrup-Schmidt, C. Berggreen and H. Stang, "Single-component Multi-rate Real Time Hybrid Simulation pilot test on a composite structure," *To be submitted,* 2016.

[45] GOM, PONTOS Live V8 Manual, Braunschweig, Germany: GOM, 2015.

[46] P.-S. B. Shing and T. Manivannan, "On the Accuracy of an Implicit Algorithm for Pseudodynamic Tests," *Earthquake Engineering and Structural Dynamics,* vol. 19, pp. 631-651, 1990.

[47] A. Bonelli and O. S. Bursi, "Generalized-alpha methods for seismic structural testing," *Earthquake Engineering and Structural Dynamics,* vol. 33, pp. 1067-1102, 2004.

[48] T. Horiuchi and M. Nakagawa, "Development of a real-time hybrid experimental system with actuator delay compensation," in *Eleventh World Conference on Earthquake Engineering*, 1996.

[49] P. A. Bonnet, »The development of multi-axis real-time substructure testing,« University of Oxford, Oxford, United Kingdom, 2006.

This page is intentionally left blank

Appendix G

Hybrid Testing of Composite Structures with Single-Axis Control - DTU Orbit (10/10/2015)

Hybrid Testing of Composite Structures with Single-Axis Control

Hybrid testing is a substructuring technique where a structure is emulated by modelling a part of it in a numerical model while testing the remainder experimentally. Previous research in hybrid testing has been performed on multi-component structures e.g. damping fixtures, however in this paper a hybrid testing platform is introduced for single-component hybrid testing. In this case, the boundary between the numerical model and experimental setup is defined by multiple Degrees-Of-Freedoms (DOFs) which highly complicate the transferring of response between the two substructures. Digital Image Correlation (DIC) is therefore implemented for displacement control of the experimental setup. The hybrid testing setup was verified on a multicomponent structure consisting of a beam loaded in three point bending and a numerical structure of a frame. Furthermore, the stability of the hybrid testing loop was investigated for different ratios of stiffness between the numerical model and test specimen. It was found that when deformations were transferred from the numerical model to the experimental setup, the hybrid test was only stable when the stiffness of the numerical model was higher than the test specimen. The hybrid test gave similar results as a numerical simulation of the full structure. The deviation between the two was primarily due to the response of the specimen in the hybrid test being one load step behind the numerical model.

General information

State: Published
Organisations: Department of Civil Engineering, Section for Structural Engineering, Department of Mechanical Engineering, Solid Mechanics, Section for Building Design, Department of Wind Energy, Wind Turbines
Authors: Waldbjørn, J. P. (Intern), Høgh, J. H. (Intern), Stang, H. (Intern), Berggreen, C. (Intern), Schmidt, J. W. (Intern), Branner, K. (Intern)
Keywords: (Hybrid testing, Hardware-in-the-loop, Substructural testing, Composites, Three point bending, Finite element modelling, high-precision control)
Number of pages: 11
Publication date: 2013

Host publication information

Title of host publication: Proceedings of the 19th International Conference on Composite Materials
Main Research Area: Technical/natural sciences
Conference: 19th International Conference on Composite Materials (ICCM 2013), Montréal, Canada, 28/07/2013 - 28/07/2013
Source: dtu
Source-ID: u::8626
Publication: Research - peer-review › Article in proceedings – Annual report year: 2013

HYBRID TESTING OF COMPOSITE STRUCTURES WITH SINGLE-AXIS CONTROL

J. Waldbjørn[1], J. Høgh[2]*, H. Stang[1], C. Berggreen[2], J. Wittrup-Schmidt[1], K. Branner[3]
[1]Department of Civil Engineering, Technical University of Denmark, Kgs. Lyngby, Denmark
[2]Department of Mechanical Engineering, Technical University of Denmark, Kgs. Lyngby, Denmark
[3]Department of Wind Energy, Technical University of Denmark, Roskilde, Denmark
* Corresponding author jhho@dtu.dk

Keywords: *hybrid testing, hardware-in-the-loop, substructural testing, composites, three point bending, finite element modelling, high-precision control*

Abstract

Hybrid testing is a substructuring technique where a structure is emulated by modelling a part of it in a numerical model while testing the remainder experimentally. Previous research in hybrid testing has been performed on multi-component structures e.g. damping fixtures, however in this paper a hybrid testing platform is introduced for single-component hybrid testing. In this case, the boundary between the numerical model and experimental setup is defined by multiple Degrees-Of-Freedoms (DOFs) which highly complicate the transferring of response between the two substructures. Digital Image Correlation (DIC) is therefore implemented for displacement control of the experimental setup. The hybrid testing setup was verified on a multicomponent structure consisting of a beam loaded in three point bending and a numerical structure of a frame. Furthermore, the stability of the hybrid testing loop was investigated for different ratios of stiffness between the numerical model and test specimen. It was found that when deformations were transferred from the numerical model to the experimental setup, the hybrid test was only stable when the stiffness of the numerical model was higher than the test specimen. The hybrid test gave similar results as a numerical simulation of the full structure. The deviation between the two was primarily due to the response of the specimen in the hybrid test being one load step behind the numerical model.

1 Introduction

In hybrid testing a structure is emulated by combining the response of an experimental- and numerical substructure. The main part of the emulated structure is modelled in a simulation and a part of special interest is tested in an experiment [1], [2]. When combining the response of the two, the behaviour of the full emulated structure can be obtained. With this technique, the response of a given substructure displaying non-linear behaviour e.g. buckling, fracture, can be investigated when exposed to the effect of the remaining structure, without conducting full-scale experiments.

Hybrid testing has previously been applied to investigate seismic protection of building structures [3], [4], [5]. For this application the load bearing structure has been simulated in a numerical model while damping fixtures has been tested experimentally, e.g. elastomer [6], stud types [7], [8], magneto-rheological [4], [9], [10]. These tests were dynamic and the focus was therefore to minimize the time lack between the numerical- and experimental component. This has been done by optimization of e.g. the numerical algorithms [11], [12], [13], and the actuator response [14], [15].

In all of these tests the numerical- and experimental component has been two separate – typically simply connected - structural components and this setup is referred to as multi-component hybrid testing. If hybrid testing is applied to a single-component structure e.g. wind turbine blade, boat hull etc. the boundary conditions between the numerical- and experimental substructure becomes more complicated. This is because the two substructures share boundaries along an edge of a structure instead of e.g. a clearly defined hinge as in the case of a hybrid test with a magneto-rheological damper [4], [9], [10]. This results in single-component hybrid testing having continuous boundaries between the two substructures, resulting in – in principle - an infinite amount of Degrees-Of-Freedom (DOF), compared to multi component hybrid testing where only a limited number of DOFs are present [1], [16]. It is therefore more complicated to monitor and control the deformations of the experimental substructure in a single-component hybrid test. This emphasizes the need for advanced measuring techniques to enable high-precision control of the experimental setup, as presented in [17].

The scope of this paper is to introduce and verify a sound base for single-component quasi-static hybrid testing. Digital Image Correlation (DIC) was implemented as a method to measure deformations to be used in the control loop. A quasi-static hybrid test on a multi component frame structure was conducted to reduce the complexity in verifying the software capabilities when handling the test response and theory. Here the numerical component was a Finite Element (FE) model of a simple frame structure and the experimental specimen a composite beam loaded in three point bending.

2 Hybrid Testing Communication Loop

The Quasi-static hybrid testing platform provides the capability to experimentally test a substructure of interest while simulating the remainder in a numerical model. The software is capable of: executing a FE-model, operating the hydraulic actuators through a multi-axial Proportional-Integral-Derivative (PID) controller and acquire data from several gauges on the test setup. The platform is operated by LabVIEW 8.6 and is executed in a state machine [18] presented in Figure 1.

An external force is applied to the numerical model **(1)** and the equivalent displacement at the shared boundary calculated for the numerical substructure in **(2)**. This displacement is transferred to the experimental substructure by the hydraulic actuators in **(3)** controlled by a feedback signal acquired on the test specimen to omit the effect of compliance in the load train cf. [17]. Finally, the restoring force – i.e. the reaction force from the test specimen - in the shared boundary of the experimental substructure is fed back to the shared boundary of the numerical substructure in order to achieve equilibrium at the interface between the two. The loop is repeated by defining the next load increment in **(1)**.

2.1 Numerical substructure (Part A)

The numerical substructure executed by **(2)** in Figure 1 is established through a link between LabVIEW 8.6 and ANSYS 12.1. The steps included in the communication between the two applications are presented in Figure 2.

The FE-model is defined through the ANSYS Parametric Design Language (APDL-script) which defines geometry, material properties, loads etc. The variable parameters in the APDL-script: external load P_{ext} and restoring force in the shared boundary R_n (see Figure 5) are identified and updated by **(1)**. The APDL-script is executed in **(2)** by the ANSYS software through the windows command prompt. The output data is returned in a text file and the displacement at the shared boundary extracted by **(3)**.

2.2 Experimental substructure (Part B)

The experimental substructure operated by **(3)** in Figure 1 is established through a link between LabVIEW 8.6 and two independent systems: the hydraulic actuator and external Data Acquisition (DAQ) system. The displacement controlled hydraulic actuator is operated through a MTS FlexTest 60 controller [19] by the TCP/IP port using a dynamic link library (DLL) [20]. The external DAQ system collects data from the measuring device DIC [21]. The steps in the communication between LabVIEW, PID-controller and external measuring device are represented in Figure 3.

The control loop is initiated in **(1)** by prescribing a displacement input to the PID-controller. Operated by the LVDT in the actuator the piston is moved towards the end level in a monotonic motion with a predefined deformation rate by **(2)**. When the predefined displacement is reached the data from the load cell along with the signal from the DIC measuring device are acquired by **(3)**. By comparing the deformation input with the actual response of the specimen a deviation is derived. If the deviation is within a given error tolerance the control loop is ready to receive the next deformation input in **(1)**. If the deviation exceeds the error tolerance the actuator is moved in the direction necessary to reduce the error with a magnitude equal to the deviation. This is achieved by repeating the entire loop from **(2)** – **(4)** until a deviation below the error tolerance is achieved.

3 Hybrid Testing Setup

A somewhat simple multicomponent frame structure presented in Figure 4 is studied to reduce the complexity in verifying the software capabilities.

The emulated structure is separated in a numerical- and experimental component. Each component along with the coupling between them is illustrated in Figure 5.

The shared boundary between the two components is defined by a discrete point with two DOFs: translation in the y- and x-direction. With the assumption of having relatively small displacements the translation in the x-direction is neglected. The global stiffness of the numerical- and experimental component named S_A and S_B respectively is defined cf. eq. (1).

$$S_A = \frac{P_{ext}}{d_n} \quad \text{and} \quad S_B = \frac{R_e}{d_e} \tag{1}$$

The global stiffness of the numerical component is 4.94 times higher than the test specimen in the shared boundary.

3.1 Experimental component (Part B)

The experimental component consists of a Glass Fibre Reinforced Polymer (GFRP) beam loaded in three point bending. The specimen has the cross sectional width and height of 45mm and 19mm respectively and includes 22 unidirectional plies of fibre mats type: L1200/G50F-E06-A from Devold AMT with a nominal area weight of 1246g/m^2. Five specimens are produced by vacuum infusion with an epoxy resin type: Airstone 760E mixed with an Airstone 776H hardener from Dow Chemicals Company. The fibre fraction is 55% [22] with the fibre mats oriented in the x-direction cf. Figure 7. The E-modulus in the direction of the fibres is by three point bending found in the range: 38.5-43.3GPa for the five specimens.

3.2 Numerical component (Part A)

The numerical component is discretized in a FE-model using an 8-node plane element with two DOFs in each node: translation in the x- and y direction. The bar connecting the numerical- and experimental component is defined by a 2-node beam element with three DOFs in each node: translation in the x- and y-direction and rotation around the z-axis. When the beam- and plane element is connected the rotation DOF is not

transferred to the plane element and the charnier is thereby obtained.

4 Three point bending

The experimental component is loaded in a 4-column MTS 810 axial test station with an axial servo-hydraulic actuator model: 244.22 which provide a maximum force of ±100kN with a stroke of ±33.00mm. The actuator is operated by a servo valve model 252.24C-04 with a capacity of 10l/s. The displacement of the actuator is measured by a linear variable differential transducer (LVDT) and the force measured by an MTS load cell model 661.19E-04 with a max capacity of 25kN. The test station is operated through a MTS FlexTest 60 PID-controller. The test rig has a loading- and support nose of 40mm - and 25mm diameter respectively cf. Figure 7. The motion of the measurement points (see Figure 7) are tracked by the commercial DIC system: ARAMIS by Optical Measuring Techniques (GOM). The side of the test specimen has been applied a random speckle pattern of white background with black dots. The resolution of the DIC sensors is 4 megapixels and the lenses are type: Titanar with a 20mm focal length. The images are divided into interrogation cells of 15x15 pixels with a shift of 2 pixel. The measuring field is 330x330mm^2 calibrated with a 250x200mm^2 calibration panel. The precision and accuracy for each measurement point obtained by the DIC system is determined to an RMS of 0.002mm and 0.009mm respectively. The accuracy of the DIC setup is evaluated by a micrometer of the type: Mitutoyo - series 164 in the range 0-50mm. The full setup of the test station including: specimen mounted in the three point bending rig and DIC camera is presented in Figure 7.

The position and numbering of the DIC measurement points along with the overall dimension of the specimen and three point bending setup is presented in Figure 7.

5 Test result

Five GFRP specimens are tested in a quasi-static multi-component hybrid testing setup presented in Figure 5. With the hydraulic actuator operated by a feedback signal acquired on the experimental substructure by DIC an error tolerance of 0.01mm is obtained cf. Figure 3. The system is loaded within the linear elastic regime by an external force P_{ext} in increments of 900N ranging from 0 to 18kN. The equivalent vertical displacement of the shared boundary is 0 to 6mm.

5.1 Hybrid Test

The hybrid test is verified by comparing the structural response in three simulations: hybrid test, full FE-model and analytical hybrid test. In the hybrid test, Part A in Figure 5 is modelled numerically and Part B is tested experimentally. In the full FE-model, Part A and B are both modelled numerically cf. figure 4. Here, the experimental component is assigned the same bending stiffness as found from a three point bending test, cf. chapter 3.1. In the analytical hybrid test Part A is modelled numerically and Part B is calculated analytically by Bernoulli-Euler theory. Here, the bending stiffness is the same as found in chapter 3.1. For test specimen four the deformation of the sheared boundary is presented as a function of the external force P_{ext} in figure 8a. To evaluate the deviation between the three simulations the discrepancy between the hybrid test, full FE-model and analytical hybrid test is presented in Figure 8b. The load step frequency of the hybrid testing loop in figure 1 is 0.09Hz.

From Figure 8, good correlation between the three simulations is achieved. A displacement error of 0.038mm between the full FE-model and analytical hybrid test is observed cf. figure 8b. This deviation is due to the restoring force in the hybrid test being one load step behind the numerical simulation of the full structure. The maximum discrepancy between the full FE-model and hybrid test is found to 0.034mm cf. figure 8b. Here the deviation is

caused by both the restoring force in the hybrid test being one load step behind the numerical simulation of the full structure along with other sources of error in the experimental component. The discrepancy between the full FE-model and hybrid test named displacement error (hybrid) and full FE-model and analytical hybrid test named displacement error (FEM) are presented in Table 1 for the remaining four specimens.
The relative error for each displacement error is given with respect to the total displacement of the shared boundary.

5.2 Test of Stability

The stability of the hybrid testing communication loop is affected by the ratio of the global stiffness in the shared boundary for the numerical- and experimental substructure, named S_A and S_B respectively, cf. eq. (1). For this reason a parametric study of the stiffness ratio between the experimental- and numerical substructure is performed. In this study the numerical component (part A, Figure 5) is defined in a FE-model while the response of the experimental component (part B, Figure 5) is calculated analytically from a Bernoulli-Euler assumption. The response at the shared boundary as a function of the external load P_{ext} is presented in Figure 9.
From Figure 9, the restoring force in the shared boundary become unstable when $S_A < S_B$. The instability is amplified when the ratio between S_A and S_B is increased. The phenomenon is avoided when the global stiffness of the numerical model is equal or higher than the experimental specimen ($S_A \geq S_B$). In the hybrid test performed in this paper the stiffness of the numerical substructure S_A is 4.94 times higher than the stiffness of the experimental substructure S_B. The hybrid loop is therefore stable. If the hybrid testing communication loop was inverted meaning that: the numerical- and experimental substructure receives a deformation- and force input respectively, instability is avoided if ($S_A \leq S_B$).

6 Discussion

Some discrepancies between the hybrid test and full FE-model was observed cf. Figure 8 and Table 1. This discrepancy is primarily due to the restoring force in the hybrid test being one load step behind the numerical simulation of the full structure cf. Table 1. This results in the overall structure displaying a lower stiffness than in the full finite element simulation. This source of error can be minimized by decreasing the size of the load step. It could also be minimized by predicting a restoring force. However, the efficiency of this method is dependent on the material behaviour of the specimen. In this study, the specimen was linear elastic making it easy to predict. However, if the test was performed on a specimen with non-linear behaviour e.g. plasticity, buckling etc. the response is harder to estimate. This is usually the case when doing hybrid testing, since the benefit of the method is that a part of a structure displaying unpredictable response can be analysed without testing the full structure [5].
The stability of the algorithm was investigated for different stiffness ratios between the numerical model and experimental structure. It was found that the hybrid test was stable when the stiffness of the numerical model was stiffer than the physical specimen, $S_A > S_B$. It was also shown that if the hybrid testing communication loop is inverted (see Figure 5) the opposite was the case. This is in general not an issue in hybrid testing, since tests are usually performed on large structures with high stiffness compared to the structural component of interest; cf. seismic testing of dampers in buildings [4], [9], [10]. However, one must consider this issue when applying hybrid testing to other types of systems, where the experimental substructure has stiffness higher than, or close to the numerical model. This issue could be addressed by predicting a restoring force for the next load step.
DIC was in this research implemented as a technique to acquire coordinates of three measurement points along the test specimen surface

cf. Figure 7. By implementing these measurements in a control loop (see Figure 3) the source of error being slack and deformations in the load train is neglected [23] [24]. Other essential data for handling of the coupling between the substructural parts could include e.g. strain measurements [25]. This could be done on the specimen surface by full field measurements, strain gauges, etc. The GFRP specimen also allows internal strain measurements by Fibre Bragg Gratings (FBG) to include stress concentrations and residual stresses in the specimen [22].

7 Conclusion

A hybrid test was performed and the response compared to a finite element simulation of the full structure. The comparison showed a small deviation primarily caused by the restoring force in the hybrid test being one load step behind the numerical simulation of the full structure. The hybrid testing setup in this study was used to prove the functionality of the hybrid testing communication loop and implement the DIC measurements to control the actuator. In the future the hybrid testing platform will be developed to handle single component structures with more advanced geometry e.g. wind turbine blades.

8 Acknowledgement

The authors acknowledge the financial support from the Danish Centre for Composite structures and Materials for Wind Turbines (DCCSM) funded by the Danish Council for Strategic Research in Sustainable Energy and Environment (Grant 09-067212).

References

[1] X. Shao, A. M. Reinhorn and M. V. Sivaselvan, "Real-Time Hybrid Simulation Using Shake Tables and Dynamic Actuators," *Journal of Structural Engineering,* vol. 137, no. 7, pp. 748-760, 2011.

[2] O. S. Bursi, A. Gonzalez-Buelga, L. Vulcan, S. A. Neild and D. J. Wagg, "Novel coupling Rosenbrock-based algorithm for real-time dynamic substructure testing," *Eartquake Engineering and Structural Dynamics,* vol. 37, pp. 339-360, 2008.

[3] K. Takanashi and M. Nakashima, "Japanese Activities on On-line Testing," *Journal of Engineering Mechanics,* vol. 113, no. 7, pp. 1014-1032, 1987.

[4] C. Chen, J. M. Ricles, T. L. Karavasilis, Y. Chae and R. Sause, "Evaluation of a real-time hybrid simulation system for performance evaluation of structures with rate dependent devices subjected to seismic loading," *Engineering Structures,* vol. 35, pp. 71-82, 2012.

[5] A. Bonelli and O. S. Bursi, "Generalized-alpha methods for seismic structural testing," *Earthquake Engineering ad Structural Dynamics,* vol. 33, pp. 1067-1102, 2004.

[6] T. L. Karavalis, J. M. Ricles, R. Sause and C. Chen, "Experimental evaluation of the seismic performance of steel MRFs with compressed elastomer dampers using large-scale real-time hybrid simulation," *Engineering Structures,* vol. 33, pp. 1859-1869, 2011.

[7] M. Ito, Y. Murata, K. Hoki and M. Nakashima, "Online Hybrid Test on Buildings with Stud-Type Damper Made of Slitted Steel Plates Stiffened by Wood Panels," *Procedia Engineering,* vol. 14, pp. 567-571, 2011.

[8] A. Jacobsen, T. Hitaka and M. Nakashima, "Online test of building frame with slit-wall dampers capable of condition asessment," *Journal of Constructional Steel Research,* vol.

66, pp. 1320-1329, 2010.

[9] Y. Z. Lin and R. E. Christenson, "Comparison of Real-time Hybrid Testing with Shake Table Test for an MR Damper Controlled Structure," *American Control Conference,* pp. 5228-5233, 2009.

[10] J. E. Carrion, B. F. Spencer Jr. and B. M. Phillips, "Real-Time Hybrid Testing of a Semi-Actively Controlled Structure with an MR Damper," in *American Control Conference*, Hyatt Regency Riverfront, St. Louis, MO, USA, 2009.

[11] R.-Y. Jung, P. B. Shing, E. Stauffer and B. Thoen, "Performance of a real-tme pseudodynamic test system considering nonlinear structural response," *Earthquake Engineering and Structural Dynamics,* vol. 36, pp. 1785-1809, 2007.

[12] G. Mosqueda and M. Ahmadizadeh, "Combined implicit or explicit integration steps for hybrid simulation," *Earthquake Engineering and Structural Dynamics,* vol. 36, pp. 2325-2343, 2007.

[13] B. Wu, G. Xu, Q. Wang and M. S. Williams, "Operator-splitting method for real-time substructure testing," *Earthquake Engineering and Structural Dynamics,* vol. 35, pp. 293-314, 2006.

[14] M. Verma and J. Rajasankar, "Improved model for real-time substructuring testing system," *Engineering Structures,* vol. 41, pp. 258-269, 2012.

[15] M. Nakashima and N. Masaoka, "Real-Time On-Line Test for MDOF Systems," *Earthquake Engineering and Structural Dynamics,* vol. 28, pp. 393-420, 1999.

[16] C. Chen, J. M. Ricles, T. M. Marullo and O. Mercan, "Real-time hybrid testing using unconditionally stable explicit CR integration algorithm," *Earthquake Engineering and Structural Dynamics,* vol. 38, pp. 23-44, 2009.

[17] J. Waldbjørn, J. Høgh, J. Wittrup-Schmidt, M. Nielsen, K. Branner, H. Stang and C. Berggreen, "Strain and Deformation Control by Fibre Bragg Grating and Digital Image Correlation," *Strain,* (to be submitted).

[18] R. Bitter, T. Mohiuddin and M. Nawrocki, LabView Advanced Programming Techniques, Boca Rotan, Florida, USA: CRC Press, 2001.

[19] MTS, "MTS Systems Corporation, FlexTest Controllers," MTS Systems Corporation, 8 Oktober 2011. [Online]. Available: https://www.mts.com. [Accessed 8 Oktober 2011].

[20] MTS, LabVIEW Programming Libraries: Model 793.00 Software, MTS Systems Corporation, 2009.

[21] GOM, ARAMIS - User Manual - Software, Braunschweig, Germany: GOM, 2006.

[22] M. W. Nielsen, J. Wittrup-Schmidt, J. Hattel, J. H. Høgh, J. P. Waldbjørn, J. Andersen and T. L. Markussen, "In-situ measurements using FBGs of process-induced strains during curing of thick glass/epoxy laminate plate: Experimental results and Numerical modeling," *Composites.*

[23] X. Fayolle, S. Galloch and F. Hild, "Controlling Testing Machines with Digital Image Correlation," *Experimental Techniques,* vol. 31, no. 3, pp. 57-63, 2007.

[24] J. Waldbjørn, J. Høgh, J. Wittrup-Schmidt, M. Nielsen, K. Branner, H. Stang and C.

Berggreen, “Strain and Deformation Control by Fibre Bragg Grating and Digital Image Correlation,” *Strain,* To be submitted.

[25] U. C. Mueller, T. Zeh, A. W. Koch and H. Baier, “Fiber Optic Bragg Grating Sensors for High-Precision Structural Deformation Control in Optical Systems,” *SPIE,* vol. 6167, 2006.

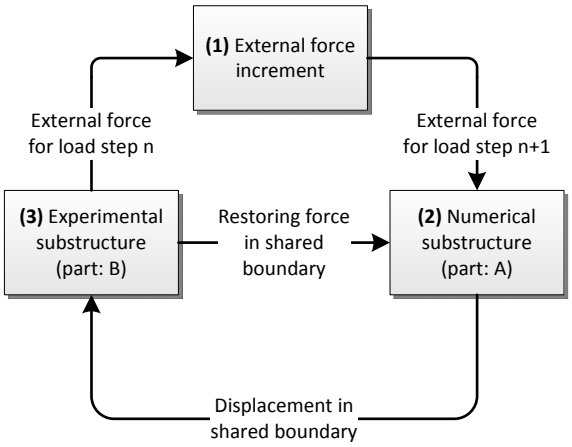

Figure 1: Dataflow in the quasi-static hybrid testing communication loop

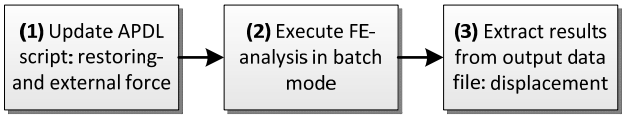

Figure 2: Dataflow in the LabVIEW and FE-analysis communication (Part A)

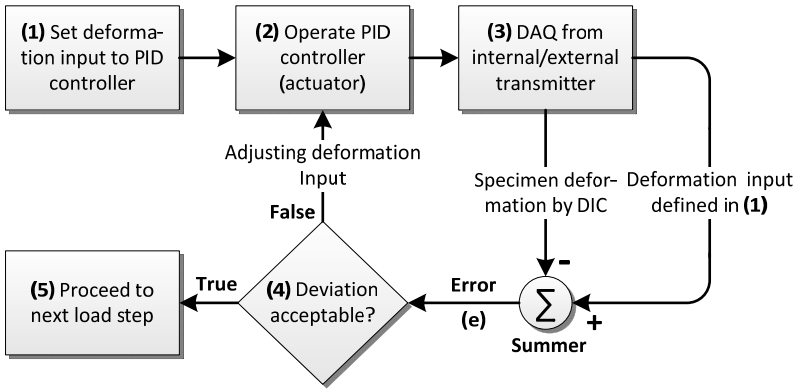

Figure 3: Dataflow in the closed single input-single output control loop (Part B)

Figure 4: Emulated structure

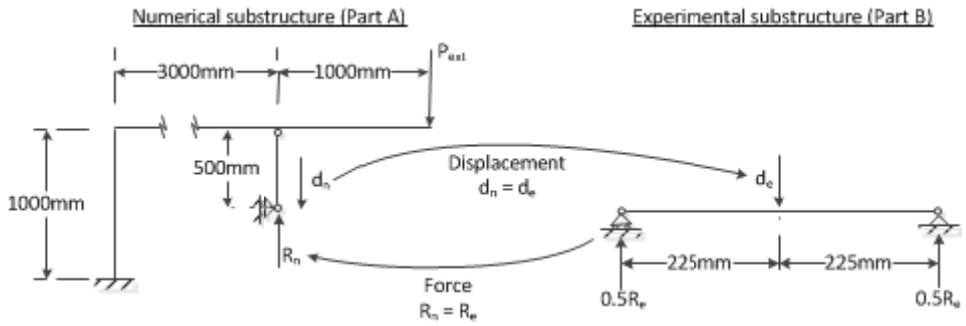

Figure 5: The emulated structure separated in: a) numerical component and b) experimental component

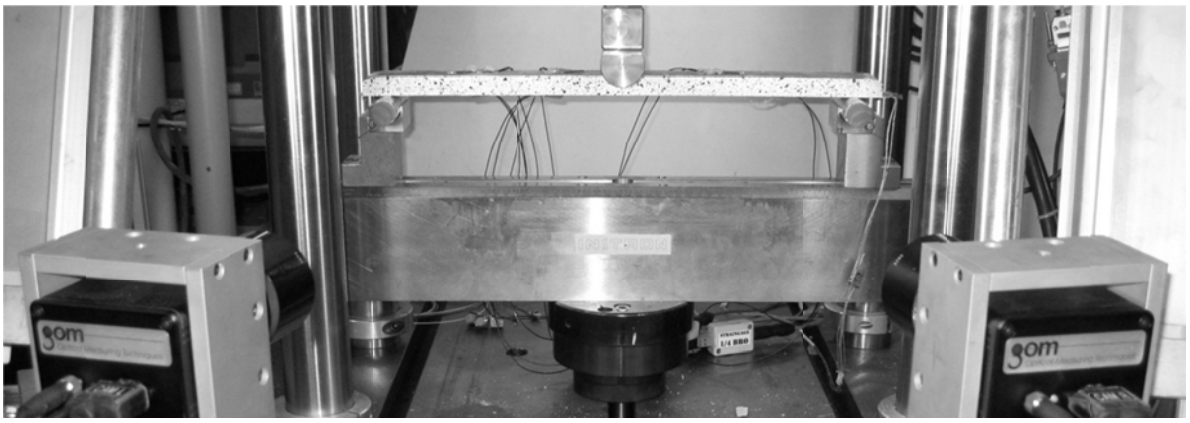

Figure 6: The three point bending setup with GFRP beam and speckle pattern

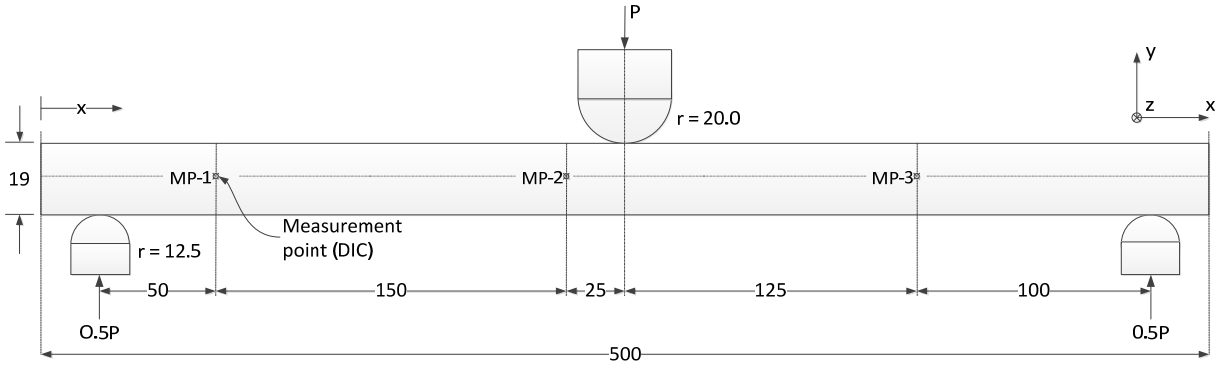

Figure 7: Dimensions of test setup and specimen along with numbering and location of DIC measurement points

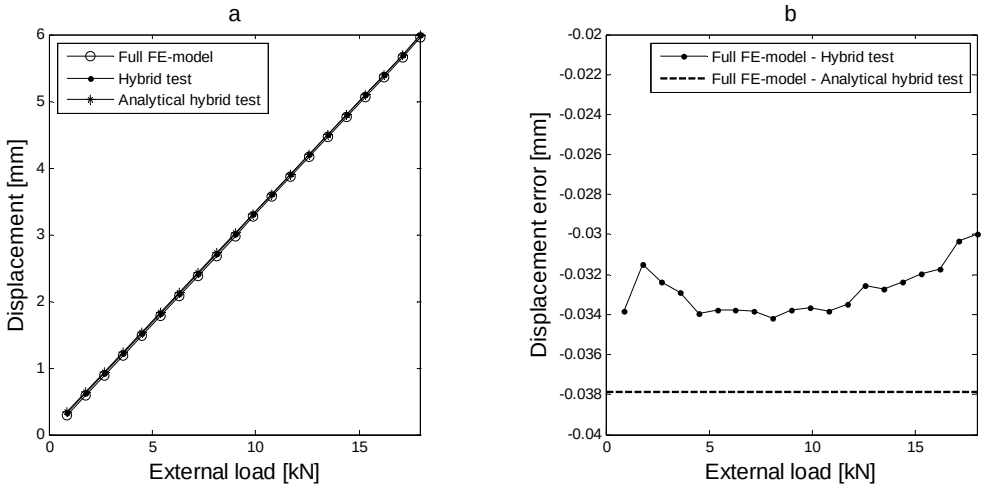

Figure 8: a) load – deformation relation at the loading point and b) discrepancy between the response of the full FE-model and hybrid test

Table 1: Displacement- and relatively error for test specimen 1 to 5

Beam number [-]	Displacement Error (FEM) [mm]	Relatively error [%]	Displacement Error (Hybrid) [mm]	Relatively error [%]
1	0.048	0.83	0.042	0.72
2	0.044	0.75	0.038	0.65
3	0.043	0.74	0.038	0.64
4	0.038	0.64	0.034	0.57
5	0.047	0.81	0.041	0.69

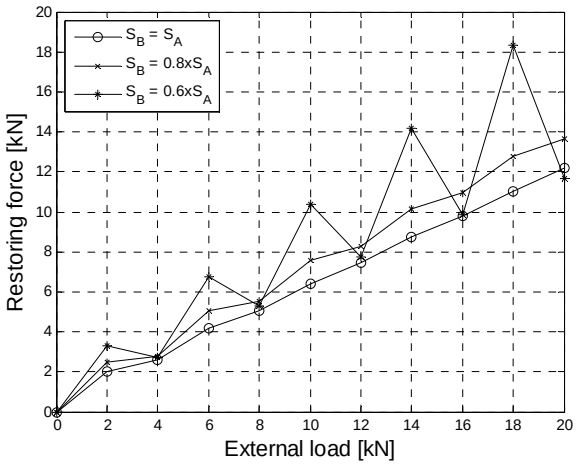

Figure 9: Restoring force in the shared boundary as a function of the external load

This page is intentionally left blank

Appendix H

Life cycle strain monitoring in glass fibre reinforced polymer laminates using embedded fibre Bragg grating sensors from manufacturing to failure

Michael W Nielsen, Jacob W Schmidt, Jacob H Høgh, Jacob P Waldbjørn, Jesper H Hattel, Tom L Andersen and Christen M Markussen

Journal of Composite Materials published online 15 January 2013
DOI: 10.1177/0021998312472221

Original Article

JOURNAL OF COMPOSITE MATERIALS

Journal of Composite Materials
0(0) 1–17

DOI: 10.1177/0021998312472221
jcm.sagepub.com

SAGE

Life cycle strain monitoring in glass fibre reinforced polymer laminates using embedded fibre Bragg grating sensors from manufacturing to failure

Michael W Nielsen[1], Jacob W Schmidt[2], Jacob H Høgh[3], Jacob P Waldbjørn[2], Jesper H Hattel[1], Tom L Andersen[3] and Christen M Markussen[3]

Abstract

A holistic approach to strain monitoring in fibre-reinforced polymer composites is presented using embedded fibre Bragg grating sensors. Internal strains are monitored in unidirectional E-glass/epoxy laminate beams during vacuum infusion, curing, post-curing and subsequent loading in flexure until failure. The internal process-induced strain development is investigated through use of different cure schedules and tool/part interactions. The fibre Bragg grating sensors successfully monitor resin flow front progression during infusion, and strain development during curing, representative of the different cure temperatures and tool/part interfaces used. Substantial internal process-induced strains develop in the transverse fibre direction, which should be taken into consideration when designing fibre-reinforced polymer laminates. Flexure tests indicate no significant difference in the mechanical properties of the differently cured specimens, despite the large differences in measured residual strains. This indicates that conventional flexure testing may not reveal residual strain or stress effects at small specimen scale levels. The internal stresses are seen to influence the accuracy of the fibre Bragg gratings within the loading regime. This study confirms the effectiveness of composite life cycle strain monitoring for developing consistent manufacturing processes.

Keywords

Strain monitoring, fibre Bragg grating sensors, curing, process-induced strains, life cycle, composite

Introduction

Fibre-reinforced polymer (FRP) composites are widely used in various industrial applications. Such materials provide low weight, excellent corrosion resistance and high strength, which are beneficial properties in, for instance, the construction of commercial wind turbine blades and civil structures. The manufacturing process of the composite structure can, however, greatly influence the performance of the part, which is dependent on the presence of voids, dry spots, matrix cracks, waviness of the ply stack and other manufacturing-related defects. Such defects can result in crack initiation when the structure is loaded and premature failure at lower loads than expected when designing the structure.

During the manufacture of thermosetting matrix composites, a material state transition of the resin occurs, from a viscous, to rubbery and glassy state during curing. It is within this transition that various mechanisms result in the development of process-induced stresses in the composite structure, which when unconstrained result in shape distortions.[1–3]

[1]Department of Mechanical Engineering, Technical University of Denmark, Denmark
[2]Department of Civil Engineering, Technical University of Denmark, Denmark
[3]Department of Wind Energy, Technical University of Denmark, Denmark

Corresponding author:
Michael W Nielsen, Department of Mechanical Engineering, Technical University of Denmark, Produktionstorvet, Bygning 425, 2800 Kongens Lyngby, Denmark.
Email: mwni@mek.dtu.dk

In cases where these process-induced stresses are sufficiently large and unavoidable, for instance due to strong internal or external constraints, they can result in various strength reducing mechanisms that support premature failure. For instance, large process-induced residual stresses are known to induce matrix cracking, interfacial debonding and delamination in fibre-reinforced composites.[1] In other works,[4–6] demonstrated that for thick-walled composite tubes, residual stresses can be so great that matrix cracking was promoted. At a micromechanic level, Nedele and Wisnom[7] showed that process-induced stresses at the fibre–matrix interface can be as large as 30 MPa, due to the combination of hoop and radial stress components. This stress magnitude is substantial considering that the typical tensile strength of epoxy matrix materials is approximately 60–65 MPa. Furthermore, due to the viscoelastic nature of the polymer matrix material, large process-induced residual stresses can also influence the long-term dimensional stability of the part, due to creep or stress relaxation behaviour.

The main mechanisms responsible for process-induced shape distortions and residual stresses are: (a) the thermal expansion mismatch of the constituent materials; (b) matrix chemical shrinkage during curing; and (c) interactions at the tool/part interface.[2,3,8–11] Of particular interest, when considering thick laminate composites is also the manufacturing cure cycle design. High cure temperatures and fast heating/cooling rates can result in highly non-uniform temperature and cure gradients within the part resulting in differential curing and subsequent development of internal stresses.[3,4–6,11] Similar effects in the form of a non-uniform distribution of in-plane shear stresses can arise due to constraints posed by tooling during processing.[10,12] A combination of the above-named residual stress mechanisms and manufacturing defects can cause local premature failure at lower load magnitudes than would otherwise be predicted in a defect-free composite structure.

In order to experimentally monitor the internal strain development during manufacturing, the use of fibre optic sensors has gained approval as a desirable in situ method.[13–24] Apparent advantages include their ease of integration structurally during the composite manufacturing phase and the minimal influence to the host part structural properties. In recent works by the authors, fibre Bragg grating (FBG) sensors were successfully embedded in a laminate composite for cure strain monitoring purposes.[19] As opposed to the use of conventional non-intrusive strain/deformation monitoring methods (e.g. using strain gauges (SGs) or digital image correlation (DIC)), embedded optical fibre sensors offer the advantage of being able to monitor local internal strains in the composite readily. Moreover, FBG sensors offer the capability to accurately monitor resin flow front progression during infusion.[14,23,24]

This study focuses on investigating the development of internal strains in glass FRP (GFRP) composites in a holistic manner during the composite life cycle using embedded FBG sensors. The term *life cycle* in this context refers to the composite life time from manufacturing using vacuum infusion and until mechanical testing, as illustrated in Figure 1. Thus, using this approach, we wish to monitor the development of process-induced internal strains and investigate the influence of these strains and residual stresses in the composite during manufacturing and testing. This study provides an approach to monitor and gain knowledge during the manufacturing procedure of FRP composites. Such manufacturing control is important if consistency in the quality of the composite is desired. In addition, information of the residual strain and stress state in the structure is important if these are to be accounted for in the design of a structural component.

FBG sensor principle

Strain monitoring using optical fibres with FBG sensors requires a light source, an interrogator unit and an appropriate data acquisition software tool. The light source transmits a broadband light spectrum through the optical fibre and the axially placed FBG sensor back-reflects light within a specific pre-defined wavelength. This back-reflected light is fed into the interrogating unit designed to measure the reflected light signal. Modulation of the reflected signal, centred along the Bragg wavelength, is linearly related to mechanical or thermal loads. The FBG wavelength variation is hence determined using[13]

$$\frac{\Delta\lambda_B}{\lambda_B^0} = K_\epsilon\left[\Delta\varepsilon_{app}^{host} + \Delta\varepsilon_{th}^{host}\right] + K_T\Delta T = K_\epsilon\Delta\varepsilon_{tot} + K_T\Delta T \tag{1}$$

where $\Delta\lambda_B$ is the change in Bragg grating wavelength and λ_B^0 the initial unstrained grating wavelength, K_ϵ and K_T are the optical fibre mechanical strain and temperature sensitivities, specific for the type of sensor used. $\Delta\varepsilon_{tot}$ is the change in total strain – a summation of the increments from the applied strain $\Delta\varepsilon_{app}^{host}$ and the host thermal strain $\Delta\varepsilon_{th}^{host}$. Equation (1) describes the linear mechanical and thermal response of the FBG sensor. When the FBG is embedded in a composite material, here on termed the host material, complete strain transfer is achieved once bonding between the optical fibre and the host material occurs. Subsequently, any mechanical straining and thermal expansion of the host material would govern the response of the FBG sensor. Knowing the temperature

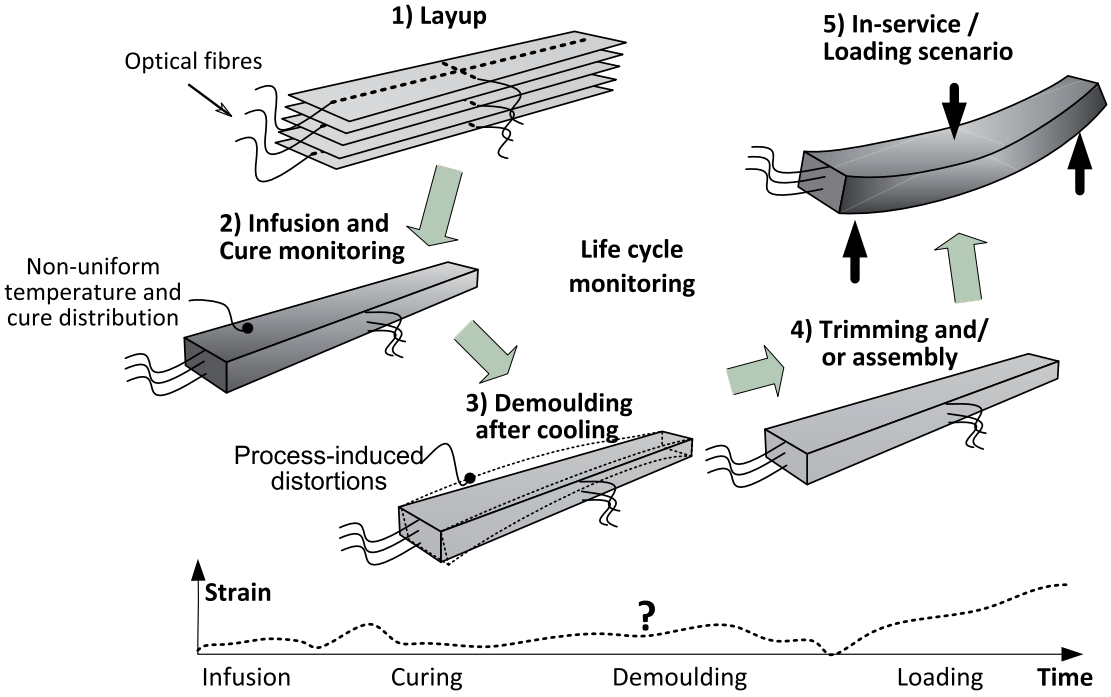

Figure 1. Schematic of life cycle monitoring approach for a GFRP laminate using embedded optical fibres where internal strains are monitored from manufacture to loading.
GFRP: glass fibre reinforced polymer.

and sensor wavelength variation, the corresponding change in host material total strain in the optical fibre axial direction can be determined using equation (1) by isolating $\Delta\varepsilon_{tot}$.

In this study, silica optical fibres provided by FOS&S, Belgium, were used, with multiple draw tower grating (DTG®) FBG sensors with an Ormocer® coating (cladding diameter 125 µm). The sensitivity coefficients K_ϵ and K_T are equal to $0.775\text{E}-6\,\mu\varepsilon^{-1}$ and $6.27\text{E}-6^{\circ}\text{C}^{-1}$, respectively. When considering the magnitudes of the mechanical strain and temperature sensitivity coefficients, it is clear that accurate temperatures at the vicinity of the sensors is needed in order to determine precise strains. It has been shown that the strain sensitivity remains constant below 180°C for this optical fibre.[20] Furthermore, DTG FBGs are known to exhibit little variation in strain-optic coefficients when loaded which is advantageous. The Ormocer coating helps reduce the sensor sensitivity to external transverse loading, hence increasing the accuracy of the axial strain measurements. An I-MON E interrogator, from Ibsen Photonics, Denmark, was used for data acquisition. The I-MON E is a stand-alone interrogation monitor with a wavelength bandwidth of 85 nm, capable of assessing <70 FBG sensor signals. The interrogator wavelength accuracy lies within 5 pm with a sampling rate of up to 970 Hz. The grating length used in this work, i.e. the effective strain measurement region, spans 4 mm of the optical fibre length at each sensor positioned along the optical fibre. In other works, where a similar length is used, no peak splitting of the back-reflected wavelength spectrum was experienced.[21,22] Peak-splitting is generally attributed to the existence of transverse loading of the sensor causing a local distortion of the reflected signal spectra. This is most likely to occur when using long gratings where a large transverse local load is present in the vicinity of the FBG sensor. By having a short grating length and using a coated fibre, this problem is greatly reduced. Studies found that good predictions of process strains in neat resin and composite laminates were achievable using a similar setup.[13,16,19]

Experimental procedure

Materials

The composite constituent materials used in this study comprise of unidirectional (UD) fibre reinforcement fabric type L1200/G50F-E06-A, from Devold AMT, with a nominal area weight of 1246 g/m^2 and a thermoset epoxy resin matrix material type Airstone 760E mixed 100 : 32 parts-by-weight with Airstone 776H hardener, from Dow Chemicals Company. The reinforcement fibre and resin matrix material used in this study are representative of materials commonly

used in commercial wind turbine blades. Material properties are summarised in Table 1. As mentioned in the introduction, epoxy resins exhibit volumetric chemical shrinkage during cross-linking, generally known to lie between 3% and 7%.[9–11] Both constituent materials used exhibit isotropic thermal expansion behaviour, as observed from Table 1.

Manufacturing procedure

In order to investigate the influence of the cure cycle profile and boundary conditions on the process-induced strain development and subsequent part performance, two different manufacturing procedures were employed, as summarised in Figure 2 and Table 2. The tool used was a transparent tempered glass plate, chosen in order to visibly ensure full wetting of the reinforcement fibres during infusion. Vacuum infusion was performed as edge infusion with resin flow in the longitudinal fibre direction in the entire length of the specimens. An Enka channel mesh and highly porous distribution net (Figure 2) are used in order to allow fast flow along the top surface of the reinforcement fabric and subsequent through-thickness wetting. Fibre layup was established using 22 layers of UD glass fibre fabric each cut to $500 \times 100\,\text{mm}^2$ ($l \times b$) and stacked symmetrically on the glass tool with the fibre backing material faced outwards. During the layup procedure, placement of optical fibres and thermocouples was conducted as described in the subsequent section. After layup, a vacuum leak test was carried out prior to infusion. The epoxy resin was mixed with the hardener and degassed in a vacuum chamber with a vacuum pressure above 95 kPa, until all foaming had subsided. Infusion was carried out at ambient temperature with a vacuum pressure of 95 kPa. The inlet hose was closed once resin flowed through the outlet hose and full impregnation of the reinforcement fibres was visible. Full wetting of the reinforcement fibres took approximately 45 min. The vacuum pressure was then reduced to 60 kPa and pressure equalisation and further compaction of the laminate was allowed for 15 min before the outlet was closed. The vacuum infused specimens were placed into pre-heated ovens at 50°C and 80°C for approximately 5 and 3 h, respectively, for the different cure cycles investigated (Table 2). The in-mould cure periods were chosen such that the resin was nearly fully cured based on differential scanning calorimetry isothermal scan data at various temperatures. Different cure temperatures were chosen in order to achieve different thermal residual stresses.

Table 1. Material properties of E-glass reinforcement fibre and epoxy resin.

	Density (kg/m^3)	Young's modulus (GPa)	Poisson's ratio	CTE ($\times 10^{-6}{}^{\circ}C^{-1}$)
UD E-glass fibre	2600	72.0[a]	0.22	5.04[a]
Epoxy resin (cured)	1040	3.116	0.32[b]	65.41[b]

CTE: coefficient of thermal expansion; UD: unidirectional.
[a]Isotropic for E-glass.
[b]Approximated value from the literature.
[c]Resin supplier data sheet.[28]

Table 2. Experimental design matrix showing layup, cure schedules and boundary conditions.

	Type A	Type B
Layup	$[0]_{22}$	$[0]_{22}$
Cure temperature[a] (°C)	50	80
Temperature hold[b] (min)	300	180
Cooling	Natural convection	Natural convection
Post-cure temperature[a] (°C)	90	–
Post-cure hold[b] (min)	120	–
Tool/part interface	Release agent[c]	Perforated release foil

[a]Pre-heated oven temperature.
[b]Temperature hold period includes heating from ambient- to pre-heated oven temperature.
[c]The tool surface was treated with release agent prior to the experiments.

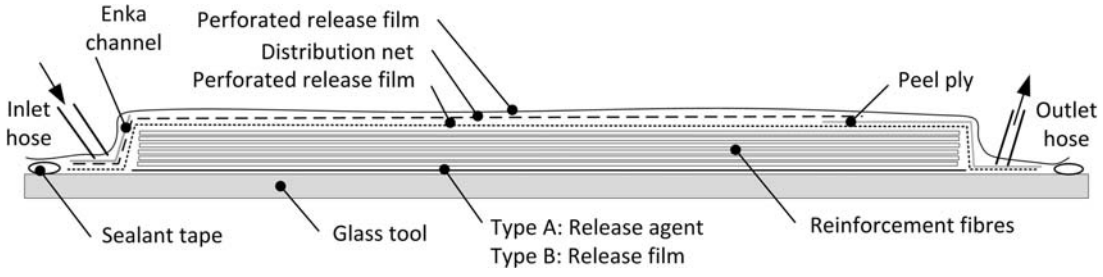

Figure 2. Schematic of vacuum infusion setup.

The cured in-mould laminates were cooled by natural convection to ambient temperature. Cooling in this manner took approximately 3.5 h and 5.5 h, respectively, for the 50°C and 80°C cure cycles. After cooling, demoulding was carried out and type A specimens were post-cured in a pre-heated oven at 90°C for 2 h. Type B specimens were not post-cured. All specimens were then cut into $500 \times 45\,\text{mm}^2$ ($l \times b$) beams. Trimming of the beam sides was done in order to ensure a constant cross section of each specimen, necessary in the mechanical tests. The manufactured specimens had a final average thickness of 19.04 mm with a variation of approximately 0.20 mm, and a fibre volume fraction of approximately 55%.

During manufacturing, two different tool/part interfacial interactions were investigated using release agent and release film (Table 2). This was done to investigate non-uniform through-thickness strain variations during manufacturing as well as the possible occurrence of locking.[11] A total of 10 laminates were manufactured using the different cure cycle and boundary conditions summarised in Table 2 evenly divided between the specimens.

Optical fibre and thermocouple sensor embedment

During the layup process, optical fibres consisting each of three FBG sensors were placed in the laminate, as illustrated in Figure 3. The optical fibres were placed along the UD reinforcement fibre direction (i.e. longitudinally) as well as perpendicular to the reinforcement fibres (transversely). This was done at three different interlayer locations along the ply stack thickness direction: between the 1st and 2nd, 11th and 12th and 21st and 22nd plies representing the laminate beam specimen top, middle and bottom planes (*Top*, *Mid* and *Bot* henceforth). In order to ensure that the optical fibres remained in place, they were *sewn* in place using the backing fibres of the reinforcement fibre fabrics, as an alternative to using adhesives, etc. In this manner, the optical fibres remained aligned but at the same time not entirely constrained. Temperature monitoring during processing was conducted using type-J (Fe-CuNi) 2×0.5 mm thermocouples, placed at various regions on the outer surface and within different layers approximately 10 mm from the edge of the laminate. Temperature data was collected using an eight-channel DaqPRO data acquisition system (Fourier systems, Barrington, USA), with a sampling frequency of 10 Hz. Data logging were commenced once infusion was initiated, as well as at different intervals at ambient temperatures between the various manufacturing steps. Hence, information revealing the internal strain development at discrete times throughout the manufacturing process was obtained from the specimens at different through-thickness layers in different reinforcement fibre directions. Strain and temperature monitoring was carried out in three 'Type A' and two 'Type B' laminate beam specimens, respectively. The remaining laminate beams without embedded sensors were solely used for mechanical test verification purposes.

Temperature logging conducted during the experiments served two purposes. First, the temperatures are used in equation (1) in order to compensate for the thermal expansion of the optical fibre and determine the total mechanical strains from the FBG data. The thermocouples are also used to monitor the exothermic reaction of the resin during curing and ensure that the specimens were cooled to the ambient temperature at the data sampling intervals. Figure 4 shows some of the specimens manufactured at various stages during the experiments.

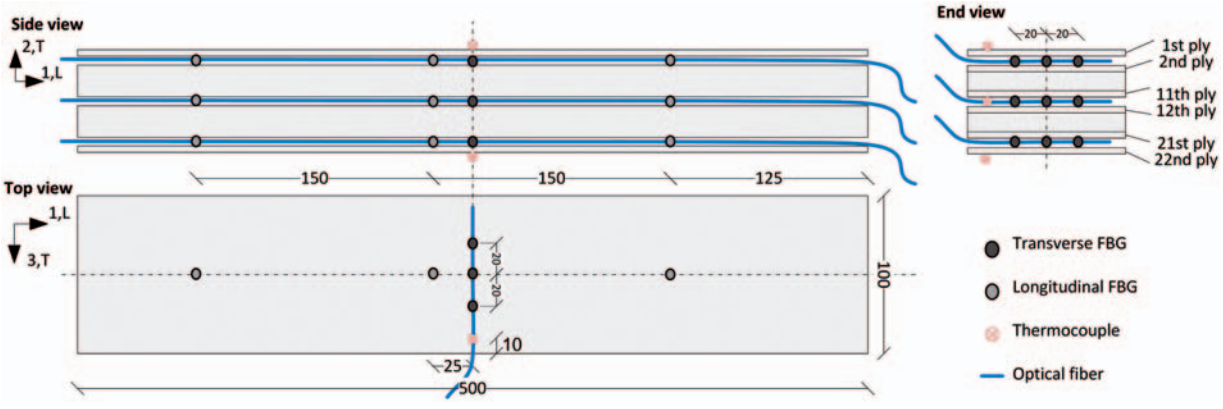

Figure 3. Schematic of laminate beam layup with FBG and thermocouple sensor placement.
FBG: fibre Bragg grating.
All dimensions are in mm.

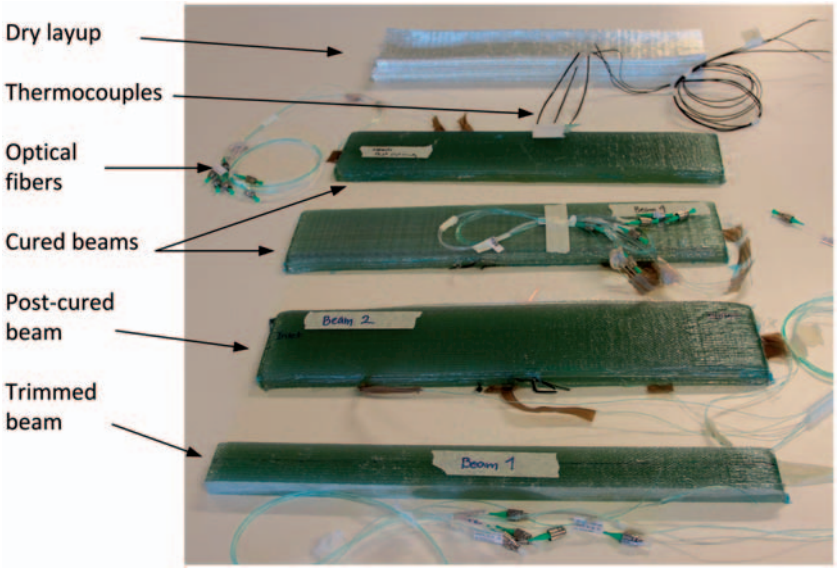

Figure 4. Laminate beam specimens at different stages in the manufacturing procedure, seen with embedded FBG sensors and thermocouples.
FBG: fibre Bragg grating.

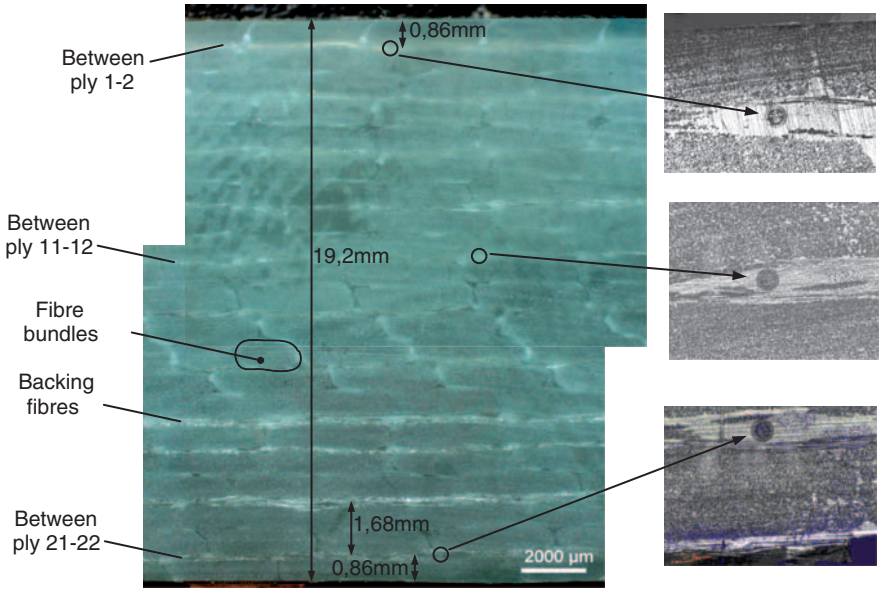

Figure 5. Image of laminate specimen cross section with close-up of inter-ply placement of optical fibres.

To ensure that the optical fibres remained at their respective laminate inter-ply locations during layup and vacuum infusion, a cross-sectional microscope analysis was conducted, after mechanical testing. Knowing the exact depth of each optical fibre is, for instance, vital for correct comparison of surface mounted SGs and embedded optical fibres. Figure 5 shows microscope images of the laminate beam cross section, showing placement of optical fibres after manufacturing. The optical fibres were found to be situated at the same inter-ply regions as during layup. It has been reported in some studies that standard 125 µm optical fibres produce a insignificant perturbation of the host material when embedded parallel to the reinforcing fibres in laminates.[25,26]

Experimental results and discussion

Strains at discrete periods during manufacturing

Figures 6 and 7 show measured total strains at discrete periods during manufacturing for type A and B

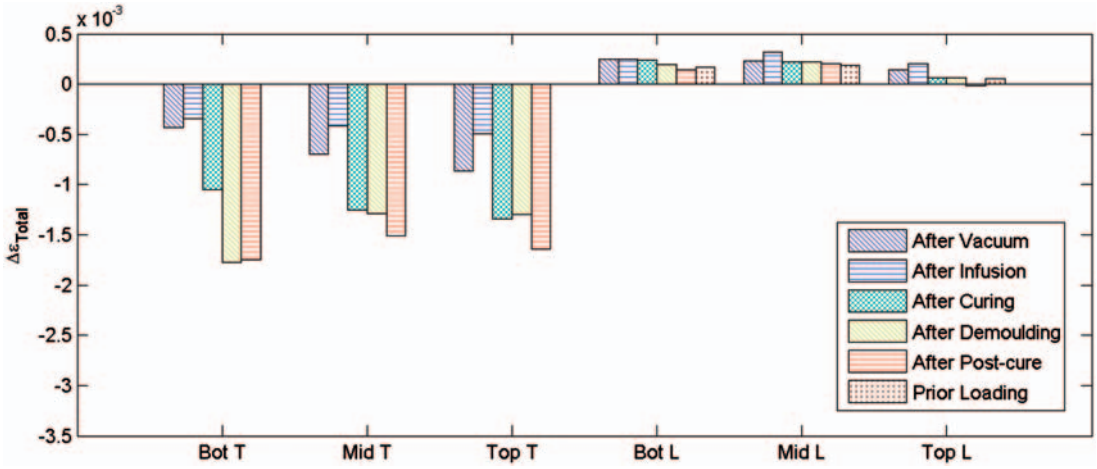

Figure 6. Average total strains at manufacturing intervals, measured at ambient temperature for type A laminate beam specimens.

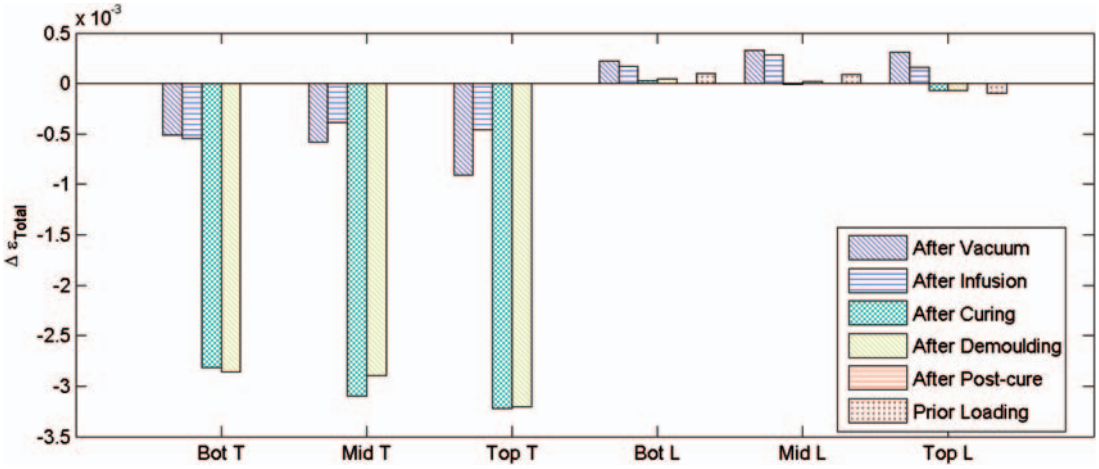

Figure 7. Average total strains at manufacturing intervals, measured at ambient temperature for type B laminate beam specimens.

laminate beams, respectively, at ambient temperature. The values presented are averages of type A and B specimens for all three FBG sensors on each optical fibre at discrete stages during manufacturing. Total strains are shown: (a) after vacuum pressure is applied; (b) after infusion (resin flow); (c) after curing; (d) after demoulding; (e) after post-curing (type A only); and finally (f) prior loading. Note that the transversely embedded optical fibres were no longer usable after cutting, hence no transverse measurements are conducted prior loading.

In both cure cycle cases shown (Figures 6 and 7), transverse total strains which are matrix dominated are seen to have higher magnitudes as compared to the longitudinal strains, which are fibre dominated, i.e. more constrained. General tendencies are as follows: upon applying vacuum pressure, a negative increment in strains are seen in the transverse direction, while a small positive increment in tensile strains arise in the longitudinal direction (here onwards *T*- and *L*-directions). The elongation longitudinally is believed to be due to re-alignment of fibres from a wavy to straight state when under pressure effectively straining the optical fibre in tension. After infusion, a slight decrease in strain magnitudes is exhibited in general. After curing, a significant negative strain increment in the *T*-direction occurs in type A and B specimens throughout the beam thickness, as well as a slight negative strain increment in the *T*-direction. This is an indication of prevailing compression/shrinkage due to the inherent mechanisms present, i.e. matrix shrinkage and thermal compression upon cooling. A significant difference in strain magnitudes after curing is seen between type A and B specimens, with larger negative strains in type B specimens. Assuming that both specimens are fully cured such that total chemical shrinkage has taken place, the difference in magnitudes owes to larger thermally induced strains in type B beams. The through-thickness strain

distribution in both cases is largest near the top surface as compared to at the tool/part interface (Bot) where tool/part interaction constrains movement. Upon demoulding, a larger strain release is exhibited at Bot T in type A specimens, as opposed to Bot T in type B beams. This is an indication that better bonding at the tool/part interface existed during curing when release agent is used at the tool/part interface as opposed to when using the perforated release foil.

Figure 8 shows the total strains for type A and B beams in the *L*- and *T*-directions compared to each other. Results are shown for stages after curing, where it is assumed that perfect bonding between the composite and optical fibre exists. After curing, a non-uniform strain distribution through the thickness is seen in both *L*- and *T*-directions. After demoulding, negative strain increments are seen at the laminate bottom plane in the *T*-direction for both beam types (Figure 8 (T-2)), indicating a tensile stress state at the bottom laminate plane after curing. This implies that a compressive stress state exists at the laminate centre while tensile stresses exist at the surfaces, which is a common stress state when an inside-out cure occurs due to exothermic peak temperatures at the centre, as also seen in Bogetti and Gillespie.[3] Moreover, for type B specimens, this is also seen at the top plane, while at the middle plane a positive strain increment is seen. When considering the through-thickness strain gradients, a more uniform distribution is generally seen in type B specimens. This indicates that weaker bonding at the tool/part interface exists when using release film, allowing for more sliding friction behaviour. This observation is supported by the fact that all type B specimens were significantly easier to separate from the glass tool during demoulding.

When considering the free-standing change in type B longitudinal strains from demoulding and prior loading (Figure 8 (L-2 to L-4)), an increase in tensile strains is seen near the beam bottom plane. This is due to visco-elastic creep, exhibited by the composite during the 6 week period in time before loading tests were commenced. Contrary to this, a decrease in tensile strains (compressive creep) is seen for type A beams after post-curing and prior loading. Positive creep strains indicate

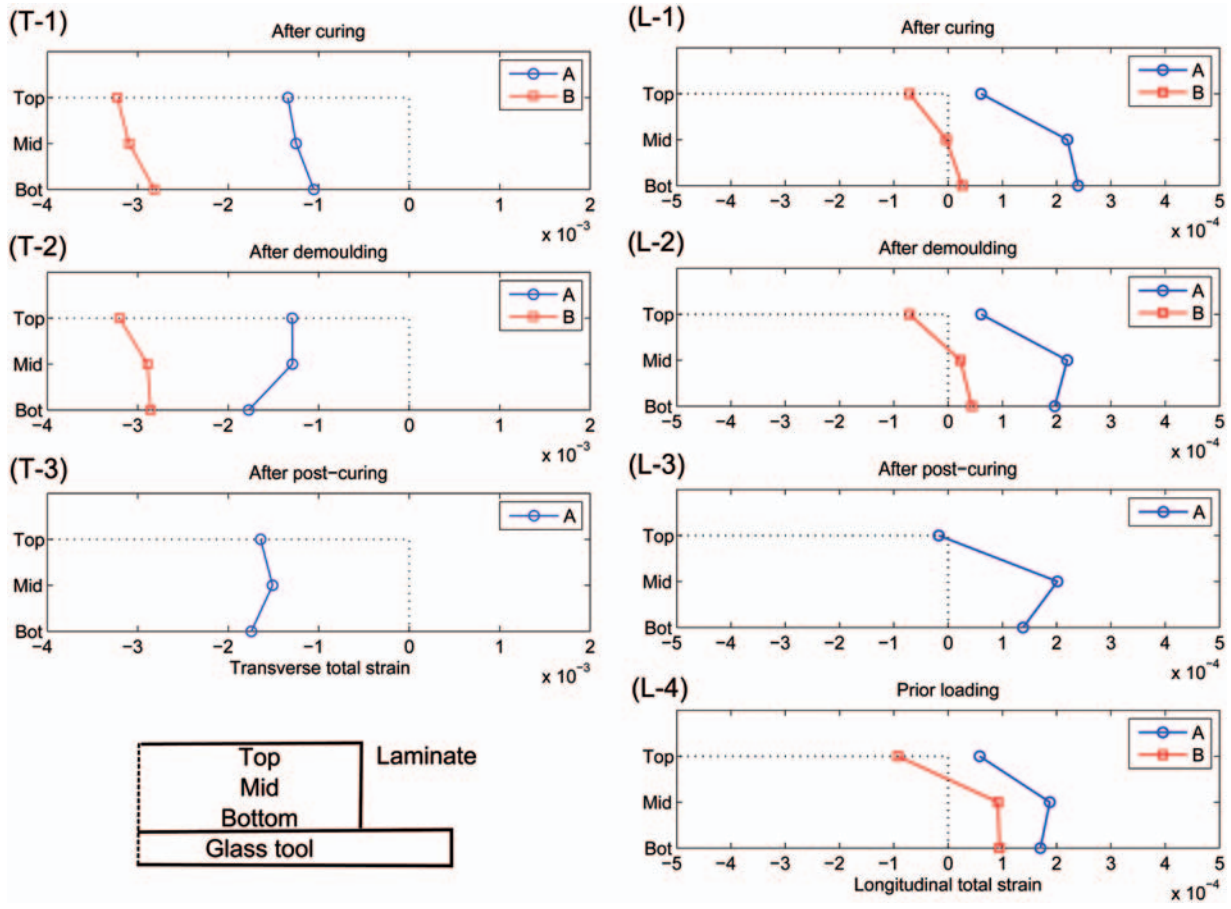

Figure 8. Average laminate type A and B transverse (T) and longitudinal (L) strains after various manufacturing stages compared to non-strained (dashed line) laminate beam state.

that a compressive stress state exists, that is not readily released as distortions after curing, but gradually with time. Nedele and Wisnom[7] and Wisnom et al.[11] found that residual stresses at a micromechanic level may not normally readily cause distortions because they may arise at a very local scale, where any deforming effects are averaged out over the larger volume of material. Hence inter-ply or microscale compressive stresses may still exist in the beams.

Strain monitoring signal quality

The quality of the strain measurements was monitored during this study by constant evaluation of the reflected light signal spectrum. This is presented for a type B laminate after curing at ambient temperature in Figure 9, compared to the reflected signal prior vacuum-bagging and infusion for longitudinally and transversely embedded FBG sensors. Due to the large compressive strains in the transverse direction after curing, the signal peaks have been shifted left to lower wavelength values. Furthermore, some distortion of the FBG spectrum is seen in the form of birefringence (peak splitting) of the Bragg peak. The peak-splitting seen indicates development of transverse loads at the vicinity of the sensors.[13,18] This could be the result of backing-fibres or perpendicular UD fibre bundles that are locally loading the optical fibres not to mention resin shrinkage stresses around each optical fibre (Figure 10). Broadening of the spectrum is also

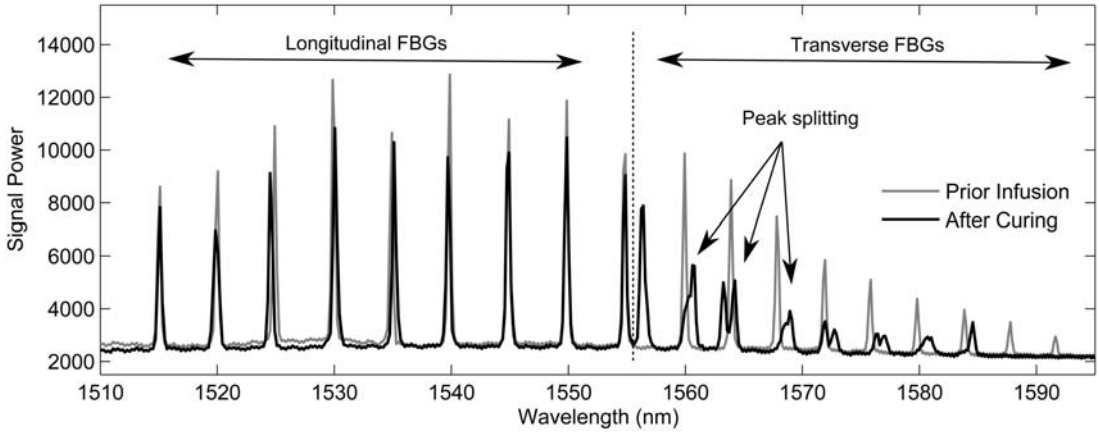

Figure 9. Wavelength signal spectrum for type B laminate after curing, showing clear signs of birefringence of the light signal (peak splitting).

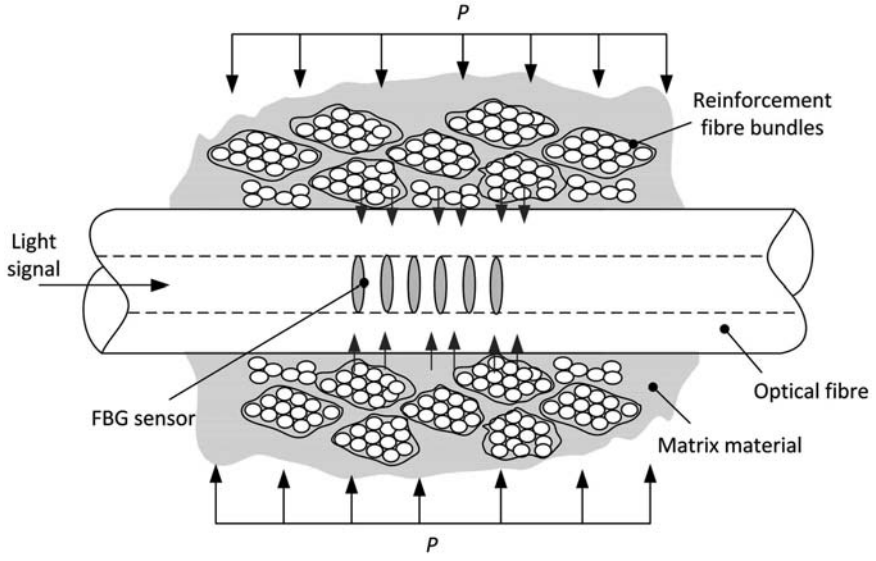

Figure 10. Illustration of mechanisms causing transverse loading of optical fibre from reinforcement fibre tows perpendicular to the optical fibre during processing.

observed, which is also an indication that transverse stress may exist.[13] Distortion is not seen in any of the signals from longitudinal sensors, but only in Type B transverse signals. Acquiring the correct discrete wavelength shift in order to determine the mechanical strain variation must, therefore, be interpreted with caution where peak-splitting of the signal is present. The data acquisition software seeks only the signal peaks above a user-defined threshold found using an *n*th-order polynomial fit for a prescribed number of expected peak signals (here 18). In this study, in order to account for these signal distortions, an approach is used where averaging of multiple peaks within a common base is performed for the discrete ambient strains presented in the previous section. The spectrum data shows that larger stresses are generally present in Type B specimens as opposed to Type A.

In situ strains during infusion

Flow front monitoring is conducted during resin infusion by monitoring the shift in wavelength of the embedded FBG sensors during vacuum infusion. Figures 11 and 12 show the strain variations during infusion for a beam specimen representative of general tendencies occurring in the *L*- and *T*-directions, respectively.

After approximately 100 s, infusion is commenced and the resin flow front reaches the L-embedded sensors near the inlet first, seen as changes in sensor 3 wavelengths at the top, mid and bottom (Figure 11). As the flow front progresses along the laminate top surface and gradually through the thickness towards the outlet, changes in wavelengths are seen in the L-embedded sensors and the corresponding T-embedded sensors (Figure 12). Hence, at different times during

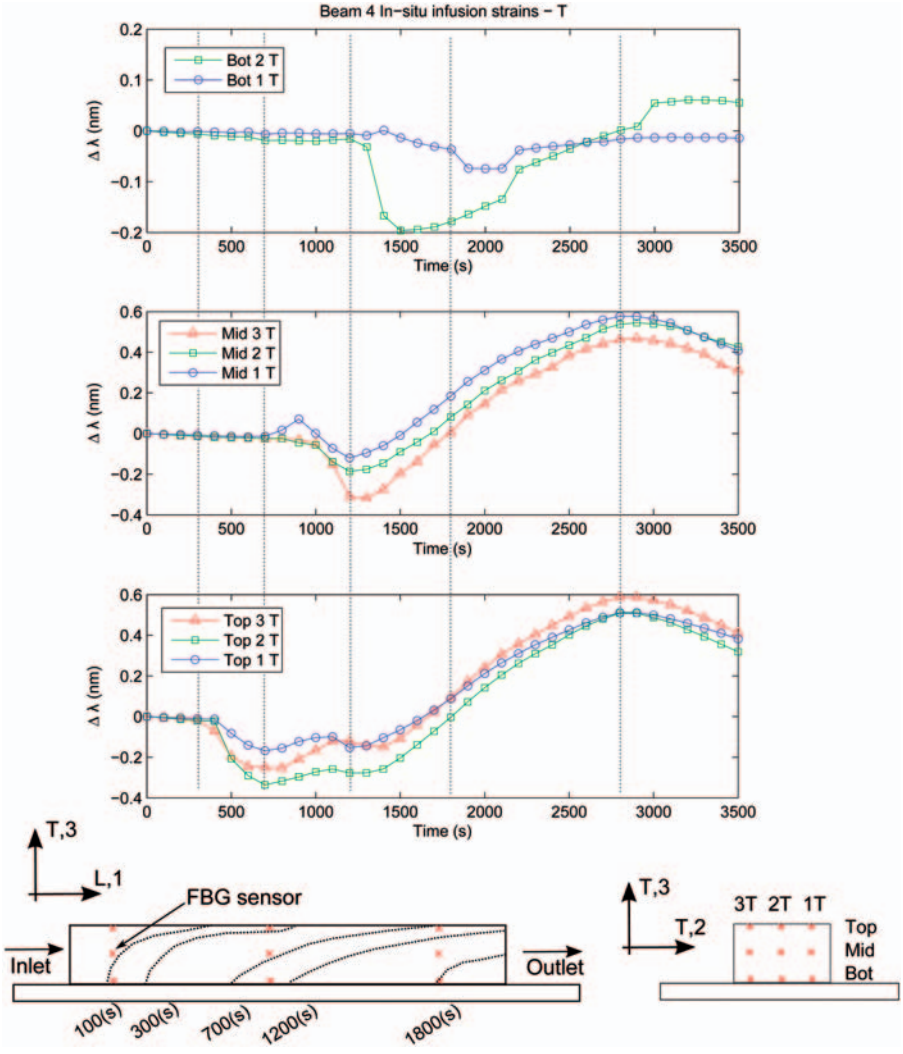

Figure 11. Variations in longitudinally embedded FBG sensor wavelengths during infusion.
Also seen is a schematic of the sensor placement from inlet to outlet and the expected flow front development.
FBG: fibre Bragg grating.

infusion, through-thickness tracking of the resin flow front in different directions is possible. After approximately time $t = 2800$ s, the inlet hose is closed, marked by changes in wavelength in all embedded sensors as the flow speed is drastically reduced.

In situ strains during curing

In Figure 13, experimentally measured temperatures for type A and B cure cycles are presented. A gap in the acquired type A temperature data is seen between time $t = 180$ and 300 min. For the sake of continuity, estimated temperature development curves are drawn, following tendencies from type B data. In both cases, the exothermic reaction during resin cross-linking as the matrix cures results in peak temperatures that are higher than the prescribed oven cure temperatures of 50°C and 80°C for type A and B, respectively. The large increase in temperatures is accredited to high heat generation rates as the matrix cures. The peak exothermic

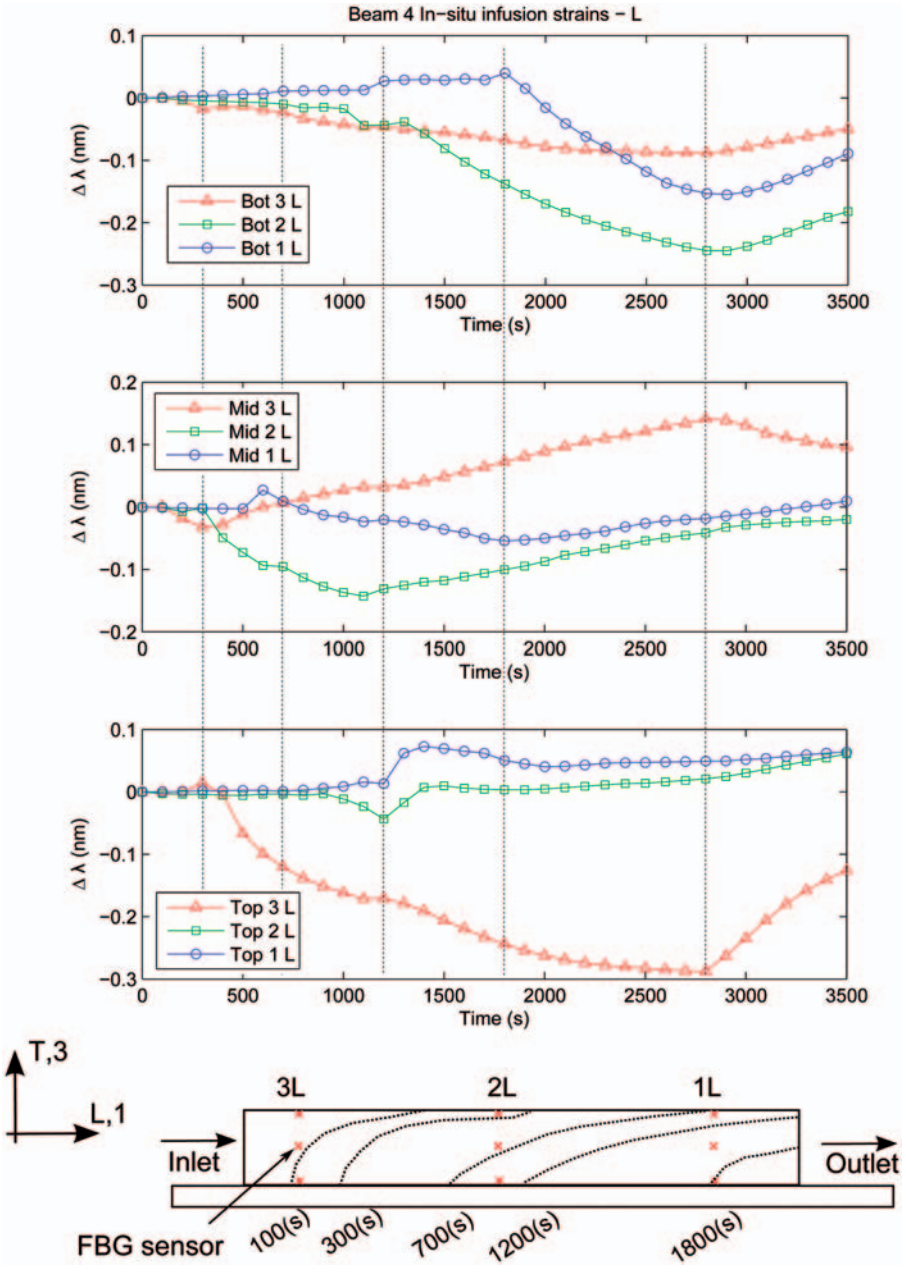

Figure 12. Variations in transversely embedded FBG sensor wavelengths during infusion.
Similarly, a schematic of the sensor placement is given and the expected flow front development, as shown in Figure 11.
FBG: fibre Bragg grating.

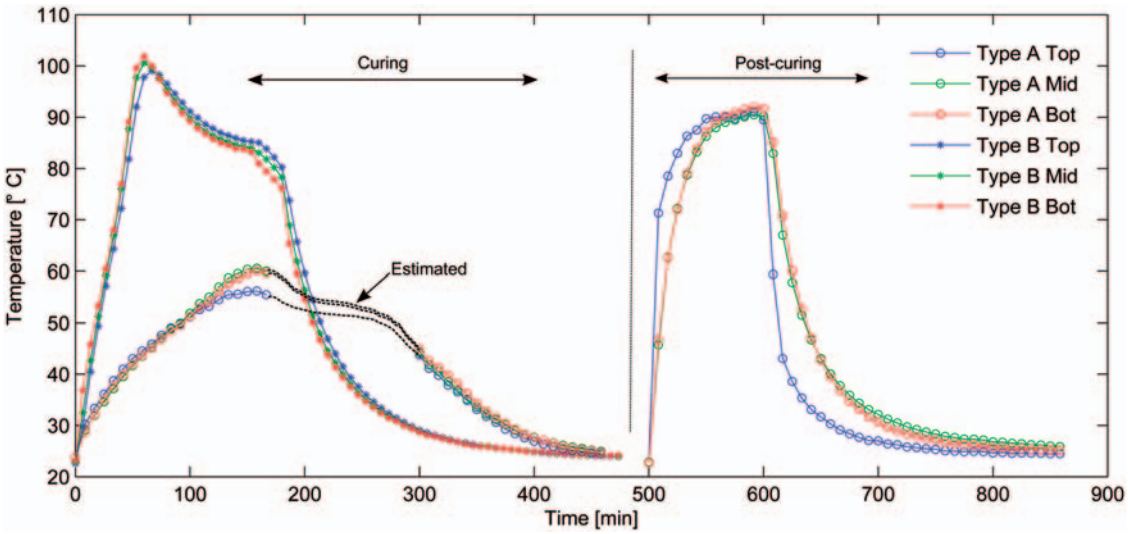

Figure 13. Temperature profiles for type A and B cure cycle laminate beam samples during curing. Note that only type A specimens are post-cured.

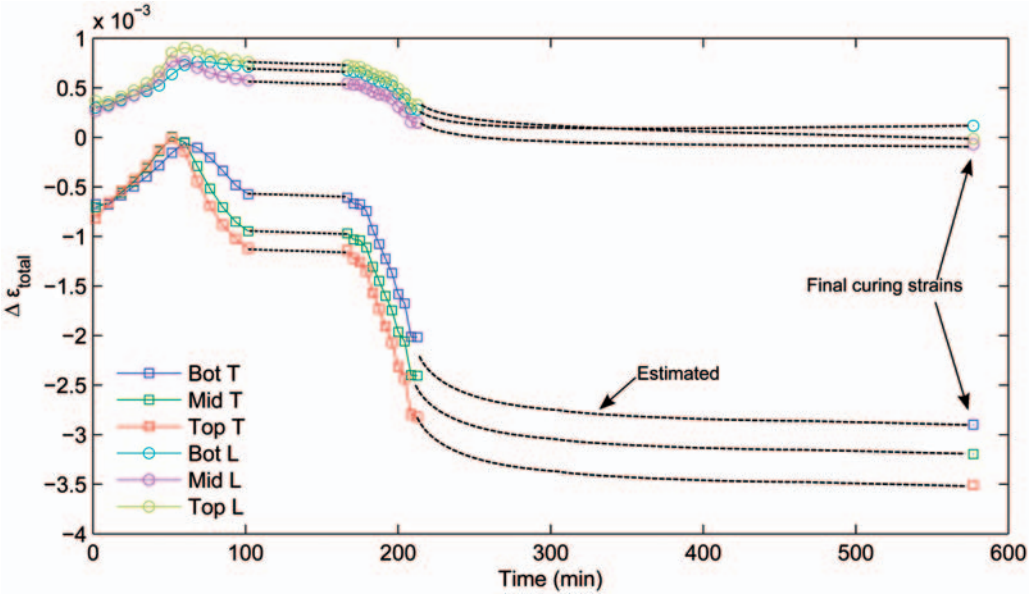

Figure 14. In situ total strain measurements during curing for type B specimen. Dotted lines are added for continuity where loss of signal occurred.

temperatures are approximately 60.1°C and 100.6°C during in mould cure, while the peak post-cure temperature is 98.3°C measured towards the end of the 90°C post-cure temperature hold for type A beam specimens. The peak temperatures are measured at the laminate mid-layer. The temperature peaks during post-curing is due to the release of residual latent heat which was not fully released during the first heating cycle.

In situ strain monitoring during curing is shown in Figure 14 for a type B beam using averaged values for top, mid and bot (T and L) sensor measurements as calculated using equation (1). Where loss of signal from the interrogator unit was encountered, dotted lines are added for the sake of continuity based on the temperature profiles observed from Figure 13 during cooling. The in situ strain development generally follows the temperatures for type B specimens well (Figure 13) depicting an increase upon heating, a peak, dwell and decrease in strains during cooling. Early in the process, thermal expansion- and chemical cure shrinkage strains occur simultaneously, resulting

in negative strains after the exothermic reaction has occurred. This is mainly seen in the transverse (matrix driven) direction. In both the L- and T-directions, the higher mechanical constraints at the bottom layer, in both T- and L-directions, result in lower negative and positive strains, respectively, as compared to strain magnitudes at mid and top. Upon the onset of cooling after approximately 160 min, negative strain increments in the T- and L-directions are seen, owing primarily to thermal contraction, assuming the resin is fully cured and total chemical cure shrinkage has occurred. The strains after cooling are also shown, corresponding to the 'after curing' strains previously shown in Figures 6 and 7.

Simple analytic calculations based on the self-consistent field micromechanic model are made to validate the cure strain magnitudes found. The effective laminate longitudinal and transverse thermal strain increments can be calculated using[3]

$$\Delta\varepsilon_L^{th} = \left[\frac{\alpha_f E_f V_f + \alpha_m E_m (1 - V_f)}{E_{1f} V_f + E_m (1 - V_f)}\right] \cdot \Delta T \tag{2}$$

$$\begin{aligned}\Delta\varepsilon_T^{th} = \Big\{&\big(\alpha_f + \nu_{12f}\alpha_f\big) V_f + (\alpha_m + \nu_m \alpha_m)\big(1 - V_f\big) \\ &- \big[\nu_{12f} V_f + \nu_m \big(1 - V_f\big)\big] \\ &\times \left[\frac{\alpha_f E_f V_f + \alpha_m E_m \big(1 - V_f\big)}{E_f V_f + E_m \big(1 - V_f\big)}\right]\Big\} \cdot \Delta T\end{aligned} \tag{3}$$

where E, α and ν are the respective constituent modulus, coefficient of thermal expansion (CTE) and Poisson's ratio and V_f the reinforcement fibre volume fraction. The subscripts f and m denote fibre and matrix specific quantities and ΔT the change in temperature. Assuming that the resin is in glassy state the instant the peak exothermic temperature is achieved, the temperature variation during the cooling phase (i.e. from the peak cure temperature to ambient) can be used to calculate the thermal strain increments. Results are summarised in Table 3.

The analytically determined transverse thermal strains coincide well with the experimentally determined FBG strain values, measured at the least constrained laminate layer, namely the top layer. A large discrepancy is seen when comparing the longitudinal strains, which could be due to the larger influence of the tool interaction along the length of the beam. It is believed that the poor agreement in analytical and experimental strains in the longitudinal fibre direction may generally owe to the positive pre-straining of the fibres in this direction once the vacuum pressure was applied and during infusion (Figures 6 and 7). Note that the analytical calculations do not take into account gelation, differential resin material CTE in rubbery and glassy state or chemical shrinkage strains. If one wishes to accurately predict these effects, numerical process models could be used.

Table 3. Analytical thermal strain increment during cooling compared to measured total strains at the laminate beam top plane.

	Type A	Type B
ΔT (°C)	−38.6	−79.6
$\Delta\varepsilon_L^{th}$	−0.281E − 3	−0.579E − 3
$\Delta\varepsilon_T^{th}$	−1.80E − 3	−3.60E − 3
$\Delta\varepsilon_L^{tot}$ − FBG	−0.06E − 3	−0.001E − 3
$\Delta\varepsilon_T^{tot}$ − FBG	−1.34E − 3	−3.50E − 3

FBG: fibre Bragg grating.

Flexural tests – Three-point bending

Although large process-induced strains were seen to develop in the T-direction during curing, only small strains were measured in the L-direction. Hence, large residual stresses in the L-direction may still exist that are not released into distortions upon demoulding or relaxed during post-curing. At a micromechanical level, resin cure shrinkage and contraction upon cooling result in a tensile stress state in the L-direction in the matrix, due to constraints posed by the reinforcement fibres. In turn, the reinforcement fibres are in a compressive stress state upholding equilibrium. Whether these residual stresses influence the composite mechanical behaviour during loading is investigated using simple flexure tests. Figure 15 shows a schematic of the flexure test beam samples and sensor placement.

The tests were conducted in a custom made three-point test rig with adjustable rolling cylindrical supports (Figure 15), using an MTS 810 axial servo-hydraulic table top test, with a ±180 mm stroke and force capacity of 25 kN. The loading and support nose cylinder diameters are 40 and 25 mm, respectively. A large nose radius was used to avoid excessive indentations and failure due to stress concentrations directly under the loading point. The test rig is connected to the load cell and hydraulic piston by serrated grips. The piston is controlled through the MTS FlexTest system by a servo valve model 525-15A-04 with a maximum flow of 10 L/s and load cell model 662.10A-05. A cross-head rate of 0.5 mm/min is used and tests are conducted until a substantial drop in the specimen load-carrying capacity is exhibited. The strain at the top and bottom surface of the test specimen is acquired from four SG located at the top and bottom surface along the same beam cross section as the embedded FBG sensors (Figure 15). Strains are measured along the laminate

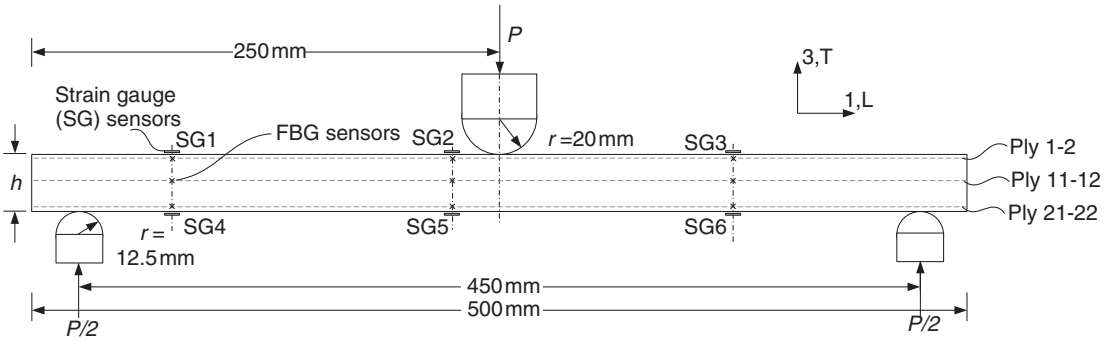

Figure 15. Schematic of three-point flexure test setup of laminate beam specimens. Also seen are the embedded FBG fibres and SGs (SG1–SG4).
FBG: fibre Bragg grating; SG: strain gauge.

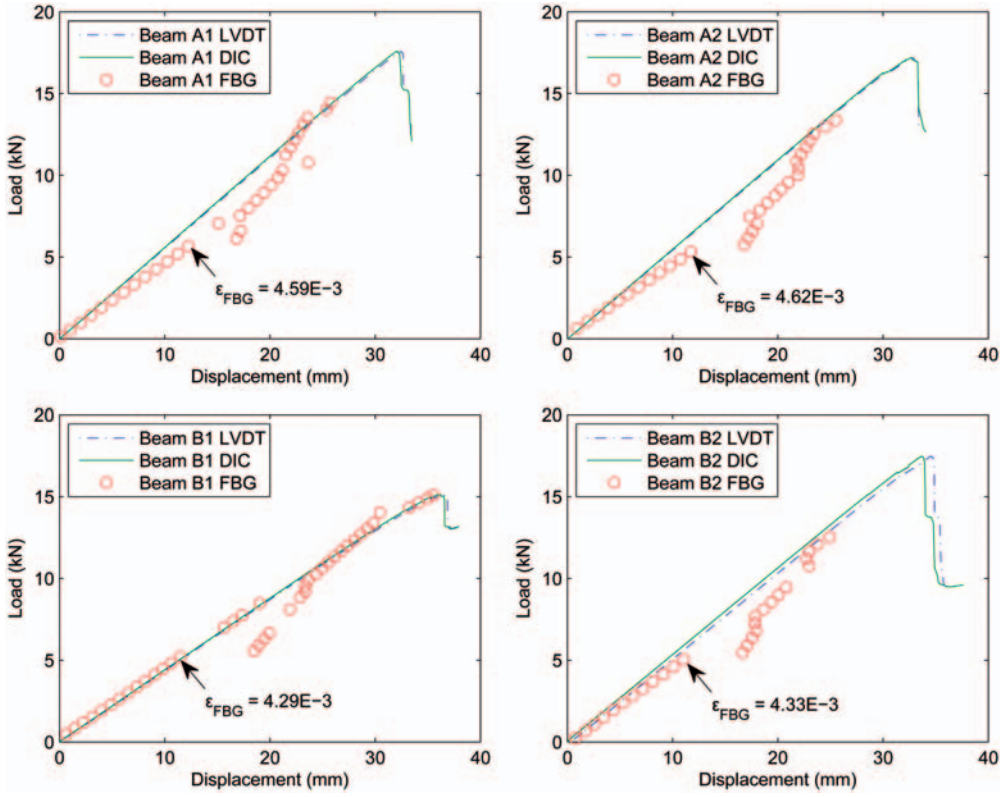

Figure 16. Flexural test load–displacement results for type A and B specimens using displacement measurements from test rig LVDT, DIC and embedded FBG sensors at laminate top centre point.
LVDT: linear variable differential transformer; DIC: digital image correlation; FBG: fibre Bragg grating.

beam longitudinal direction. Furthermore, DIC as well as the test rig linear variable differential transformer (LVDT) sensor is used to measure displacements during loading. DIC measurements are performed in order to avoid using inaccurate LVDT displacement results that may also take into account deformation of the test rig.

Results and discussions

Figure 16 shows the flexural response of beam specimens type A and B using load–displacement plots. Displacements are shown for the embedded FBG, DIC and the test rig LVDT data for comparison. The data represents vertical displacements at the

laminate/loading nose contact point. The LVDT and DIC displacements correspond well throughout the loading range, which indicates that no significant deformations occur in the test rig itself. FBG strains measured at the laminate top centre (and bottom centre for validation) are converted to vertical displacements using the following geometric relations

$$\delta = \rho[1 - \cos(\theta)]$$

where

$$\rho = \frac{h/2}{\Delta\varepsilon_{\{FBG\}}} \text{ and } \theta = \sin^{-1}\left(\frac{L/2}{\rho}\right) \quad (4)$$

In equation (4) δ is the vertical displacement, ρ the chord length and θ is the angle of curvature. A good agreement between the FBG, DIC and LVDT displacements is seen in the early stages of loading, albeit gradually diverging. The FBG displacements increase linearly with the load until a threshold strain is reached (ε_{FBG} in Figure 16) after which the signal becomes sporadic and inconsistent, marking sensor failure. The strain is also seen to be lower in type B beams due to the higher initial process-induced strains which lower the fracture strain of the optical fibre. The strain range of the FBG is given by the supplier to be approximately 5000 με, which both type A and B specimens in Figure 16 lie below, more so for type B beams. This may indicate that the slight compressive pre-straining of the FBG sensors in the *L*-direction during processing (see Figure 8 (L-4)) decreases the strain to failure of the sensors.

Flexural test results from all beam specimens were collected using load–DIC displacement data. From the test results, the flexural modulus E_f of each beam is found using the slope of the load–displacement curves along the linear regime as[27]

$$E_f = \frac{S^3 m}{4bh^3} \quad (5)$$

where S is the support span, b the width and h the thickness of the beams. The flexural strength of the respective specimens is the stress at the surface upon failure, calculated assuming a linear stress–strain relationship up to failure as[27]

$$\sigma_{cr} = \frac{3P_{cr}S}{2bh^2} \quad (6)$$

Table 4. Flexural test modulus, failure load and flexural strength for all tested specimens.

	Type A					Type B				
	A 1	A 2	A3	A 4	Average	B 1	B 2	B 3	B4	Average
h (mm)	19.10	18.56	19.17	19.10	18.98	19.56	19.45	19.05	19.42	19.37
E_f (GPa)	39.26	40.60	39.36	38.06	39.32	37.86	38.45	38.65	38.70	38.23
P_{cr} (kN)	17.583	16.593	17.198	15.992	16.84	18.312	17.156	17.468	17.930	17.72
σ_{cr} (MPa)	708.04	722.55	701.89	657.54	697.53	717.92	680.24	721.88	712.92	708.32

Respective beam specimen thickness (h) measured at the laminate centre, are also seen.

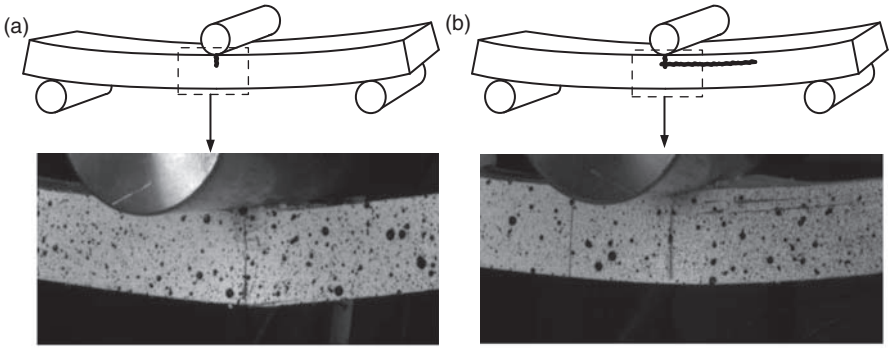

Figure 17. Images capturing failure progression using DIC during fracture. Failure starts for most specimens as compressive fracture at the top laminate layer (a), and later develops to compressive fracture with interlaminar shear (b).
DIC: digital image correlation.

where P_{cr} is the load at the moment of fracture. The experimentally determined flexural modulus and failure load is presented for all specimens in Table 4 as well as the flexural strength of each specimen, determined using equation 6. From Table 4, beam type A and B average failure loads are 16.84 and 17.72 kN, respectively, resulting in average flexural strength values of 697.5 and 708.3 MPa, respectively. As these results highly depend on the thickness of the specimens (as h is squared in equation (6)) substitution of P_{cr} in equation (6) with normalised failure loads for 20 mm thick beam specimens is conducted resulting in average flexural strength values of 771.1 and 716.5 MPa for type A and B specimens, respectively. Note that in Table 4, no distinct differences are seen between beam specimens with embedded optical fibres (i.e. A1, A2, B1 and B2) and without.

DIC was also utilised to monitor the onset of failure (Figure 17). For all 10 beam specimens, failure modes were first visible after the maximum load was reached. From the DIC images, the first failure modes seen for a majority of the specimens was compressive fracture at the top surface, followed second by a number of specimens exhibiting compressive fracture with interlaminar shear. No distinct failure mode type accredited to only type A or B specimens was visible.

Conclusion

A life cycle approach where strain monitoring using embedded FBG sensors in E-glass/epoxy composite laminate beam specimens from manufacturing to failure in three-point bending was conducted. The embedded FBG sensors successfully monitored resin flow front progression during infusion and internal strain development during curing as well as at subsequent intervals until loading to failure. Process-induced strains were seen to reflect the differences in processing temperatures and tool/part interface interactions well. Laminates cured at 80°C for 3 h induced larger internal strains than those cured at 50°C for 5 h. It was shown that process-strains in the transverse reinforcement fibre direction were large enough to result in a decrease in FBG signal quality due to peak splitting and signal distortion for specimens cured at 80°C. No such signal distortions were seen in specimens cured at 50°C for 5 h with subsequent post-curing at 90°C for 2 h. Flexural tests were conducted showing no significant effect of the process-induced stresses and strains on the longitudinal flexural stiffness or failure strength of the specimens. This could owe to the simplicity of the analysed UD laminate beam specimens, which readily releases most residual stresses due to lack of significant internal or external constraints. Furthermore, it can be questioned whether small specimens, similar to the beams used in this study, are representative measures for the behaviour of large FRP structures. In such structures, thicker laminate sections and complex geometries incorporating internal constraints could play a role, not to mention the likelihood of including manufacturing defects such as voids, dry spots or matrix cracks to name a few. However, a difference in the failure strain of the embedded FBG sensors was seen for specimens cured at 50°C and post-cured at 90°C as compared to specimens cured at 80°C with the latter resulting in lower sensor failure strains. Hence, if embedded FBG sensors are to be used for in-service strain monitoring of composite structures where large deformations are expected, process-induced pre-straining of the FBG sensors should be taken into account.

The manufacturing and loading strain monitoring conducted in this study can be utilised to validate an integrated numerical process and loading model where the effects of process-induced residual stresses on the composite response under loading and failure strength can be analysed. Moreover, use of embedded FBG sensors offers the ability to measure and track part consistency during processing. The procedure presented in this article is applicable for strain monitoring of composite structures from manufacture to in-service use.

Funding

This study is supported by Danish Energy Agency through the Energy Technology Development and Demonstration Programme (EUDP). The supported EUDP-project is titled 'Demonstration of new blade design using manufacturing process simulations' and has journal no. 64009-0094. The support is gratefully acknowledged.

Conflict of interest

None declared.

References

1. Favre JP. Residual thermal stresses in fibre reinforced composite materials - a review. *J Mech Behav Mater* 1988; 1(1–4): 37–53.
2. Hahn HT. Effects of residual stresses in polymer/matrix composites. *J Astronaut Sci* 1984; 32(2): 253–267.
3. Bogetti TA and Gillespie JW. Process-induced stress and deformation in thick-section thermoset composite laminates. *J Compos Mater* 1992; 26: 626–659.
4. Kim KS and Hahn HT. Residual stress development during processing of graphite/epoxy composites. *Compos Sci Technol* 1989; 36: 121–132.
5. Zhao LG, Warrior NA and Long AC. A micromechanical study of residual stress and its effect on transverse failure in polymer-matrix composites. *Int J Solids Struct* 2006; 43: 5449–5467.
6. Stone MA, Schwarz IF and Chandler HD. Residual stresses associated with post-cure shrinkage in GRP tubes. *Compos Sci Technol* 1997; 57: 47–54.

7. Nedele MR and Wisnom MR. Three-dimensional finite element analysis of the stress concentration at a single fibre break. *Compos Sci Technol* 1994; 51(4): 517–524.
8. Johnston A. *An integrated model of the development of process-induced deformation in autoclave processing of composite structures*. PhD Thesis, University of British Columbia, Vancouver, Canada, 1997.
9. Svanberg JM. *Predictions of manufacturing induced shape distortions - high performance thermoset composites*. PhD Thesis, Luleå University of Techology, Luleå, Sweden, 2002.
10. Twigg G, Poursartip A and Fernlund G. Tool-part interaction in composites processing. Part II: numerical modelling. *Composites Part A* 2004; 35: 135–141.
11. Wisnom MR, Gigliotti M, Ersoy N, et al. Mechanisms generating residual stresses and distortion during manufacture of polymer-matrix composite structures. *Composites Part A* 2006; 37: 522–529.
12. Fernlund G, Rahman N, Courdji R, et al. Experimental and numerical study of the effect of cure cycle, tool surface, geometry, and lay-up on the dimensional fidelity of autoclave-processed composite parts. *Composites Part A* 2002; 33: 341–351.
13. Luyckx G, Voet E, Lammens N, et al. Strain measurements of composite laminates with embedded fibre Bragg gratings: criticism and opportunities for research. *Sensors* 2011; 11: 384–408.
14. Eum SH, Kageyama K, Murayama H, et al. Process/health monitoring for wind turbine blade by using FBG sensors with multiplexing techniques. In: *Proceedings of SPIE 2008 conference*, Perth, Australia, 14–18 April, 2008, vol. 7004, pp.5B1–5B4.
15. Khoun L, de Oliviera R, Michaud V, et al. Investigation of process-induced strains development by fibre Bragg grating sensors in resin transfer moulded composites. *Composites Part A* 2011; 42: 274–282.
16. Parlevliet P, Voet E, Bersee H, et al. Process monitoring with FBG sensors during vacuum infusion of thick composite laminates. In: *Proceedings of 16th ICCM conference*, Kyoto, Japan, 3–8 July 2007.
17. De Waele W. *Structural monitoring of composite elements using optical fibres with Bragg sensors*. PhD Thesis, Ghent University, Ghent, Belgium, 2002.
18. Guemes JA and Mendez JM. Response of Bragg grating fiber-optic sensors when embedded in composite laminates. *Compos Sci Technol* 2002; 62: 959–966.
19. Nielsen MW, Schmidt JW, Hattel JH, et al. In-situ measurement using FBGs of process-induced strains during curing of thick glass/epoxy laminate plate: experimental results and numerical modelling. *Wind Energy* 2012. DOI: 10.1002/we.1550.
20. Mulle M, Collombet F, Olivier P, et al. Assessment of cure-residual strains through the thickness of carbon-epoxy laminated using FBGs Part II: technological specimen. *Composites Part A* 2009; 40: 1534–1544.
21. Parlevliet E, Bersee H and Beukers A. Measurement of (post-) curing strain development with fibre Bragg gratings. *Polym Test* 2010; 29: 291–301.
22. de Oliviera R, Lavanchy S, Chatton R, et al. Experimental investigation of the effect of the mould thermal expansion on the development of internal stresses during carbon fibre composite processing. *Composites Part A* 2008; 39: 1083–1090.
23. Eum SH, Kageyama K, Murayama H, et al. Resin flow front monitoring for VARTM using fiber Bragg gratings. In: *Proceedings 16th ICCM conference*, Kyoto, Japan, 8–13 July 2007.
24. Gupta N and Sundaram R. Fiber optic sensors for monitoring flow in vacuum enhanced resin infusion technology (VERITy) process. *Composites Part A* 2009; 40(8): 1065–1070.
25. Saton K, Fukuchi K, Kurosawa Y, et al. Polyimide-coated small-diameter optical fiber sensors for embedding in composite laminate structures. *Proc SPIE* 2001; 4328: 285–294.
26. Jensen DW and Sirkis JS. Integrity of composite structures with embedded optical fibers. In: Udd E (ed.) *Fiber optic smart structures*. New York: Wiley, 1995, pp.109–129.
27. Hodgkinson JM. *Mechanical testing of advanced fibre composites*. Boca Raton, FL: CRC Press, 2000.
28. Dow Chemical Company. Airstone Infusion systems, Form No. 296-01856-0808-BH, 2012.

This PhD dissertation presents a single-component hybrid simulation approach for substructural scale testing of large composite structures. A communication loop, which accommodates single-component hybrid simulation is designed and implemented in LabVIEW. The system is verified within the quasi-static and real-time regime for the operation of a shared boundary including a discrete point with up to three degrees-of-freedom. Finally, an initial strategy is presented to form the basis for an upcoming single-component hybrid simulation on an SSP34m wind turbine blade.

DTU Civil Engineering
Technical University of Denmark

Brovej 118
2800 Kgs. Lyngby

www.byg.dtu.dk

ISBN 9788778774477
ISSN 1601-2917